**UNIVERSITY OF SOUTHAMPTON**

FACULTY OF PHYSICAL SCIENCES AND ENGINEERING

Physics and Astronomy

# Continuum limit of $D$ and $D_s$ decay constants with Moebius domain wall fermions at physical pion masses

by

**Justus Tobias Tsang**

Thesis for the degree of Doctor of Philosophy

January 2017

UNIVERSITY OF SOUTHAMPTON

ABSTRACT

FACULTY OF PHYSICAL SCIENCES AND ENGINEERING
Physics and Astronomy

Doctor of Philosophy

# CONTINUUM LIMIT OF $D$ AND $D_S$ DECAY CONSTANTS WITH MOEBIUS DOMAIN WALL FERMIONS AT PHYSICAL PION MASSES

by Justus Tobias Tsang

The inclusion of heavy quarks, such as the charm quark, poses difficulties in Lattice QCD simulations. These need to be overcome in order to make predictions of hadronic observables including a charm quark such as the decay constants $f_D$ and $f_{D_s}$. We first establish the region of validity of simulating heavy quarks with domain wall fermions (DWFs) in a feasibility study. We then carry out dynamical simulations with RBC/UKQCD's $N_f = 2 + 1f$ ensembles at three lattice spacings ($a^{-1} = 1.73 - 2.77\,\text{GeV}$) including two physical pion mass ensembles. From this we make a prediction for the decay constants $f_D$ and $f_{D_s}$ and, using experimental input, the corresponding CKM matrix elements.

In the first part of this work we investigate the suitability of domain wall fermions (DWF) as a lattice regularisation for heavy quarks. We generate four quenched QCD gauge ensembles with the tree-level improved Symanzik gauge action and inverse lattice spacings in the range $2.0 - 5.7\,\text{GeV}$. On these we carry out an exploratory study to identify a region in the DWF parameter space that displays minimal cut-off effects. We find this region for the domain wall height $M_5 = 1.6$ allowing for bare heavy quark masses satisfying $am_h \lesssim 0.4$, independent of the lattice spacing. Below this limit we maintain desirable features of DWF such as approximate chiral symmetry and $O(a)$-improvement. Based on this, we carry out a detailed scaling study of the decay constants of heavy-strange pseudoscalar mesons and the dispersion relation of heavy-heavy and heavy-strange pseudoscalar mesons. We find mild $a^2$ discretisation effects for the heavy-strange decay constants and the heavy-strange dispersion relation. The cut-off effects for the heavy-heavy pseudoscalar dispersion relation are somewhat more pronounced. On our ensembles we find $a^4$ effects for heavy masses beyond the charm quark mass and large momenta ($|p| \sim 1.6\,\text{GeV}$). The findings of the pilot study establish the basis for simulations of charm quarks with domain wall fermions.

In the second part of the presented work we simulate heavy-light and heavy-strange pseudoscalar mesons on RBC/UKQCD's $2 + 1f$ ensembles with pion masses as low

as 139 MeV and inverse lattice spacings ranging from 1.73 GeV to 2.77 GeV. From this data we extract the decay constants $f_D$ and $f_{D_s}$. We devise two different fit ansätze to process this data and carry out a full systematic error analysis. We find $f_D = 208.7(2.8)_{\text{stat}} \left(^{+2.1}_{-1.8}\right)_{\text{sys}}$ MeV, $f_{D_s} = 246.4(1.9)_{\text{stat}} \left(^{+1.3}_{-1.9}\right)_{\text{sys}}$ MeV and $f_{D_s}/f_D = 1.1667(77)_{\text{stat}} \left(^{+60}_{-46}\right)_{\text{sys}}$.

Finally, using experimental input we extract the corresponding CKM matrix elements. We find $|V|_{cd} = 0.2185(50)_{\text{exp.}} \left(^{+35}_{-37}\right)_{\text{lat}}$ and $|V|_{cs} = 1.011(16)_{\text{exp.}} \left(^{+11}_{-\ 9}\right)_{\text{lat}}$ where the first error comes from the experimental input and the second from our determination of the decay constants. We compare our results with the existing literature and find good agreement between our central values and competitive errors. This work constitutes the basis of RBC/UKQCD's wider charm physics program.

# Contents

# List of Figures

# List of Tables

## Declaration of Authorship

I, Justus Tobias Tsang , declare that the thesis entitled *Continuum limit of $D$ and $D_s$ decay constants with Moebius domain wall fermions at physical pion masses* and the work presented in the thesis are both my own, and have been generated by me as the result of my own original research. I confirm that:

- this work was done wholly or mainly while in candidature for a research degree at this University;
- where any part of this thesis has previously been submitted for a degree or any other qualification at this University or any other institution, this has been clearly stated;
- where I have consulted the published work of others, this is always clearly attributed;
- where I have quoted from the work of others, the source is always given. With the exception of such quotations, this thesis is entirely my own work;
- I have acknowledged all main sources of help;
- where the thesis is based on work done by myself jointly with others, I have made clear exactly what was done by others and what I have contributed myself;
- parts of this work have been published as: [10], [11], [12], [13], [14], [15], [16] and [17]

Signed:.....

Date:.....

# Acknowledgements

First and foremost I want to thank Dr Andreas Jüttner for his supervision, help, patience and support during the last four years.

I would like to thank Marina Kristić Marinković, Francesco Sanfilippo and Peter Boyle for help throughout the different projects and Shoji Hashimoto at K.E.K. for kindly hosting me there for collaborative work. I would like to thank all my coauthors for the different projects for their fruitful collaboration, help and cross checks. Many useful comments, discussions and suggestions by members of the lattice group in Southampton in particular and of the RBC/UKQCD collaborations have aided this work.

I want to thank the SHEP group and in particular my fellow presenters for *Accelerate!* for all their support and an inspiring environment.

In addition to many helpful conversations I would like to thank Andrew Meadowcroft and all other members of *Doppelkopf* for four fantastic years in Southampton. I thank the badminton clubs of the University of Southampton for providing me with some balance.

Last but not least I want to thank the European Research Council for supporting my work. I acknowledge that the research leading to these results has received funding from the European Research Council under the European Unions Seventh Framework Programme (FP7/2007-2013) / ERC Grant agreement 279757. I further acknowledge the use of the IRIDIS High Performance Computing Facility, and associated support services at the University of Southampton, in the completion of this work. I also gratefully acknowledge computing time granted through the STFC funded DiRAC facility (grants ST/K005790/1, ST/K005804/1, ST/K000411/1, ST/H008845/1).

# Nomenclature

| | |
|---|---|
| BC | Boundary Condition |
| C | Charge Conjugation |
| CG | Conjugate Gradient |
| CKM | Cabibbo-Kobayashi-Maskawa |
| DWF | Domain Wall Fermions |
| EM | Electromagnetic |
| EW | Electroweak |
| EWSB | Electroweak Symmetry Breaking |
| FCNC | Flavour Changing Neutral Currents |
| FLAG | Flavour Lattice Averaging Group |
| FT | Fourier Transform |
| GIM | Glashow-Iliopoulos-Maiani |
| HDCG | Hierarchically Deflated Conjugate Gradient |
| HMC | Hybrid Monte Carlo |
| HQ | Heavy Quark |
| HQET | Heavy Quark Effective Theory |
| J | Spin |
| L | Local |
| LQCD | Lattice Quantum Chromodynamics |
| MCMC | Markov Chain Monte Carlo |
| MDWF | Moebius Domain Wall Fermions |
| NP | New Physics |
| NPR | Non-Perturbative Renormalisation |
| NRQCD | Non-relativistic Quantum Chromodynamics |
| P | Parity |
| PCAC | Partially Conserved Axial Current |
| PDG | Particle Data Group |
| PS | Pseudoscalar |
| QCD | Quantum Chromodynamics |
| QED | Quantum Electrodynamics |
| QFT | Quantum Field Theory |
| QM | Quantum Mechanics |

| | |
|---|---|
| RGE | Renormalisation Group Equation |
| RHQ | Relativistic Heavy Quark |
| S | Smeared |
| SDWF | Shamir Domain Wall Fermions |
| SM | Standard Model |
| snk | Sink |
| SR | Special Relativity |
| src | Source |
| SSB | Spontaneous Symmetry Breaking |
| T | Time Reversal |
| UV | Ultraviolet |

# Chapter 1

# Introduction

The aim of particle physics is to probe our understanding of the forces governing nature at the smallest length scales. We have a well established theoretical model of the known fundamental particles called the *Standard Model* (SM), which describes their interactions under the strong, the weak and the electromagnetic forces. Whilst this model is in good agreement with experimentally measured observables, it still stands in contrast to some observations that indicate shortcomings. For example, it fails to explain dark matter and dark energy. This implies that there is yet unknown *New Physics* (NP), which particle physicists hope to discover and understand.

To date, we lack a clear indication of discrepancies between theoretical predictions (from the SM) and experimental measurements. This situation might change with the accumulation of more experimental data at current and future experiments, and the associated increase in precision. However, to be able to draw conclusions from this we also need to reduce the theoretical uncertainty to a comparable precision. One way in which the validity of the SM can be tested is by over-constraining its parameters by studies of different processes which involve the same parameters.

Many predictions from the SM can be made to high precision by analytical calculations, however there are some, in particular concerning processes involving the strong force at low energies, for which this is not the case. In such cases one has to resort to alternative methods, such as effective theories or other non-perturbative tools. Methods concerned with large scale numerical simulations of non-perturbative dynamics are described collectively by the fields of Lattice Quantum Field Theories (LQFTs), which in the case of the strong interaction is Lattice Quantum Chromodynamics (LQCD).

In this work, we develop a formalism that allows us to simultaneously simulate charm quarks and physical light quarks, whilst maintaining control over all systematic errors. This is done by first carrying out a pilot study in chapter 5 to test our mechanism, which is then used in large scale simulations including ensembles with physical pion

masses. From these simulations we make a prediction for quantities (the decay constants) associated with charmed mesons. In combination with experimentally measured data and other known inputs, this leads to the determination of two of the fundamental parameters of the SM.

The main result of the pilot study is the region of parameter space in which we can simulate heavy quarks with Moebius domain wall fermions (MDWF), defined by

$$\begin{aligned} M_5 &= 1.6 \qquad \text{and} \\ am_h &\lesssim 0.4. \end{aligned} \tag{1.1}$$

Here $M_5$ is a parameter specific to our choice of discretising the fermions action, called domain wall fermions (DWFs), whilst $a$ is the lattice spacing and $m_h$ is the mass of the heavy quark in bare units.

Our main prediction from simulations with physical pion masses are the $D$ and $D_s$ decay constants $f_D$ and $f_{D_s}$, respectively, their ratio and the Cabibbo-Kobayashi-Maskawa (CKM) matrix elements $|V_{cd}|$ and $|V_{cs}|$. The numerical results are

$$\begin{aligned} f_D &= 208.7(2.8)_{\text{stat}} \left(^{+2.1}_{-1.8}\right)_{\text{sys}} \text{ MeV} \\ f_{D_s} &= 246.4(1.9)_{\text{stat}} \left(^{+1.3}_{-1.9}\right)_{\text{sys}} \text{ MeV} \\ \frac{f_{D_s}}{f_D} &= 1.1667(77)_{\text{stat}} \left(^{+60}_{-46}\right)_{\text{sys}} \\ &\text{and} \\ |V_{cd}| &= 0.2185(50)_{\text{exp}}(^{+35}_{-37})_{\text{lat}} \\ |V_{cs}| &= 1.011(16)_{\text{exp}}(^{+11}_{-\ 9})_{\text{lat}}. \end{aligned} \tag{1.2}$$

Combined with determinations of other CKM matrix elements this allows for a test of the unitarity of the CKM matrix and therefore of the SM.

Whilst these are quantities that have been computed in the past, to date there is only one other result that simulates directly at physical pion masses [18] and our result is amongst the most precise determinations. Furthermore, our mechanism extends beyond the physical value of the charm quark mass and could, in the future, be used to extrapolate to predictions for mesons containing a $b$ quark. Finally, our set-up allows for the inclusion of charm quarks in the wider RBC/UKQCD physics programme, allowing for other quantities to be determined.

The remainder of this thesis is structured as follows: In chapter 2 a brief introduction to the SM and its properties is presented. In chapter 3 we will introduce Lattice QCD and its methods, followed by a more detailed discussion of our particular formulation of Lattice QCD, namely domain wall fermions (DWFs) in chapter 4. In chapter 5 we will introduce and summarise the results of the pilot study which explores the possible parameter space of our simulations. Having found an optimal point in this parameter

space, in chapter 6 we then present the study of the decay constants at physical pion masses, which produces the main results of this thesis. Finally, we summarise our results and outline possible applications and future work in chapter 7.

I note that the following three chapters do not present original work but rather summarise knowledge I have obtained from textbooks, reviews, lectures and discussions. I want to explicitly acknowledge some quantum field theory (QFT) textbooks [9, 19, 20], lattice quantum chromodynamics (LQCD) text books [21–24] and reviews published by the Particle Data Group (PDG) [1]. I want to particularly highlight that I obtained a significant part of the knowledge presented in this chapter from *Part III of the Mathematical Tripos* which I took in 2011/12.

# Chapter 2

# The Standard Model of Particle Physics

The Standard Model (SM) describes the interactions of the known fundamental (as opposed to composite) particles under the strong, the weak, and the electromagnetic forces. The SM is based on symmetries, which we can observe in nature. In particular, it is a quantum gauge theory, meaning it is described by a local gauge group. It is defined by constructing the most general Lagrangian that satisfies these symmetries.

In the following, we will first outline the underlying symmetries of the SM (section 2.1), then we will introduce the particle content of the SM in section 2.2, before constructing the Lagrangians of the *electroweak sector* and the *strong sector* in sections 2.3 and 2.4, respectively. From this we will derive the CKM matrix in section 2.5 and discuss how we can determine these in practice in section 2.6. Finally Heavy Quark (HQ) physics is discussed in section 2.7.

## 2.1 Symmetries of the Standard Model

The SM Lagrangian includes all Lorentz invariant terms, whilst also being gauge invariant under $SU(3)_C$, $SU(2)_L$ and $U(1)_Y$ gauge symmetries.

There are also three important discrete symmetries called *parity* (P), *charge conjugation* (C) and *time reversal* (T). Parity reverses the spatial coordinates of each point in space-time, whilst time reversal reverses time, i.e.

$$\begin{aligned} x^\mu = (x_0, \boldsymbol{x}) &\xrightarrow{P} x^\mu_P = (x_0, -\boldsymbol{x}) \\ x^\mu = (x_0, \boldsymbol{x}) &\xrightarrow{T} x^\mu_T = (-x_0, \boldsymbol{x})\,. \end{aligned} \tag{2.1}$$

Charge conjugation interchanges particles with their antiparticles. If an interaction obeys any of the above discrete symmetries, it means that physical processes do not change under this transformation.

Experimentally, it is found that the strong force and electromagnetism obey parity as a symmetry, but the weak interaction does not [25, 26]. We will see how this is reflected in the Lagrangian of the weak interaction in section 2.3. It was postulated that the weak interaction might still conserve combined charge conjugation and parity (CP), but is was shown experimentally in 1964 that this is not the case [27]. However, the strong and the electromagnetic forces obey CP symmetry and all three forces obey combined CPT symmetry.

The SM is a quantum gauge theory, and therefore has a local gauge group. This gauge group is

$$SU(3)_{\mathrm{C}} \times SU(2)_{\mathrm{L}} \times U(1)_{\mathrm{Y}}, \tag{2.2}$$

where $C$ stands for *colour*, $L$ stands for *left-handed weak isospin* and $Y$ stands for *Hypercharge*. Throughout this chapter we will see how these symmetries give rise to the force carriers of the SM and reproduce the known interactions. Any term that is included in the Lagrangian of the SM is required to leave said Lagrangian invariant under any of these symmetry transformations.

$SU(2)_L \times U(1)_Y$ is referred to as the *electroweak sector* [28–30] and will be discussed in section 2.3. Whilst this is a symmetry of the Lagrangian, it is spontaneously broken by the vacuum. This phenomenon is called electroweak symmetry breaking (EWSB) [31–34] and gives rise to a number of interesting properties. In particular, this gives rise to the CKM matrix [35, 36], which will be introduced and discussed in section 2.5. $SU(3)_C$ is the gauge group of quantum chromodynamics [37], which gives rise to the strong force. Its properties will be discussed in section 2.4.

## 2.2 Particle Content

In this section, we will give a brief introduction of the fundamental particles present in the SM. Particles with odd-half-integer spin (1/2) are known as *fermions*, particles with integer spin (0, 1) as *bosons*. The fermions come in three *generations* and are further split into *leptons* and *quarks*. The leptons are comprised of the charged leptons (electron $e$, muon $\mu$ and tau $\tau$), each of which has a corresponding neutral *neutrino* ($\nu_e$, $\nu_\mu$, $\nu_\tau$). Composite particles that contain bound states of quarks are called *hadrons*. The known hadrons are *mesons* (containing a quark and an anti-quark) and *baryons* (containing three quarks). Table 2.1 presents a summary of these particles and their interactions.

| | Particles | strong | weak | EM | spin | el. charge |
|---|---|---|---|---|---|---|
| Fermions | charged leptons ($e$, $\mu$, $\tau$) | ✗ | ✓ | ✓ | 1/2 | -1 |
| | neutral leptons ($\nu_e$, $\nu_\mu$, $\nu_\tau$) | ✗ | ✓ | ✗ | 1/2 | 0 |
| | up-type quarks ($u$, $c$, $t$) | ✓ | ✓ | ✓ | 1/2 | +2/3 |
| | down-type quarks ($d$, $s$, $b$) | ✓ | ✓ | ✓ | 1/2 | -1/3 |
| Bosons | photon ($\gamma$) | ✗ | ✗ | ✓ | 1 | 0 |
| | $W^\pm$ | ✗ | ✓ | ✓ | 1 | $\pm$1 |
| | $Z$ | ✗ | ✓ | ✗ | 1 | 0 |
| | gluons ($g$) | ✓ | ✗ | ✗ | 1 | 0 |
| | Higgs | ✗ | ✓ | ✗ | 0 | 0 |

Table 2.1: The known particles of the SM and some of their properties.

## 2.3 Higgs and Electroweak Theory

The *electroweak* part of the SM corresponds to the $SU(2)_L \times U(1)_Y$ part of the gauge group (2.2). As hinted at in the name, the *electroweak* theory [28–30] combines the theory of the *weak interaction* with Quantum Electrodynamics (QED). We have already mentioned that the weak interaction breaks parity, so we will need to ensure that this feature is reproduced by the SM. In the following we will show how spontaneous symmetry breaking (SSB) [31–34] causes the symmetry group $SU(2)_L \times U(1)_Y$ to break into $U(1)_{EM}$ due to the Higgs potential. We will show how this gives rise to the gauge bosons for the weak ($W^\pm, Z^0$) and the electromagnetic force ($\gamma$). In 2012, the Higgs boson was independently discovered by two experiments at CERN, namely by the ATLAS [38] and CMS [39] groups, confirming the final missing piece of the SM.

### 2.3.1 Gauge Fields and the Field Strength Tensor

For the remainder of this chapter (unless stated otherwise), the Einstein summation convention is used, meaning that repeated indices are summed over. We will start by introducing the terms of the Lagrangian that are purely gauge dependent. The corresponding term in the Lagrangian is

$$\mathcal{L}_{\text{gauge}}(x) = -\frac{1}{4} F_{\mu\nu}(x) F^{\mu\nu}(x), \tag{2.3}$$

where the *field strength tensor* $F_{\mu\nu}$ is defined as

$$F_{\mu\nu} = [D_\mu, D_\nu], \tag{2.4}$$

and the covariant derivative $D_\mu$ depends on the underlying gauge symmetry. For $SU(2) \times U(1)$ we have

$$D_\mu = \partial_\mu + igA^a_\mu(x)\tau^a + i\frac{1}{2}g' B_\mu(x) Y. \tag{2.5}$$

Here $\tau^i = \sigma^i/2$ are the $SU(2)$ generators, defined in terms of the Pauli matrices $\sigma^i$ and the index $i = 1, 2, 3$. Some properties of these generators are listed in Appendix A.1.1. $Y$ is the generator of $U(1)_Y$, called *weak-hypercharge*. The gauge fields $A_\mu(x)$ and $B_\mu(x)$ are elements of $SU(2)_L$ and $U(1)_Y$ respectively, $g$ and $g'$ are the couplings of the gauge fields.

### 2.3.2 Fermions in the Standard Model

In the SM, a fermion $\psi$ of mass $m$ is introduced by including a term of the form

$$\mathcal{L}_{\text{Dirac}} = \overline{\psi}(x)\left(i\not{D} - m\right)\psi(x) \tag{2.6}$$

in the Lagrangian. Here $\not{D} = \gamma^\mu D_\mu$, where $\gamma^\mu$ are the Dirac gamma matrices obeying the Clifford algebra as described in Appendix A.2 and $D_\mu$ is the covariant derivative appropriate to the fermions under consideration, e.g. (2.5) for the case of the electron.

We can decompose fermions into a *left-handed* and a *right-handed* part, such that

$$\begin{aligned} \psi &= \psi_L + \psi_R \\ \psi_L &= P_-\psi = \frac{1}{2}\left(\mathbb{1} - \gamma^5\right)\psi \\ \psi_R &= P_+\psi = \frac{1}{2}\left(\mathbb{1} + \gamma^5\right)\psi, \end{aligned} \tag{2.7}$$

where $\gamma_5 = i\gamma_0\gamma_1\gamma_2\gamma_3$. The Dirac part of the Lagrangian (2.6) then becomes

$$\begin{aligned} \mathcal{L}_{\text{Dirac}} &= \overline{\psi}\left(i\not{D} - m\right)\psi \\ &= \left(\overline{\psi}_L i\not{D}\psi_L + \overline{\psi}_R i\not{D}\psi_R\right) - m\left(\overline{\psi}_L\psi_R + \overline{\psi}_R\psi_L\right). \end{aligned} \tag{2.8}$$

Equation (2.8) remains invariant under a rotation of the left-handed and right-handed components by the same phase $\alpha$, $\psi_{L,R} \to e^{i\alpha}\psi_{L,R}$. This $U(1)$ symmetry is known as a *vector symmetry* with the conserved Noether current $J^\mu_V = \overline{\psi}\gamma^\mu\psi$ associated with fermion number. So for the case of leptons, this shows that the lepton number is conserved.

We will now treat left-handed and right-handed fermions differently. We place the left-handed ones into $SU(2)_L$ doublets and the right-handed ones into $SU(2)_L$ singlets. We will see that this ensures that the weak interaction does not obey parity in section 2.3.4.

For $m_f = 0$ we additionally have a so-called *chiral symmetry* or *axial symmetry* $U(1)_A$, where left-handed and right-handed components rotate with a different phase, i.e. $\psi \to e^{i\alpha\gamma^5}\psi$. This is most easily seen in the chiral basis in which $\gamma_5$ is diagonal. The form the gamma matrices take in this basis is presented in Appendix A.2. The associated Noether current for this process is $J^\mu_A = \overline{\psi}\gamma^\mu\gamma_5\psi$ with divergence $\partial_\mu J^\mu_A = 2im\overline{\psi}\gamma_5\psi$, so it is only conserved in the massless limit.

### 2.3.3 Electroweak Symmetry Breaking

In addition to the field strength tensors associated with the $SU(2)_L$ and $U(1)_Y$ gauge groups the electroweak sector includes the Higgs field $\phi$, which enters the Lagrangian as

$$\begin{aligned} \mathcal{L}_{\text{EWSB}} &= (D_\mu \phi)^\dagger (D^\mu \phi) - V(\phi) \\ V(\phi) &= -\mu^2 |\phi|^2 + \lambda |\phi|^4 , \end{aligned} \tag{2.9}$$

where $\mu$ and $\lambda$ are positive real coefficients and $\phi$ is the Higgs fields which is a complex scalar field of the group $SU(2)_L$. $D_\mu$ is the covariant derivative for $SU(2)_L \times U(1)_Y$. We can choose the gauge such that $\phi = \frac{1}{\sqrt{2}} \begin{pmatrix} \phi^+ \\ \phi^0 \end{pmatrix}$ becomes $\phi = \frac{1}{\sqrt{2}} \begin{pmatrix} 0 \\ \phi^0 \end{pmatrix}$ where $\phi^0$ is real. $V(\phi)$ has a non trivial minimum at $|\phi| \neq 0$ and hence acquires a *vacuum expectation value* (vev) $v$

$$\langle \phi \rangle = \frac{1}{\sqrt{2}} \begin{pmatrix} 0 \\ v \end{pmatrix} = \frac{1}{\sqrt{2}} \begin{pmatrix} 0 \\ \sqrt{\frac{2\mu^2}{\lambda}} \end{pmatrix} . \tag{2.10}$$

Note that transformations

$$\phi \to e^{i\alpha^i(x)\tau^i} e^{i\beta(x)/2} \phi, \tag{2.11}$$

with $\alpha^1 = \alpha^2 = 0$ and $\alpha^3 = \beta$ leave $\langle \phi \rangle$ invariant, leaving an intact symmetry even after acquiring the vev, i.e. after *spontaneous symmetry breaking*. This gives rise to one massless gauge boson - the photon.

We now substitute the definition of the covariant derivative (2.5) and the transformation (2.11) into the Lagrangian (2.9) at the point defined by (2.10) and collect terms quadratic in the fields. From this we obtain the masses of the gauge bosons. With the re-definitions of the fields and the generators

$$\begin{aligned} W^\pm_\mu &= \frac{1}{\sqrt{2}} \left( A^1_\mu \mp i A^2_\mu \right) && \text{with} && \tau^\pm = \tau^1 \pm i\tau^2 \\ Z^0_\mu &= \frac{1}{\sqrt{g^2 + g'^2}} \left( g A^3_\mu - g' B_\mu \right) && \text{with} && \cos^2\theta_W \tau^3 - \sin^2\theta_W Y \\ A_\mu &= \frac{1}{\sqrt{g^2 + g'^2}} \left( g A^3_\mu + g' B_\mu \right) && \text{with} && Q = \tau^3 + Y, \end{aligned} \tag{2.12}$$

we find the coefficients of the quadratic terms in these redefined fields to be

$$\begin{aligned} m_W &= g \frac{v}{2} \\ m_Z &= \sqrt{g^2 + g'^2} \frac{v}{2} \\ m_A &= 0. \end{aligned} \tag{2.13}$$

So we find one massless gauge boson $A_\mu$ (the photon) and three massive gauge bosons ($W^\pm$ and $Z$). The charge associated with the remaining $U(1)_{EM}$ symmetry is the electric

charge $Q$, which can be determined by noting that $Q = \tau^3 + Y\mathbb{1}$. Here the quantum numbers $\tau_3$ and $Y$ are the third component of the *weak-isospin* and the *weak hypercharge*, respectively.

Note that at tree-level we can relate the masses $m_W$ and $m_Z$ by

$$m_W = m_Z \cos\theta_W, \tag{2.14}$$

where $\theta_W$ is the *Weinberg angle* defined by

$$\tan\theta_W = \frac{g'}{g}, \qquad \sin\theta_W = \frac{g'}{\sqrt{g^2+g'^2}}, \qquad \cos\theta_W = \frac{g}{\sqrt{g^2+g'^2}}. \tag{2.15}$$

Using this, the covariant derivative for leptons can be written as

$$D_\mu = \partial_\mu - \frac{1g}{\sqrt{2}}\left(W_\mu^+\tau^+ + W_\mu^-\tau^-\right) - \frac{ig}{\cos\theta_W}Z_\mu\left(\tau^3 - \sin^2\theta_W Q\right) - ieA_\mu Q, \tag{2.16}$$

where we defined the unit charge $e = |e| = g\sin\theta_W$.

Within the SM, neutrinos are massless (even though there is now experimental evidence of small neutrino masses [40, 41]). We have seen in (2.8) that the mass term connects left-handed and right-handed parts of a fermion. This means a massless particle (such as the neutrino) has no way to flip chirality and can therefore remain purely left-handed.

Recall further (compare table 2.1) that neutrinos only interact weakly, whilst charged leptons interact weakly and electromagnetically, but not strongly. The $W$ boson only couples to left-handed fermions [28–30]. The electroweak theory is constructed by treating the electron and the neutrino in the same way, by placing the purely left-handed neutrino and the left-handed part of the electron in a doublet $l_e(x)$, which forms a representation of the $SU(2)$ group called *weak-isospin*. The right-handed part of the electron is put into an *weak iso-singlet* $r_e(x)$

$$\begin{aligned} l_e(x) &= \begin{pmatrix} \nu_e(x) \\ e_L(x) \end{pmatrix} \\ r_e(x) &= e_R(x). \end{aligned} \tag{2.17}$$

Ensuring that $e_L$ and $e_R$ carry an electric charge of $-e$ and $\nu_l$ is electrically neutral implies that

$$Ql_e = \begin{pmatrix} 0 & 0 \\ 0 & -1 \end{pmatrix} l_e \qquad\qquad Qr = -r. \tag{2.18}$$

Given $Q = \tau^3 + Y\mathbb{1}$ and $\tau^3 = \frac{\sigma^3}{2}$ we can conclude eigenvalues for $\nu_L$, $e_L$ and $e_R$, which are listed in table 2.2

| fermion | $\tau^3$ | $Y$ | $Q$ |
|---|---|---|---|
| $\nu_L$ | $1/2$ | $-1/2$ | $0$ |
| $e_L$ | $-1/2$ | $-1/2$ | $-1$ |
| $e_R$ | $0$ | $-1$ | $-1$ |
| $u_L$ | $1/2$ | $1/6$ | $2/3$ |
| $u_R$ | $0$ | $2/3$ | $2/3$ |
| $d_L$ | $-1/2$ | $1/6$ | $-1/3$ |
| $d_R$ | $0$ | $-1/3$ | $-1/3$ |

Table 2.2: The electroweak quantum numbers of the fermions of the SM

### 2.3.4 Interactions between Leptons and Gauge Bosons

To incorporate all generations, we will now extend our definition of $l_e$ and $r$ to $L$ and $R$:

$$\begin{aligned} L(x) &= \begin{pmatrix} l_e(x) & l_\mu(x) & l_\tau(x) \end{pmatrix} \\ R(x) &= \begin{pmatrix} r_e(x) & r_\mu(x) & r_\tau(x) \end{pmatrix}. \end{aligned} \tag{2.19}$$

The different generations only differ in their masses, so in particular the quantum numbers listed in table 2.2 are the same for all generations.

After EWSB the part of the Lagrangian that governs interactions between the leptons and the gauge bosons is given by

$$\begin{aligned} \mathcal{L}_{\text{int}}^{\text{lept}} &= g\overline{L}\gamma^\mu W_\mu^a \tau^a L - g' \left( \frac{1}{2}\overline{L}\gamma^\mu B_\mu L + \overline{R}\gamma^\mu B_\mu R \right) \\ &= g\left( J^{\mu+} W_\mu^+ + J^{\mu-} W_\mu^- + Z_\mu^0 J_Z^\mu \right) + eA_\mu J_{EM}^\mu. \end{aligned} \tag{2.20}$$

The four currents are given by

$$\begin{aligned} J_W^{\mu+} &= \frac{1}{\sqrt{2}} \left( \overline{\nu}_L \gamma^\mu e_L \right) \\ J_W^{\mu-} &= \frac{1}{\sqrt{2}} \left( \overline{e}_L \gamma^\mu \nu_L \right) \\ J_Z^\mu &= \frac{1}{\cos\theta_W} \left( \sum_{P=L,R} \overline{P}\gamma^\mu \left( \tau^3(P) + \sin^2\theta_W Y(P) \right) P \right) \\ J_{EM}^\mu &= \sum_{P=L,R} \overline{P}\gamma^\mu Q(P) P. \end{aligned} \tag{2.21}$$

The first two currents only couple to left-handed particles and hence have the $J = V - A$ structure typical for the weak interaction. Here $V$ and $A$ stand for the *vector* and *axial*

| quark | mass/MeV | $\overline{MS}$-scale | charge/$e$ | $I$ | $I_z$ | $\mathcal{S}$ | $\mathcal{C}$ | $\mathcal{B}$ | $\mathcal{T}$ |
|---|---|---|---|---|---|---|---|---|---|
| up ($u$) | $2.3^{+0.7}_{-0.5}$ | 2 GeV | 2/3 | 1/2 | +1/2 | 0 | 0 | 0 | 0 |
| down ($d$) | $4.8^{+0.5}_{-0.3}$ | 2 GeV | −1/3 | 1/2 | −1/2 | 0 | 0 | 0 | 0 |
| strange ($s$) | $95 \pm 5$ | 2 GeV | −1/3 | 0 | - | -1 | 0 | 0 | 0 |
| charm ($c$) | $1.275 \pm 0.025 \times 10^3$ | $m_c$ | 2/3 | 0 | - | 0 | 1 | 0 | 0 |
| bottom ($b$) | $4.180 \pm 0.03 \times 10^3$ | $m_b$ | −1/3 | 0 | - | 0 | 0 | -1 | 0 |
| top ($t$) | $\sim 1.7 \times 10^5$ | $m_t$ | 2/3 | 0 | - | 0 | 0 | 0 | 1 |

Table 2.3: The six quarks of the SM and their masses and quantum numbers. The light quarks up and down have isospin quantum numbers whilst the heavy quarks have quantum numbers Strangeness ($\mathcal{S}$), Charm ($\mathcal{C}$), Bottom ($\mathcal{B}$) and Top ($\mathcal{T}$) [1].

current respectively defined by

$$\begin{aligned} J_\mu(x) &= \overline{\psi}_1(x)\gamma_\mu\left(\mathbb{1} - \gamma_5\right)\psi_2(x) \\ V_\mu(x) &= \overline{\psi}_1(x)\gamma_\mu\psi_2(x) \\ A_\mu(x) &= \overline{\psi}_1(x)\gamma_\mu\gamma_5\psi_2(x), \end{aligned} \tag{2.22}$$

where $\psi_1(x)$ and $\psi_2(x)$ are fermions. We note that $V$ and $A$ transform differently under parity, i.e. $V - A \xrightarrow{P} V + A$, so parity is not conserved under the weak interaction, in agreement with what we set out to describe. However, $V$ and $A$ also transform opposite to each other under charge conjugation, so combined CP *is* conserved. Another observation is that no flavour changing neutral currents (FCNC) are present.

## 2.4 Quantum Chromodynamics

We now turn to Quantum Chromodynamics (QCD), i.e. the gauge field theory of quarks and gluons and their interactions, also known as *the strong force*. The properties of the six known quarks such as their masses and their quantum numbers are summarised in table 2.3. In this section and the corresponding appendices we will summarise the relevant features and definitions needed for the purpose of this thesis.

### 2.4.1 QCD Lagrangian

QCD is described by the $SU(3)_C$ part of (2.2) [37, 42]. The Lagrangian density of QCD is given by

$$\mathcal{L}_{\text{QCD}} = -\frac{1}{4}F^C_{\mu\nu}(x)F^{C\,\mu\nu}(x) + \sum_f \overline{\psi}_{f,\,a}(x)\left(i\not{D}_{ab} - m_f\delta_{ab}\right)\psi_{f,\,b}(x), \tag{2.23}$$

where the index $f$ runs over the $N_f = 6$ flavours that are present in the theory, here the 6 quarks. Both terms of (2.23), the field strength tensor and the fermionic part, are similar to terms we encountered in the previous section. In the following we will explain their ingredients in more detail.

The gauge group $SU(3)$ has 8 generators $t^C = \frac{1}{2}\lambda^C$, where $\lambda^C$ are the Gell-Mann matrices and the index $C$ runs from 1 to 8. The generators $t^C$ are traceless anti-hermitian $3 \times 3$ matrices. Their elements can be written as $t^C_{ab}$ where $a, b = 1, 2, 3$ and $a, b$ are referred to as *colour indices*. The 8 generators of $SU(3)$ are listed in Appendix A.1.2. In the following, unless stated otherwise, lower case Greek letters ($\mu$ and $\nu$) run over the space time components $t, x, y, z$ (labelled 0 to 3), lower case Roman letters ($a, b$) are colour indices that run from 1 to 3 where $N_C$ is the number of colours defined by $SU(N_C)$ so $N_C = 3$ for QCD. Finally upper case Roman letters ($C$) run over the 8 generators $t^C_{ab}$ of the gauge group, which are themselves $3 \times 3$ matrices.

The potential or gauge field $A_\mu$ can be decomposed into its components as

$$A_{\mu,ab}(x) = A^C_\mu(x) t^C_{ab}. \tag{2.24}$$

For any group element $g(x)$ of the local gauge group $G$, i.e. $g(x) \in G = SU(3)$, it transforms as

$$A_\mu(x) \to A'_\mu(x) = g(x) A_\mu(x) g^{-1}(x) - \frac{1}{g_s}(\partial_\mu g(x)) g^{-1}(x), \tag{2.25}$$

where $g_s$ is not to be confused with a group element but is the coupling constant. Under the same local gauge transformation $g(x) \in SU(3)$ fermions $\psi(x)_f$ transform as

$$\psi_{f,a}(x) \to \psi'_{f,a}(x) = g_{ab}(x) \psi_{f,b}(x). \tag{2.26}$$

Similarly to the electroweak case (compare (2.5)), we construct the covariant derivative $D_\mu$ such that the Lagrangian remains invariant under the gauge transformation (2.25). One obtains

$$D_\mu = \partial_\mu + g_s A_\mu = \partial_\mu + g_s A^C_\mu t^C, \tag{2.27}$$

where the colour indices are suppressed. By construction equations (2.25), (2.26) and (2.27) ensure gauge invariance of the Lagrangian.

Now we can define the gluonic field strength tensor $F_{\mu\nu}$ (compare (2.4)) as

$$\begin{aligned} F_{\mu\nu} &= [D_\mu, D_\nu]\,, \\ F^C_{\mu\nu} &= \partial_\mu A^C_\nu - \partial_\nu A^C_\mu + g_s [A_\mu, A_\nu]^C \\ &= \partial_\mu A^C_\nu - \partial_\nu A^C_\mu + g_s i f^{ABC} A^A_\mu A^B_\nu, \end{aligned} \tag{2.28}$$

where $f^{ABC}$ are the structure constants of $SU(3)$ and $F_{\mu\nu} = F^C_{\mu\nu} t^C$. This already illustrates one of the most important implications of (2.23). Due to its *non-abelian* structure, QCD allows for gluon self-interactions; i.e. 3-gluon vertices ($ggg$) with coupling strength proportional to $g_s$, and 4-gluon vertices ($gggg$) with coupling strength proportional to $g_s^2$, are present.

In principle, one could also add a *theta term* proportional to $\theta \epsilon_{\mu\nu\rho\sigma} F^{\mu\nu} F^{\rho\sigma}$ to the Lagrangian (2.23). Whilst this term obeys gauge and Lorentz invariance it would break $CP$ invariance for QCD. However, experimentally, this term seems to be absent with bounds of $|\theta| \lesssim 10^{-10}$ [1, 43]. This is known as the *strong CP problem*.

From (2.23) we can see that QCD has $6 + 1$ fundamental parameters ($N_f = 6$ quark masses and the coupling $g_s$). This means that after fixing the quark masses and the coupling constant $g_s$, QCD is fully defined.

### 2.4.2 Confinement and Asymptotic Freedom

In QCD the value of the coupling constant $g_s$ or equivalently the coupling strength $\alpha_s$, defined by

$$\alpha_s(\mu) = \frac{g_s^2(\mu)}{4\pi}, \tag{2.29}$$

depends on the renormalisation scale $\mu$ at which a process is considered. We define the $\beta$ function as

$$\beta(\alpha_s) = \mu^2 \frac{\mathrm{d}\alpha_s}{\mathrm{d}\mu^2}, \tag{2.30}$$

where $\mu$ is the energy scale of the process under consideration. If the (arbitrary) renormalisation scale $\mu^2$ is taken to be close to the typical momentum transfer $Q^2$ of a process, the value of the coupling constant $g$ at this scale indicates the effective strength of the interaction. This behaviour with scale can be understood from the *Renormalisation Group Equation* (RGE) of the coupling strength. This results in the QCD $\beta$ function [1, 20]

$$\beta(\alpha_s) = -\frac{33 - 2n_f}{12\pi} \alpha_s^2 + \mathcal{O}(\alpha_s^3). \tag{2.31}$$

Note that $n_f$ here is the *effective* number of (approximately) massless flavours, i.e. the number of flavours satisfying $m_f \ll \mu$. Measurements of the coupling strength as a function of the energy scale are shown in figure 2.1 [1].

One important feature of (2.31) is that for $n_f \leq N_f = 6$ the leading term is negative. This implies that for large energy scales $\mu$ the coupling constant gets small leading to the phenomenon known as *Asymptotic Freedom* [44, 45].

From figure 2.1 we can see that at low energy scales $Q$ the coupling strength increases, yielding strong interactions at low energies. This causes the phenomenon of *confinement* [46], i.e. the behaviour that quarks are very tightly bound and only appear in

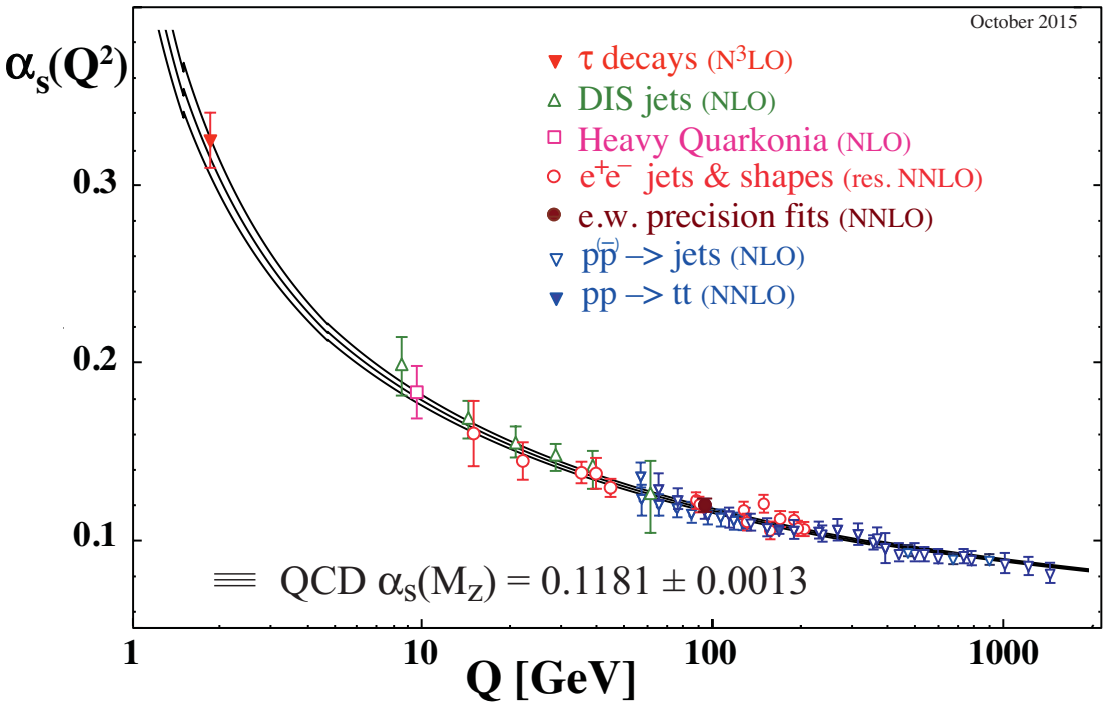


Figure 2.1: Experimental evidence for the running of the strong coupling constant. The figure is taken from ref [1].

bound states which form colour singlets. In particular, this implies that the standard perturbative approach of ordering processes by powers of the coupling constant is inapplicable in this regime.

### 2.4.3 Symmetries of QCD

In addition to gauge and Lorentz invariance, the Lagrangian (2.23) displays further symmetries. Recall that fermions can be split into left-handed and right-handed parts and that the only term in the Lagrangian that mixes the two is proportional to the mass of the fermion. We have already seen that fermions obey a $U(1)_V$ vector symmetry $\psi_{L,R} \to e^{i\alpha}\psi_{L,R}(x)$. For the case of QCD, flavour is a conserved quantity so each of the $N_f = 6$ flavours are individually conserved. The electroweak sector allows for flavour changing currents so quark flavour is not a conserved quantity in the SM, but the total number of quarks is. Similar to the lepton number in the case of leptons, we define the *baryon number* $B$, which is conserved in QCD, as

$$B = \frac{1}{3}\sum_f Q_{f,V}. \tag{2.32}$$

We have also seen before that a massless fermion ($m_f = 0$) possesses an additional $U(1)_A$ *axial* or *chiral* symmetry $\psi_{L,R} \to e^{i\alpha\gamma_5}\psi$. This symmetry rotates left-handed and

right-handed components with a different phase, and is most easily seen in the chiral basis. The form the gamma matrices take in this basis is presented in Appendix A.2.

For $N$ massless flavours these symmetries can be generalised to a *flavour symmetry* by placing the flavours into a multiplet and allowing for simultaneous left-handed and right-handed rotations, yielding $U(N)_L \times U(N)_R$ [47, 48]. This symmetry group can be decomposed as $SU(N)_L \times SU(N)_R \times U(1)_A \times U(1)_V$. We have already seen that $U(1)_V$ gives rise to baryon number conservation ((2.32)). When quantising the theory, one finds that in addition to the term $im\overline{\psi}\gamma_5\psi$, an additional term proportional to $\epsilon_{\mu\nu\rho\sigma}F^{\mu\nu}F^{\rho\sigma}$ arises in the divergence of the axial current [49, 50]. This is called the *axial anomaly* and means that $U(1)_A$ is not a symmetry, even in the massless limit.

The fact that quarks have a non-vanishing mass, breaks chiral symmetry explicitly, but the three (two) lightest quarks are (much) lighter than the typical interaction scale of QCD (typically defined by $\Lambda_{QCD} \approx 250 - 700\,\text{MeV}$ [1]), so QCD possesses *approximate* chiral symmetry. We introduce the mass matrix

$$\mathcal{M} = \text{diag}(m_u, m_d, m_s) \tag{2.33}$$

and place the three quark fields into a multiplet to write the Dirac part of the lightest three flavours of the QCD Lagrangian (2.23) as

$$\begin{pmatrix} \overline{\psi}_u(x) \\ \overline{\psi}_d(x) \\ \overline{\psi}_s(x) \end{pmatrix} \left(i\not{D} - \mathcal{M}\right) \begin{pmatrix} \overline{\psi}_u(x) & \overline{\psi}_d(x) & \overline{\psi}_s(x) \end{pmatrix} = \overline{\Psi}(x)\left(i\not{D} - \mathcal{M}\right)\Psi(x). \tag{2.34}$$

One can show that the associated Noether currents of $SU(3)_A \times SU(3)_V$ are

$$\begin{aligned} J_A^{a,\mu} &= i\overline{\Psi}(x)\gamma^\mu\gamma^5\frac{\lambda^a}{2}\Psi(x) \quad \text{and} \\ J_V^{a,\mu} &= i\overline{\Psi}(x)\gamma^\mu\frac{\lambda^a}{2}\Psi(x), \end{aligned} \tag{2.35}$$

respectively, and have divergences

$$\begin{aligned} \partial_\mu J_A^{a,\mu} &= i\overline{\Psi}\left\{\mathcal{M}, \lambda^a\right\}\Psi \quad \text{and} \\ \partial_\mu J_V^{a,\mu} &= i\overline{\Psi}\left[\mathcal{M}, \lambda^a\right]\Psi. \end{aligned} \tag{2.36}$$

Here the $\lambda^a$ are the generators of the symmetry group, in the case presented here $SU(3)$ (cf. Appendix A.1.2). Whilst we considered three *light quarks* here ($SU(3)$), the same discussion holds for restricting to only two quarks considered to be light ($SU(2)$), i.e. only considering the up and the down quark as light.

For mass degenerate quarks, i.e. $m_u = m_d = m_s = \overline{m}$ the commutator $[\mathcal{M}, \lambda^a]$ vanishes and $SU(3)_V$ becomes an exact symmetry. In the limit of $SU(2)$ this symmetry is called

*isospin*.

The first line of (2.36) is called the *non-singlet axial Ward Identity* (AWI) and its right-hand-side only vanishes for zero quark masses. For degenerate but non-zero quark masses the left-hand-side of the AWI becomes proportional to the pseudoscalar density [47]. Since $m_u$, $m_d$ and (to a lesser degree) $m_s$ are small compared to the typical interaction scale of QCD, the AWI is only slightly broken. From Goldstone's theorem we expect pseudo-Goldstone bosons corresponding to the broken generators of $SU(N)_A$. When considering $SU(3)$ these are the eight pseudoscalar mesons which can be written as multiplets of $SU(3)_V$ [47, 51, 52], often expressed as

$$\begin{pmatrix} \frac{1}{\sqrt{2}}\pi^0 + \frac{1}{\sqrt{6}}\eta^0 & \pi^+ & K^+ \\ \pi^- & -\frac{1}{\sqrt{2}}\pi^0 + \frac{1}{\sqrt{6}}\eta^0 & K^0 \\ \overline{K}^- & \overline{K}^0 & -\sqrt{\frac{2}{3}}\eta^0 \end{pmatrix}. \tag{2.37}$$

Since the masses of the up and the down quarks are small, chiral symmetry should only be slightly broken. One can show that if this symmetry is approximately intact there should be a negative parity partner for the nucleon $N^*$, however this is not seen in experiments, indicating that spontaneous chiral symmetry breaking (S$\chi$SB) must occur [1, 9, 51, 52] (in addition to explicit chiral symmetry breaking by the quark masses).

### 2.4.4 Interactions between Quarks and Gauge Bosons

Quarks interact via the weak, strong and electromagnetic force. To allow for interactions between quarks and electroweak gauge bosons, in analogy to the above, we put pairs of left-handed quarks into $SU(2)$ doublets and the right-handed parts into $SU(2)$ singlets. We differentiate between *up-type* quarks $u$, $c$, $t$ and *down-type* quarks $d$, $s$, $b$. We define

$$\begin{aligned} U_L &= (u_L, c_L, t_L) & U_R &= (u_R, c_R, t_R) \\ D_L &= (d_L, s_L, b_L) & D_R &= (d_R, s_R, b_R). \end{aligned} \tag{2.38}$$

We now form $SU(2)$ doublets $Q_L^i = (U_L^i \; D_L^i)$ where $i$ labels the generation, i.e.

$$Q_L^T = \begin{pmatrix} U_L^i & D_L^i \end{pmatrix}^T = \begin{pmatrix} (u_L & d_L), & (c_L & s_L), & (t_L & b_L) \end{pmatrix}^T, \tag{2.39}$$

whilst the entries of $U_R$ and $D_R$ form singlets.

The sums in the electromagnetic and neutral currents ($J^\mu_{EM}$ and $J^\mu_Z$) from (2.21) now run over $P \in \{L, R, Q_L, U_R, D_R\}$. The charged currents $J^{\mu+}_W$ and $J^{\mu-}_W$ get additional contributions of $1/\sqrt{2}\,\left(\overline{U}_L\gamma^\mu D_L\right)$ and $1/\sqrt{2}\,\left(\overline{D}_L\gamma^\mu U_L\right)$, respectively. The corresponding values of $Q$, $Y$ and $\tau^3$ are listed in table 2.2.

### 2.4.5 Interactions between Fermions and Higgs

Let us now focus on the Higgs-Yukawa term for fermions, i.e. the terms that couple the scalar $\phi$ to the fermions. We have seen previously that a mass term necessarily mixes left-handed and right-handed components, but due to the different quantum numbers of left-handed and right-handed components, a simple mass term would not be gauge invariant. Instead, we introduce terms of the form

$$\mathcal{L}^{\mathrm{e}}_{\mathrm{Yukawa}} = -\lambda_e \bar{l}_e \cdot \phi \, e_R + h.c., \tag{2.40}$$

mixing left-handed and right-handed components. There the dot product is between the $SU(2)$ doublets $\phi$ and $\overline{\psi}_L$. When the scalar field assumes a vacuum expectation value (vev) $v$, this gives rise to fermion masses. In (2.40) we assumed a single generation. Substituting in the vev, for the case of the electron we get

$$\mathcal{L}^{\mathrm{e}}_{\mathrm{Yukawa}} = -\frac{1}{\sqrt{2}} \lambda_e v \overline{e}_L e_R + h.c., \tag{2.41}$$

so

$$m_e = \frac{1}{\sqrt{2}} \lambda_e v. \tag{2.42}$$

We can generalise this to multiple generations of leptons (labelled by $l$) by writing

$$\mathcal{L}^{\mathrm{lepton}}_{\mathrm{Yukawa}} = -\sum_l \lambda_l \overline{L}_l \cdot \phi \, R_l + h.c.\,. \tag{2.43}$$

For quarks the same principle holds, but since there are two types of right-handed quarks, there are two terms in the Yukawa term of the Lagrangian. We obtain

$$\mathcal{L}^{\mathrm{quark}}_{\mathrm{Yukawa}} = -\sqrt{2} \left( \lambda_d^{ij} \underbrace{\overline{Q}^i_{L,a} \phi_a \, D^j_R}_{(I)} - \lambda_u^{ij} \underbrace{\overline{Q}^i_{L,a} \epsilon_{ab} \phi^\dagger_b U^j_R}_{(II)} \right) + h.c., \tag{2.44}$$

where $\epsilon_{ab}$ is the antisymmetric tensor of $SU(2)$ ($a, b \in \{1, 2\}$) and $i, j \in \{1, 2, 3\}$ label the three generations of quarks. We can note that $CP$ transforms $(I)$ and $(II)$ into their hermitian conjugates, so as long as $\lambda_d^{ij}$ and $\lambda_u^{ij}$ are real the Yukawa term of the Lagrangian is $CP$ invariant.

Contrary to the lepton sector, different generations are connected by the matrices $\lambda_d^{ij}$ and $\lambda_u^{ij}$. However, these can be diagonalised using unitary matrices to obtain a basis of mass eigenstates:

$$\begin{aligned} \lambda_u &= T_u \Lambda_u S_u^\dagger \\ \lambda_d &= T_d \Lambda_d S_d^\dagger, \end{aligned} \tag{2.45}$$

where the matrices $\Lambda_{u,d}$ are now diagonal and $S_{u,d}, T_{u,d} \in U(3)$. Now transform the fields as

$$\begin{aligned} U_L^i &\mapsto T_u^{ij} U_L^j & \qquad U_R^i &\mapsto S_u^{ij} U_R^j \\ D_L^i &\mapsto T_d^{ij} D_L^j & \qquad D_R^i &\mapsto S_d^{ij} D_R^j \end{aligned} \tag{2.46}$$

and note that the two components of the $SU(2)$ doublet $Q_L$ transform differently. Then at the vev, one obtains

$$\begin{aligned} \mathcal{L}_{\text{Yukawa}}^{\text{quark}} &= -v\overline{D}_L^i \Lambda_d^{ij} D_R^j - v\overline{U}_L^i \Lambda_u^{ij} U_R^j + h.c. \\ &= -\sum_i \left( m_D^i \overline{D}_L^i D_R^i + m_U^i \overline{U}_L^i U_R^i \right), \end{aligned} \tag{2.47}$$

where $m_{D,U}^i = v\Lambda_{D,U}^{ii}$ (no summation) are the quark masses. However, the transformation (2.46) will have to be carried out for the entire Lagrangian, in particular for the weak currents. This gives rise to the famous CKM matrix [35, 36], which will be discussed in the next section.

## 2.5 The Cabibbo-Kobayashi-Maskawa Matrix

We will now apply the rotations (2.46) to the weak currents, e.g

$$J_W^{\mu+} = \overline{U}_L'^i \gamma^\mu D_L'^i \to \overline{U}_L^j T_u^{ji\dagger} \gamma^\mu T_d^{ik} D_L^k = \overline{U}_L^j \gamma^\mu V_{CKM}^{jk} D_L^k. \tag{2.48}$$

The matrix $T_u^{ij\dagger} T_d^{jk} = V_{CKM}^{ik}$ is the Cabibbo-Kobayashi-Maskawa (CKM) matrix [35, 36]. It relates the mass eigenstates $d$, $s$, $b$ to flavour eigenstates $d'$, $s'$, $b'$.

$$\begin{pmatrix} d' \\ s' \\ b' \end{pmatrix} = \begin{pmatrix} V_{ud} & V_{us} & V_{ub} \\ V_{cd} & V_{cs} & V_{cb} \\ V_{td} & V_{ts} & V_{tb} \end{pmatrix} \begin{pmatrix} d \\ s \\ b \end{pmatrix} = V_{CKM} \begin{pmatrix} d \\ s \\ b \end{pmatrix}. \tag{2.49}$$

In the SM the CKM matrix is unitary, i.e. it satisfies

$$V_{CKM}^\dagger V_{CKM} = V_{CKM} V_{CKM}^\dagger = \mathbb{1}. \tag{2.50}$$

This leads to conditions of the form

$$\begin{aligned} \sum_{D=d,s,b} |V_{UD}|^2 &= 1 \qquad \text{for } U \in \{u,c,t\} \\ \sum_{U=u,c,t} |V_{UD}|^2 &= 1 \qquad \text{for } D \in \{d,s,b\} \\ \sum_{D=d,s,b} V_{U_1 D} V_{U_2 D}^* &= 0 \qquad \text{for } U_1 \neq U_2 \\ \sum_{U=u,c,t} V_{U D_1} V_{U D_2}^* &= 0 \qquad \text{for } D_1 \neq D_2. \end{aligned} \tag{2.51}$$

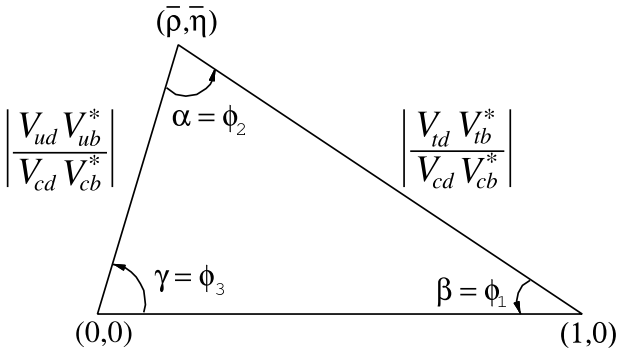


Figure 2.2: Schematic illustration how unitarity can be represented as a unitarity triangle. For further explanations, refer to the text.

The former two equations arise from the diagonal entries of (2.50), the latter two from the off-diagonal entries. If the left-hand side of either of the first two equations adds up to a number different than one this would indicate new physics (NP). If they add up to less than one, one possible interpretation is a hint for a fourth generation. The second type of equation can be interpreted as a so-called *unitarity triangle*. To see this, pick for example $D_1 = d$, $D_2 = b$ in the last equation of (2.51) and consider $V_{Ud}V_{Ub}^*$ as a vector in the complex plane. Then the unitarity constraint implies

$$V_{ud}V_{ub}^* + V_{cd}V_{cb}^* + V_{td}V_{tb}^* = 0 \qquad \Rightarrow \qquad \frac{V_{ud}V_{ub}^*}{V_{cd}V_{cb}^*} + \frac{V_{td}V_{tb}^*}{V_{cd}V_{cb}^*} = -1. \tag{2.52}$$

If this equation holds, this traces out a closed triangle in the complex plane with lengths 1, $\left|\frac{V_{td}V_{tb}^*}{V_{cd}V_{cb}^*}\right|$ and $\left|\frac{V_{ud}V_{cd}^*}{V_{cd}V_{cb}^*}\right|$ as shown in figure 2.2 which is taken from the PDG [1]. Experimental data combined with theoretical predictions can predict the lengths of these sides of this triangle as well as the angles. Unitarity corresponds to the triangle being closed.

A complex $3 \times 3$ matrix has 9 complex, or equivalently 18 real parameters. Unitarity provides 9 constraints, leaving the CKM matrix with 9 degrees of freedom: 3 rotations and 6 phases. We can use relative phases of the quark fields to absorb 5 of these 6 phases into redefinitions of the quark fields, leaving one physical phase in the CKM matrix. This implies that $\lambda_u^{ij}$ and $\lambda_d^{ij}$ can be complex and hence, the Yukawa term of the Lagrangian allows for $CP$-violation in the Standard model. This is the only known source of direct CP violation in the SM.

The CKM matrix is often parameterised in terms of the 4 remaining degrees of freedom [53, 54]. Most commonly used is the *Wolfenstein parametrisation*. This introduces 3 real parameters ($\lambda$, $A$ and $\rho$) and one complex phase $\eta$. Up to $O(\lambda^4)$ the CKM matrix

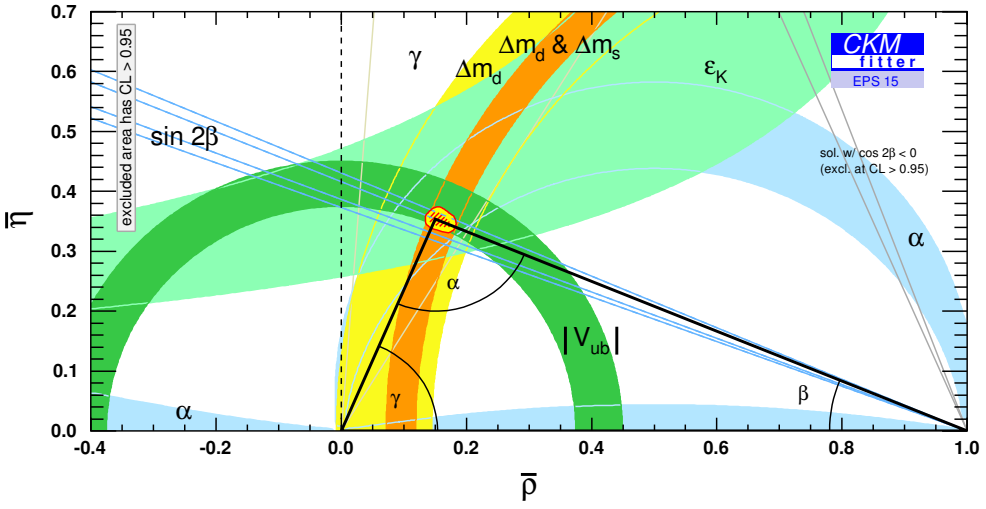


Figure 2.3: Current uncertainties in the unitarity triangle plotted in the $\bar{\rho} - \bar{\eta}$ plane. The plot is taken from [2].

then reads

$$V_{CKM} = \mathbb{1} + \begin{pmatrix} -\lambda^2/2 & \lambda & A\lambda^3(\rho - i\eta) \\ -\lambda & -\lambda^2/2 & A\lambda^2 \\ A\lambda^3(1 - \rho - i\eta) & -A\lambda^2 & 0 \end{pmatrix} + \mathcal{O}(\lambda^4). \tag{2.53}$$

The variables $\rho$ and $\eta$ can be related to more convenient variables $\overline{\rho}$ and $\overline{\eta}$, which ensure that $\overline{\rho} + i\overline{\eta} = -\left(V_{ud}V_{ub}^*\right) / \left(V_{cd}V_{cb}^*\right)$. Since $\overline{\rho} = \rho\left(1 + \lambda^2 + \cdots\right)$, the parametrisation (2.53) is the same for both choices [1, 2, 54, 55]. A global fit combining theoretical and experimental data and imposing unitarity currently gives [1, 2, 56]

$$\begin{aligned} \lambda &= 0.22537(61) \\ A &= 0.814\,\left(^{+23}_{-24}\right) \\ \overline{\rho} &= 0.117(21) \\ \overline{\eta} &= 0.353(13). \end{aligned} \tag{2.54}$$

The fact that $\overline{\eta}$ is different from zero, means that there is indeed a complex phase and the CKM matrix does allow for CP violation.

The current status of the various constraints is collected by the CKM-fitter collaboration [2]. The latest values as shown by this collaboration are presented in figure 2.3.

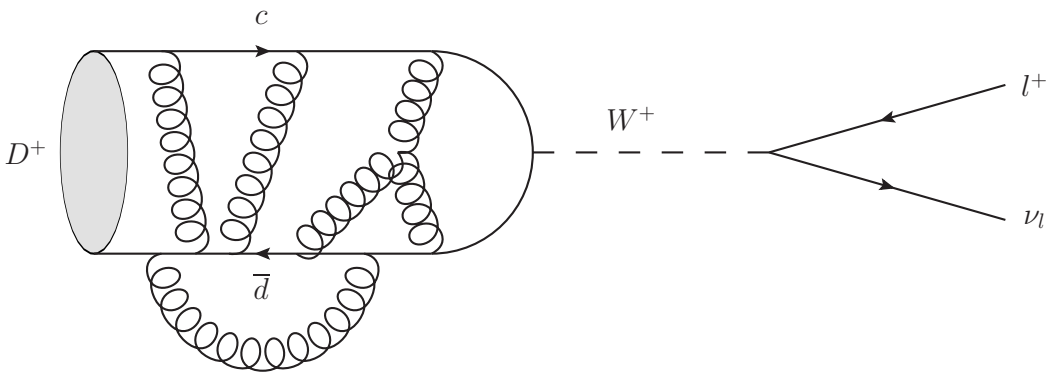


Figure 2.4: Pictorial representation of the decay $D^+ \to l^+\nu_l$ at leading order in $\alpha_{\mathrm{EM}}$. The shown gluons are non-perturbative and indicate strong interactions.

## 2.6 Extracting CKM Matrix Elements

To test the unitarity of the CKM matrix by means of equations of the type (2.51), we need to determine the CKM-matrix elements from first principles. Equation (2.48) shows that the elements of the CKM matrix indicate the strength of a particular interaction. For example, consider the leptonic decay $D_s^+ \to l^+\nu_l$ with $q = d, s$ at leading order. A schematic diagram for this process, without electromagnetic interactions, is shown in figure 2.4.

Since the mass of the $W$ boson ($m_W^{\pm} = 80.385(15)\,\mathrm{GeV}$ [1]) is significantly larger than the typical energy of a weak process considered in this work, we can construct an effective Lagrangian by integrating out the $W$ boson propagator. The *effective* interaction Lagrangian of the weak interaction is given by

$$\mathcal{L}_W = -\frac{G_F}{\sqrt{2}} J^{\alpha}(x)^{\dagger} J_{\alpha}(x), \tag{2.55}$$

where $G_F$ is the *Fermi constant* and $J_\alpha(x)$ is given by (2.22).

The decay rate $\Gamma$ of the leptonic decay $D_{(s)}^+ \to l^+\nu_l$ is given by

$$\Gamma(D_{(s)}^+ \to l^+\nu_l) = \frac{G_F^2 \tau_{D_{(s)}}}{8\pi} |V_{cq}|^2 f_{D_{(s)}}^2 m_l^2 m_{D_{(s)}} \left(1 - \frac{m_l^2}{m_{D_{(s)}}^2}\right)^2 + \mathcal{O}(\alpha_{\mathrm{EM}}) + \mathcal{O}(\alpha_{\mathrm{EW}}). \tag{2.56}$$

Here the meson mass $m_{D_{(s)}}$, the lepton mass $m_l$ and the mean lifetime $\tau_{D_{(s)}}$ are known experimental inputs, whilst the decay rate $\Gamma$ is measured experimentally. If the value of the CKM matrix is precisely known experimentally or from some other calculation, the SM prediction (2.56) can be tested. If the CKM matrix element is not precisely known, then theoretical predictions of the decay constant $f_{D_{(s)}}$ combined with the experimental

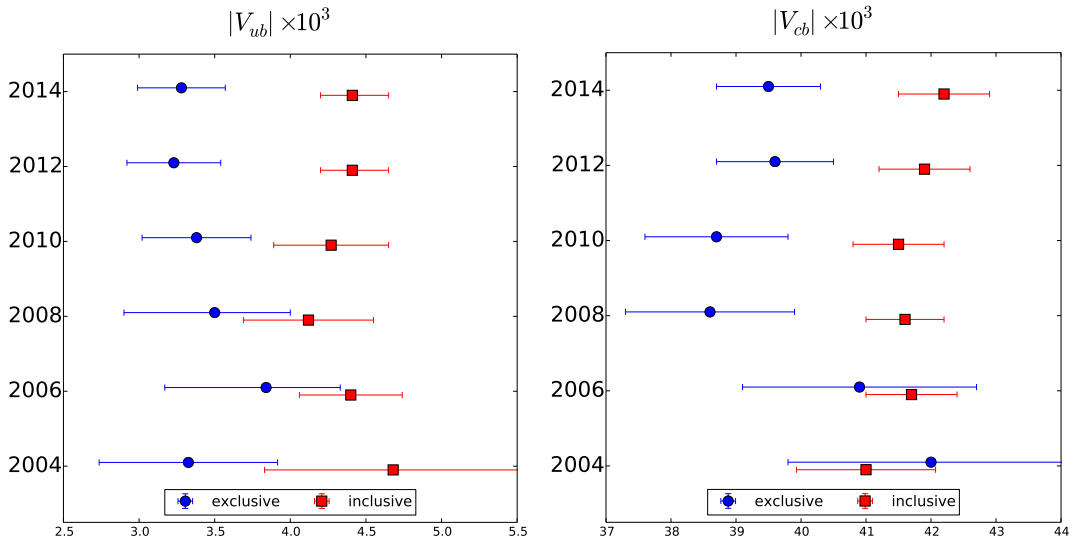


Figure 2.5: Historic development of the determination of $V_{ub}$ (left) and $V_{cb}$ (right) from inclusive (red squares) and exclusive (blue circles). The shown data is compiled from the world averages presented in ref [1] and previous editions [3–7].

measurement of $\Gamma$ yield a value of the CKM matrix element under consideration. Furthermore, the same CKM matrix element can appear in more than one process. E.g. $V_{cd}$ appears in $D^+ \to l^+\nu_l$ and $D^0 \to \pi^- l^+\nu_l$ as well as the decays of their respective antiparticles. Ignoring electromagnetic interactions between the quarks and the $W$ boson, the quarks and the leptons, and the $W$ boson and the leptons, (i.e. considering the minimal order in $\alpha_{EM}$) we can schematically write an experimental observable $\Gamma$ as a product of a CKM matrix element $V_{CKM}$, *weak* and *electromagnetic* contributions and strong contributions, in particular,

$$\Gamma_{\text{exp.}} = V_{CKM}\ (\text{WEAK})\,(\text{EM})\,(\text{STRONG})\,. \tag{2.57}$$

The weak and electromagnetic contributions can be calculated perturbatively, whilst the strong contributions are calculated non-perturbatively on the lattice.

Unitarity of the first row and column of the CKM matrix have been extensively tested and at the current precision the data is compatible with unitarity [57]. In the other two columns(rows) there are still larger uncertainties, which need to be reduced for a precise test of the SM. Most famously, as shown in figure 2.5, there is a persistent tension between the determination of the world average of the CKM matrix elements $V_{ub}$ (left) and $V_{cb}$ (right) from inclusive (unspecified final state) and exclusive (specified final state) processes [1].

## 2.7 Heavy Quarks

The SM has six quarks: up ($u$), down ($d$), strange ($s$), charm ($c$), bottom ($b$) and top ($t$). Table 2.3 summarises their masses and quantum numbers [1] and shows that their masses differ over many orders of magnitude. Whilst $SU(2)$ ($SU(3)$) still appears to be a good flavour symmetry for the light up and down (up, down and strange) quarks, the charm, bottom and top quarks are too massive to be considered "light". The top quark has a mean half-time of $\tau \sim 10^{-24}\,s$ and is expected to decay too quickly to form bound states [58]. Contrary to the top quark, the charm and the bottom quarks - which are often referred to as *Heavy Quarks*(HQ) - do form bound states and produce a wide range of experimentally measurable processes.

Heavy quarks have been studied in many different experiments including (but not limited to) CLEO (CLEO-I, CLEO-II, CLEO-III and CLEO-c at Cornell University, Ithaca, NY, 1979-2008), Belle (K.E.K., Tsukuba, Japan, 1999-2010), BaBar (SLAC, California, 1999-2008). Currently BES III (Beijing, China, 2008-current) and LHCb (CERN, Geneva, Switzerland, 2010 - current) as well as the multi-purpose experiments ATLAS and CMS explore the properties of particles including charm and bottom quarks and in the near future (∼2018) with Belle II a new $B$-factory is expected to start taking measurements. With this large variety of experimental efforts in charm and bottom physics it is important that the theoretical predictions arising from the SM are continuously improved to match the experimental precision.

There are a number of effective theory approaches [23, 59] for treating bound states that contain *Heavy Quarks*. These include *heavy quark effective theory* (HQET) and *non-relativistic QCD* (NRQCD). HQET [60–66] applies to systems with one heavy quark of mass $m_H$ and one or more light quarks. In the static limit ($m_H \to \infty$) the heavy quark is stationary at the center of the coordinate system. HQET then expands around this point in powers of $1/m_H$. Since the energy scale, $\Lambda$, of the light quarks is of the order of a few hundred MeV, the expansion parameter in HQET for a charmed meson is $\frac{\Lambda}{m_c} \approx 1/5$ and may not be a good approximation at leading and subleading order [67, 68]. NRQCD [69] is concerned with quarkonia states (containing a heavy quark and its antiquark) $Q\overline{Q}$ and expands in the (non-relativistic) quark velocity $v$.

Whilst these effective theory approaches have a small expansion parameter for the case of the bottom quark, the charm quark is in a region where one has to check the convergence of the effective theory. In addition, effective theories introduce additional parameters that would need to be tuned for numerical simulations, which is costly. Furthermore, for numerical simulations, some cancellations rely on the light quarks to be simulated with the same action as the charm quark (e.g. GIM mechanism [70]), which would not be possible if an effective theory approach is chosen for the charm quark. For this reason we aim to make predictions for charm quantities from direct simulations. However, the mass of the charm quark is at the limit of what is achievable in current simulations, so

we need to assess in detail whether simulating the charm quark directly is feasible. We will first investigate this for our choice of fermion discretisation in chapter 5.

# Chapter 3

# Lattice Quantum Chromodynamics

In this chapter we will introduce the basic features of Lattice QCD. After a brief motivation in section 3.1, in section 3.2 we will outline how to discretise QCD. More specifically we will focus on the gauge field in 3.3 and on the fermion fields in 3.4. In section 3.5 we will discuss how to include dynamical fermions into our simulations. We will outline how we can assign physical scales to the simulated data in section 3.6. In section 3.7 we will explain how we can extract hadronic observables from the simulations. Finally, section 3.8 gives a brief summary of the systematic errors that arise in lattice QCD simulations. As this chapter is a review and not original work, it relies on a number of sources from which I obtained my knowledge. In addition to the cited original work, this includes [21–24] as well as knowledge obtained in lectures, discussions, workshops and conferences.

## 3.1 The Need for Lattice QCD

As mentioned above (recall figure 2.1 in 2.4.2), at low energies QCD is non-perturbative. This means that the "standard" approach (called perturbation theory) of calculating diagrams 'order-by-order' in the coupling constant is bound to fail. To overcome this problem various approaches have been devised. These include QCD sum rules [71–73] (for a summary, see e.g. ref [74]), AdS/CFT (AdS/QCD) approaches [75] and effective theories such as Heavy Quark Effective Theory (HQET) [60–62, 66] and chiral perturbation theory ($\chi$PT), just to name a few.

Whilst most other approaches are based on some further ad hoc model assumptions and/or are limited in the range where they are applicable, Lattice QCD (LQCD) is able to provide ab initio predictions. LQCD numerically simulates QCD starting directly

on the Lagrangian level and all systematic errors can be systematically improved provided sophisticated algorithms, understanding of the underlying discrete field theory, and sufficient computing power. So Lattice Quantum Chromodynamics is a systematically improvable tool to make ab initio predictions about the nature of QCD in the regime where the coupling is strong.

## 3.2 The Idea of Lattice QCD

The expectation value of an observable in the path integral formalism in Minkowski space is given by

$$\langle \mathcal{O} \rangle = \frac{1}{Z} \int \mathcal{D}[\Phi]\, \mathcal{O}(\Phi) \exp\left(iS[\Phi]\right), \tag{3.1}$$

where $\Phi$ is short for all involved fields and $Z$ is determined by requiring $\langle 1 \rangle = 1$. We can Wick rotate [76] ($t \to i\tau$) the path integral (2.23) into Euclidean space [46, 77]. Upon Wick rotation the path integral turns into

$$\langle \mathcal{O} \rangle = \frac{1}{Z} \int \mathcal{D}[\Phi]\, \mathcal{O}(\Phi) \exp\left(-S_E[\Phi]\right), \tag{3.2}$$

where $S_E$ is real and positive. However, (3.2) is infinite dimensional and therefore ill-defined. This is overcome by restricting the degrees of freedom to a finite (though very large) number of degrees of freedom by placing the theory on a finite lattice. As we will see, this allows for numerical Markov Chain Monte Carlo (MCMC) simulations of QCD and therefore for the estimation of hadronic observables.

The minus sign in (3.2) enables us to re-interpret the factor $\exp\left(-S_E[\Phi]\right)$ as a Boltzmann weight, allowing for a statistical estimation of $\langle \mathcal{O} \rangle$. This is done by sampling the phase space with a MCMC simulation to obtain a set of $N$ field configurations $\mathcal{T}_i$ and estimating the integral numerically as

$$\langle \mathcal{O} \rangle \approx \frac{1}{N} \sum_i \mathcal{O}(\mathcal{T}_i) + O\left(\frac{1}{\sqrt{N}}\right). \tag{3.3}$$

Provided the $\mathcal{T}_i$ are drawn with the correct probability, i.e.

$$P(\mathcal{T}_i) \propto \exp\left(-S_E[\mathcal{T}_i]\right) \tag{3.4}$$

and sample all of the phase space correctly (ergodicity), this gives a statistical estimate of the expectation value of the observable $\mathcal{O}$ [46, 78].

We render (3.2) finite dimensional by introducing a 4-dimensional lattice of length $L_\mu$ in the $\mu$ direction and a finite lattice spacing $a$. It is conventional to choose the cubical spatial volume, i.e. $L_x = L_y = L_z \equiv L$ and a larger time extent $T$. From this we obtain a 4-volume $V_4 = L^3 \times T$ and a spatial volume $V_3 = L^3$. Formally, the lattice is defined

as the set of points

$$\Lambda = \left\{ an_\mu : n_i = 0, 1, \ldots, N-1; n_4 = 0, 1, \ldots, N_T - 1, n_\mu \in \mathbb{N}^0 \right\}, \tag{3.5}$$

where $N$ and $N_T$ are integers. Derivatives are replaced by finite differences and integrals by Riemann sums, i.e.

$$\int \mathrm{d}^4x \, f(x) \to a^4 \sum_{n \in \Lambda} f(n). \tag{3.6}$$

Note that this renders the path integral finite-dimensional. By placing the simulation into a finite volume we need to choose appropriate boundary conditions (BCs). It is customary to work with *periodic* BCs but *anti-periodic*, *open* and *twisted* [79, 80] BCs have also been used.

The finite volume causes momentum modes to be quantised, whilst the discrete nature of the lattice causes momenta to be restricted to the Brillouin zone. The set of accessible Fourier momenta $\tilde{\Lambda}$ for the case of *periodic* BCs is restricted to

$$\tilde{\Lambda} = \left\{ p_\mu = \frac{\pi}{aX_\mu} n_\mu \, : \, -X_\mu \leq n_\mu < X_\mu, n_\mu \in \mathbb{Z} \right\}. \tag{3.7}$$

QCD has ultraviolet (UV) divergences which need to be removed. This is usually done by first regulating the theory by introducing a maximum momentum $\Lambda$ or a *cut-off* and then matching this regularised theory to some renormalisation scheme. On the lattice the regularisation is automatically enforced, since the inverse lattice spacing provides a cut-off and therefore acts as a UV regulator. In addition, the finite volume introduces an infrared (IR) regulator. The correct physics is therefore recovered in the limit where the cut-off is taken to infinity.

In the case of QCD, we have two types of fields: fermionic fields $q$ and $\overline{q}$ live on the lattice sites, whilst gauge fields $U_\mu$ live on the links between neighbouring sites. This is illustrated in figure 3.1 [1] and will be discussed in more detail in the subsequent sections of this chapter. In addition to the finite volume and the finite lattice spacing, a further discrepancy between the lattice simulation and nature is the symmetry of space-time. The lattice reduces Poincaré symmetry to that of a hypercube. For states with non-vanishing momentum this symmetry is reduced even further. In any lattice simulation we need to carefully and systematically remove those effects, i.e. we must understand how to obtain the value an observable $\mathcal{O}$ takes in nature from measured values of $\mathcal{O}(a, V)$. To do this, we need to keep all physical parameters that define the theory fixed, meaning we take the continuum limit along a *line of constant physics*. The extrapolation to vanishing lattice spacing is called the *continuum limit*.

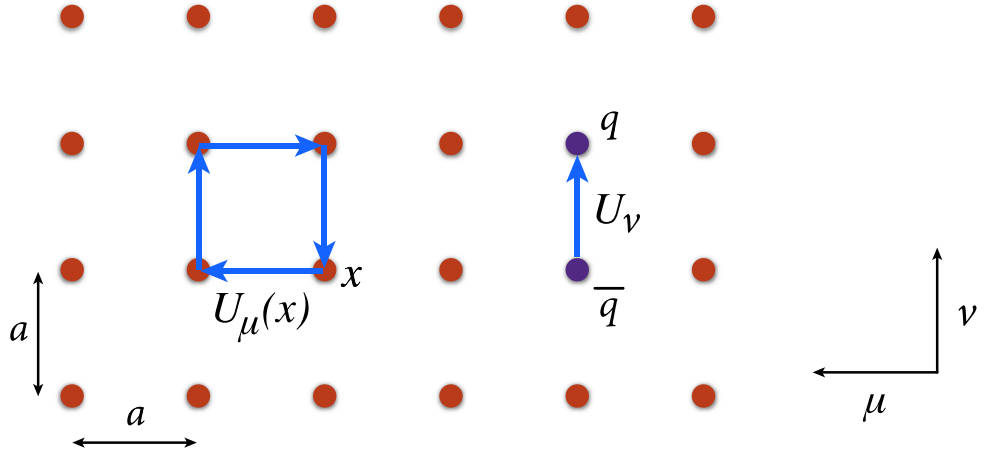


Figure 3.1: Schematic illustration of a two dimensional lattice taken from ref [1].

## 3.3 Discretising QCD

Recall the QCD action (2.23) (suppressing colour indices and considering only a single fermion flavour)

$$\begin{aligned} S_{\text{QCD}} &= \int \mathrm{d}^4x\, \mathcal{L}_{\text{QCD}} \\ &= \int \mathrm{d}^4x \left( -\frac{1}{4} F^C_{\mu\nu} F^{C,\mu\nu} + \overline{\psi} \left( i \not{D} - m_f \right) \psi \right) \\ &= S_G[A] + S_F[\overline{\psi}, \psi, A]. \end{aligned} \tag{3.8}$$

In the last line of (3.8) we have split the action into the pure gauge part $S_G$ and the fermionic part $S_F$. After rescaling $gA^a_\mu \to A^a_\mu$ for later convenience, the Euclidean versions of these read

$$\begin{aligned} S_G &= \frac{1}{2g^2} \int \mathrm{d}^4x\, F^C_{\mu\nu}(x) F^C_{\mu\nu}(x) \\ S_F &= \int \mathrm{d}^4x\, \overline{\psi} \left( \gamma^E_\mu D_\mu + m \right) \psi, \end{aligned} \tag{3.9}$$

where $\gamma^E_\mu$ refers to the Euclidean version of the gamma matrices which are summarised in Appendix A.2. Note that in Euclidean space there is no distinction between upper and lower indices. Further note that the pre-factor in $S_G$ now explicitly involves the coupling.

When discretising the action (3.9) we replace continuous derivatives $\partial_\mu$ by finite differences. This is not a unique choice, since one can choose the forward ($\partial_\mu$), backward ($\partial^*_\mu$)

or symmetric $((\partial_\mu + \partial^*_\mu)/2)$ derivative. We define

$$\begin{aligned} \partial_\mu \phi(x) &= \frac{1}{a}\left(\phi(x + a\hat{\mu}) - \phi(x)\right) \\ \partial^*_\mu \phi(x) &= \frac{1}{a}\left(\phi(x) - \phi(x - a\hat{\mu})\right), \end{aligned} \tag{3.10}$$

where $\hat{\mu}$ is a unit vector in the $\mu$ direction. For brevity, we will now set $a = 1$, but will reintroduce it again when considering the leading order of discretisation effects.

Recalling that the gauge transformations (2.25) and (2.26) have been constructed to ensure gauge invariance of the action, we require this to also hold for the discretised version. On the lattice we choose an $SU(3)$ element $\Omega(x)$ for each lattice site $x$. So in analogy with (2.26) we then get

$$\begin{aligned} \psi(n) &\to \psi'(n) = \Omega(n)\,\psi(n) \\ \overline{\psi}(n) &\to \overline{\psi}'(n) = \overline{\psi}(n)\,\Omega^\dagger(n). \end{aligned} \tag{3.11}$$

However, the discretised form of the kinetic term mixes fields at neighbouring sites and introduces terms like $\overline{\psi}(n)\psi(n+\hat{\mu})$, which would no longer be gauge invariant since

$$\overline{\psi}(n)\,\psi(n+\hat{\mu}) \to \overline{\psi}(n)\,\Omega^\dagger(n)\,\Omega(n+\hat{\mu})\,\psi(n+\hat{\mu}). \tag{3.12}$$

Instead we introduce a new field $U_\mu(n)$ with a direction $\mu$ and require that

$$U_\mu(n) \to U'_\mu(n) = \Omega(n)\,U_\mu(n)\,\Omega^\dagger(n+\hat{\mu}). \tag{3.13}$$

$U_\mu(n)$ is called a *link variable* and can be understood as linking the lattice site $x$ to the lattice site $n + \hat{\mu}$, as illustrated in figure 3.1. Now the quantity

$$\overline{\psi}(n)\,U_\mu(n)\,\psi(n+\hat{\mu}) \tag{3.14}$$

is gauge invariant. We are now in a position to define the discretised fermion action. Using the symmetric discrete derivative and replacing the integral by a sum over all lattice sites we get

$$S_F[\overline{\psi},\psi,U] = \sum_{n\in\Lambda} \overline{\psi}(n)\left[\sum_\mu \gamma_\mu \frac{U_\mu(n)\,\psi(n+\hat{\mu}) - U_{-\mu}(n)\,\psi(n-\hat{\mu})}{2} + m\psi(n)\right]. \tag{3.15}$$

Note that this does *not* use the Einstein summation convention. For convenience we define a backwards pointing link $U_{-\mu}$ as

$$U_{-\mu}(n) = U^\dagger_\mu(n-\hat{\mu}). \tag{3.16}$$

Using (3.11) and (3.13) it is easy to verify that gauge invariance is satisfied. Fermions described by (3.15) are called *naïve fermions* - more about this later.

The link variables $U_\mu(n)$ are related to the lattice gauge fields $A_\mu$ by

$$U_\mu(n) = \exp\left(iA_\mu(n)\right). \tag{3.17}$$

Unlike the continuum theory, we treat the Lie algebra-valued fields $A_\mu(n)$ as the fundamental degrees of freedom as opposed to the Lie group-valued fields $U_\mu(n)$.

Now that we have defined the link variables $U_\mu(n)$ we need to construct a discrete version of the gauge action in (3.9) that is built from these objects. To do this, first notice that taking the product of the link variables along any path $\mathcal{P}_{xy}$ from $x$ to $y$

$$P[\mathcal{P}_{xy}] = \prod_{\mathcal{P}_{xy}} U_\mu(n) = U_\mu(x)\, U_{\mu_1}(x+\hat{\mu}_1)\cdots U_{\mu_{k-1}}(y-\hat{\mu}_{k-1}) \tag{3.18}$$

transforms as

$$P[\mathcal{P}_{xy}] \to \Omega(x)\, P[\mathcal{P}_{xy}]\, \Omega^\dagger(y) \tag{3.19}$$

since all intermediate matrices $\Omega$ cancel. In particular, there are two types of gauge invariant objects that can be built from this. The first option is to attach quark fields on either side of $P$, the second one is to choose $\mathcal{P}$ to be a closed loop and to take the trace over the matrices $\Omega$. The simplest choice for such a closed loop is the *plaquette* $U_{\mu\nu}(x)$ (compare figure 3.1), defined by

$$U_{\mu\nu}(x) = U_\mu(x)\, U_\nu(x+a\hat{\mu})\, U_\mu^\dagger(x+a\hat{\nu})\, U_\nu^\dagger(x). \tag{3.20}$$

From this we can construct the Wilson gauge action [46] $S_G[U]$ as

$$S_G[U] = \frac{2}{g^2} \sum_{n\in\Lambda} \sum_{\mu<\nu} \Re[\mathrm{tr}(1 - U_{\mu\nu}(n))]. \tag{3.21}$$

Reintroducing $a$, substituting (3.17) and (3.20) into (3.21) and Taylor expanding $A_\mu(n+\hat{\nu})$ as

$$A_\mu(n+\hat{\nu}) = A_\mu(n) + a\,\partial_\nu A_\mu(n) + O(a^2), \tag{3.22}$$

demonstrates the equivalence to the continuum version (3.9) in the limit $a \to 0$. More precisely

$$S_G[U] = \frac{a^4}{2g^2} \sum_{n\in\Lambda} \sum_{\mu,\nu} \mathrm{tr}(F_{\mu\nu}(n) F_{\mu\nu}(n)) + O(a^2), \tag{3.23}$$

so the leading discretisation errors are $O(a^2)$.

We have now constructed a discrete version of the QCD action (3.9), which reproduces the continuum action in the limit $a \to 0$.

One can modify these to *improved* actions to eliminate the leading $O(a)$ lattice artefacts. Such improved gauge actions include the tree-level improved Symanzik gauge action [81, 82] and the Iwasaki gauge action [83–85].

## 3.4 Fermion Actions and Chiral Symmetry

In this section we will discretise the fermion action. We will first investigate the properties of *naïve* fermions as formulated in (3.15). We will find that these lead to unphysical additional particles called *doublers*. We will then see how these can be removed by adding the *Wilson term* [46] and how this leads to the loss of chiral symmetry. We will briefly introduce the Nilsen-Ninomiya theorem [86] which will lead us to chiral fermions and the domain wall formulation discussed in chapter 4.

### 3.4.1 Naïve Fermions

Recall the fermion action $S_F[\overline{\psi}, \psi, U]$ for a single flavour with mass $m$ as defined in (3.15). We can rewrite this bilinear into matrix form introducing the *naïve Dirac operator* $D(n|m)$ connecting lattice sites $n$ and $m$. We define it as

$$S_F[\overline{\psi}, \psi, U] = a^4 \sum_{n,m\in\Lambda} \sum_{a,b} \sum_{\alpha,\beta} \overline{\psi}(n)^{\ a}_{\alpha}\ D(n|m)^{\ ab}_{\alpha\beta}\ \psi(m)^{\ b}_{\beta}. \tag{3.24}$$

In addition to the space-time indices $n$ and $m$, the Dirac operator also carries Dirac indices (Greek letters) and colour indices (Roman letters). Comparing (3.15) and (3.24) we find the naïve form of the Dirac operator to be

$$D(n|m)^{\ ab}_{\alpha\beta} = \sum_{\mu} (\gamma_\mu)_{\alpha\beta} \frac{U_\mu(n)_{ab}\, \delta_{n+\hat{\mu},m} - U_{-\mu}(n)_{ab}\, \delta_{n-\hat{\mu},m}}{2a} + m\, \delta_{\alpha\beta}\, \delta_{ab}\, \delta_{n,m}. \tag{3.25}$$

In the free case ($U_\mu(n) = \mathbb{1}$) this operator can be inverted analytically to obtain the propagator of a free fermion. We start by transforming the Dirac operator into Fourier space. One obtains

$$\begin{aligned} \tilde{D}(p|q) &= \frac{1}{|\Lambda|} \sum_{n,m\in\Lambda} e^{-ip\cdot na} D(n|m) e^{iq\cdot ma} \\ &= \frac{1}{|\Lambda|} \sum_{n,m\in\Lambda} e^{-i(p-q)\cdot na} \left( \sum_{\mu} \gamma_\mu \frac{e^{iq_\mu a} - e^{-iq_\mu a}}{2a} + m\mathbb{1} \right) \\ &= \delta_{p,q} \tilde{D}(p), \end{aligned} \tag{3.26}$$

where $|\Lambda| = N^3 \times N_T$ is the total number of lattice sites and $\tilde{D}(p)$ is

$$\tilde{D}(p) = m\mathbb{1} + \frac{i}{a} \sum_{\mu} \gamma_\mu \sin p_\mu a. \tag{3.27}$$

The inverse of (3.27) is given by

$$\tilde{D}(p)^{-1} = \frac{\mathbb{1}m - ia^{-1} \sum_\mu \gamma_\mu \sin p_\mu a}{m^2 + a^{-2} \sum_\mu \sin^2 p_\mu a}. \tag{3.28}$$

The inverse of the position space Dirac operator is found by transforming $\tilde{D}(p)^{-1}$ back into position space, i.e.

$$D^{-1}(n|m) = \frac{1}{|\Lambda|}\sum_{\tilde{\Lambda}} \tilde{D}(p)^{-1} e^{ip\cdot(n-m)a}, \qquad \text{where } p \in \tilde{\Lambda}. \tag{3.29}$$

The inverse of the Dirac operator is the *quark propagator*. Since poles in the propagator correspond to physical particles and therefore the simulated particle spectrum, we now investigate the poles of the massless ($m = 0$) free propagator in momentum space. Contrary to the continuum formulation which has exactly one pole at $p = 0$, we find that the lattice formulation of naïve fermions has 16 poles in the Brillouin zone $\tilde{\Lambda}$ (since $\sin^2(p_\mu a)$ vanishes for $p_\mu = 0$ and $p_\mu = \pi/a$). This means instead of one physical particle (with a pole at $p_\mu = (0,\ 0,\ 0,\ 0)$) we describe 15 additional particles, the *doublers*. These unphysical particles will need to be removed from the theory.

### 3.4.2 Wilson Fermions

Since we need to take the continuum limit $a \to 0$ to recover the continuum theory, we may add any irrelevant (i.e. higher dimensional) operators, i.e. terms that disappear in this limit. The first suggestion for how to remove doublers came from Wilson [46] and makes use of this property. Wilson proposed to add a dimension-five term, such that the momentum space Dirac operator becomes

$$\tilde{D}(p) = \tilde{D}^{\text{naïve}}(p) + \mathbb{1}\frac{1}{a}\sum_{\mu}\left(1 - \cos\left(p_\mu a\right)\right), \tag{3.30}$$

where we momentarily wrote out the factors of $a$. For $p_\mu = 0$ this term does not change the propagator, leaving the physical pole unchanged. However, each momentum component with $p_\mu = \pi/a$ behaves as an additional mass term and adds a contribution of $2/a$ to the propagator, causing the additional particles to become infinitely heavy and therefore to decouple from the theory in the limit of $a \to 0$. We can find the form of the Wilson term for the case of the free theory by Fourier transforming the additional term in (3.30) back into position space to obtain

$$D(n|m)^{\text{Wilson}} = D(n|m)^{\text{naïve}} - a\sum_{\mu}\frac{\delta_{n+\hat{\mu},m} - 2\delta_{n,m} + \delta_{n-\hat{\mu},m}}{2a^2}. \tag{3.31}$$

The additional term is proportional to a discretised Laplacian. In the presence of a gauge field these derivatives can be made gauge invariant by inserting link variables as before (compare (3.15)) leading to the forward and backward covariant derivatives (recall that we set $a = 1$)

$$\begin{aligned} D_\mu(n)\psi(n) &= U_\mu(n)\psi(n+\hat{\mu}) - \psi(n) \\ D^*_\mu(n)\psi(n) &= \psi(n) - U_\mu(n-\hat{\mu})\psi(n-\hat{\mu}). \end{aligned} \tag{3.32}$$

With this the Wilson Dirac operator then reads

$$\begin{aligned} D(n|m)^{\text{Wilson}}_{\substack{ab\\ \alpha\beta}} &= \sum_{\mu} (\gamma_\mu)_{\alpha\beta} \frac{U_\mu(n)_{ab}\,\delta_{n+\hat{\mu},m} - U_{-\mu}(n)_{ab}\,\delta_{n-\hat{\mu},m}}{2a} + m\,\delta_{\alpha\beta}\,\delta_{ab}\,\delta_{n,m} \\ &\quad - \sum_{\mu} \frac{U_\mu(n)_{ab}\,\delta_{n+\hat{\mu},m} - 2\delta_{n,m}\,\delta_{ab}\,\delta_{\alpha\beta} + U_{-\mu}(n)_{ab}\,\delta_{n-\hat{\mu},m}}{2a} \\ &= \left(m + \frac{4}{a}\right)\delta_{n,m}\,\delta_{ab}\,\delta_{\alpha\beta} - \frac{1}{2a}\sum_{\mu=\pm1}^{\pm4} (\mathbb{1} - \gamma_\mu)_{\alpha\beta}\,U_\mu(n)_{ab}\delta_{n+\hat{\mu},m}. \end{aligned} \tag{3.33}$$

We have now formulated a theory in which the doublers decouple in the continuum limit, but as we shall see this comes at the expense of chiral symmetry. Whilst this is not a problem in principle and can be recovered in the continuum, it poses problems for renormalisation procedures, since it induces mixing between different operators that is otherwise not present. It also affects cut-off effects, in particular, the leading order discretisation errors of a theory that possesses chiral symmetry is $O(a^2)$, so simulations are automatically $O(a)$-improved. Therefore, maintaining chiral symmetry is a desirable feature of a chosen fermion discretisation.

### 3.4.3 The Nielsen-Ninomiya Theorem and its Implications

We will now return to chiral symmetry as outlined in section 2.4.3. We recall that the massless continuum fermion action remained invariant under transformations of the form

$$\psi \to e^{i\alpha\gamma_5}\psi \qquad \overline{\psi} \to \overline{\psi}e^{i\alpha\gamma_5}. \tag{3.34}$$

This invariance holds if the massless Dirac operator $D$ anti-commutes with $\gamma_5$, so the condition for chiral symmetry can be rewritten as

$$\{D, \gamma_5\} = D\gamma_5 + \gamma_5 D = 0. \tag{3.35}$$

Recalling the Wilson fermion action (3.31), it is apparent that the Wilson term does *not* obey chiral symmetry, even for vanishing quark masses. Moreover, the Nielsen-Ninomiya Theorem [86] states that it is impossible to find a Dirac operator in an even-dimensional Euclidean space-time that satisfies all the following conditions simultaneously. Our presentation of the Nielson-Ninomiya theorem follows the formulation of ref [87] in ref [22].

1. $\tilde{D}(p)$ is a periodic, analytic function of $p_\mu$. This ensures the locality of the coordinate space Dirac operator.

2. $\tilde{D}(p) \propto \gamma_\mu p_\mu$ for $a\,|p_\mu| \ll 1$. This ensures that the Dirac operator has the desired continuum form as the continuum limit is approached.

3. $\tilde{D}(p)$ is invertible everywhere except $p_\mu = 0$. This condition ensures that it is possible to calculate a propagator and the absence of doublers in the theory.

4. $\tilde{D}(p)$ satisfies (3.35). This is the statement that guarantees chiral symmetry.

There are a number of different fermion formulations that will give up one of these conditions. We have already encountered Wilson fermions which do not obey chiral symmetry. Naïve fermions have 16 doublers. Staggered fermions [88] have four *tastes* and Creutz fermions [89] reduce the number of particles simulated by the fermion propagator to two. In chapter 4 we will see how domain wall fermions can circumvent this theorem by generalising the condition for chiral symmetry.

## 3.5 Dynamical Fermions and Ensemble Generation

We have seen how to discretise the gauge field in section 3.3 and the fermionic part in the previous section. Before moving on to extracting hadronic observables we need to address how to simulate *dynamical* fermions, i.e. fermions that exist in the gluonic sea.

When considering the fermion action (3.24) one can see that it is quadratic in the quark fields. So we can integrate the quark fields in the partition function $Z$ (compare (3.2)) analytically [90, 91]. Taking into account that fermions obey Fermi-Dirac statistics (i.e. *anti*-commute) and therefore are represented by Grassmann variables, we find that

$$\begin{aligned} Z &= \int \mathcal{D}[\Psi, \overline{\Psi}, U] \, \exp\left( -S_G[U] - \sum_f^{N_f} S_F[\Psi_f, \overline{\Psi}_f, U] \right) \\ &= \int \mathcal{D}[U] \left( \prod_f^{N_f} \det\left[D_f[U]\right] \right) \exp\left(-S_G[U]\right). \end{aligned} \tag{3.36}$$

The sea quarks are captured in the $N_f$ factors of the determinant of the Dirac operator with the corresponding mass of the fermion. When simulating dynamical fermions, the probability distribution that is sampled is

$$P \propto \left( \prod_f^{N_f} \det\left[D_f[U]\right] \right) \exp\left(-S_G[U]\right), \tag{3.37}$$

so the determinant is absorbed into the probability distribution and acts as a weight factor [21, 78]. This poses algorithmic challenges, since unlike the gauge action, the determinant is highly non-local, i.e. includes the gauge fields at all points of the lattice. So depending on whether sea-quarks are neglected (the *quenched approximation*) or included, different algorithms are more or less suited to generate the Markov Chain of gauge configurations. We will list the algorithms which were employed for the generation

of the ensembles mentioned in this thesis. Amongst others, algorithms relevant to Lattice QCD include the heat-bath algorithm [92], over-relaxation [93–95] and hybrid Monte Carlo [96] (HMC). In practice we simulate *commuting pseudo fermions* $\Phi$ [97] by noting that

$$\det D = \int \mathcal{D}[\Phi] \exp\left(-\Phi(n) D^{-1}(n|m)\Phi(m)\right). \tag{3.38}$$

So given a starting field configuration $\mathcal{T}_\prime$, this configuration is then evolved as a Markov Chain to create *trajectories* $\mathcal{T}_i$ with the correct probability distribution, as given by (3.37). The sum of all these trajectories is called an *ensemble*. At the beginning of generating an ensemble, the system needs to *thermalise* before reaching an equilibrium. After that one needs to address the *autocorrelation* between successive trajectories in the algorithm. For this one typically looks at the behaviour of a (slowly varying) observable $\mathcal{O}$ and calculates the autocorrelation time $\tau_{\text{int}}$. One then restricts the *configurations* in the ensemble to be for example every $\tau_{\text{int}}$th trajectory.

On all ensembles used in the remainder of this thesis we determined the autocorrelation time $\tau_{\text{int}}$ of the so-called *topological charge* $Q_{\text{top}}$. This is assumed to couple strongly to the slowest evolving mode of the algorithm [98]. The topological charge is defined as

$$Q_{\text{top}} = \frac{1}{32\pi^2} a^4 \sum_{n,\mu,\nu} \text{tr}\left[F_{\mu\nu}(n)\tilde{F}_{\mu\nu}(n)\right]. \tag{3.39}$$

However, for algorithms which are invariant under parity (such as the ones we are using), it has been shown that it is sufficient to look at the slowest varying parity invariant mode [98]. So for our purposes we can consider $\tau_{\text{int}}(Q^2_{\text{top}})$ rather than $\tau_{\text{int}}(Q_{\text{top}})$ which varies more rapidly.

## 3.6 Scale Setting

Full QCD has 7 parameters that need to be fixed: the 6 quark masses and the coupling constant. The large number of orders of magnitude separating the light and the heavy quarks (compare table 2.3) makes is very difficult to include all 6 quarks in a single simulation. Instead simulations are often restricted to a smaller number of sea quarks, i.e. $N_f = 2$, $N_f = 2+1$ or $N_f = 2+1+1$ flavours. The 2 refers to the fact that up and down quarks are treated as mass-degenerate light quarks. This reduces the number of parameters even further. For example, in our $N_f = 2+1$ flavour simulations we need to fix three parameters: the coupling constant, the light (degenerate up and down) quark mass and the strange quark mass. For example, this can be done by using the values $m_\pi$, $m_K$ and $m_\Omega$ as physical inputs to set the values of $m_l$, $m_s$ and $a$ respectively. Furthermore, since this thesis is concerned with charm physics we also need to fix the charm quark mass (e.g. using $m_D$, $m_{D_s}$ or $m_{\eta_c}$), even though for the remainder of this thesis we will only consider valence charm quarks.

| State | $J^{PC}$ | $\Gamma$ | Mesons |
|---|---|---|---|
| Scalar | $0^{++}$ | $\mathbb{1}$ | $a_0$, $f_0$, ... |
| Pseudoscalar | $0^{-+}$ | $\gamma^5$ | $\pi$, $K$, $D$, $D_s$, $\eta_c$... |
| Axial vector | $1^{++}$ | $\gamma^i\gamma^5$ | $a_1$, $f_1$,... |
| Vector | $1^{--}$ | $\gamma^i$ | $\rho$, $\omega$,... |
| Tensor | $1^{+-}$ | $\gamma^i\gamma^j$ | $b_1$, $h_1$ ,... |

Table 3.1: Quantum numbers for bilinear operators of the form (3.40) in the continuum [1, 9]. $J$ is the spin, $P$ and $C$ are parity and charge conjugation respectively. The presented list is only exemplary and presents some of the lightest states as well as states of particular interest to this work.

Once we have set the scale $a$ using some physical input (such as $m_\Omega$) we can also relate this to a more precisely measurable gluonic quantity. There are a number of such quantities e.g. the Sommer scale [99] or the Wilson flow [100, 101].

## 3.7 Extraction of Hadronic Observables

A lattice calculation evaluates the path integral (3.2) numerically by carrying out a *measurement* on each configuration and from this deduces a stochastic estimate of the expectation value of an observable $\mathcal{O}$ (compare (3.3)). Now that we have discretised the action and produced ensembles with the correct probability distribution, it remains to address the properties of the operators $\mathcal{O}$ of which we want to deduce expectation values. We then need to connect the expectation values $\langle\mathcal{O}\rangle$ to hadronic observables.

### 3.7.1 Operators and Observables

Different hadrons differ by their quantum numbers such as spin ($J$), parity ($P$) and charge conjugation ($C$). To deduce hadronic matrix elements we need to identify *interpolating operators* that create states with the correct quantum numbers from the vacuum. In nature we only observe colour singlets, so we will construct such states. The most general mesonic form for a local colour-singlet operator $\mathcal{O}$ at some position $x_{\text{op}} = (\boldsymbol{x}_{\text{op}}, t_{\text{op}})$ is given by local quark bilinears of the form

$$\mathcal{O}(x_{\text{op}}) = \overline{\psi}_{f_1}(x_{\text{op}})\Gamma\psi_{f_2}(x_{\text{op}}). \tag{3.40}$$

Here $\Gamma$ is some Dirac structure, and $f_1$ and $f_2$ refer to the flavour of the respective quark fields. Table 3.1 lists some of the different choices of $\Gamma$ and the quantum numbers that are induced by these.

In this thesis we will be concerned with properties of pseudoscalar mesons such as pions, kaons and the $D$ and $D_s$ mesons and the $\eta_c$ meson. This means that we will consider

Dirac structures $\Gamma$ for pseudoscalars ($\gamma_5$), axial vector currents ($\gamma_\mu\gamma_5$) and vector currents ($\gamma_\mu$). We project to an operator of definite momentum using a discrete Fourier Transform (FT)

$$\tilde{\mathcal{O}}(\boldsymbol{p}_{\text{op}}, t_{\text{op}}) = \frac{1}{\sqrt{|\Lambda_3|}} \sum_{\boldsymbol{n}\in\Lambda_3} \mathcal{O}(\boldsymbol{x}, t_{\text{op}}) e^{-i\boldsymbol{x}\cdot\boldsymbol{p}_{\text{op}}}, \tag{3.41}$$

where $|\Lambda_3|$ is the number of lattice sites in the three-volume $V_3$. Given periodic boundary conditions, the (discrete) values the spatial momentum $\boldsymbol{p}_{\text{op}}$ is allowed to take are

$$\boldsymbol{p} \in \frac{2\pi}{L}\boldsymbol{n} \qquad \text{where } n_i \in \{-X_i/2+1, \cdots, X_i/2\}. \tag{3.42}$$

The observables under consideration will be masses ($m$) and energies ($E(\boldsymbol{p})$) and matrix elements. In particular, we will calculate the Euclidean matrix element $\langle 0|\,\mathcal{A}_4\,|P(\boldsymbol{p})\rangle$ of a pseudoscalar meson $P$. From this we extract the *decay constant* $f_P$ which enters the decay rate (compare e.g. (2.56)) using

$$\langle 0|\,\mathcal{A}_4\,|P(\boldsymbol{p})\rangle \equiv E_P(\boldsymbol{p}) f_P. \tag{3.43}$$

This holds exactly for the *conserved* axial vector current $\mathcal{A}$. However, as will be discussed later in chapter 4, we can instead use a local version $A$ of this current which then needs to be renormalised (compare (4.15)).

The next point that needs to be addressed is how physical quantities such as masses, energies and matrix elements can be deduced from expectation values of these operators.

Consider the expectation value of the product of two interpolating operators, one ($\mathcal{O}^\dagger_{\text{src}}$) that creates a state at some source (src) position and one ($\mathcal{O}_{\text{snk}}$) that destroys said state at some sink (snk) position. By translational invariance we can fix the source position to be the origin $x_{\text{src}} = (\boldsymbol{0}, 0)$. We then insert a complete set of states $\sum_n \frac{|n\rangle\langle n|}{2E_n}$ with $E_0 \le E_1 \le E_2 \cdots$ to get

$$\begin{aligned}
C_2(\boldsymbol{p}, t) &\equiv \sum_{\mathbf{x}} e^{-i\boldsymbol{p}\cdot\boldsymbol{x}} \left\langle 0 \middle| \mathcal{O}_{\text{snk}}(\boldsymbol{x}, t)\mathcal{O}^\dagger_{\text{src}}(\boldsymbol{0}, 0) \middle| 0 \right\rangle \\
&= \sum_{\mathbf{x}} e^{-i\boldsymbol{p}\cdot\boldsymbol{x}} \sum_n \frac{1}{2E_n(\boldsymbol{p_n})} \left\langle 0 \middle| \mathcal{O}_{\text{snk}}(\boldsymbol{x}, t) \middle| n \right\rangle \left\langle n \middle| \mathcal{O}^\dagger_{\text{src}}(\boldsymbol{0}, 0) \middle| 0 \right\rangle \\
&= \sum_n \sum_{\mathbf{x}} e^{-i\boldsymbol{p}\cdot\boldsymbol{x}} \frac{1}{2E_n(\boldsymbol{p_n})} \left\langle 0 \middle| e^{Ht - i\mathbf{P}\cdot\mathbf{x}} \mathcal{O}_{\text{snk}}(\boldsymbol{0}, 0) e^{-Ht + i\mathbf{P}\cdot\mathbf{x}} \middle| n \right\rangle \left\langle n \middle| \mathcal{O}^\dagger_{\text{src}}(\boldsymbol{0}, 0) \middle| 0 \right\rangle \\
&= \sum_n \sum_{\mathbf{x}} e^{i(\boldsymbol{p_n}-\boldsymbol{p})\cdot\boldsymbol{x}} \frac{1}{2E_n(\boldsymbol{p_n})} \left\langle 0 \middle| \mathcal{O}_{\text{snk}}(\boldsymbol{0}, 0) \middle| n \right\rangle \left\langle n \middle| \mathcal{O}^\dagger_{\text{src}}(\boldsymbol{0}, 0) \middle| 0 \right\rangle e^{-E_n(\boldsymbol{p_n})t} \\
&= \sum_n \frac{1}{2E_n(\boldsymbol{p_n})} \left\langle 0 \middle| \mathcal{O}_{\text{snk}}(\boldsymbol{0}, 0) \middle| n \right\rangle \left\langle n \middle| \mathcal{O}^\dagger_{\text{src}}(\boldsymbol{0}, 0) \middle| 0 \right\rangle e^{-E_n(\boldsymbol{p_n})t} \Big|_{\boldsymbol{p_n}=\boldsymbol{p}} \\
&= \sum_n \frac{Z_{\text{snk},n} Z^*_{\text{src},n}}{2E_n(\boldsymbol{p})} e^{-E_n(\boldsymbol{p})t},
\end{aligned} \tag{3.44}$$

where we have defined $Z_{i,n} = \langle 0| \mathcal{O}_i |n\rangle$ for $i = \text{src}, \text{snk}$ and assumed the temporal extent $T$ of the lattice to be sufficiently large that we can consider the initial and final state well separated. So for sufficiently large $t$, all states with $E_n > E_0$ are exponentially suppressed. So the dominating state is the ground state of the particle, i.e. with the lowest energy which has the quantum numbers induced by $\mathcal{O}$. Assuming we are in the region of $t$ where the ground state of the desired particle dominates, we can fit the correlator data to the functional form (3.44) and extract the energies and matrix elements. Due to the boundary conditions, we will also have a backwards travelling part with the same exponential $e^{-E_n(T-t)}$. The sign of this distribution depends on the time-reversal behaviour of the observables, in particular for $\mathcal{O}_{\text{snk}} = \mathcal{O}_{\text{src}}$ the contributions have the same sign whilst for e.g. $\mathcal{O}_{\text{snk}} = \gamma_5$, $\mathcal{O}_{\text{src}} = \gamma_4\gamma_5$ the contributions have the opposite sign. The former case amounts to a $\cosh\left[(T/2-t)\, E(\boldsymbol{p})\right]$ time behaviour, whilst the latter leads to $\sinh\left[(T/2-t)\, E(\boldsymbol{p})\right]$.

### 3.7.2 Propagators

We now tackle the question of how to compute $\left\langle \mathcal{O}_{\text{snk}}(x)\mathcal{O}^\dagger_{\text{src}}(0)\right\rangle$ in practice. For simplicity, we consider the same operator $\mathcal{O}(x) = \overline{u}(x)\gamma_5 d(x)$ which creates a charged pion at the source and the sink and place the source position at the origin. We calculate the expectation value of this operator creating a pion from the vacuum at $x_{\text{src}} = (\mathbf{0}, 0)$, propagating to the *sink* $x_{\text{snk}} = (\boldsymbol{x}_{\text{snk}}, t_{\text{snk}})$ where it annihilates into the vacuum again.

From Wick's theorem [102] we know that the time ordered product $\mathcal{T}$ is the sum of all possible contractions. For simplicity we project to $\boldsymbol{p} = \mathbf{0}$ and consider $\mathcal{O}_{\text{snk}} = \mathcal{O}_{\text{src}} = \overline{u}\gamma_5 d$. We obtain

$$\begin{aligned} C_2(t)|_{\boldsymbol{p}=0} &= \sum_{\boldsymbol{x}} \left\langle 0\right| \mathcal{T}\mathcal{O}(\boldsymbol{x},t)\, \mathcal{O}^\dagger(\mathbf{0},0) \left|0\right\rangle \\ &= \sum_{\boldsymbol{x}} \langle 0|\, \mathcal{T}\, \overline{u}(\boldsymbol{x},t)\gamma_5 d(\boldsymbol{x},t)\ \overline{d}(\mathbf{0},0)\gamma_5 u(\mathbf{0},0)\, |0\rangle \\ &= \frac{1}{Z}\int \mathcal{D}[\overline{\psi},\psi,U] e^{-S_E[\overline{\psi},\psi,U]} \sum_{\boldsymbol{x}} \overline{u(\boldsymbol{x},t)\gamma_5 \overline{d(\boldsymbol{x},t)\overline{d}(\mathbf{0},0)}\gamma_5 u(\mathbf{0},0)} \\ &= \frac{1}{Z}\int \mathcal{D}[\overline{\psi},\psi,U] e^{-S_E[\overline{\psi},\psi,U]} \sum_{\boldsymbol{x}} \mathrm{tr}[\gamma_5 S_d(\mathbf{0},0|\boldsymbol{x},t)\gamma_5 S_u(\boldsymbol{x},t|\mathbf{0},0)], \end{aligned} \tag{3.45}$$

where we have used $\gamma_\mu\gamma_5^\dagger\gamma_\mu = -\gamma_5$ and $\{\gamma_\mu,\gamma_5\} = 0$ (cf Appendix A.2). More generally, for two flavour off-diagonal quarks (i.e. a charged current; compare (2.48)) we get

$$\begin{aligned} C(t)|_{\boldsymbol{p}=\mathbf{0}} &= \left\langle [\overline{q}_1(x)\Gamma_{\text{snk}} q_2(x)]\, [\overline{q}_1(0)\Gamma_{\text{src}} q_2(0)]^\dagger \right\rangle \\ &= \pm\frac{1}{Z}\int \mathcal{D}[\overline{\psi},\psi,U] e^{-S_E[\overline{\psi},\psi,U]} \sum_{\boldsymbol{x}} \mathrm{tr}[\Gamma_{\text{snk}} S_{q_2}(0|x)\Gamma_{\text{src}} S_{q_1}(x|0)], \end{aligned} \tag{3.46}$$

where the $\pm$ depends on the exact structure of $\Gamma_{\text{src}}$ and $\Gamma_{\text{snk}}$. Most of the mesons we will consider are flavour off-diagonal, i.e. have two distinct valence quarks (in particular this is true for $D$ and $D_s$), and therefore do not have quark-disconnected diagrams. In the case of flavour diagonal valence quarks there are additional possibilities for the Wick contractions, i.e. quark-disconnected pieces, that need to be taken into account. In the case of the (fictitious) $\eta_s$ and the $\eta_c$ and $J/\Psi$, such quark-disconnected contributions exist and must in principle be considered.

So to carry out a measurement on a given configuration, the key ingredient to calculating masses and matrix elements is to invert the Dirac operator $D$ to find the *propagator*. The equation that needs to be solved for this (using the Einstein summation convention) is

$$D(n|m)^{\;ab}_{\alpha\beta} S(m|r)^{\;bc}_{\beta\epsilon} = \delta_{ac}\,\delta_{\alpha\epsilon}\,\delta_{n,r}. \tag{3.47}$$

The Dirac operator is a large object, so to calculate its inverse we need to make use of numerical solvers. However, contrary to the Dirac operator, which is a large but *sparse* matrix, the propagator is not sparse. It is a square matrix of size $(|\Lambda| \times 4_{\text{spin}} \times 3_{\text{colour}})^2$. A lattice typical to the presented work has spatial extent $N = 48$ and temporal extent $N_T = 96$. Even numerically it is not feasible to calculate this inversion exactly in full.

Instead we only calculate one column of the inverse matrix by solving the linear equation (suppressing spin and colour indices into vector/matrix notation)

$$\sum_{\boldsymbol{y},t} D(\boldsymbol{x},t|\boldsymbol{y},t')\psi(\boldsymbol{y},t') = \eta(\boldsymbol{x},t). \tag{3.48}$$

Here $D$ is the Dirac operator of the used fermion discretisation, $\eta$ is the *source vector* and $\psi$ is the desired solution vector, which is the propagator from the source to all other points. We solve the above twelve times for each source position - once for each combination of spin and colour. The exact choice of possible source vectors $\eta$ will be discussed in section 3.7.4. From solving (3.48) we obtain the solution vector $\psi(\boldsymbol{y},t)$ as

$$\psi(\boldsymbol{x},t) = \sum_{\boldsymbol{y},t'} S(\boldsymbol{x},t|\boldsymbol{y},t')\eta(\boldsymbol{y},t'), \tag{3.49}$$

which is the column of the propagator from the source to all other points.

Having found $D_{q_1}^{-1}(x|x_{\text{src}})$, (3.46) suggests that we also need to find the propagator $D_{q_2}^{-1}(x_{\text{src}}|x)$ from all points $x$ back to the source position $x_{\text{src}}$. However, we can utilise $\gamma_5$-*hermiticity* present in nearly all incarnations of the Dirac operator, which relates $D^\dagger$ to $D$ as

$$D^\dagger = \gamma_5 D \gamma_5. \tag{3.50}$$

This property also holds for the inverse Dirac operator, allowing to efficiently compute two point functions by noting that

$$S^\dagger(\boldsymbol{x}, t|\mathbf{0}, 0) = \gamma_5 S(\mathbf{0}, 0|\boldsymbol{x}, t)\gamma_5. \tag{3.51}$$

Large efforts within the lattice field theory community are directed at finding efficient algorithms to solve the linear equation (3.48), tailored to the exact form of the chosen fermion discretisation and therefore the form of the Dirac matrix. We will just briefly mention two such solvers, which have been used in the data generation for the works presented here. The first one is the *Conjugate Gradient* (CG) algorithm [103] (reviewed for example in ref [104]) which is an iterative method suitable for symmetric, positive definite matrices. The second one is the *Hierarchically Deflated Conjugate Gradient* (HDCG) algorithm, developed by P. Boyle [105]. This was vital in particular for the calculation of many physical light quark propagators, which are numerically very costly as the Dirac matrix becomes more and more ill-conditioned as the quark masses are reduced.

When computing heavy quark propagators with CG-type algorithms round-off errors can affect the result [106]. To ensure that this is not the case, we implemented and monitored the *time slice residual* [106] defined as

$$r_t = \max_t \left( \frac{|D\psi - \eta|_t}{|\psi|_t} \right), \tag{3.52}$$

where $D$ is the Dirac operator, $\eta$ the source vector and $\psi$ the solution vector. The norm $|x|_t$ is defined as the norm of the vector $x$ restricted to the time slice $t$.

### 3.7.3 Effective Mass

Recall that LQCD simulations always provide statistical estimates of observables which therefore have a statistical uncertainty. This means that (3.44) suggests that there is a time slice $t_{\text{min}}$ from which onwards the excited state contamination is sufficiently suppressed to be subleading to the statistical uncertainty. In the region of $t_{\text{min}} < t < T - t_{\text{min}}$ one assumes the correlation function to be dominated by the ground state. So in this region we can fit the data to the ansatz (3.44) and extract the energy and the matrix elements of the ground state. One problem that needs to be addressed is how to find this time slice $t_{\text{min}}$. To achieve statistical accuracy it is desirable to be able to choose this value as small as possible, since the signal-to-noise ratio grows over time [107, 108]. Ways of achieving this are presented in section 3.7.4.

The *effective mass* $m_{\text{eff}}(t)$ provides a visual measure to test whether or not a correlation function is dominated by the ground state for a given time $t$. There are a number of

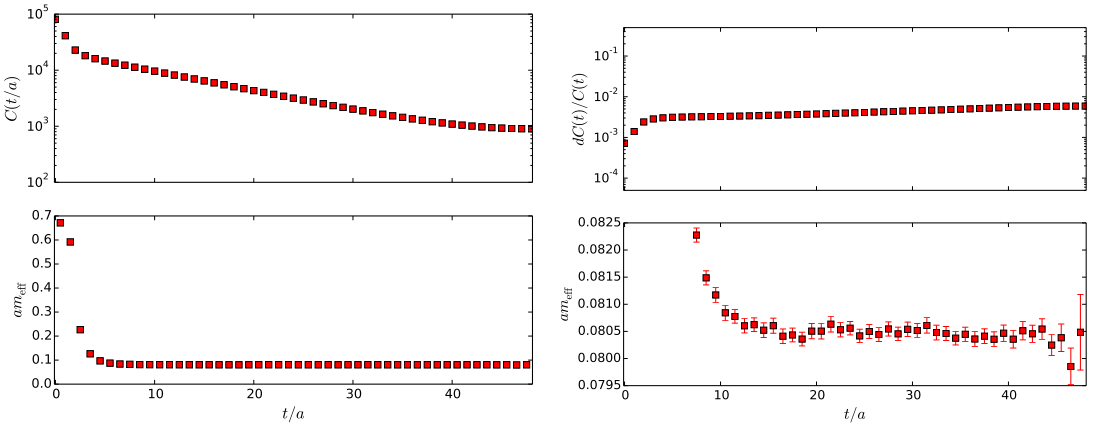


Figure 3.2: *left*: Example of a pseudoscalar meson correlation function $C(t)$ (top panel) and the associated effective mass $am_{\text{eff}}$ (bottom panel) on the coarser physical pion mass ensemble of RBC/UKQCD ($m_\pi = 139\,\text{MeV}$, $a^{-1} = 1.73\,\text{GeV}$; later introduced as **C0**). The example here is shown for a light-light meson. *right*: The top panel shows the relative error on the same correlation function as a function of time, whilst the bottom panel simply zooms into the plateau region of the effective mass.

different ways to define this quantity. Taking into account the backwards travelling contribution, (3.44) is modified to

$$C_2(t)|_{\boldsymbol{p}=\boldsymbol{0}} = \sum_n \frac{Z^*_{\text{src},n}\, Z_{\text{snk},n}}{E_n}\, e^{-E_n T/2}\, \frac{e^{E_n(T/2-t)} \pm e^{-E_n(T/2-t)}}{2}, \tag{3.53}$$

where $Z_{\text{src}}$ and $Z_{\text{snk}}$ are the matrix elements between the QCD vacuum and the operator at the source and the sink respectively as defined before. Equation (3.53) can be rewritten in terms of a hyperbolic cosine or hyperbolic sine, respectively. In the following we will denote cosh and sinh as func. The convention for the effective mass that is used in the remainder of this thesis is given by $am_{\text{eff}}$ satisfying

$$\frac{C(t+a)}{C(t)} = \frac{\text{func}\left[(t+a-\frac{T}{2})m_{\text{eff}}\right]}{\text{func}\left[(t-\frac{T}{2})m_{\text{eff}}\right]}. \tag{3.54}$$

The main feature of the effective mass is the fact that the exponential decay is removed so that a visual inspection of the data becomes more feasible.

The left-hand side of figure 3.2 shows the behaviour of the correlation function and the effective mass as a function of time for the example of a light-light meson on one of RBC/UKQCD's physical pion mass ensembles. The right-hand side of the same figure shows the relative error of the correlation function as well as a zoom into the region where the effective mass plateaus. We can clearly identify a plateau towards the centre of the lattice, starting from time slices $t_{\text{min}}/a \sim 15$. This suggests that in this region the correlation function is dominated by the ground state and the excited states have decayed

away. This means that one can now fit the expected functional form, as suggested by (3.44) to the data obtained for $t \in [t_{\text{min}}, t_{\text{max}}]$ where $t_{\text{max}}$ is usually chosen to be $T/2$[1]. Naturally, one needs to verify that small perturbations of $t_{\text{min}}$ and $t_{\text{max}}$ have no influence on the obtained fit results to assess systematic errors arising from the choice of fit range.

### 3.7.4 Sources and Smearing

Figure 3.3 shows that for mass non-degenerate mesons the signal-to-noise ratio grows exponentially [107, 108] with time, so it is desirable to decrease $t_{\text{min}}$ as much as possible. Rewriting the matrix elements as $Z_n$ for brevity, we can re-express (3.44) as

$$\begin{aligned} C_2(t) &= \sum_n \frac{1}{2E_n} |Z_n|^2 e^{-E_n t} \\ &= \frac{1}{2E_0} |Z_0|^2 e^{-E_0 t} + \frac{1}{2E_1} |Z_1|^2 e^{-E_1 t} + \cdots \\ &= \frac{1}{2E_0} |Z_0|^2 e^{-E_0 t} \left( 1 + \frac{E_0}{E_1} \frac{|Z_1|^2}{|Z_0|^2} e^{-\Delta E t} + \cdots \right). \end{aligned} \tag{3.55}$$

We see that the contamination of excited states at a given time $t$ depends on the difference $\Delta E = E_1 - E_0$ between the energy of the lowest lying state $E_0$ and the next higher state with the same quantum numbers $E_1$. This implies a bound in $t_{\text{min}}$ below which one no longer fits the pure ground state. Additionally, this difference $E_1 - E_0$ decreases as the quark masses get heavier, leading to less suppression of the excited states and correspondingly later plateaus than in the case of light quarks. To reliably extract hadronic observables from this, one can fit the $n$ first excited states. This leads to an increase in fit parameters and one has to be careful that the choice of $t_{\text{min}}$ does not influence the fit result. Alternatively one can choose a spatially extended or *smeared* source that approximates the spatial form of the physical ground state wave function more closely than a naive point source. This results in decreasing the ratio $|Z_1|^2 / |Z_0|^2$ in (3.55) and therefore suppresses the contamination of excited states stronger for *earlier* time slices.

However, if one is interested not only in energies but also in the matrix elements (as in the case of the decay constants), one has to take care to extract the matrix elements from *local* operators, i.e. not smeared ones. This can still be achieved when using smeared sources, e.g. by placing the operator of interest at the sink and smearing the sources. Alternatively one can produce correlation functions with smeared as well as local sources and fit them simultaneously. This increases the number of fit parameters in the fit, but also the amount of data that enters the fit. One type of such spatially extended sources extensively used throughout this thesis is Gaussian smearing [109]. The idea here is to

[1] Data points at the centre of the temporal extent of the lattice are prone to be undersampled and typically have large error bars. For such cases - which we will frequently encounter as we increase the mass splitting between the two quark masses - we often choose $t_{\text{max}} < T/2$.

apply a smearing operator $H$ to the source in a gauge-covariant fashion. The smearing operator we use has 2 parameters: the number of Jacobi iterations $N$ that the smearing operator $H$ is applied and the *smearing radius* $r$, defined in the following. The smearing operator acts in colour space (so we suppress the trivial Dirac indices) and is defined by

$$[H\eta]_a(\boldsymbol{n}) = \sum_b \sum_{\boldsymbol{m}} \left( \delta_{\boldsymbol{n},\boldsymbol{m}}\delta_{ab} + \frac{r^2}{4N}\Delta[U]_{ab}(\boldsymbol{n},\boldsymbol{m}) \right) \eta_b(\boldsymbol{m}), \tag{3.56}$$

where $\Delta[U]$ is the gauge covariant Laplace operator in the spatial directions, i.e.

$$\Delta[U](\boldsymbol{n},\boldsymbol{m}) = \sum_{j=1}^{3} 2\delta_{\boldsymbol{n},\boldsymbol{m}} - U_j(\boldsymbol{n},t)\delta_{\boldsymbol{n}+\hat{j},\boldsymbol{m}} - U_j(\boldsymbol{n}-\hat{j},t)^\dagger \delta_{\boldsymbol{n}-\hat{j},\boldsymbol{m}}. \tag{3.57}$$

In the above we have suppressed colour indices into matrix/vector notation for notational convenience. The smeared source $\eta^S$ now is found from applying the smearing operator $H$ $N$ times to the original source $\eta^L$ where a summation over all space points is implicit (since we keep $t$ fixed), i.e.

$$\eta^S = H^N \eta^L. \tag{3.58}$$

In the limit of $N \to \infty$ this becomes a Gaussian of width $r$. Note that we can also smear the quark field *after* the inversion, i.e. at the sink. For a meson consisting of two flavour off-diagonal quarks, having unsmeared and smeared sources and sinks this allows for $2^4 = 16$ combinations of the smearing.

The effect of smearing can be seen in the left-hand side of figure 3.3. The figure shows the effective mass for a strange-heavy meson on the ensemble Q3 (introduced later, compare table 5.1). In all four cases, the source and the sink of the strange quark are local, whilst the source (1st index) and sink (2nd index) of the heavy quark can be local (L) or smeared (S). One can clearly see an earlier approach to the plateau for the smeared cases, allowing for the inclusion of earlier time slices into the fit.

So far we considered *point sources*, i.e. sources which are located on a single site of the lattice (compare 3.47) and are sensitive to local fluctuations of the gauge field. In addition they do not make use of the entire volume [110], so to maximise the information extracted one would need to place many point sources across the volume and hence have to perform many inversions of the Dirac operator. An increase in precision can be obtained from using $N_{\text{hit}}$ stochastic sources $\eta_{a\alpha}(\boldsymbol{x},t_x)$ (for fixed $t_x$) with colour and spin indices $a$ and $\alpha$, respectively and sitting at the site $x$, provided their (hit-)expectation value satisfies

$$\left\langle \eta^{(n)}_{a,\alpha}(\boldsymbol{x},t_x)\eta^{(n)\dagger}_{b,\beta}(\boldsymbol{y},t_x) \right\rangle_n \equiv \frac{1}{N_{\text{hit}}} \sum_{n=1}^{N_{\text{hit}}} \eta^{(n)}_{a,\alpha}(\boldsymbol{x},t_x)\eta^{(n)\dagger}_{b,\beta}(\boldsymbol{y},t_x) \overset{N_{\text{hit}}\to\infty}{\to} \delta_{ab}\delta_{\alpha\beta}\delta_{\boldsymbol{x},\boldsymbol{y}} \tag{3.59}$$

in the large-hit-limit (i.e. the limit $N_{\text{hit}} \to \infty$). Furthermore, it is worth noticing that the gauge and the hit average commute, so even by only placing as few as a single

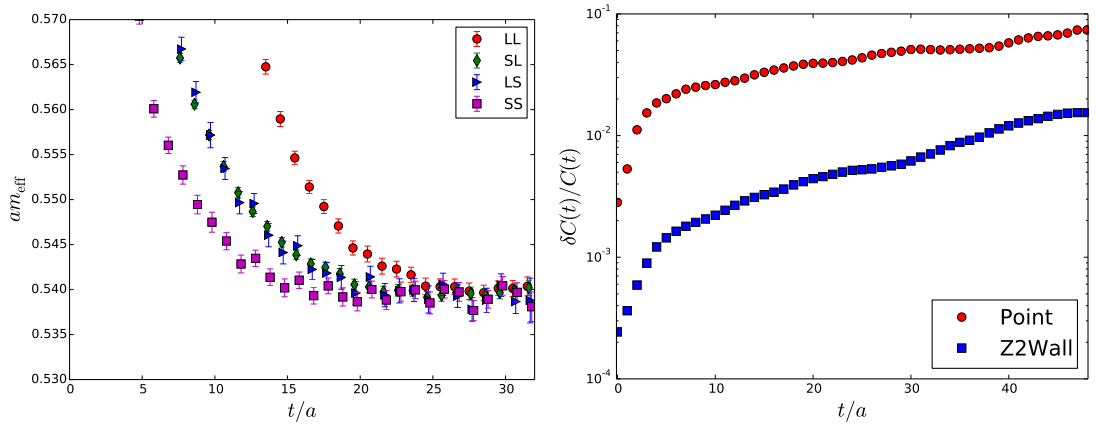


Figure 3.3: Impact of source/sink smearing and $\mathbb{Z}_2$-Wall sources illustrated for a heavy-strange pseudoscalar meson. *left*: Effect of smearing on the observed plateau on the ensemble Q3 from the quenched pilot study with point sources. The first letter in the legend refers to whether the source of the heavy quark is local (L) or smeared (S)). Similarly the second letter refers to the sink. *right*: Same cost comparison of the statistical accuracy of the correlation function between a point source and a $\mathbb{Z}_2$-Wall source on the ensemble C0.

stochastic source on each configuration the correct large hit behaviour is recovered [110]. Placing such stochastic sources across the entire spatial volume allows for full volume averaging. One distribution $\mathcal{D}$ which has been advocated [111, 112] is that of complex $\mathbb{Z}_2 \times \mathbb{Z}_2$ numbers, i.e.

$$\mathcal{D} = \left\{ z \in \frac{1}{\sqrt{2}} (\pm 1 \pm i) \right\}. \tag{3.60}$$

Recall the definition of the two-point correlation function (of flavour off-diagonal operators) projected to zero momentum in terms of the propagators (compare (3.46)) and insert a delta function in spin, colour and space-time into it. Assuming that the large hit limit is satisfied, we obtain

$$\begin{aligned}
C(t_x, t_y) &= \left\langle \sum_{\boldsymbol{x},\boldsymbol{y}} \mathrm{tr}[\Gamma_{\mathrm{snk}} S_{q_2}(\boldsymbol{y}, t_y | \boldsymbol{x}, t_x) \Gamma_{\mathrm{src}} S_{q_1}(\boldsymbol{x}, t_x | \boldsymbol{y}, t_y)] \right\rangle_{\mathrm{g}} \\
&= \left\langle \sum_{\boldsymbol{x},\boldsymbol{y},\boldsymbol{z}} \mathrm{tr}\left[ \Gamma_{\mathrm{snk}} S_{q_2}(\boldsymbol{y}, t_y | \boldsymbol{x}, t_x) \left\langle \eta(\boldsymbol{x}) \eta^\dagger(\boldsymbol{z}) \right\rangle_n \Gamma_{\mathrm{src}} S_{q_1}(\boldsymbol{z}, t_z | \boldsymbol{y}, t_y) \right] \right\rangle_{\mathrm{g}} \Bigg|_{t_x = t_z} \\
&= \left\langle \sum_{\boldsymbol{x},\boldsymbol{y},\boldsymbol{z}} \mathrm{tr}\left[ \Gamma_{\mathrm{snk}} S_{q_2}(\boldsymbol{y}, t_y | \boldsymbol{x}, t_x) \eta(\boldsymbol{x}) \eta(\boldsymbol{z})^\dagger \Gamma_{\mathrm{src}} \gamma_5 S^\dagger_{q_1}(\boldsymbol{y}, t_y | \boldsymbol{z}, t_z) \gamma_5 \right] \right\rangle_{\mathrm{n,g}} \Bigg|_{t_x = t_z} \\
&= \left\langle \sum_{\boldsymbol{x},\boldsymbol{y},\boldsymbol{z}} \mathrm{tr}\left[ \Gamma_{\mathrm{snk}} S_{q_2}(\boldsymbol{y}, t_y | \boldsymbol{x}, t_x) \eta(\boldsymbol{x}) \Gamma_{\mathrm{src}} \gamma_5 \left[ S_{q_1}(\boldsymbol{y}, t_y | \boldsymbol{z}, t_z) \eta(\boldsymbol{z}) \right]^\dagger \gamma_5 \right] \right\rangle_{\mathrm{g,n}} \Bigg|_{t_x = t_z}.
\end{aligned} \tag{3.61}$$

Here $\langle \cdot \rangle_g$ and $\langle \cdot \rangle_n$ represent the gauge average and the large hit limit, respectively. Further, we omitted the hit index $(n)$ of the source vectors $\eta^{(n)}(\boldsymbol{x})$ as well as suppressed

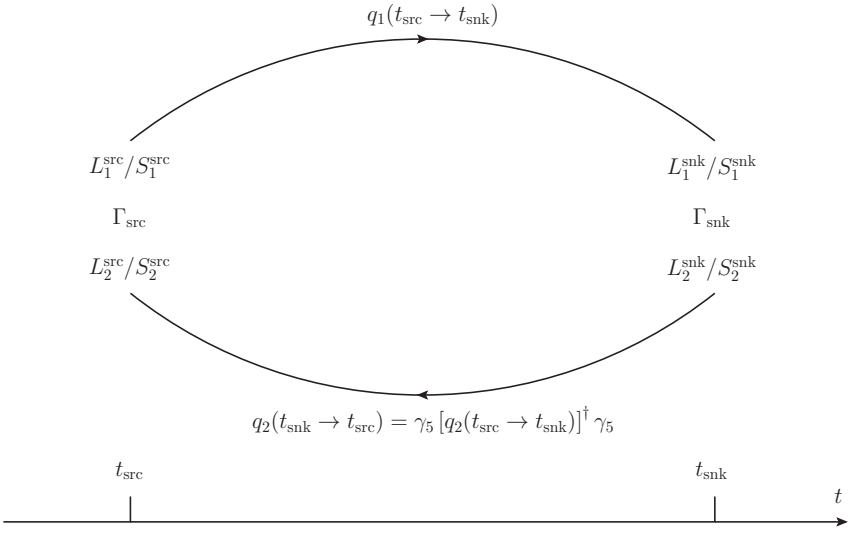


Figure 3.4: Schematic quark flow diagram for a general mesonic two point function.

spin and colour indices into vector/matrix notation. In the second line we inserted a delta function in spin, colour and space and assumed the large hit limit (3.59) to be satisfied. In the third line we used $\gamma_5$-hermiticity of the propagator(3.51) and the fact that the large hit limit and the gauge limit commute. We also assumed that the source vectors $\eta^{(n)}(\boldsymbol{x})$ are diagonal in spin space, and noted that $(\Gamma_{\text{snk}}\gamma_5)^\dagger$ is diagonal in colour space, so the multiplication of these two terms can be interchanged.

Equation (3.61) shows that for a given time slice $t_{\text{src}}$, we can use the same noise vector for both propagators, introducing noise only once. It also means that we only need to invert the Dirac matrix once per flavour. So at the expense of introducing noise, we can sample the full 3-volume of the source time-plane with one inversion. This is known as the *one-end-trick* [110, 113]. In the remainder of this thesis, these sources will be referred to as $\mathbb{Z}_2$-Wall sources [110]. Other noise reduction techniques include *low-mode-averaging* [114, 115], *all-mode-averaging* [116–118], deflation [119] and distillation [120] but will not be discussed in detail as they go beyond the scope of this thesis.

The limitation of $\mathbb{Z}_2$-Wall sources is the fact that we lose the possibility of projecting to momenta other than zero. This is not a problem for observables such as masses and decay constants, but for example for dispersion relation studies we have to restrict ourselves to point sources. It is worth noticing that we can (and will) combine the two methods and produce Gaussian smeared $\mathbb{Z}_2$-Wall sources to have the benefit of both strategies.

Figure 3.4 is a schematic QCD quark flow diagram summarising the constructions we use for a generic meson two point function. We first pick a source time-plane $t_{\text{src}}$ and - for the case of $\mathbb{Z}_2$-Wall sources - $\eta_{a\alpha}(\boldsymbol{x})$, which is diagonal in spin, randomly drawn from

the distribution $\mathcal{D}$ at every spatial position $\boldsymbol{x}$. In the case of a point source we simply choose one site and place the source there. We then optionally apply Gaussian smearing at the source ($L_i^{\text{src}}$ for local or $S_i^{\text{src}}$ for smeared) before solving the equation (3.48) for each flavour $f$ present in the problem, hence producing all propagators of interest ($q_1$ and $q_2$ in the figure). We can then again apply the smearing to the sink position of the propagator ($L_i^{\text{snk}}$ for local or $S_i^{\text{snk}}$ for smeared). Here $i$ labels the propagator under consideration. Finally we insert all desired spin structures $\Gamma_{\text{src}}$ and $\Gamma_{\text{snk}}$ at source and sink and project to the desired momenta ($\boldsymbol{p} = \boldsymbol{0}$ for $\mathbb{Z}_2$-Wall sources).

### 3.7.5 Statistical Methods - Resampling

Whilst for observables which are directly measured (*primary observables*), it is possible to assign a statistical error directly, this becomes more difficult for deduced or *secondary* observables, particularly if they are determined non-linearly from the underlying data. This is usually done by *resampling*. In this thesis we will adopt the *bootstrap* resampling method [121, 122], (which is a generalisation of the *jackknife* resampling method), which we will briefly outline in the following.

Assume that $N_{\text{conf}}$ independent measurements have been taken. We will create $N_{\text{Boot}}$ *bootstrap samples*. Each bootstrap sample is found by randomly drawing $N_{\text{conf}}$ measurements from the $N_{\text{conf}}$ measurements that were carried out, but **with** replacement. We now treat the $N_{\text{boot}}$ samples as our measurements and every treatment to the data is carried out *bootstrap sample-by-bootstrap sample*. The statistic error for any quantity (primary or secondary) can now be determined from the bootstrap distribution of this quantity. We stress, that the error assigned by any resampling method is an *estimate*, i.e. has an uncertainty itself [123].

### 3.7.6 Correlator Fits

In all cases the data is first folded before further processing, i.e. symmetrised around $t = T/2$ and then only the range $0 \leq t \leq T/2$ is considered. Within this range an interval $[t_{\text{min}}, t_{\text{max}}]$ is chosen and the data of time slices inside this interval will enter into the fit. Fits are performed as a numerical iterative procedure by means of a least square fit of the data to the functional form $f(t)$ that we expect. In particular, we minimise $\chi^2$ defined by

$$\chi^2 = (C(t_i) - f(t_i))\,\text{cov}_{ij}^{-1}\,(C(t_j) - f(t_j))\,. \tag{3.62}$$

Here $C(t_i)$ is the value of the correlation function on the time slice $t_i$ and cov the covariance matrix. From these fits we then extract the parameters that enter the functional form (3.53), in particular we obtain matrix elements and energies. The estimated

covariance matrix that enters the fit is defined as

$$\mathrm{cov}_{ij} = \frac{1}{A}\sum_{k=1}^{N}\left(C^{(k)}(t_i) - \langle C(t_i)\rangle\right)\left(C^{(k)}(t_j) - \langle C(t_j)\rangle\right), \tag{3.63}$$

where $N$ is the number of measurements that enter the fit, $C^{(k)}$ is the $k$th measurement of the correlation function and the normalisation $A$ depends on the exact resampling that is used to obtain the statistical errors. In particular, $A = N(N-1)$ if the raw data is used, $A = N/(N-1)$ for Jackknife resampling and $A = N$ for Bootstrap resampling. In the limit of infinite data ($N \to \infty$) the estimated covariance converges to the true covariance matrix. With finite statistics, the covariance matrix may be poorly estimated and ill-conditioned (i.e. numerically close to singular). In this case a *correlated fit* (as defined by (3.62)) often does not converge and one restricts the covariance matrix (3.63) to its diagonal part before inverting. This is referred to as an *uncorrelated fit*.

An indication for the goodness-of-fit is the reduced $\chi^2$,

$$\chi^2_{\mathrm{red}} = \chi^2/\mathrm{d.o.f}, \tag{3.64}$$

where d.o.f is the number of degrees of freedom, i.e. the difference between the measured data points that enter the fit and the number of parameters the fit needs to determine. For a correlated fit, the value of $\chi^2$ in combination with the number of degrees of freedom also has a probabilistic interpretation to asses how good the fit is. For a correlated fit and a sufficiently large number of degrees of freedom to a known fit function, most probable value is $\chi^2_{\mathrm{red}} = 1$.

In the case where we neglect correlations by performing an uncorrelated fit, even though the data has inherent correlations, there is no probabilistic interpretation of the value of $\chi^2$ but merely serves as an indication.

## 3.8 Systematic Errors

Additional to the inherent statistical error, the lattice methodology necessarily introduces some systematic errors that need to be removed and controlled. The finite volume causes 'around-the-world' effects, i.e. self-interactions between particles at lattice sites $n$ and their counterpart across the boundary of the system. For a given particle of mass $m$ these effects are expected to be exponentially suppressed by $e^{-mL}$ [124]. This means that the lightest hadron of the system determines the volume needed to keep these finite volume effects at bay, which in any dynamical simulation is the pion. It is found that for $m_\pi L \gtrsim 4$ finite volume effects are at the percent level [125].

Some discretisation errors are expected to grow as powers of $am_q$ where $m_q$ are the quark masses [1]. It follows that discretisation effects will grow quickly as the mass $m_q$ of the

heaviest quark under consideration is increased. To be able to simulate large values of the quark mass without introducing large discretisation errors, small lattice spacings are needed [126, 127]. To ensure control over discretisation errors, it is important to calculate the same physical observables on lattices with different lattice spacings and then fit this to a polynomial in the lattice spacing $a$ to extrapolate to $a = 0$. This is known as a *continuum limit*. A number of lattice discretisations ensure automatic $\mathcal{O}(a)$-improvement, meaning discretisation errors proportional to the lattice spacing are not present. In this case the first term that needs to be fitted when determining lattice artefacts are $\mathcal{O}(a^2)$. This is the case for domain wall fermions, which will be discussed in detail in the next chapter.

The constraints imposed by simultaneously keeping discretisation and finite volume errors under control become more and more restrictive as the ratio between the lightest and the heaviest simulated mass decreases. In particular the pion mass $m_\pi$ and the bare heavy quark mass $m_h$ are required to satisfy

$$L^{-1} \ll m_\pi < m_h < a^{-1}. \tag{3.65}$$

This enforces a bound on the range of masses and energies that can be simulated on a given ensemble and is one of the reasons why ensembles with physical pions masses have only recently become feasible. Further systematic errors arise from the assumptions one makes in lattice QCD simulations. Up to date, most collaborations treat the up and the down quark as mass degenerate (strong isospin) and ignore electromagnetic effects (weak isospin). Throughout the remainder of this thesis these assumptions will also be made here.

# Chapter 4

# Domain Wall Fermions on the Lattice

In the previous chapter we have seen that a Dirac operator satisfying (3.35) is not suitable to simulate chiral symmetry on the lattice. We will now generalise this condition of chiral symmetry and introduce domain wall fermions ([128] and further developments in refs [129–132]) to see how we can circumvent the Nielsen-Ninomiya Theorem [86].

This chapter is organised as follows. After briefly outlining how a fifth dimension can circumvent the Nielson-Ninomiya Theorem in section 4.1 we will discuss the formulation of domain wall fermions in section 4.2. Finally we will outline the relation between DWFs and the Ginsparg-Wilson relation in section 4.3.

## 4.1 Effects of a Domain Wall in an Infinite Fifth Dimension

Assume a fermion that lives in 5 dimensions. The usual 4 infinite space-time dimensions with coordinates $x$, $y$, $z$, $t$ as well as a fifth dimension with coordinate $s$. Furthermore, we will assume an s-dependent mass term that flips sign at $s = 0$, i.e.

$$m(s) = \begin{cases} +m & s > 0 \\ -m & s < 0 \end{cases} . \tag{4.1}$$

We assume that the gauge field with which the fermion interacts lives in the 4 usual space-time dimensions. The Dirac equation this fermion $\Psi$ needs to satisfy then reads

$$\left[\not{D} + \gamma_5 \partial_s + m(s)\right] \Psi(x_\mu, s) = 0, \tag{4.2}$$

where $D$ is some 4-d Dirac operator. We can now transform (4.2) into an eigenvalue problem by separation of variables, assuming a solution of the form

$$\Psi(x_\mu, s) = \sum_n \left[a_n(s)P_R + b_n(s)P_L\right]\psi_n(x), \tag{4.3}$$

where

$$P_{R,L} = P_\pm = \frac{\mathbb{1} \pm \gamma_5}{2}. \tag{4.4}$$

Substituting this into (4.2) one obtains

$$\begin{aligned} \left[\partial_s + m(s)\right] a_n(s) &= \alpha_n b_n(s) \\ \left[-\partial_s + m(s)\right] b_n(s) &= \alpha_n a_n(s) \\ \left(\not{D} + \alpha_n\right)\psi_n(x) &= 0, \end{aligned} \tag{4.5}$$

for some eigenvalues $\alpha_n$. We can now note, that for $\alpha_n = 0$ the last line is the Dirac equation for a massless fermion. Furthermore, for the case of $\alpha_n = 0$ the equations for $a_n(s)$ and $b_n(s)$ decouple and are easily solved to give

$$\begin{aligned} a_n(s) &= A\, e^{-\int_0^s m(s')\mathrm{d}s'} = A\, e^{-\int_0^s m|s|\mathrm{d}s'} \\ b_n(s) &= B\, e^{+\int_0^s m(s')\mathrm{d}s'} = B\, e^{+\int_0^s m|s|\mathrm{d}s'}. \end{aligned} \tag{4.6}$$

However, the solution $b_n(s)$ is not normalisable and therefore not a physical solution. So, in summary, there is an infinite tower of fermions $\psi_n(x)$ with masses $|\alpha_n| > 0$ (*bulk modes*) and a single massless right-handed fermion exponentially localised near the defect at $|s| = 0$.

On the lattice we will always have to choose a finite fifth dimension. This implies that we will necessarily have more than one defect, e.g. choose a compact fifth dimension of extend $2s_0$ with periodic boundary conditions ($\Psi(s) = \Psi(s + 2s_0)$) and a mass term $m(s) = m\,|s|\,/s$ with two defects (at $s = 0$ and $s = s_0$). Now, contrary to before, both solutions are normalisable and we find two exponentially localised massless chiral modes; the previous right-handed mode at $s = 0$ and a left-handed mode at $s = \pm s_0$. However, recalling that terms breaking chiral symmetry mix left-handed and right-handed components and that these modes are exponentially localised a distance $s_0$ apart this residual chiral symmetry breaking is expected to be small. We will define a measure for this residual chiral symmetry breaking, called the *residual mass* in the next section.

## 4.2 Domain Wall Fermions on the Lattice

Following on from the previous section, the idea in the formulation of domain wall fermions is to simulate a 5-dimensional lattice with chiral fermions bound to a 4-dimensional slice of this fifth dimension. However, in a numerical simulation we are not

able to simulate a continuous or infinite fifth dimension. So we extend the 4-dimensional lattice volume $\Lambda$ defined in (3.5) to a 5-dimensional volume $\Lambda_5 = \Lambda \times L_s$ where $L_s$ is the finite extent of the fifth dimension

$$\Lambda_5 = \{(an_\mu, s) \,:\, an_\mu \in \Lambda; s \in 0, \cdots, L_s - 1\}\,. \tag{4.7}$$

The action for a 5-dimensional fermion $\Psi$ (single flavour) of mass $m_f$ reads (spin and colour indices are suppressed into matrix/vector notation)

$$S_F^{DW}[\overline{\Psi}, \Psi, U](m_f, M_5) = \sum_{(n,s),(m,t)\in\Lambda_5} \overline{\Psi}(n,s) D_5^{DW}(n,s|m,t;m_f,M_5)\Psi(m,t), \tag{4.8}$$

where the gauge fields $U_\mu(n)$ live in the 4-dimensional space. We will see that $m_f$ is indeed the fermion mass and will discuss the impact of the *domain wall height* $M_5$ subsequently. We note that to cancel a bulk infinity that arises in the $L_s \to \infty$ limit, we also include a bosonic Pauli-Villars type term into the action which is given by [133]

$$S_{PV}[\overline{\Phi}, \Phi, U](1, M_5) = \overline{\Phi}(n,s) D_5^{DW} \Phi(n,s|m,t;1,M_5)\Phi(m,t). \tag{4.9}$$

The domain wall Dirac operator $D_5^{DW}$ can be decomposed into two parts, one that is *parallel* and one that is *orthogonal* to the 4-dimensional space-time slices:

$$D_5^{DW}(n,s|m,t;m_f,M_5) = \delta_{s,t} D^{\parallel}(n|m;M_5) + \delta_{n,m} D^{\perp}(s|t;m_f). \tag{4.10}$$

The orthogonal term connects the sites in the fifth dimension and is given by

$$\begin{aligned} D^{\perp}(s|t;m_f) = \delta_{s,t} &- (1-\delta_{s,L_s-1})\, P_L\, \delta_{s+1,t} - (1-\delta_{s,0})\, P_R\, \delta_{s-1,t} \\ &+ m_f\, (P_L\, \delta_{s,L_s-1}\, \delta_{0,t} + P_R\, \delta_{s,0}\, \delta_{L_s-1,t})\,. \end{aligned} \tag{4.11}$$

We can see that the surface terms are eliminated by the term $1-\delta_{s,L_s-1}$ and $1-\delta_{s,0}$, respectively. We note that the only term that mixes the 4-dimensional slices at $s = 0$ and $s = L_s - 1$ is proportional to the constant $m_f$ which resembles a mass term (compare (2.8)). In particular, for $m_f = 0$ the boundaries are not directly connected since the only terms that mix the 4-dimensional slices at $s = 0$ and $s = L_s - 1$ are proportional to $m_f$, in agreement with our interpretations as the fermion mass.

We define the 4-dimensional fermion fields $\psi$ and $\overline{\psi}$ from the fields at the boundaries of the fifth dimension, as

$$\begin{aligned} \psi(n) &= \psi_L(n) + \psi_R(n) = P_L\Psi(n,0) + P_R\Psi(n,L_s-1) \\ \overline{\psi}(n) &= \overline{\psi}_L(n) + \overline{\psi}_R(n) = \overline{\Psi}(n,0)P_R + \overline{\Psi}(n,L_s-1)P_L. \end{aligned} \tag{4.12}$$

So the 4-dimensional fermion is constructed as a superposition of a left-handed mode at $s = 0$ and a right-handed mode at $s = L_s - 1$. The scalar density is now given by

$$\begin{aligned}\overline{\psi}(n)\psi(n) &= \left[\overline{\Psi}(n, L_s - 1)P_L + \overline{\psi}(n, 0)P_R\right]\left[P_L\Psi(n, 0) + P_R\Psi(n, L_s - 1)\right] \\ &= \overline{\Psi}(n, L_s - 1)P_L\Psi(n, 0) + \overline{\Psi}(n, 0)P_R\Psi(n, L_s - 1). \\ &= \overline{\psi}_R(n)\psi_L(n) + \overline{\psi}_L(n)\psi_R(n).\end{aligned} \tag{4.13}$$

However, due to the finiteness of the fifth dimension, there are additional contributions that mix the left-handed and the right-handed modes due to the propagation through the fifth dimension, leading to a *residual chiral symmetry breaking*. This gives rise to a small mass term called the *residual mass*. More about this later.

The parallel term is the usual Wilson Dirac operator as defined in (3.33), however we replace the mass $m$ by $-M_5$ where the new parameter $M_5$ is the *domain wall height*.

We define the *local* four-dimensional axial and vector currents as

$$\begin{aligned}V_\mu^a(n) &= \overline{\psi}(n)t^a\gamma_\mu\psi(n) \\ A_\mu^a(n) &= \overline{\psi}(n)t^a\gamma_\mu\gamma^5\psi(n).\end{aligned} \tag{4.14}$$

These are related to the *conserved currents* $\mathcal{V}_\mu^a(n)$ and $\mathcal{A}_\mu^a(n)$ by multiplicative renormalisation constants $\mathcal{Z}_V$ and $\mathcal{Z}_A$ respectively, i.e.

$$\begin{aligned}\mathcal{Z}_A A_\mu^a(n) &= \mathcal{A}_\mu^a(n) \\ \mathcal{Z}_V V_\mu^a(n) &= \mathcal{V}_\mu^a(n).\end{aligned} \tag{4.15}$$

For exact chiral symmetry these renormalisation constants are related by $\mathcal{Z}_A = \mathcal{Z}_V$ [134]. The conserved vector current is uniquely defined by

$$\mathcal{V}_\mu^a(n) = \sum_{s=0}^{L_s-1} j_\mu^a(n, s), \tag{4.16}$$

where

$$j_\mu^a(n, s) = \frac{1}{2}\left[\overline{\psi}(n + \hat{\mu}, s)(1 + \gamma_\mu)U_{n,\mu}^\dagger t^a\psi(n, s) - \overline{\psi}(n, s)(1 - \gamma_\mu)U_{n,\mu}t^a\psi(n + \hat{\mu}, s)\right]. \tag{4.17}$$

The conserved axial current (for $m_f = 0$ and $L_s = \infty$) we use is derived in ref [135]. The axial current satisfies the partially conserved axial Ward identity (PCAWI). In particular $\mathcal{A}_\mu^a$ has a non-zero divergence [131] and satisfies

$$\Delta_\mu\mathcal{A}_\mu^a(n) = 2m_f J_5^a(n) + 2J_{5q}^a(n), \tag{4.18}$$

where

$$\begin{aligned} J_5^a(n) &= -\overline{\Psi}(n, L_s-1)P_L t^a \Psi(n,0) + \overline{\Psi}(n,0)P_R t^a \Psi(n, L_s-1) \\ &= \overline{\psi}(n)\gamma_5 t^a \psi(n) \equiv P^a(n) \\ J_{5q}^a(n) &= -\overline{\Psi}(n, L_s/2-1)P_L t^a \Psi(n, L_s/2) + \overline{\Psi}(n, L_s/2)P_R t^a \Psi(n, L_s/2-1), \end{aligned} \tag{4.19}$$

and $\Delta_\mu f(n) = f(n) - f(n-\hat{\mu})$. In particular the current $J_{5q}^a(n)$ is defined at the midpoint of the fifth dimension and is sensitive to the residual chiral symmetry breaking effects from the propagation of the left-handed and right-handed modes across the fifth dimension and $J_5^a(n)$ is the pseudoscalar density. We quantify this effect of residual chiral symmetry breaking by the *residual mass* which we will now define from expectation values of (4.18). In practice we measure correlation functions projected to zero momentum, given by

$$\begin{aligned} \sum_{\boldsymbol{n}} a \left\langle \Delta_\mu \mathcal{A}_\mu(n) P(0) \right\rangle &= \sum_{\boldsymbol{n}} \left\langle \left[ 2am_f P(n) + 2J_{5q}(n) \right] P(0) \right\rangle \\ &= 2am_f \sum_{\boldsymbol{n}} \left\langle P(n)P(0) \right\rangle + 2 \sum_{\boldsymbol{n}} \left\langle J_{5q}(n) P(0) \right\rangle \\ &= 2 \sum_{\boldsymbol{n}} \left\langle P(n)P(0) \right\rangle \left( am_f + \frac{\sum_{\boldsymbol{n}} \left\langle J_{5q}(n)P(0) \right\rangle}{\sum_{\boldsymbol{n}} \left\langle P(n)P(0) \right\rangle} \right). \end{aligned} \tag{4.20}$$

We can see that the second term in the last line of (4.20) has the form of a mass term. We define the effective residual mass $am_{\text{res}}^{\text{eff}}(t)$ to be exactly this quotient, i.e.

$$am_{\text{res}}^{\text{eff}}(t) = \frac{\sum_{\boldsymbol{n}} \left\langle J_{5q}(\boldsymbol{n}, t) P(\boldsymbol{0}, 0) \right\rangle}{\sum_{\boldsymbol{n}} \left\langle P(\boldsymbol{n}, t) P(\boldsymbol{0}, 0) \right\rangle}. \tag{4.21}$$

So to extract the residual mass $am_{\text{res}}$ we look for a plateau region in (4.21), and fit the data to a constant. As long as the value of $m_{\text{res}}$ is sufficiently small compared to $m_f$ the four dimensional fermions as defined by (4.12) are chiral to a good approximation.

## 4.3 The Ginsparg-Wilson Equation

The first step of resolving how chiral fermions might be simulated in a doubler free theory arose from the rediscovery of the *Ginsparg-Wilson equation* [136], suggesting a modification to (3.35) that disappears in the continuum, namely

$$D(x|y)\gamma_5 + \gamma_5 D(x|y) = aD(x|z)\gamma_5 D(z|y). \tag{4.22}$$

Left and right multiplying this by $D^{-1}(x'|x)$ and $D^{-1}(y|y')$ respectively and relabelling $x \to x'$ and $y \to y'$ one obtains

$$\gamma_5 D^{-1}(x|y) + D^{-1}(x|y)\gamma_5 = a\gamma_5\delta(x-y). \tag{4.23}$$

So for $x \neq y$ this reduces to the condition for chiral fermions (3.35) whilst for $x = y$ this gives rise to a contact term on the right-hand side.

The importance of the Ginsparg-Wilson equation comes from the fact that we can define a modified chiral transformation which reproduces the continuum one in the limit of $a \to 0$, namely

$$\psi \to e^{i\alpha\gamma_5(\mathbb{1}-\frac{a}{2}D)}\psi \qquad \overline{\psi} \to \overline{\psi}e^{i\alpha(\mathbb{1}-\frac{a}{2}D)\gamma_5}. \tag{4.24}$$

If $D$ is a Dirac operator obeying (4.22), then this is a symmetry of the massless action. Using the generalised $\gamma_5$ ($\hat{\gamma}_5$) and generalised projectors ($\hat{P}_{R,L}$)

$$\begin{aligned} \hat{\gamma}_5 &= \gamma_5(\mathbb{1} - aD) \\ \hat{P}_R &= \frac{\mathbb{1} + \hat{\gamma}_5}{2} \\ \hat{P}_L &= \frac{\mathbb{1} - \hat{\gamma}_5}{2}, \end{aligned} \tag{4.25}$$

and noting that

$$D\hat{P}_{R,L} = \hat{P}_{L,R}D, \tag{4.26}$$

we can split the spinor into a left-handed and a right-handed part, analogous to the continuum definitions

$$\psi_{L,R} = \hat{P}_{L,R}\psi \qquad \overline{\psi}_{R,L} = \overline{\psi}P_{R,L}. \tag{4.27}$$

As in the continuum theory, the massless part of the fermion action does not mix left-handed and right-handed components, whilst the mass term does.

There are two commonly used formulations that make use of the Ginsparg-Wilson relation (4.22). The first one, *domain wall fermions* was presented above and approximates (4.22), recovering exact chiral symmetry in the limit $L_s \to \infty$. The second one are the *overlap fermions* [137, 138]. It is possible to show that they are equivalent in the limit of $L_s \to \infty$ [139, 140].

Overlap fermions are found to be computationally more expensive than domain wall fermions. Furthermore, recently a re-formulation of the traditional *Shamir domain wall fermions* (SDWF) [129–132] was found to obtain the same level of residual chiral symmetry breaking with a smaller extent of the fifth dimension [141–143]. These are referred to as *Moebius domain wall fermions* (MDWF). The exact formulation of the domain wall fermions used in the subsequent chapters is described in ref [144].

# Chapter 5

# Heavy Quarks - A Pilot Study with Domain Wall Fermions

Recalling the discussion about effective theory descriptions of systems containing heavy quarks (HQET and NRQCD) from section 2.7 one could imagine to try and make predictions from these instead of full relativistic QCD simulations. On the lattice there is one further approach of dealing with heavy quarks, namely the relativistic heavy quark (RHQ) action [145–147]. In addition to it not being clear a priori whether HQET and NRQCD converge fast enough for the charm quark, NRQCD has the shortcoming that it is impossible to take a well defined continuum limit ($a \to 0$). This introduces a systematic error that is difficult to estimate and control. Whilst the RHQ action can in principle be used to make predictions for quantities containing charm quarks, it requires tuning of more parameters as well as additional calculations of renormalisation constants.

As advertised in chapter 4, DWFs are automatically $O(a)$-improved, which is of particular importance since quantities containing heavy quarks can be affected by strong cut-off effects. Furthermore, it simplifies the renormalisation procedure. However, accessible lattice spacings in state-of-the-art ensembles are limited due to *critical slowing down* [98, 148, 149]. In this chapter, we will establish a formulation of domain wall fermions that allows for the simultaneous simulation of light and charm quarks. We designed the following pilot study to determine a region in the domain wall parameter space in which one can feasibly simulate heavy quarks (charm and beyond) whilst keeping discretisation effects under control.

After a brief phenomenological motivation (section 5.1), we will outline our strategy in section 5.2. Section 5.3 introduces the ensembles used in this study. Section 5.4 summarises the initial scan in parameter space leading to the run set-up presented in 5.5 for further investigation of the scaling of some basic observables. Section 5.6 summarises our findings, leading to the conclusions presented in section 5.7.

## 5.1 Phenomenological Motivation

Experimentally there is a wide activity in charm and bottom physics. For example, in the case of leptonic decay rates of $D$ and $D_s$ mesons, experiments such as CLEO-c [150–153], BESIII [154], Belle [155] and BaBar [156] have produced a wide range of results. Meanwhile, LHCb is still ongoing and Belle II will soon start taking measurements. With such a projected increase in experimental data, we need to work to reduce the theoretical uncertainties to fully exploit the experimental results. For example, as discussed previously (compare section 2.5), we need theoretical input of the decay constants to extract the CKM-matrix elements from this.

There are a number of different calculations on the lattice which require a valence charm quark ($f_D$, $f_{D_s}$, $D$ and $D_s$ semi-leptonic decays, contributions to the Hadronic Vacuum Polarisation (HVP),...). Additionally, there are also an increasing number of $2+1+1f$ simulations. To exploit symmetry arguments such as the Glashow-Iliopoulos-Maiani (GIM) mechanism [70], it is important to use the same discretisation between the charm and the lighter quarks. Finally if we manage to push the heavy quark mass beyond the charm quark mass and towards the regime of bottom physics, we might be able to provide a fully relativistic description of $b$-like quarks. Even if we are unable to reach as far as the mass of the $b$-quark, Methods such as the *ratio method* [157, 158] can be used to make contact with the physical bottom mass.

## 5.2 Outline of the Pilot Study

The main purpose of this study is to investigate whether there is a region in the domain wall parameter space ($M_5$,$L_s$) for which we can find desirable features to simulate heavy quarks, in particular charm. Amongst these desirable features we hope to find that basic observables such as the decay constants $f_D$ and $f_{D_s}$ have small discretisation effects. We also investigate how well the dispersion relation is reproduced by the lattice data. As part of this study we establish an upper bound in the bare input quark mass $am_h^{\max}$ below which our discretisation is suitable.

To keep the numerical cost feasible and with view of having a testing ground we decided to carry out this pilot study in a quenched theory. This neglects the need to calculate the (expensive) determinants in (3.36). It also allows for cheaper algorithms such as over-relaxed [94, 95] heat-bath [92] in the production of the gauge ensembles. No sea-quark masses need to be tuned and the reach in the lattice spacing is extended by *brute force*. So we can mitigate critical slowing [98, 148, 149] to some extent. Because we are mainly interested in the effect of the heavy quark, we can reduce the cost even further, by simulating a small volume of $L \approx 1.6$fm. It is desirable to keep this volume fixed amongst the different ensembles, to ensure the same finite size effects and to have

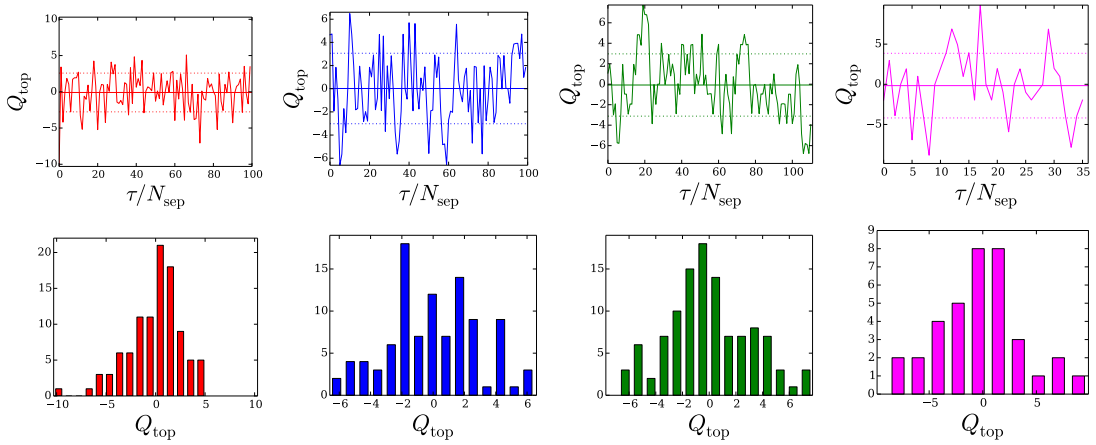


Figure 5.1: Topological charge evolution and histograms of the different ensembles. From left to right the lattice spacing decreases from $a^{-1} = 2.0\,\text{GeV}$ (left) to $a^{-1} = 5.7\,\text{GeV}$. The exact parameters are given in tables 5.1 and 5.2. The first row shows the topological charge as measured on every $N_{\text{sep}}$th (compare values in table 5.1) trajectory. The bottom row shows the corresponding histograms.

similar accessible Fourier momenta (compare (3.7)). Since a quenched theory does not approximate nature well, results from this study are only taken as a guideline, but we expect that the qualitative features carry over to the dynamical case.

The pure gauge ensembles generated for this study are presented in section 5.3. On these gauge ensembles we calculated mesonic two point functions of two mass degenerate heavy quarks (heavy-heavy meson) for a variety of different values of $(M_5, L_s)$ presented in section 5.4. For the optimal choice found here we then did a full scaling study of the meson dispersion relation (section 5.6.3) (heavy-heavy and heavy-strange mesons) and the decay constants (section 5.6.4) (heavy-strange mesons).

## 5.3 Ensembles

Since the main purpose of this study was to establish the cut-off effects of heavy-light quantities, the main aim for the ensemble generation was a large range in lattice spacings[1]. To achieve this whilst keeping the computational cost bearable, we simulated pure gauge configuration in a comparably small constant spatial volume of $L \approx 1.6\,\text{fm}$. The chosen gauge action is tree-level improved Symanzik [81, 82] and was generated with the Heat-bath algorithm [92, 94, 95]. We generated $SU(3)$ ensembles at $\beta = 4.41$, 4.66, 4.89 and 5.20. The coarser three ensembles were produced with CHROMA [159] (with added heat-bath routines), whilst the finest ensemble was generated by a code which is

[1]The ensembles were generated by Marina Kristić Marinković (Q1-Q3) and Francesco Sanfilippo (Q4) under supervision of Andreas Jüttner and Peter Boyle. This includes the numerical ensemble generation, the measurement of the Wilson flow and the topological charge and the determination of autocorrelation times.

| Name | $\beta$ | $L^3 \times T/a^4$ | $N_{\text{sweeps}}$ | $\tau_{\text{int}}(Q_{\text{top}})$ | $\tau_{\text{int}}(Q^2_{\text{top}})$ | $N_{\text{sep}}$ | $N_{\text{confs}}$ |
|---|---|---|---|---|---|---|---|
| Q1 | 4.41 | $16^3 \times 32$ | 10k | 15(3) | 10.5(1.6) | 100 | 100 |
| Q2 | 4.66 | $24^3 \times 48$ | 20k | 160(60) | 74(22) | 200 | 100 |
| Q3 | 4.89 | $32^3 \times 64$ | 600k | 200(100) | 170(80) | 500 | 111 |
| Q4 | 5.20 | $48^3 \times 96$ | 1.4M | 28000(13000) | 12000(4000) | 40000 | 59(36) |

Table 5.1: Ensemble properties of the quenched gauge ensembles: Lattice sites, number of sweeps, autocorrelation time and number of configurations. On the fine ensemble additional configurations were generated later, so some measurements take the original 36 configurations whilst others have the full statistics of 59.

| Name | $\beta$ | Plaquette | $w_0/a$ | $a^{-1}$[GeV] | $L$[fm] |
|---|---|---|---|---|---|
| Q1 | 4.41 | 0.62637(3) | 1.767(3) | 2.037(08) | 1.550(6) |
| Q2 | 4.66 | 0.651421(12) | 2.499(8) | 2.861(09) | 1.655(5) |
| Q3 | 4.89 | 0.671257(5) | 3.374(11) | 3.864(12) | 1.634(5) |
| Q4 | 5.20 | 0.694149(4) | 5.007(28) | 5.740(22) | 1.650(6) |

Table 5.2: Ensemble properties of the quenched gauge ensembles: Plaquette, Wilson flow measurement, Lattice spacing and physical volume. Note that the uncertainty of $w_0^{\text{phys}}$ is propagated into the uncertainty of physical quantities.

specifically optimised for the IBM BG/Q [160]. We gratefully acknowledge the use of the IRIDIS High Performance Computing Facility in Southampton (generation of the ensembles Q1-Q3) and computing time on the BG/Q in Edinburgh, granted through the STFC funded DiRAC facility (generations of the ensemble Q4 and all subsequent measurements).

Throughout the ensemble generation the topological charge $Q$ (compare (3.39)) was monitored (measured with the GLU package [161]).

The square of the topological charge $Q^2_{\text{top}}$ is assumed to couple strongly to the slowest evolving mode in the evolution of the algorithm [98] (cf. section 3.5). The autocorrelation time of $Q^2_{\text{top}}$ was then calculated. In the following we restrict ourselves to trajectories spaced by $N_{\text{sep}} \geq 2\,\tau_{\text{int}}(Q^2_{\text{top}})$ [123]. The values of $\tau_{\text{int}}(Q^2_{\text{top}})$ (measured in number of sweeps), $N_{\text{sep}}$ and the resulting number of configurations are given in table 5.1. The topological charge $Q_{\text{top}}$ measured on these configurations is shown in figure 5.1

The lattice spacing was determined using the Wilson flow [100, 101] taking the value $w_0^{\text{phys}} = 0.17245(99)\text{fm}$ [144][2]. The main ensemble parameters are listed in table 5.2.

## 5.4 Scan of the Domain Wall Parameter Space

In a first step we scanned the domain wall parameter space $(M_5, L_s)$ and the heavy quark masses $am_h$. To this end we calculated heavy-heavy two-point functions for a

[2]Note that the value in [10] differs as it used $w_0^{\text{phys}} = 0.176(2)\text{fm}$ from [101]

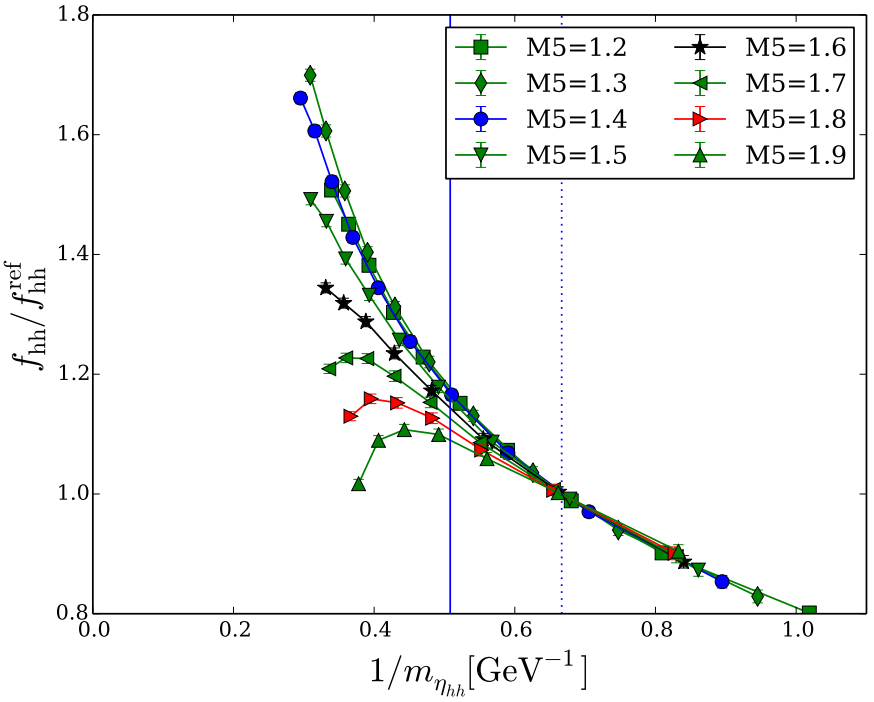


Figure 5.2: Scan in $M_5$ for a range of heavy quark masses on the coarsest ensemble (Q1). The vertical blue dotted line is the normalisation point, whilst the solid blue line is the physical charm mass defined by the $\eta_c = 2.9836(6)\,\mathrm{GeV}$ [1].

variety of values of $(M_5, L_s, am_h)$ on the coarsest two ensembles. In the remainder of this chapter we will ignore quark disconnected contributions to $\eta_c$ (compare section 3.7.2). This is justified since these are expected to be small [162] and since this study is designed to give a qualitative understanding of the limitations of domain wall fermions to simulate heavy quarks. On the coarsest ensemble (Q1) we simulated values of $M_5 \in \{1.2, 1.3, 1.4, 1.5, 1.6, 1.7, 1.8, 1.9\}$, keeping $L_s = 12$ fixed and varying $0.1 < am_h < 0.9$.

As discussed in section 4.2 decay constants need to be renormalised by a renormalisation factor $\mathcal{Z}_A$ (compare (4.15)). Since we are not interested in making physical predictions from the quenched theory, we instead build ratios to cancel the renormalisation constants. These renormalisation constants are mass-independent in the limit of $a \to 0$, so any mass dependence they display at a finite lattice spacing can be interpreted as a discretisation effect. To do this we build the ratio

$$\frac{f_{hh}(m_{\eta_c})}{f_{hh}(m^{\mathrm{ref}})} \equiv \frac{f_{hh}}{f_{hh}^{\mathrm{ref}}}, \tag{5.1}$$

where we chose $m^{\mathrm{ref}} = 1.5\,\mathrm{GeV}$. To obtain $f^{\mathrm{ref}}$ we simply linearly interpolate the values around $m_{hh} \sim 1.5\,\mathrm{GeV}$ to this value. The results of this first scan are shown in figure 5.2. We observe the appearance of a *kink* when going beyond a certain critical mass $am_h^{\mathrm{crit}}$ which depends on the value of $M_5$ which is typically around $am_h^{\mathrm{crit}} \gtrsim 0.4$. Recall

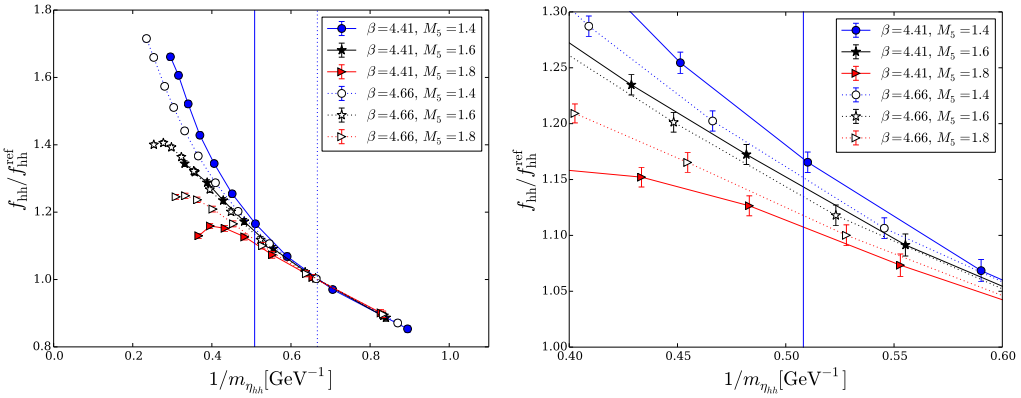


Figure 5.3: Overlay of three values of $M_5$ for the two coarsest ensembles Q1 (closed symbols) and Q2 (open symbols). The left panel shows the entire range, whilst the right panel zooms into the region around the physical charm quark mass. Again the vertical blue dotted line is the normalisation point, whilst the solid blue line is the physical charm mass defined by the $\eta_c = 2.9836(6)\,\mathrm{GeV}$ [1]

.

the existence of bulk modes in the fifth dimension (cf. (4.6) in section 4.1) and that their behaviour depends on the values of $M_5$ and $m_f$. Beyond this critical value (i.e. at the location of the 'kink') the displayed behaviour is non-physical. Such a limitation of domain wall fermions is expected from the free theory [163, 164] due to the energy scales of the bulk modes not being well separated from the energy scale of the desired state. For these reasons we restricted ourselves to the region in $am_h$ up to this kink.

We observe that in the region far below the charm quark mass, the different curves are close to each other, whilst for $am_h \sim am_c$ a significant effect is observed. This indicates that discretisation effects are strongly $M_5$ dependent. Also the reach in the heavy-heavy pseudoscalar mass before the appearance of this kink depends strongly on the chosen value of $M_5$. For example, $M_5 = 1.9$ (the upwards facing green triangles) just about allows to reach charm (for the present lattice spacing), whilst $M_5 = 1.6$ (black stars) or $M_5 = 1.2$ (green squares) allow to reach further in the heavy quark mass.

In a second run we reproduced a subset of the $M_5$ ($M_5 \in \{1.4, 1.6, 1.8\}$) values on the next finer ensemble (Q2). A flat continuum limit is indicated by values on Q1 and Q2 which lie on top of each other. The result of this scan is presented in figure 5.3. It can clearly be seen that the values $M_5 = 1.4$ and $M_5 = 1.8$ indicate large cut-off effects with opposite signs, whilst for $M_5 = 1.6$ the approach to the continuum appears to be flatter. This was found to be the optimal choice (black stars) amongst the simulated values.

It now remains to investigate this behaviour and see whether other quantities are linked to this behaviour around $am_h \gtrsim 0.4$. As introduced in (4.21) the residual mass $m_{\mathrm{res}}$ gives an indication of the residual chiral symmetry breaking. For domain wall fermions to approximate chiral symmetry well, this quantity is required to remain small. For

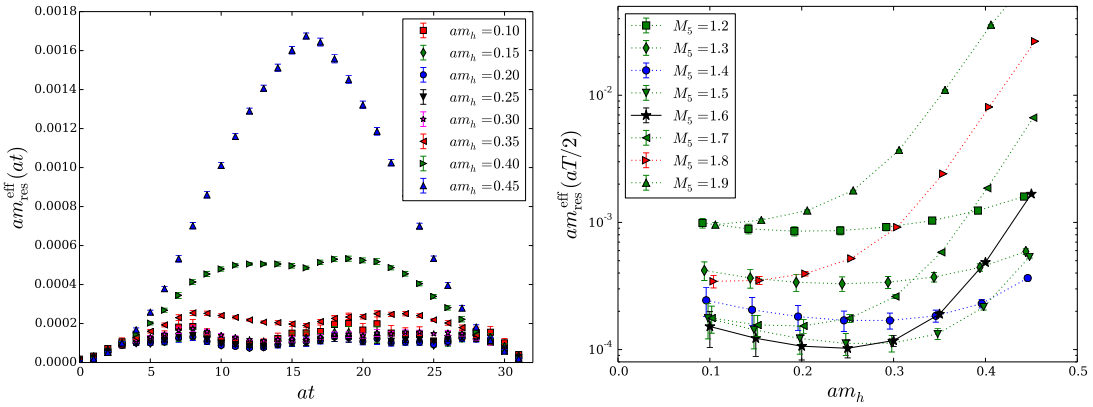


Figure 5.4: *left*: Effective residual mass as a function of time for a variety of input quark masses for a choice of $M_5 = 1.6$ and $L_s = 12$ on the coarsest ensemble (Q1). *right*: The residual mass taken from the central time slice as a function of the bare input quark mass for varying values of $M_5$ on the coarsest ensemble (Q1).

sufficiently large times the time dependence of the numerator and denominator should cancel, so that we expect the *effective residual mass* (i.e. the value of the residual mass as a function of the time slice) to plateau in that region. As can be seen from the left-hand panel of figure 5.4, this is indeed the case for small input quark masses. However, for an input quark mass of $am_h > 0.4$ the effective residual mass does no longer plateau and does not remain bounded. This happens to be in the same region where we observe the kink in figures 5.2 and 5.3. Lacking a plateau to which we can fit a constant, we instead take the central time-slice as an indication of the value of the residual mass. The described behaviour persists for all values of $M_5$ as can be seen from the right-hand panel of the same figure (note the logarithmic scale on this panel). For this reason we restrict our future simulations to values of $am_h \lesssim am_h^{\rm crit} = 0.4$. Attempts to increase the extent of the fifth dimension reduced the absolute value of the residual mass but did not change the qualitative behaviour observed in the left panel of figure 5.4.

So we have established an upper bound on the input quark mass ($am_h^{\rm crit} \gtrsim 0.4$) as well as a choice of the domain wall height ($M_5 = 1.6$), yielding indications of small cut-off effects. Finally, even on the coarsest lattice spacing, we are able to reach the physical value of the charm quark mass whilst observing the upper bound described above. For $am_h \leq 0.4$ by inspection figure 5.4 gives values of $am_{\rm res} < 0.0005$ which corresponds to a residual mass in physical units of $m_{\rm res} < 1\,\text{MeV}$. Since (for otherwise fixed physics) the residual mass decreases as we approach finer lattice spacings (compare e.g. ref [144]), we chose $L_s = 12$ to be a sufficiently safe bound. In summary our choices are

$$\begin{aligned} M_5 &= 1.6 \\ am_h \lesssim am_h^{\rm crit} &= 0.4 \\ L_s &= 12. \end{aligned} \tag{5.2}$$

| Name | $\beta$ | smearing radius | | $am_s$ | | $am_h$ | | |
|---|---|---|---|---|---|---|---|---|
| | | $\mathbb{P}$ | $\mathbb{Z}_2$ | $\mathbb{P}$ | $\mathbb{Z}_2$ | start | step | stop |
| Q1 | 4.41 | 2.8 | 4.5 | 0.034, 0.036 | 0.036, 0.037 | 0.1 | 0.05 | 0.4 |
| Q2 | 4.66 | 4.0 | 6.0 | 0.024, 0.026 | 0.024, 0.026 | 0.066 | 0.033 | 0.396 |
| Q3 | 4.89 | 8.8 | 7.5 | 0.018, 0.020 | 0.018, 0.020 | 0.07 | 0.04 | 0.39 |
| Q4 | 5.20 | 11.7 | 11.7 | 0.011, 0.013 | 0.0118, 0.0133 | 0.04 | 0.04 | 0.28 |

Table 5.3: Simulated strange and heavy input quark masses $am_h$ and the choices of smearing radii for heavy quark masses. The simulated bare quark masses are quoted in lattice units for the MDWF action. The heavy quark masses starting from "start" with a step of "step" and ending at "end" are simulated. $r_{sm}^{\mathrm{P}}$ and $r_{sm}^{\mathbb{Z}_2}$ refer to the choice of the smearing parameter for the Gaussian smearing of the source/sink of the propagators for the point and $\mathbb{Z}_2$ noise sources, respectively. For the Gaussian smearing we employed 400 smearing iterations. All measurements are carried out with MDWF with parameters $L_s = 12$.

With this set of parameters we will now carry out a series of studies on all four ensembles to investigate the exact continuum limit scaling.

## 5.5 Run Set-Up

We are interested in the pseudoscalar dispersion relation as well as the pseudoscalar decay constants. We therefore decided to do two separate studies: the first study employs point sources propagators to allow for definite momentum projections whilst the second one uses stochastic sources [110] leading to better statistics due to volume averaging and is representative of our strategy for the dynamical $N_f = 2 + 1$ runs at physical pion masses. For the point source data set we projected to momenta $a\boldsymbol{p} = \frac{2\pi}{X}\boldsymbol{n}$ with $|\boldsymbol{n}|^2 = 0, 1, \cdots, 3$.

Given the small volume, we employed Gaussian source/sink smearing [109, 165] (compare section 3.7.4) to improve the overlap of the ground state with the vacuum. Whilst $\mathbb{Z}_2$ sources are just point sources distributed over a large volume, the effect of smearing is the same between the two. Finding the optimal smearing radius was an iterative process, so the chosen smearing radii differ between the two studies. Once a smearing radius was determined on the coarsest ensemble, it was then scaled by the ratio of lattice spacings for the other ensembles. Table 5.3 lists the smearing radii and the bare simulated strange and heavy quark masses. For cost reasons we only simulated local strange quarks, but simulated and contracted all combinations of local and smeared heavy quarks. In all cases we monitored the *time slice residual* as defined in (3.52).

| Name | $\beta$ | $\mathbb{P}$ | | | $\mathbb{Z}_2$ | | |
|---|---|---|---|---|---|---|---|
| | | $N_{\text{confs}}$ | $N_{\text{hits}}$ | $N_{\text{meas}}$ | $N_{\text{confs}}$ | $N_{\text{hits}}$ | $N_{\text{meas}}$ |
| Q1 | 4.41 | 100 | 8 | 800 | 100 | 2 | 200 |
| Q2 | 4.66 | 100 | 8 | 800 | 100 | 1 | 100 |
| Q3 | 4.89 | 111 | 8 | 888 | 111 | 1 | 111 |
| Q4 | 5.20 | 36 | 8 | 288 | 59 | 2 | 118 |

Table 5.4: Number of measurements for the simulations with point sources ($\mathbb{P}$) and Z2-Wall sources ($\mathbb{Z}_2$). $N_{\text{confs}}$ is the number of configurations on which we have measured, $N_{\text{hits}}$ is the number of different measurements on the same configuration.

## 5.6 Analysis

To investigate the continuum scaling of the dispersion relation and the decay constants, we produced strange-strange, strange-heavy and heavy-heavy two-point functions. From fitting these to the expected functional form (compare (3.53)) we extract masses, energies and decay constants. This is described in section 5.6.1. We then fix the strange quark mass for all strange-strange and strange-heavy observables as outlined in section 5.6.2. In a final step we interpolate the observables at the physical strange quark mass to reference heavy meson masses ($m_{D_s}$ or $m_{\eta_c}$) before taking the continuum limit. This is done for the pseudoscalar dispersion relation in section 5.6.3 and for the pseudoscalar decay constants in section 5.6.4.

As mentioned previously, we generated two distinct data sets corresponding to the two source types. The statistics for the two data sets are listed in table 5.4. In the case of the point sources, the origin was translated in space and time between consecutive measurements to sample more of the lattice volume. In both studies measurements on the same configuration but on different source positions were binned into one effective measurement. For the point source correlation functions we averaged all possible spatial orientations of $\boldsymbol{p}$ for a given $\boldsymbol{p}^2$. I.e. for $\boldsymbol{n}^2 = 1$ we average $(\pm 1, 0, 0)$, $(0, \pm 1, 0)$ and $(0, 0, \pm 1)$.

### 5.6.1 Correlation Function Fits

There is an important difference in our simulations for the decay constants and the dispersion relation. For the former we are interested in *matrix elements* and therefore need to resolve the individual amplitudes $Z_{\text{src}}$ and $Z_{\text{snk}}$ as introduced in equation (3.53). In the study of the latter, we are interested in the masses and energies only, so we can restrict ourselves to fitting the time behaviour without disentangling the product $Z_{\text{src}} Z_{\text{snk}}$.

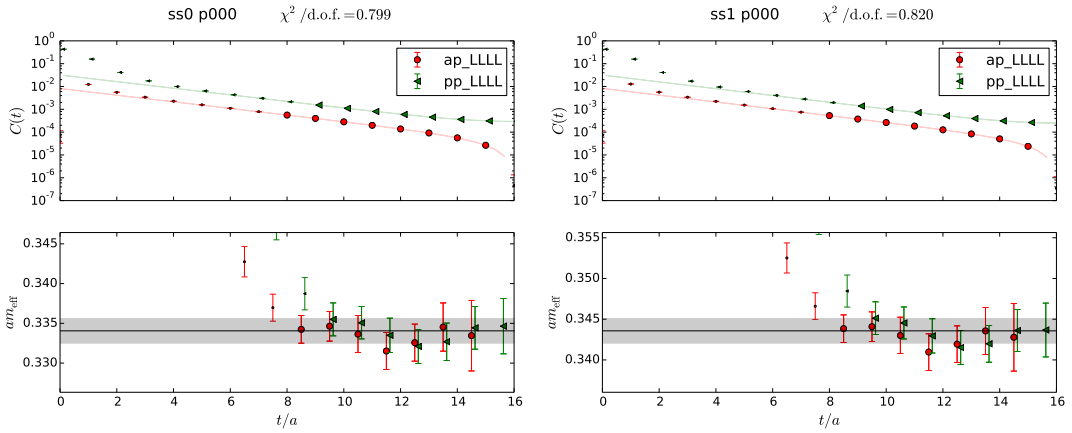


Figure 5.5: Example correlation function fit for a strange-strange meson on Q1 in the dispersion relation study. The left (right) plot corresponds to the lighter (heavier) simulated strange quark mass. In each case, the top panel corresponds to the correlator data that is actually fitted, whilst the bottom panel denotes the effective mass as defined in (3.54). The lines in both plots are the fit results, the larger symbols are data points that enter into the fit. Here $a$ and $p$ correspond to $A$ and $P$ in (5.3), respectively; $LLLL$ indicates that both operators are local at source and sink.

For strange-heavy mesons we have 4 smearing combinations (heavy quark local/smeared at source/sink). For the decay constant analysis we choose

$$\{\Gamma_{\rm src}, \Gamma_{\rm snk}\} \in \{P \equiv \gamma_5, A \equiv A_4 = \gamma_4\gamma_5\}, \tag{5.3}$$

again leading to 4 different combinations. In the following we will drop the subscript 4 and take it to be understood that $A$ refers to the time component of the axial vector current. All combinations of smearings and the Dirac structures (used here) induce states of the same energies, so the correlation functions can be fitted simultaneously. Let us recall the most general functional form (at sufficiently large $t$) of the correlation function

$$\langle \mathcal{O}_{\rm snk}(t)\mathcal{O}_{\rm src}(0)\rangle = \frac{Z^{ac}_{\rm src} Z^{bd}_{\rm snk}}{2m}\left(e^{-mt} \pm e^{-m(T-t)}\right), \tag{5.4}$$

where the gamma structure in $\mathcal{O}_{\rm src}$, $\mathcal{O}_{\rm snk}$ can be $P$ or $A$ and $a$ ($c$) correspond to the source smearing ($L$ or $S$) for the first (second) quark field and $b$ ($d$) to the sink smearing. For the decay constant analysis we are interested in the *local* matrix element $\langle 0| A^{\rm LL}_\mu |D_s\rangle$ (compare (3.43)), where LL corresponds to both quark fields being local at the operator. The simplest way to achieve this would be to insert $A$ at the source and the sink and leave all quark fields local at source and sink, however the signal quality is a lot better for other correlators, so a combined fit of multiple correlators is favourable. Figure 5.5 shows the example of a correlation function fit for the case of a strange-strange meson on the coarsest ensemble. The results for the correlation function fits for the strange-heavy mesons for the decay constant as well as the dispersion relation study are summarised

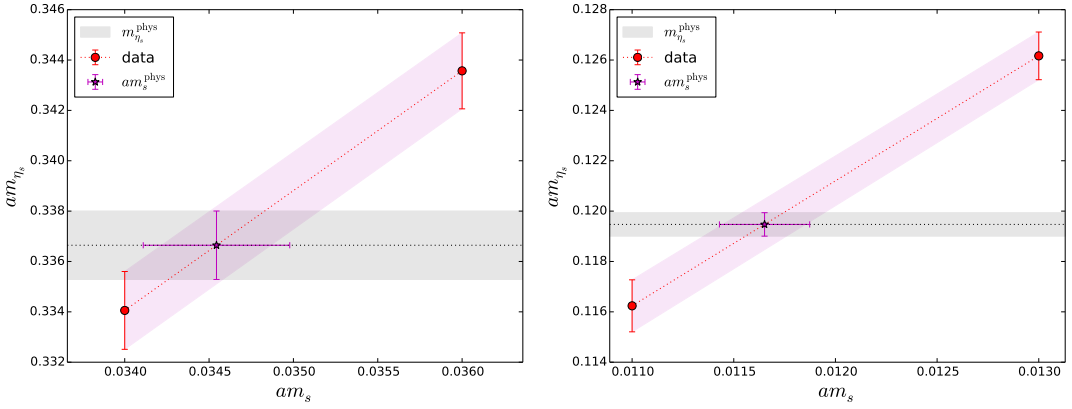


Figure 5.6: Example of the interpolation to the physical strange quark mass for the ensembles Q1 (left) and Q4 (right) in the point-source study. The red data points are the simulated strange quark masses and the corresponding $\eta_s$ masses. The black error band shows the value of $m_{\eta_s} = 0.6858(40)\,\text{GeV}$ converted into lattice units. The magenta data point shows the result of the fit determining $am_s^{\text{phys}}$.

| Name | $\beta$ | $\mathbb{P}$-source | | | $\mathbb{Z}_2$-source | | |
|---|---|---|---|---|---|---|---|
| | | $am_s^1$ | $am_s^2$ | $am_s^{\text{phys}}$ | $am_s^1$ | $am_s^2$ | $am_s^{\text{phys}}$ |
| Q1 | 4.41 | 0.034 | 0.036 | 0.03454(43) | 0.036 | 0.037 | 0.03455(63) |
| Q2 | 4.66 | 0.024 | 0.026 | 0.02434(22) | 0.024 | 0.026 | 0.02416(36) |
| Q3 | 4.89 | 0.018 | 0.020 | 0.01774(17) | 0.018 | 0.020 | 0.01805(33) |
| Q4 | 5.20 | 0.011 | 0.013 | 0.01165(22) | 0.0118 | 0.0133 | 0.01145(31) |

Table 5.5: Simulated strange quark masses on all ensembles for $\mathbb{Z}_2$-Wall sources (left) and point sources (right) as well as the *physical* value in both cases.

in Appendix B in tables B.1 to B.4 and B.5 to B.8, respectively.

### 5.6.2 Interpolation to the *Physical* Strange Quark Mass

To be able to take a continuum limit of strange-heavy quantities such as $f_{D_s}$ we need to ensure that the strange quark mass that is used reproduces the same physics on each ensemble. So on each ensemble we fix the bare strange quark mass by using the fictitious particle $\eta_s$ consisting of a strange and an anti-strange quark but no disconnected contributions. A value for the mass of this $\eta_s$ is given in [166] to be $m_{\eta_s} = 0.6858(40)\,\text{GeV}$. We first find the *physical* strange quark mass by linearly interpolating $m_{\eta_c}(am_s)$ to this value and then interpolate $\mathcal{O}(am_s)$ to this value for all observables $\mathcal{O}$ which include a strange quark. The results of this interpolation are summarised in table 5.5 and an example is shown in figure 5.6. Note that the values obtained for the two different source types are compatible within stochastic errors.

Now that we have found the physical strange quark mass we linearly interpolate all quantities involving a strange quark to this value.

### 5.6.3 Dispersion Relation

We know that in the continuum the dispersion relation implies that the energy $E$ of a particle is related to its spatial momentum $\boldsymbol{p}$ and its mass $m$ by

$$E^2(m, \boldsymbol{p}) = m^2 + \boldsymbol{p}^2. \tag{5.5}$$

We want to test whether our discretisation of the heavy quark can reproduce this result in the continuum limit. At finite lattice spacing this relation is modified to

$$\sinh^2\left(\frac{aE}{2}\right) = \sinh^2\left(\frac{am}{2}\right) + \sum_{i=1}^{3} \sin^2\left(\frac{ap_i}{2}\right). \tag{5.6}$$

Recall that the Fourier momenta accessible on a lattice of spatial extent $L$ are limited to $\tilde{\Lambda}$, i.e. $\boldsymbol{p} = \frac{2\pi}{L}\boldsymbol{n}$ where $\boldsymbol{n}$ is a vector of integers. This implies that the slightly different volumes (compare table 5.2) of the different ensembles cause slightly different momenta. We correct for this by defining a reference volume $L^{\text{ref}} = 1.648\text{fm}$ and interpolating the simulated momenta $\boldsymbol{p}^{\text{sim}}$ to the Fourier momenta allowed in this volume. This correction is done according to

$$E^{\text{ref}} = 2a^{-1}\sinh^{-1}\sqrt{\sinh^2\left(\frac{aE^{\text{sim}}}{2}\right) - \sum_{i=1}^{3}\sin^2\left(\frac{ap_i^{\text{sim}}}{2}\right) + \sum_{i=1}^{3}\sin^2\left(\frac{ap_i^{\text{ref}}}{2}\right)}. \tag{5.7}$$

Figure 5.7 shows the simulated data and the correction to the reference momenta. We can see that the heavy-strange mesons are only mildly affected by lattice artefacts, whilst for heavy-heavy mesons with large heavy quark masses the lattice artefacts become significant. We can also see that lattice artefacts grow with the momentum. We note that even on the coarsest ensemble ($a^{-1} \sim 2\,\text{GeV}$) we are nearly able to reach the physical value of the charm quark mass.

We now introduce reference masses

$$\begin{aligned} m_{sh}^{\text{ref}} &= 1.3\,\text{GeV}, 1.6\,\text{GeV}, 1.9690\,\text{GeV}(= m_{D_s}^{\text{phys}}) \text{ and } 2.4\,\text{GeV} \\ m_{hh}^{\text{ref}} &= 2.0\,\text{GeV}, 2.5\,\text{GeV}, 2.9836\,\text{GeV}(= m_{\eta_c}^{\text{phys}}) \text{ and } 3.5\,\text{GeV} \end{aligned} \tag{5.8}$$

to fix the heavy quark mass to be the same on the different ensembles and interpolate the data to these reference values. This means we now have obtained a set of energies $E$ at the same momentum $\boldsymbol{p}$ with the same orientation at the same reference mass and - if present - with the same strange quark mass. We are now in the position to carry out the continuum limit for each reference mass and each momentum using two different

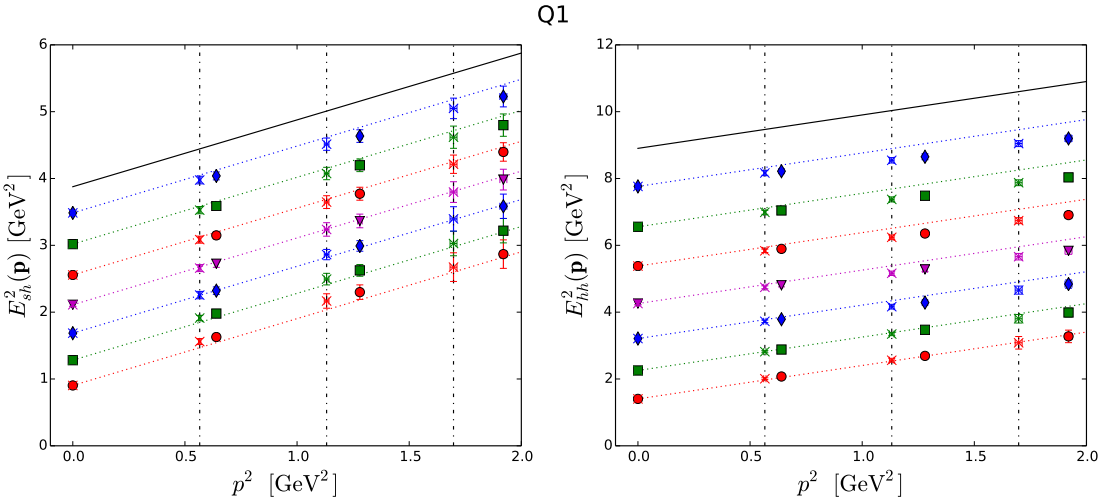


Figure 5.7: Dispersion relation of heavy-strange (left) and heavy-heavy (right) mesons on the coarsest ensemble (Q1). The coloured data points correspond to the simulated data at the given momenta and heavy quark masses. The dotted coloured lines corresponds to the expected continuum dispersion relation. The solid black lines indicate the physical values of the $D_s$ (left) and the $\eta_c$ mesons (right). The black vertical dash-dotted lines introduce the reference momenta defined by $L^{\text{ref}}$ with the momentum-corrected data points on top (coloured crosses).

ansätze

$$\begin{aligned} E^2(a=0) &= E^2(a) + C_2 a^2 \qquad \text{and} \\ E^2(a=0) &= E^2(a) + D_2 a^2 + D_4 a^4. \end{aligned} \tag{5.9}$$

Figure 5.8 shows examples of such continuum limits for the case of a heavy-strange meson at the physical $D_s$ (left) as well as for a heavy-heavy meson at $m_{hh}^{\text{ref}} = 2.5\,\text{GeV}$ (right). We note that the correlator quality of the ensemble Q3 was poor for large momenta ($|\boldsymbol{n}|^2$) leading to large error bars. The solid red and dash-dotted blue lines show a continuum limit according to the first equation of (5.9) including all ensembles and only the finest three, respectively. The green dotted line are a continuum limit fit to all data points using the second line of (5.9). We can see that in the case of the heavy-strange mesons (left), the continuum behaviour is very flat even at the largest simulated momentum and the physical $D_s$ meson mass. For heavy-heavy mesons the continuum limit is flat and well behaved for the smallest (top right) and the largest (bottom right) momentum. However, $\mathcal{O}(a^4)$ effects become present for the coarsest ensemble at $\boldsymbol{n} = (1,1,0)$ (middle right). However, leaving out the coarsest ensemble of fitting the $\mathcal{O}(a^4)$ effects gives acceptable results. The fact that the largest momentum appears to be less affected by discretisation effects, might arise due to the larger error bars.

Figure 5.9 shows the continuum limit for all reference masses and all momenta. The dotted lines depict the continuum dispersion relation for a meson of the given mass. We

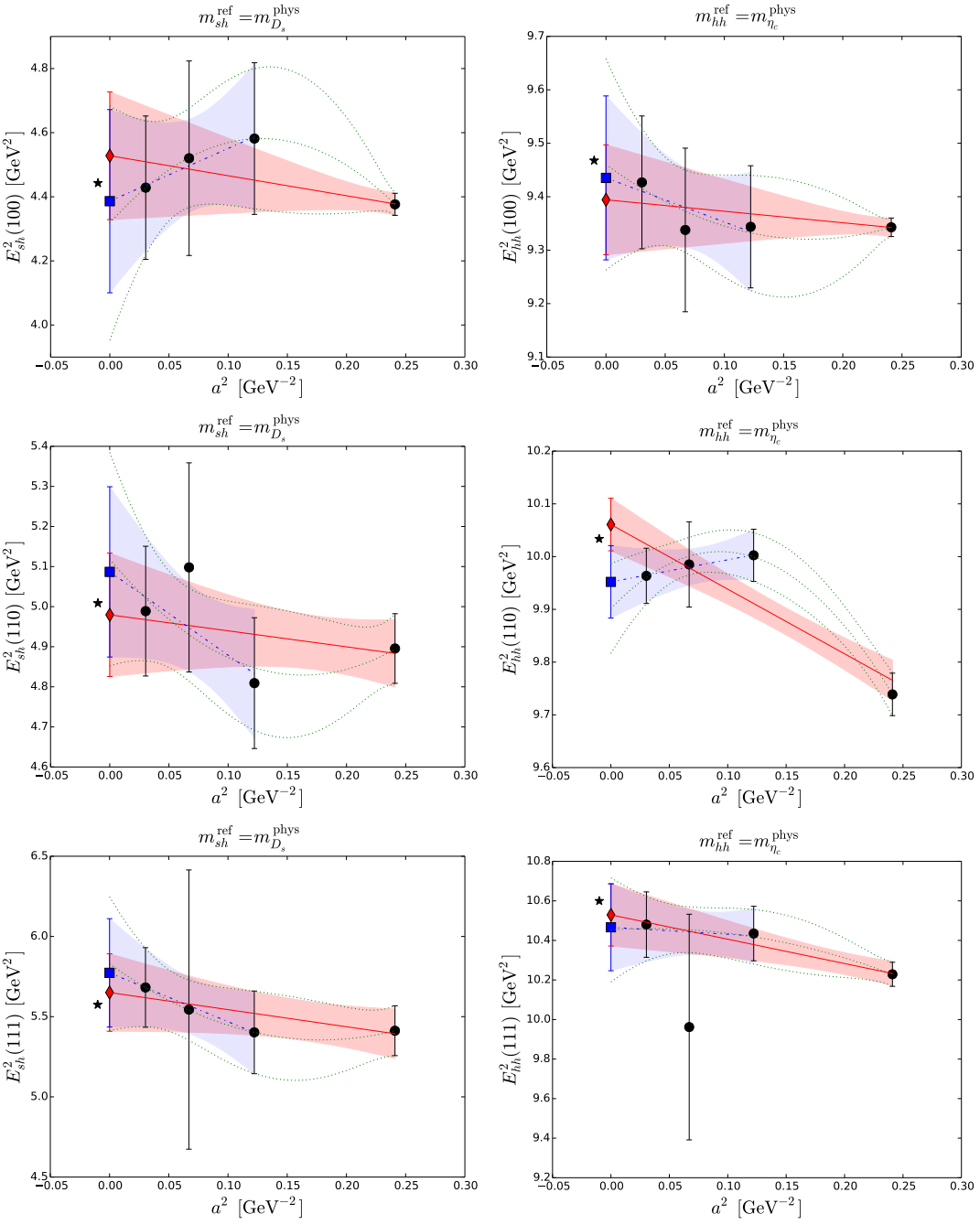


Figure 5.8: Examples of the continuum limits of the pseudoscalar dispersion relation for heavy-strange (left) and heavy-heavy (right) mesons for the three different reference momenta (increasing from top to bottom) at the physical charm quark mass. The black circles correspond to the data at finite lattice spacings. Note that the large error bar for the ensemble Q3 in the right column arises from poor quality of the correlator data at large momenta. The red diamonds and the corresponding solid line and error band show the result of the continuum limit extrapolation using all four ensemble and assuming $\mathcal{O}(a^2)$ effects only (compare the first line of (5.9)). The blue squares, the dash-dotted line and the blue error band show the results of the same fit-ansatz but neglecting the coarsest ensemble. The green dotted lines show the results of a fit-ansatz including $\mathcal{O}(a^4)$ effects (second line of (5.9)). Finally the star is the energy of the meson computed using the continuum dispersion relation (5.5) and the meson rest mass.

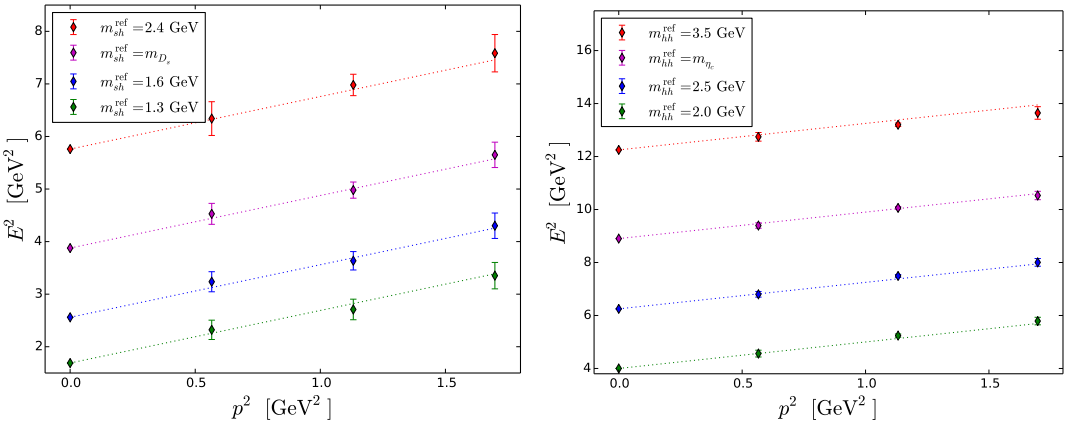


Figure 5.9: Continuum extrapolated results for the heavy-strange (left) and heavy-heavy (right) meson energy as a function of the momentum for the different reference masses. Each dotted line depicts the continuum dispersion relation (5.5) for the associated reference mass. All fit result shown arise from the fits of the form presented in the first line of (5.9). For the heaviest reference mass ($m_{sh} = 2.4\,\text{GeV}$ and $m_{hh} = 3.5\,\text{GeV}$ respectively), only the three finer ensembles enter the continuum limit since the heavy mass reach of the coarsest ensemble is not sufficient. This results in the larger error bars.

see that the continuum dispersion relation is reproduced by our lattice data, in particular for heavy-strange mesons. This is promising for dynamical studies of heavy-light mesons.

### 5.6.4 Decay Constants

In this section we examine the behaviour of heavy-strange decay constants. This is one of the prime quantities that we aim to make a prediction for from the full $2+1f$ theory. To do this we define the quantity $\Phi_P$

$$\Phi_P = f_P\sqrt{m_P}, \tag{5.10}$$

where $P$ is a pseudoscalar meson, and $f_P$ and $m_P$ are the decay constant and meson mass of $P$ respectively. Heavy Quark Effective Theory predicts that in the static limit ($m_P \to \infty$), $\Phi_P$ tends to a constant and that one can expand $\Phi_P$ near the static limit as a polynomial in $1/m_P$. For the purpose of the work presented here, we do *not* make use of HQET and therefore neglect any matching between HQET and our data. However, we still find it convenient to consider the quantity $\Phi$ rather than the decay constant itself, since it behaves more linearly in the inverse heavy meson mass as we will see later. We stress, that this is purely a choice and that no assumptions of HQET enter in the decay constant study. Having interpolated the decay constant data to the physical strange quark mass we now follow a similar procedure as in the dispersion

relation study and introduce reference heavy meson masses to fix the heavy quark mass to be the same on all ensembles. One further complication arises from the need to renormalise the decay constant data before being able to combine data from different ensembles. Since this is only an exploratory study and since we do not aim to make any phenomenologically relevant predictions from the data presented in this chapter, we decided to eliminate the need to renormalise the data by following the approach presented in section 5.4. So in addition to the reference masses (5.8) we introduce a normalisation mass $m_{sh}^{\text{norm}} = 1.0\,\text{GeV}$ and define the ratio $R_{sh}$ to be

$$R_{sh}(m_{sh}^{\text{ref}}) = \frac{f_{sh}^{\text{ref}}\sqrt{m_{sh}^{\text{ref}}}}{f_{sh}^{\text{norm}}\sqrt{m_{sh}^{\text{norm}}}}. \tag{5.11}$$

Figure 5.10 shows the continuum limits of $R_{sh}$ at the various reference masses. We consider two different approaches to the continuum limit, namely

$$\begin{aligned} R_1(a) &\equiv R(a=0) + D_2\,a^2, \\ R_1(a) &\equiv R(a=0) + E_2\,a^2 + E_4\,a^4. \end{aligned} \tag{5.12}$$

The results are illustrated in figure 5.10 as solid and dashed lines with error bands, respectively, and the resulting fit coefficients are listed in table 5.6.

For the two lightest reference masses, 1.3 and 1.6 GeV, the slope of the continuum limit is compatible with zero. For higher masses the continuum limit starts exhibiting a significant slope. In fact, the dimensionless term $D_2 a^2/R\,(a=0)$, which indicates the fractional amount of discretisation errors, is around 3% for the physical $D_s$ meson on the coarsest ensemble ($a^{-1} \approx 2\,\text{GeV}$), and of $\mathcal{O}\,(2\%)$ on the next finest one ($a^{-1} \approx 2.9\,\text{GeV}$). At the level of statistical precision achieved here the fits reveal only a very mild sensitivity to higher order ($O(a^4)$) coefficients: $E_4$ is compatible with zero within one standard deviation. These results are promising indicate that we are able to simulate $D$ and $D_s$ meson decay constants in the full $2+1f$ theory without having to remove large discretisation effects.

## 5.7 Conclusion

In our choice of the domain wall action we find a region in parameter space ($M_5 = 1.6, am_h \lesssim 0.4$) which allows for the simulation of the physical charm quark mass on lattices with inverse lattice spacings as small as $a^{-1} \sim 2\,\text{GeV}$. We tested the continuum limit behaviour of some basic quantities of interest such as the dispersion relation and the decay constants. We recover the correct continuum behaviour of the dispersion relation for heavy-strange and heavy-heavy mesons for the first three accessible Fourier momenta. In the case of heavy-strange mesons, the approach to the continuum of the dispersion relation is very flat and for our level of precision can be well described by

| $m_{sh}^{\text{ref}}$[GeV] | $R_{a=0}$ | $D_2$[GeV$^2$]<br>$E_2$[GeV$^2$] | -<br>$E_4$[GeV$^4$] | $\chi^2$/dof | $p$ |
|---|---|---|---|---|---|
| 1.3 | 1.223(05) | 0.08(05) | | 0.15 | 0.86 |
| | 1.219(09) | 0.17(16) | -0.37(64) | 0.02 | 0.89 |
| 1.6 | 1.418(09) | 0.01(08) | | 0.07 | 0.93 |
| | 1.417(16) | -0.04(28) | 0.1(1.0) | 0.12 | 0.73 |
| $m_{D_s}$ | 1.616(14) | -0.23(11) | | 0.43 | 0.65 |
| | 1.631(25) | -0.53(43) | 1.1(1.5) | 0.43 | 0.51 |
| 2.4 | 1.819(27) | -1.16(32) | | 1.71 | 0.19 |
| | 1.902(71) | -3.9(2.1) | 17(14) | - | - |

Table 5.6: Results of the continuum limit extrapolation for the heavy-strange decay constants. For a given reference mass, the first line summarises the results for the linear extrapolation in $a^2$, the second line the quadratic extrapolation in $a^2$. We also show corresponding results for the $\chi^2$/dof and $p$-values. Note that obeying $am_h \lesssim 0.4$ bounds the reach in the heavy quark mass such that for the reference mass 2.4 GeV only the three finer ensembles are considered. Since this leaves no degrees of freedom in the fit, we cannot assign a value for $\chi^2$/dof or a $p$-value.

$\mathcal{O}(a^2)$ effects. As the bare input charm quark mass increases, heavy-heavy mesons show $\mathcal{O}(a^4)$ effects for large momenta. The heavy-strange decay constants also show a flat approach to the continuum up to the physical charm quark mass. Since we expect these features to carry over to the dynamical case, these results are encouraging for the simulation of charm quarks with domain wall fermions. In addition to allowing for an additional parameter choice ($M_5$) influencing the approach to the continuum, this allows to incorporate the GIM [70] mechanism for simulations with DWF light quarks, as has been recently demonstrated [167].

The outcomes of this chapter constitute the foundation for the next chapter, as it enables us to study the decay constants of $D$ and $D_s$ mesons in a dynamical theory with $N_f = 2 + 1$ on the RBC/UKQCD ensembles with physical pion masses [144].

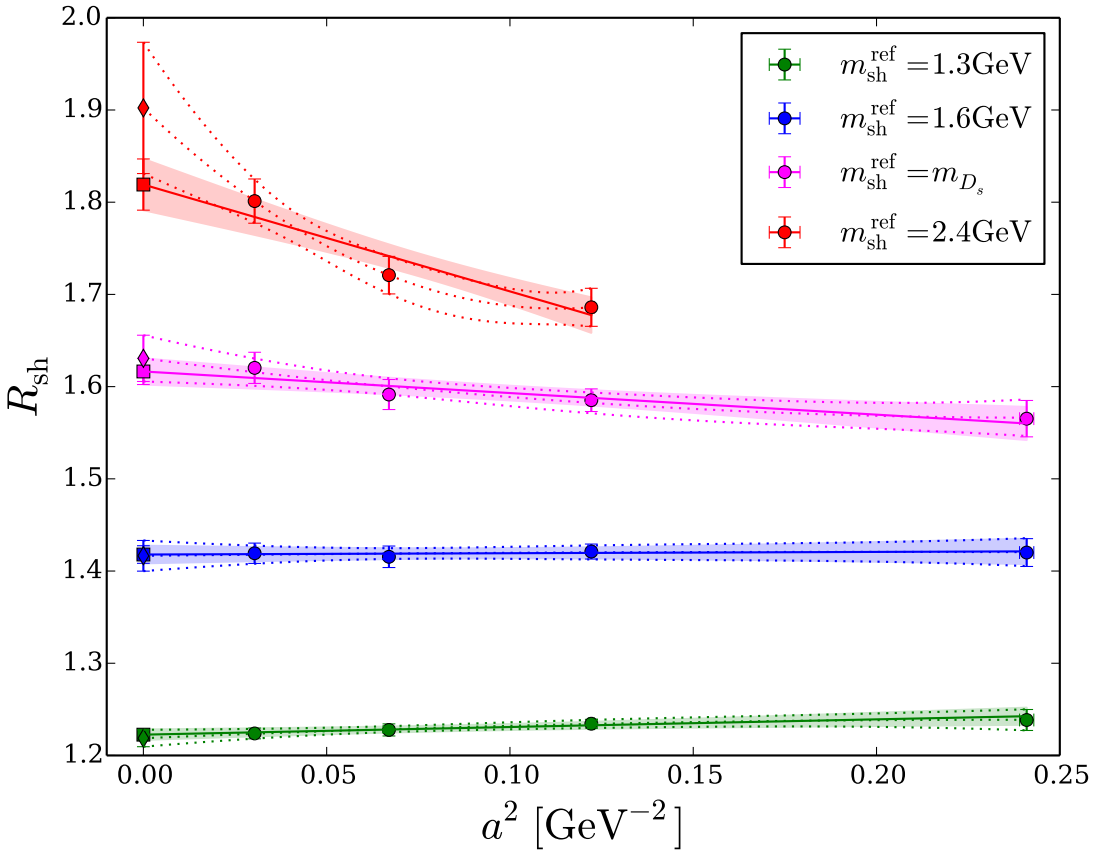


Figure 5.10: Continuum limit of the ratio of heavy-strange decay constants at different reference pseudoscalar masses with linear (dashed shaded error band, square-symbols) and quadratic (dotted lines, diamond symbols) polynomials in $a^2$.

# Chapter 6

# $D$ and $D_s$ Decay Constants from $N_f = 2 + 1$ Lattice QCD

After a brief review of the literature in section 6.1, we present our study of the decay constants $D$ and $D_s$ mesons, yielding a prediction for $f_D$ and $f_{D_s}$ as well as the corresponding CKM matrix elements [12]. For the purpose of this study we simulated light-light, light-heavy, strange-heavy and heavy-heavy pseudoscalar mesons on 7 different ensembles with pion masses ranging from 139 to 430 MeV and inverse lattice spacings ranging from 1.73 to 2.77 GeV. These ensembles are described in section 6.2. The set-up of our simulation of the heavy quark was strongly guided by the findings of the pilot study presented in the previous chapter and is summarised in section 6.3. From fits to the correlation functions we extracted masses and matrix elements and hence decay constants as described in section 6.4. In section 6.5, we then inter/extrapolate the data to physical quark masses ($m_l$, $m_s$ and $m_c$) and vanishing lattice spacing. We assess the outcome of this analysis and give a quantitative estimation of the systematic errors in section 6.6. Finally, we extract the corresponding CKM matrix elements and compare our results to the published literature in section 6.7.

## 6.1 Review of Previous Results

Experimentally the quantities $|V_{cd}|\, f_{D^+}$ and $|V_{cs}|\, f_{D_s^+}$ can be determined (compare section 6.7). The current global averages, stated by the Particle Data Group (PDG) [168] are

$$|V_{cd}| f_{D^+} = 45.91(1.05)\,\text{MeV} \qquad \text{and} \qquad |V_{cs}| f_{D_s^+} = 250.9(4.0)\,\text{MeV}, \tag{6.1}$$

combining the results from CLEO-c [152, 169–174], BES [175], Belle [176] and BaBar [177].

On the theoretical side, a number of lattice calculations of $f_{D^+}$ and $f_{D_s^+}$ have been published in the past, using a variety of different fermion discretisations. In particular,

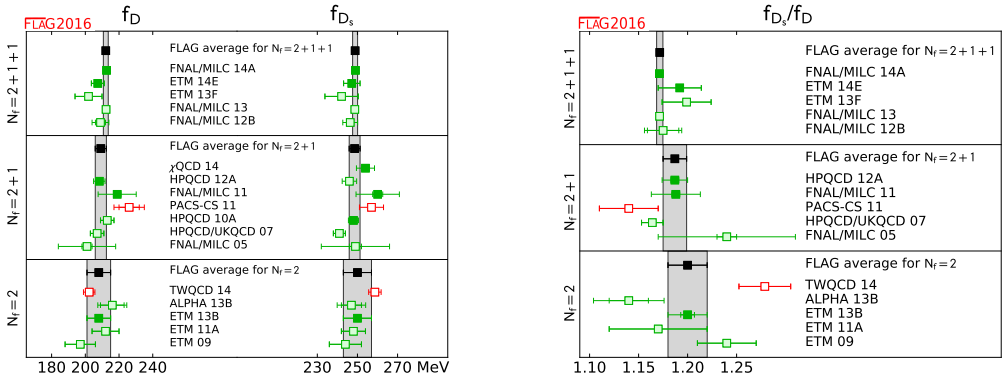


Figure 6.1: Summary of lattice predictions for $f_D$ and $f_{D_s}$ (left) and their ratio (right) [8]

the choice of the charm quark discretisation ranges from highly improved staggered quarks [178], the Fermilab approach [145], the overlap operator [137], Osterwalder-Seiler fermions [179] to Wilson fermions [46]. The Flavour Lattice Average Group (FLAG) [8, 57, 180] summarises these results and publishes global averages (based on selection criteria). Figure 6.1 is taken from the most recent report of the Flavour Lattice Averaging Group (FLAG) [8] and shows the current status of lattice predictions for $f_D$ and $f_{D_s}$ and their ratio, summarising the results from refs [18, 158, 162, 181–194]. The results are ordered by the number of flavours in the sea, in particular results for $N_f = 2 + 1$ [162, 185–187] and $N_f = 2 + 1 + 1$ [18, 181, 183] are stated. Given that theoretical predictions of $f_D$ and $f_{D_s}$ have now reached sub-percent precision, independent determinations of these quantities are vital. It is important to note that for a given number of sea flavours the most precise results (refs [18, 183] for $N_f = 2+1+1$ and refs [162, 187] for $N_f = 2 + 1$) are based on an overlapping set of gauge configurations and are therefore not completely independent results. We aim to carry out an independent computation of these decay constants with domain wall fermions in the sea as well as in the valence sector. In particular we will use the physical pion mass ensembles of the RBC/UKQCD collaborations [144] and utilise the charm quark discretisation presented in the previous chapter.

## 6.2 Ensembles

The ensembles used for this study are summarised in table 6.1. All ensembles use the Iwasaki gauge action [83–85] and have 2+1 flavours in the sea. One of the main improvements of recent lattice QCD calculations, is the inclusion of (near) physical pion mass ensembles. We make use of two such ensembles [144] labelled C0 ('C' for 'coarse') and M0 ('M' for 'medium'). This eliminates the need for a large chiral extrapolation, which to date is a source of large systematic uncertainties. Whilst these ensembles existed prior

| $\beta$ | Name | $L^3 \times T/a^4$ | $a^{-1}$[GeV] | $L$ [fm] | $m_\pi$[MeV] | $m_\pi L$ |
|---|---|---|---|---|---|---|
| 2.13 | C0 | $48^3 \times 96$ | 1.7295(38) | 5.4760(24) | **139** | 3.863(05) |
| 2.13 | C1 | $24^3 \times 64$ | 1.7848(50) | 2.6532(15) | 340 | 4.570(10) |
| 2.13 | C2 | $24^3 \times 64$ | 1.7848(50) | 2.6532(15) | 430 | 5.790(10) |
| 2.25 | M0 | $64^3 \times 128$ | 2.3586(70) | 5.3539(31) | **139** | 3.781(05) |
| 2.25 | M1 | $32^3 \times 64$ | 2.3833(86) | 2.6492(19) | 300 | 4.072(11) |
| 2.25 | M2 | $32^3 \times 64$ | 2.3833(86) | 2.6492(19) | 360 | 4.854(12) |
| 2.31 | F1 | $48^3 \times 96$ | 2.774(10) | 3.4141(24) | 235 | 4.053(06) |

Table 6.1: This table summarises the main parameters of the used ensembles. All of these use the Iwasaki gauge action with $2 + 1$ flavours in the sea.

to this work, to obtain a controlled continuum limit we created a gauge ensemble at a third lattice spacing (labelled F1, 'F' for 'fine'). Aiming for an inverse lattice spacing of $a^{-1} \sim 2.8\,\text{GeV}$ and physical pion masses whilst maintaining the constraint of $m_\pi L \gtrsim 4$ (compare section 3.8) requires $N \gtrsim 80$ which was not computationally feasible. Instead we chose to allow for a slightly heavier pion mass of $m_\pi \sim 235\,\text{MeV}$, allowing for a lattice with $N = 48$ sites per spatial direction. This however forces us to have a small extrapolation in the pion mass. Therefore, to investigate the pion mass dependence of the observables, we also included RBC/UKQCD's older $2 + 1f$ ensembles with pion masses between 300 MeV and 430 MeV labelled C1, C2 [195, 196] and M1, M2 [197].

The scale is set in one global fit that includes further ensembles not listed here. The physical inputs to determine the light and strange quark masses and the scale are $m_\pi$, $m_K$ and $m_\Omega$ respectively. The details of this global fit are described in ref [144] and we repeated this fit after including results for $\omega_0$, $t_0$, $f_\pi$, $m_\pi$, $f_K$ and $m_K$ for the ensemble F1, leading to the values listed in table 6.2. On all ensembles the Wilson flow [100, 101] was measured. As an outcome of this global fit we obtain the physical light and strange quark masses as well as the value $w_0^{\text{phys}} = 0.8742(46)\,\text{GeV}^{-1}$ [144] to relate measurements of the Wilson flow to physical units.

Table 6.2 lists the parameters of the light and strange quark sector. The S/M column refers to *Shamir* [129, 131] or *Moebius* [141] domain wall fermions. $M_5$ and $L_s$ are the domain wall height and the extent of the fifth dimension as described before. $am_l^{\text{sea}}$ and $am_s^{\text{sea}}$ are the degenerate up/down mass and the strange quark mass that propagate in the sea. $am_s^{\text{phys}}$ and $a^{-1}$ are outputs of the global fit described in [144] with the addition of the new fine ensemble. There are peculiarities to note from this table:

(a) Even though $\beta$ is the same amongst all the coarse (medium) ensembles there is a slight shift in the lattice spacing between the physical point ensemble C0 (M0) and the non-physical pion mass ensembles C1, C2 (M1, M2). This is due to the change in action from Shamir to Moebius. However, the parameters of the Moebius domain wall fermions were chosen, such that the approach to the continuum limit

| Name | S/M | $M_5$ | $L_s$ | $am_l^{\text{sea}}$ | $am_s^{\text{sea}}$ | $am_s^{\text{phys}}$ | $a^{-1}$[GeV] |
|---|---|---|---|---|---|---|---|
| C0 | M | 1.8 | 24 | 0.00078 | 0.0362 | 0.03580(16) | 1.7295(38) |
| C1 | S | 1.8 | 16 | 0.005 | 0.04 | 0.03224(18) | 1.7848(50) |
| C2 | S | 1.8 | 16 | 0.01 | 0.04 | 0.03224(18) | 1.7848(50) |
| M0 | M | 1.8 | 12 | 0.000678 | 0.02661 | 0.02540(17) | 2.3586(70) |
| M1 | S | 1.8 | 16 | 0.004 | 0.03 | 0.02477(18) | 2.3833(86) |
| M2 | S | 1.8 | 16 | 0.006 | 0.03 | 0.02477(18) | 2.3833(86) |
| F1 | M | 1.8 | 12 | 0.002144 | 0.02144 | 0.02132(17) | 2.774(10) |

Table 6.2: Ensemble parameters for the light sector of RBC/UKQCD's $N_f = 2 + 1f$ Iwasaki gauge action ensembles.

as well as the leading oder discretisation effects agree, making it feasible to combine data from both incarnations of the domain wall action into the same analysis[1] For the purpose of this work, we simply take the lattice spacings as defined in table 6.1.

(b) There is a mistuning between the strange quark mass $am_s^{\text{sea}}$ in the sea and the physical strange quark mass $am_s^{\text{phys}}$. Whilst we have partially quenched the strange quark mass to its physical value on the ensembles C1, C2, M1 and M2, we simulated the unitary sea quark mass on the remaining ensembles (C0, M0, F1). However, this mistuning is at most 5% and we will discuss in section 6.5.1 how this is taken into account.

## 6.3 Run Set-Up

For the physical point ensembles (C0, M0) and the fine ensembles (F1) the physical strange quark mass was not known yet at the beginning of runs relevant to this work. We therefore simulated the *unitary* (i.e. $am_s = am_s^{\text{sea}}$) strange quark mass. Contrary to this, for the auxiliary ensembles (C1, C2, M1, M2) the physical strange quark mass was known prior to these runs, so we directly simulated the *physical* strange quark masses $am_s^{\text{phys}}$.

Recall from chapter 5 that we found the optimal region in the domain wall parameter space for heavy quarks to be $M_5 = 1.6$, $L_s = 12$ and $am_h \lesssim 0.4$. For this reason we simulated the heavy quarks with these values for a number of heavy quark masses satisfying the bound $am_h \lesssim 0.4$. The exact choice of all simulated masses is summarised in table 6.4. On the coarser physical point ensemble we additionally simulated one data point above this bound, i.e. $am_h = 0.45$ to check whether this bound indeed applies. When consulting the residual mass (compare (4.21)), which served as indicator

[1] More detail concerning this can be found in ref [144].

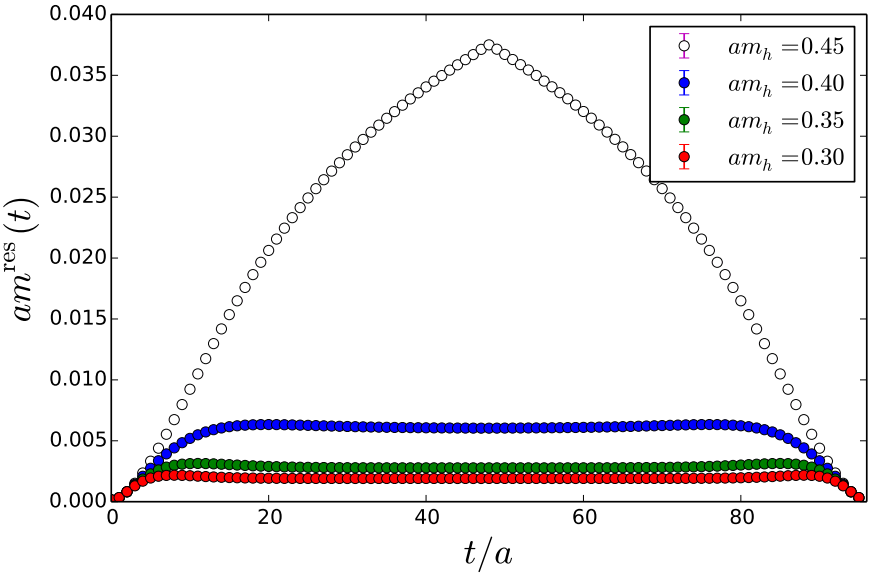


Figure 6.2: The time behaviour of the residual mass for the coarser physical pion mass ensemble (C0). The bound established in the quenched study of $am_h \leq 0.4$ still holds in the dynamical case.

| Name | start | step | stop | hits | $N$ | total |
|---|---|---|---|---|---|---|
| C0 | 420 | 20 | 2160 | 48 | 88 | 4224 |
| C1 | 4690 | 40 | 8650 | 32 | 100 | 3200 |
| C2 | 3050 | 20 | 5050 | 32 | 101 | 3232 |
| M0 | 1200 | 20 | 2780 | 32 | 80 | 2560 |
| M1 | 770 | 20 | 2410 | 32 | 83 | 2656 |
| M2 | 580 | 20 | 2080 | 16 | 76 | 1216 |
| F1 | 4000 | 40 | 7240 | 48 | 82 | 3936 |

Table 6.3: Number of measurements and trajectories on which we measured. Measurements were carried out between *start* and *stop* in intervals of *step*. $N$ is the total number of configurations, *hits* the number source positions of the stochastic noise sources.

for unphysical behaviour in the quenched study we find that this does indeed plateau for $am_h \leq 0.4$ but no longer plateaus for $am_h > 0.4$. This is shown in figure 6.2.

Table 6.3 summarises the number of measurements on each of the ensembles. To improve the statistical signal we employed $\mathbb{Z}_2$-Wall sources [110] (c.f. section 3.7.4) on a large number of time planes, shown by the column *hits* in table 6.3. This was made possible by the use of the HDCG algorithm [105] for the light (including strange) quark sector. All heavy quark propagators were inverted with a standard CG solver [103]. The stopping criterion was chosen, by monitoring the time slice residual (compare (3.52) in section 3.7.2) to ensure convergence.

| Name | $am_l$ | $am_s$ | $am_h^{\text{bare}}$ |
|---|---|---|---|
| C0 | 0.00078 | $am_s^{\text{sea}}$ | 0.3, 0.35, 0.4, 0.45 |
| C1 | 0.005 | $am_s^{\text{phys}}$,$am_s^{\text{sea}}$ | 0.3, 0.35, 0.4 |
| C2 | 0.01 | $am_s^{\text{phys}}$ | 0.3, 0.35, 0.4 |
| M0 | 0.000678 | $am_s^{\text{sea}}$ | 0.22, 0.28, 0.34, 0.4 |
| M1 | 0.004 | $am_s^{\text{phys}}$,$am_s^{\text{sea}}$ | 0.22, 0.28, 0.34, 0.4 |
| M2 | 0.006 | $am_s^{\text{phys}}$ | 0.22, 0.28, 0.34, 0.4 |
| F1 | 0.002144 | $am_s^{\text{sea}}$ | 0.18, 0.23, 0.28, 0.33, 0.4 |

Table 6.4: Moebius domain wall parameters for the heavy quarks of all ensembles. All quoted values for $am_h$ are bare quark masses in lattice units. As described in the text, the value indicated in red was only used to verify our assumptions about the applicability of the quenched pilot study to the dynamical case.

## 6.4 Correlation Function Fits

As described in sections 3.7.4 and 3.7.6 we need to determine the range $t \in [t_{\text{min}}, t_{\text{max}}]$ for each correlation function in which we fit the data to the functional dependence to then extract masses and decay constants. Correlation functions typical for this work are shown in figure 6.3 and figure 6.4.

Note that the scale is the same for all top panels in figures 6.3 and 6.4. We find that the data is very clean for correlation functions of two mass-degenerate quarks (figure 6.3), but gets very noisy as the difference in mass between the two quarks increases 6.4 as expected from the *Lepage argument* [107, 108]. In particular this implies that the $D$ meson is far noisier than the $D_s$ meson and that data on M0 is noisier than on C0. Additionally, we observe that the signal-to-noise ratio also gets poorer as the light quarks approach the physical values, so the ensembles presented here have the worst plateaus of this study. Since the simulations leading to the data presented here, were part of a larger measurement program, with the light quark propagators being used for a number of different applications which required local interpolators, Gaussian source and sink smearing would have been prohibitively expensive [16, 198–200].

By a first visual inspection of figure 6.4 we note that due to the constraint $am_h \lesssim 0.4$ we are unable to reach the physical charm quark mass on the coarse ensembles ($am_{\text{PS}} \sim 0.97 \Rightarrow m_{\text{PS}} \sim 1.7\,\text{GeV}$). However, on the medium ensembles ($am_{\text{PS}} \sim 0.89 \Rightarrow m_{\text{PS}} \sim 2.1\,\text{GeV}$) we are able to go slightly beyond the physical charm quark mass.

Since our primary interest are the decay constants of $D$ and $D_s$ mesons, we need to extract $Z_A \equiv \langle 0 | A_4 | P \rangle$ for $P = D, D_s$. From the top panels in figures 6.3 and 6.4 we can see that the operator insertions $\langle aa \rangle$ and $\langle pa \rangle$ give larger errors than $\langle ap \rangle$ and $\langle pp \rangle$. So we fit the correlation function data of the latter two ($\langle ap \rangle$ and $\langle pp \rangle$ where the first operator is inserted at the sink and the second one at the source) to the functional form

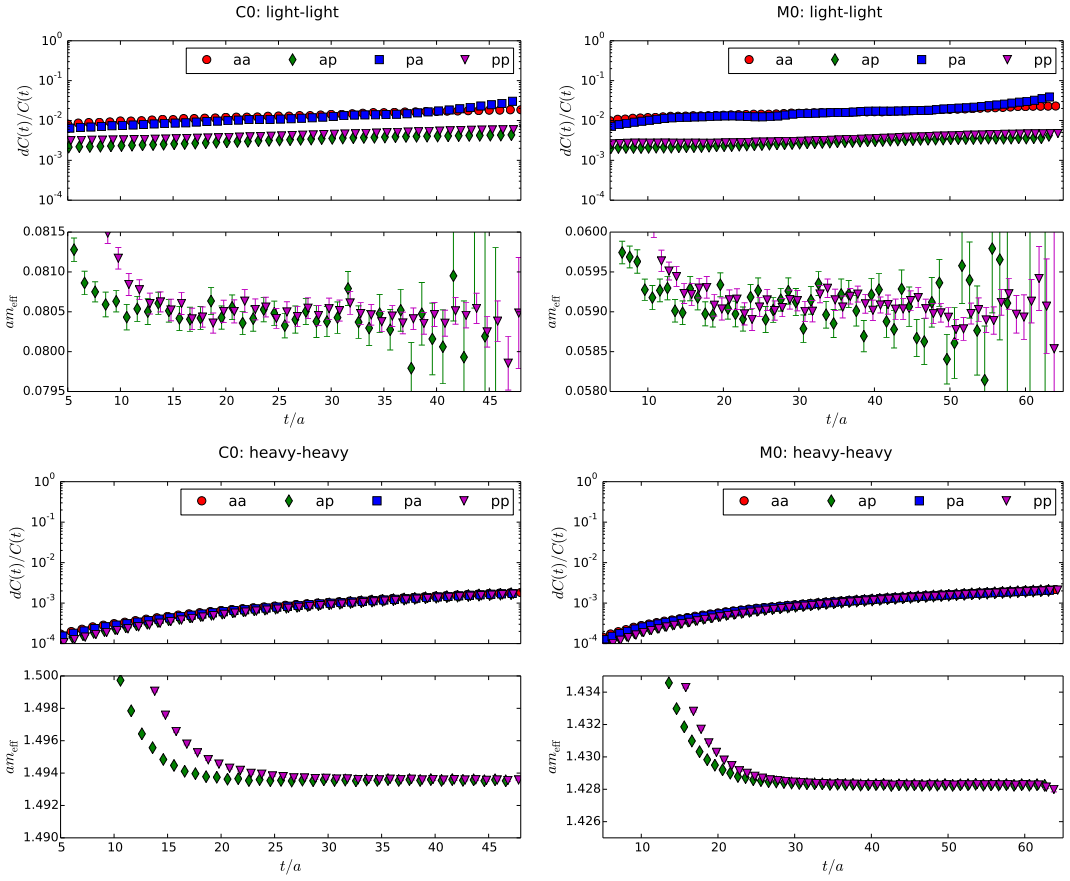


Figure 6.3: *left*: Coarser physical point ensemble (C0). *right*: Finer physical point ensemble (M0). The top plots show the pion, whilst the bottom plots show the heaviest simulated mass point ($am_h = 0.4$) for the connected part of the $\eta_c$. In each plot the top panel shows the relative error on the correlation function for all four combinations of operators listed in (5.3). The bottom panel shows the effective mass for the combinations *ap* and *pp* only, as these are statistically more precise.

of the correlation function. We can also see that the signal deteriorates in the center of the lattice. We found that restricting to $t_{\mathrm{max}} < T/2$ aids in the fit of the correlation function. The correlation function of the $\langle pp \rangle$ channel settles into the ground state later than the $\langle ap \rangle$ channel which will play a role when considering excited state fits.

The underlying data was folded (compare section 3.7.6) in all cases. Following this, the fitting strategy for this study was threefold:

1. Uncorrelated ground state fits:
   The first approach was to fit the ground state in an uncorrelated fashion to have a benchmark for further more evolved fitting procedures.

2. Correlated ground state fits:
   Where possible we investigated correlated fits. This becomes a problem when data

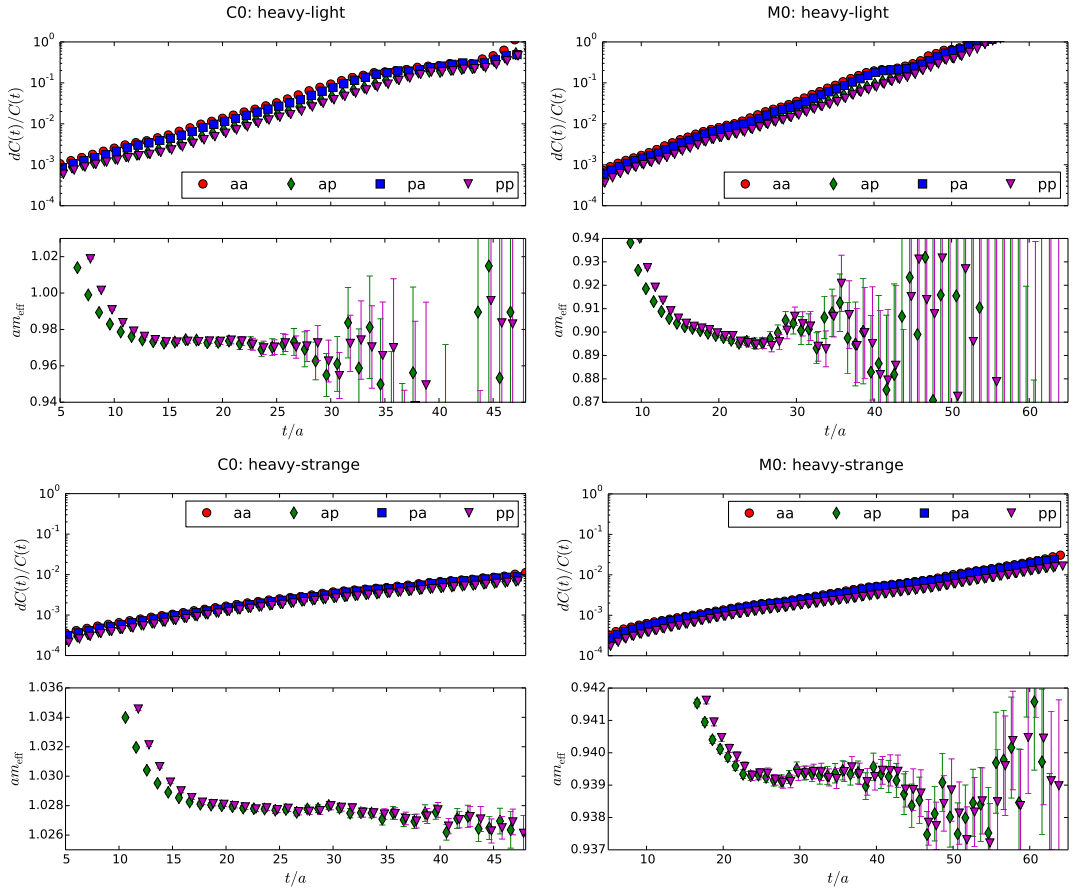


Figure 6.4: *left*: Coarser physical point ensemble (C0). *right*: Finer physical point ensemble (M0). The top plots shows heavy-light correlation functions ($D$-like), whilst the bottom plots show heavy-strange correlation functions ($D_s$-like). In all cases the simulated heavy quark satisfies $am_h = 0.4$. In each plot the top panel shows the relative error on the correlation function for all four combinations of operators listed in (5.3). The bottom panel shows the effective mass for the combinations *ap* and *pp* only, as these are statistically more precise.

that enters the fit has large errors leading to large uncertainties in the covariance matrix. This can lead to an ill-conditioned covariance matrix and therefore unstable fits. We investigated a number of ways to try and circumvent this as will be discussed in this section.

3. Uncorrelated excited state fits:
   To be able to reduce the value of $t_{\rm min}$ we chose to fit not just the ground state but also the first excited state for the cases where we are interested in the matrix elements rather than just the masses, namely for the heavy-light and the heavy-strange correlation functions.

Given the complications we found for correlated fits (numerically ill-conditioned covariance matrix) we did not consider correlated excited state fits.

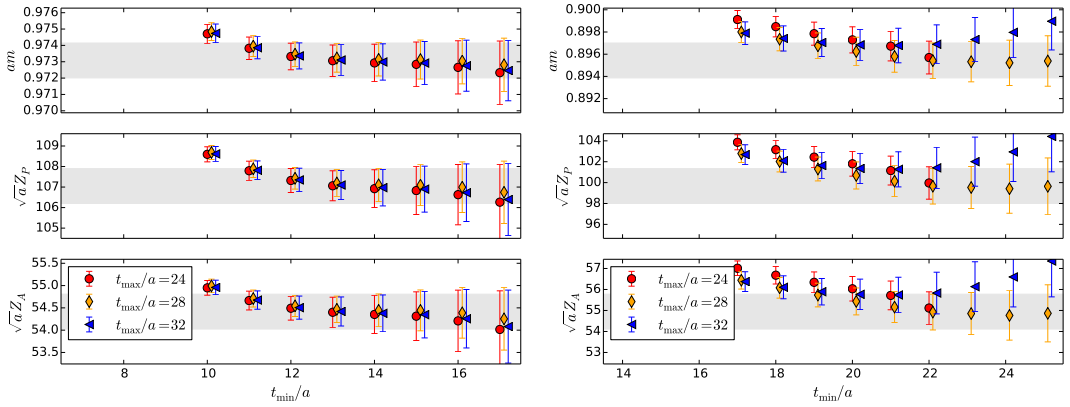


Figure 6.5: Variation of fit parameters for the example of the heaviest heavy-light meson ($am_h = 0.4$) on the two physical pion mass ensembles (left: C0, right: M0). The data shown is for the case of uncorrelated ground state fits. The grey band are the results from an uncorrelated ground state fit with $t/a \in [14, 30)$ in the case of C0 and $t/a \in [22, 27)$ in the case of M0.

In addition to the heavy-light and heavy-strange correlation functions, the interpolation to vanishing lattice spacing and physical quark masses requires the pion mass and in some cases the $\eta_c$ mass. Since masses are measured very precisely (compare figure 6.3), we restricted ourselves to simple uncorrelated ground state fits to extract these quantities. For consistency we also fitted $m_K$ and the results we found for $m_\pi$ and $m_K$ are in good agreement with ref [144].

Whilst other methods are available to increase the signal one can extract such as distillation [120] and formulating a generalised eigenvalue problem [23], this was too costly for the present study. We aim to include these methods as well as source and sink smearing in future work.

Figure 6.5 shows uncorrelated ground-state fit results for a heavy-light meson in the case of the C0 and the M0 ensemble. In both cases the heaviest heavy quark mass ($am_h = 0.4$) is shown. The horizontal grey bands show the chosen fit result. In the case of the C0 ensemble, the data is well behaved and the central value of the fit results does not depend strongly on the choice of $t_{\mathrm{min}}$, provided this is chosen sufficiently large ($t_{\mathrm{min}}/a \geq 13$). We can also not resolve any dependence on the choice of $t_{\mathrm{max}}$. In the case of the ensemble M0 the situation is different. We can observe a dependence with $t_{\mathrm{min}}$ as well as $t_{\mathrm{max}}$. Furthermore, figure 6.4 shows that the plateau is very short in the case of M0 ($22 \lesssim t/a \lesssim 26$). This leads to the need to explore different approaches.

The next step was to attempt correlated ground state fits. The results for the example of M0 are shown in figure 6.6. We can see that the results strongly depend on the choice of $t_{\mathrm{min}}$ but plateau in the region of $t_{\mathrm{min}}/a \gtrsim 23$ as expected from the uncorrelated ground state fits (compare figure 6.5). However, this still leaves us with comparably short plateaus, so instead we attempt to also fit the first excited state.

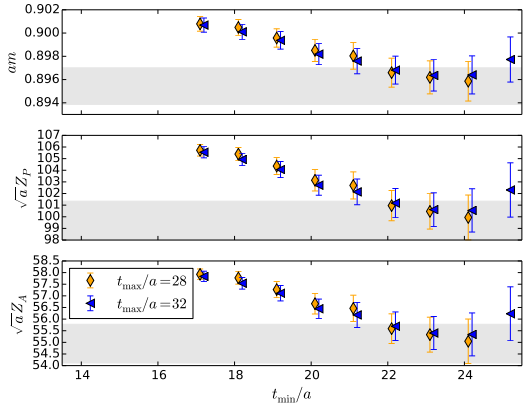


Figure 6.6: Variation of fit parameters for the example of the heaviest heavy-light meson ($am_h = 0.4$) on M0. The data shown is for the case of correlated ground state fits. The grey bands are the results from an uncorrelated ground state fit with $t/a \in [22, 27)$ in the case of M0.

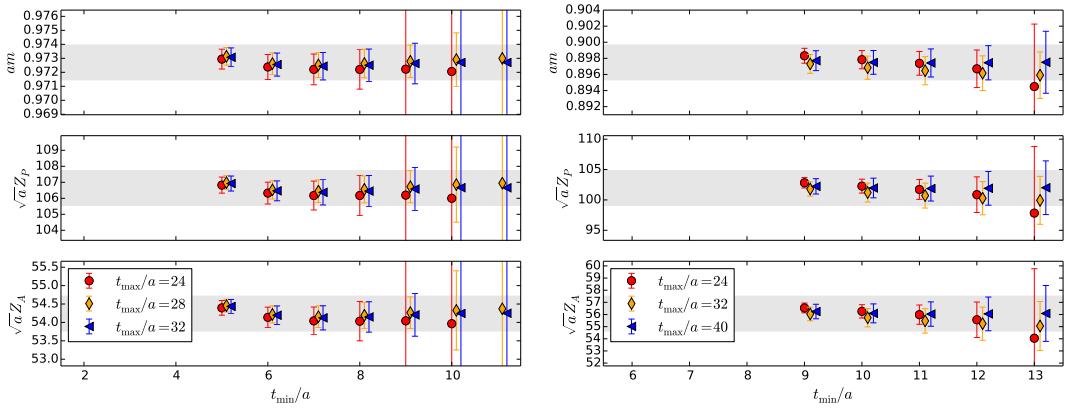


Figure 6.7: Variation of fit parameters for the example of the heaviest heavy-light meson ($am_h = 0.4$) on the two physical pion mass ensembles (left: C0, right: M0). The data shown are the fit results for the mass and matrix elements of the ground state obtained from uncorrelated fits including the first excited state. The grey band are the results from an uncorrelated excited state fit with $t/a \in [8, 30)$ in the case of C0 and $t/a \in [12, 41)$ in the case of M0.

One way to cope with the short and noisy plateau is to additionally fit the first excited state. We systematically vary $t_{\mathrm{min}}$ and $t_{\mathrm{max}}$ again to find a range over which small variations in the fit range do not have any impact on the final result. To be able to resolve the first excited state we need to reduce $t_{\mathrm{min}}$ to a value smaller than that for the ground state fit. We stress that we are not actually interested in the results for the first excited state in this study, so that our main interest is stability of the fit with respect to the ground state fit results. Figure 6.7 shows this variation again in the case of heavy-light mesons for the heaviest simulated heavy quark mass for the case of the two physical pion mass ensembles. The large error bars on some of the data points with

large $t_{\text{min}}$ arise when we no longer have sufficient data to sufficiently constrain the two states.

As can be seen from the grey bands in figures 6.5 and 6.7, the fit ranges $t_{\text{min}}$ and $t_{\text{max}}$ have been chosen conservatively, such that variations in the fit range are compatible with the fitted result. This has been checked for all correlation functions and ensures that we do not have to account for a systematic error from the choice of the fit range. I summarise the results of the correlation functions fits for pions, $D$, $D_s$ and $\eta_c$ in tables C.1, C.2, C.3 and C.4.

## 6.5 Further Analysis

Having obtained data for observables $\mathcal{O}$ at finite lattice spacing $a$ and simulated quark masses $m_l$, $m_s$ and $m_h$ it now remains to find the value of these observables at the physical values of the quark masses as well as at vanishing lattice spacing. Furthermore, we need to renormalise the data to be able to make contact with experiment.

The analysis is split into two parts. We first renormalise the data and correct for the mistuning in the strange quark mass that is present on some ensembles (compare table 6.2). Since the correction of the mistuning corrects the bare matrix elements, the order in which these two steps are done does not matter. In a second step we then explore two different approaches of obtaining results at the physical value of the light and charm quark masses as well as at vanishing lattice spacing.

From the quenched study as well as a first inspection of the data produced here, we empirically found that the quantity

$$\Phi_P = f_P \sqrt{m_P} \tag{6.2}$$

(where $P = D, D_s$) behaves linearly in the inverse heavy mass. For this reason we will carry out the analysis using a simple polynomial ansatz in $1/m_H$ where $H = D, D_s, \eta_c$ to describe $\Phi_P$ (compare e.g. figure 6.11). We will remove $\sqrt{m_P}$ only in the final step.

### 6.5.1 Strange Quark Mass Mistuning

The mistuning between the physical mass $m_s^{\text{phys}}$ and the simulated sea quark mass on each ensemble is listed in table 6.5. From this we see that the mistuning on C0 and M0 is 1.1 and 4.8% respectively. The mistuning on F1 is below 1% and compatible with zero. On C1, C2, M1 and M2 we simulated directly at the physical strange quark mass, so no mistuning is present in the valence mass. We neglect any partial quenching effects since this is only a sea quark effect and expected to be subdominant to the valence effect which we will quantify to be very small. However, on C1 and M1 we also simulated all

| | $am_s^{\text{sea}}$ | $am_s^{\text{phys}}$ | $\Delta m_s$ | $am_s^{\text{sim}}$ |
|---|---|---|---|---|
| C0 | 0.0362 | 0.03580(16) | -0.0112(45) | $am_s^{\text{sea}}$ |
| C1 | 0.04 | 0.03224(18) | (-0.2407(69)) | $am_s^{\text{phys}}$,$am_s^{\text{sea}}$ |
| C2 | 0.04 | 0.03224(18) | - | $am_s^{\text{phys}}$ |
| M0 | 0.02661 | 0.02540(17) | -0.0476(70) | $am_s^{\text{sea}}$ |
| M1 | 0.03 | 0.02477(18) | (-0.2111(88)) | $am_s^{\text{phys}}$,$am_s^{\text{sea}}$ |
| M2 | 0.03 | 0.02477(18) | - | $am_s^{\text{phys}}$ |
| F1 | 0.02144 | 0.02132(17) | -0.0056(80) | $am_s^{\text{sea}}$ |

Table 6.5: Comparison of $am_s^{\text{phys}}$ and $am_s^{\text{sea}}$. The mistuning is defined as $\Delta m_s = (m_s^{\text{phys}} - m_s^{\text{uni}})/m_s^{\text{phys}}$. $am_s^{\text{sim}}$ lists which strange quark masses have been simulated.

heavy-strange quantities with a unitary strange quark mass, allowing to determine the slope $\alpha_{\mathcal{O}}$ for each observable $\mathcal{O}$ which we then apply to correct for the mistuning. The slope $\alpha_{\mathcal{O}}$ is defined by

$$\mathcal{O}^{\text{phys}} = \mathcal{O}^{\text{uni}} \left(1 + \alpha_{\mathcal{O}} \Delta m_s\right), \tag{6.3}$$

where $\Delta m_s = (m_s^{\text{phys}} - m_s^{\text{sea}})/m_s^{\text{phys}}$. The $\alpha_{\mathcal{O}}$ are defined so that they are dimensionless. The values we find for $\alpha$ for the observables $m_{D_s}$, $f_{D_s}$ and $\Phi_{D_s}$ are tabulated in table 6.6 and shown in figure 6.8. The values for $\alpha_{\mathcal{O}}$ on the coarse and medium ensembles can be directly deduced from the simulated data on C1 and M1, respectively and is shown in the left plot in figure 6.8. The vertical solid black line corresponds to the physical value of the charm quark mass. From the left-hand side of the same figure we can see that the values of $\alpha_{\mathcal{O}}$ have a mass and a lattice spacing dependence, i.e. $\alpha_{\mathcal{O}} = \alpha_{\mathcal{O}}(a, m_h)$. So to obtain the values of $\alpha$ for the fine ensemble, we need to undertake additional extrapolations. First we extrapolate the data in the inverse heavy meson mass to the values which were simulated on ($m_h^{\text{ref}}$). This extrapolation is shown by the faint red (coarse) and blue (medium) points in the right-hand side of figure 6.8. In a second step we extrapolate this value to the lattice spacing of the fine ensemble for each reference mass to obtain the green data points in the same figure. This is done according to

$$\begin{aligned} \alpha(a, m_h) &= \alpha(a, m_h^{\text{ref}}) + C_0 \left( \frac{1}{m_{\eta_c}} - \frac{1}{m_{\eta_c}^{\text{phys}}} \right) \\ \alpha(a, m_h^{\text{ref}}) &= \alpha(0, m_h^{\text{ref}}) + C_1\, a^2. \end{aligned} \tag{6.4}$$

Choosing the heavy meson that fixes the heavy quark mass to be the $\eta_c$ masses that we simulated on the fine ensemble ensures that we remain independent of any valence light and strange quarks.

Note that no valence light quark is present in the considered quantities. Therefore, we assume the value of $\alpha$ to be independent of the light sea quark and just apply it directly to the simulated data to obtain $\mathcal{O}^{\text{phys}}$ for the cases where the unitary rather than the physical strange quark mass was simulated. Another advantage of this procedure is that

| spacing | $am_h$ | $\alpha_m$ | $\alpha_f$ | $\alpha_\Phi$ |
|---|---|---|---|---|
| coarse | 0.30 | 0.06026(31) | 0.0967(18) | 0.1262(20) |
| | 0.35 | 0.05341(33) | 0.0982(22) | 0.1243(24) |
| | 0.40 | 0.04801(37) | 0.0994(27) | 0.1229(29) |
| medium | 0.22 | 0.06353(55) | 0.1064(41) | 0.1375(43) |
| | 0.28 | 0.05335(70) | 0.1113(65) | 0.1375(68) |
| | 0.34 | 0.04650(89) | 0.1171(98) | 0.140(10) |
| | 0.40 | 0.0417(11) | 0.124(14) | 0.145(15) |
| fine | 0.18 | 0.06630(80) | 0.1083(51) | 0.1408(53) |
| | 0.23 | 0.0562(10) | 0.1167(94) | 0.1442(99) |
| | 0.28 | 0.0490(12) | 0.123(13) | 0.147(14) |
| | 0.33 | 0.0437(14) | 0.127(16) | 0.148(16) |
| | 0.40 | 0.0383(16) | 0.131(19) | 0.150(19) |

Table 6.6: Values of $\alpha$ for the three observables ($\mathcal{O} = m_{D_s}, f_{D_s}, \Phi_{D_s}$). Details about how these were determined can be found in the text.

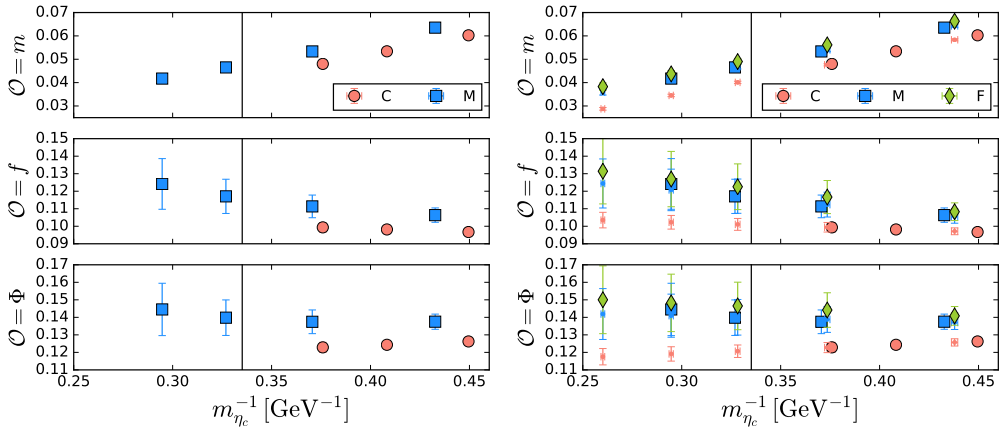


Figure 6.8: *left:* The values of $\alpha$ for the coarse (red circles) and medium (blue squares) ensembles as a function of the inverse $\eta_c$ mass. The black vertical solid line corresponds to the physical value of $m_{\eta_c}$ from ref [1]. *right:* In addition to the data from the left plot, the small red and blue symbols show the values of $\alpha$ extrapolated to the values of the $\eta_c$ masses measured on the fine ensemble. The green diamonds are then obtained from extrapolating this to the lattice spacing of the fine ensemble (compare (6.4)).

the uncertainty of the physical strange quark mass $am_s^{\text{phys}}$ is automatically propagated by creating a bootstrap distribution for $am_s^{\text{phys}}$ with the correct width. Building the products $\alpha_\mathcal{O} \times \Delta m_s$ (compare the values in tables 6.5 and 6.6) we can see that the correction needed is indeed small and below %-level in all cases.

To assess the systematic error from this procedure we consider the next term in the expansion (6.3). This would be of the form $\frac{1}{2}\beta_\mathcal{O} (\Delta m_s)^2$. Assuming that $\beta_\mathcal{O}$ has a similar magnitude to $\alpha_\mathcal{O}$, i.e. ($|\beta_\mathcal{O}| \lesssim 0.2$) and using the largest mistuning with $|\Delta m_s| < 0.05$, the correction is bounded by 0.025%. For $\Phi_{D_s}$ this corresponds to an uncertainty of $0.00009\,\text{GeV}^{3/2}$, for $f_{D_s}/f_D$ to an uncertainty of 0.0003. Given the small values of these

corrections, we neglect effects of the mistuning of the strange quark in the sea as these are expected to be smaller.

### 6.5.2 Renormalisation

To make contact between lattice regulated data and quantities in a continuum theory, we need to find the renormalisation constants to renormalise the heavy-light current. Since we use a mixed current, i.e. we use a different value of $M_5$ for the light and strange quarks ($M_5 = 1.8$) to the heavy quarks ($M_5 = 1.6$), we do not have a conserved current. However, since this is only a small modification of the action, we assume the impact on renormalisation constants to be small. In all of the following we will extract the renormalisation constants from the light-light current and then attach a systematic error devised from a non-perturbative renormalisation (NPR) study. Within the Rome-Southampton scheme [201] the effects of changing the action[2] are investigated. The estimate of the systematic error arising from this is found to be below percent level and is discussed in more detail in section 6.6.

The light-light renormalisation constant can be found from fitting the time behaviour of the relation

$$Z_A^{\text{eff}}(t) = \frac{1}{2}\left[\frac{C(t-1/2)+C(t+1/2)}{2L(t)} + \frac{2C(t+1/2)}{L(t-1)+L(t+1)}\right] \tag{6.5}$$

to a constant [135, 144]. Here $C(t)$ is the conserved point-split current defined on the links between the lattice sites [135] whilst $L(t)$ is the local current defined on the lattice sites.

The folded time behaviour of the light-light current for all ensembles scaled to the interval $[0, 1)$ is shown in figure 6.9. As expected we can see a lattice spacing dependence. The slight difference between C1 and C2 (M1 and M2) arises from the slightly different light quark mass $m_l$. We can also identify a plateau region to which we can fit a constant to obtain the values of the renormalisation constants. The results of these fits are listed in table 6.7 and are in good agreement with [144].

### 6.5.3 A First Impression of the Data

Before moving to the analysis of the discretisation errors, the chiral behaviour and the heavy quark dependence, we will take a brief look at the data in figures 6.10 and 6.11.

Figure 6.10 shows the ratio of decay constants as a function of the inverse of the mass of the $\eta_c$ meson. This figure confirms our earlier observation that we are not able to reach the physical value of the charm quark mass on the coarse ensembles C0, C1 and C2. We

[2] Done by A. Khamseh under the supervision of P. Boyle and L. Del Debbio

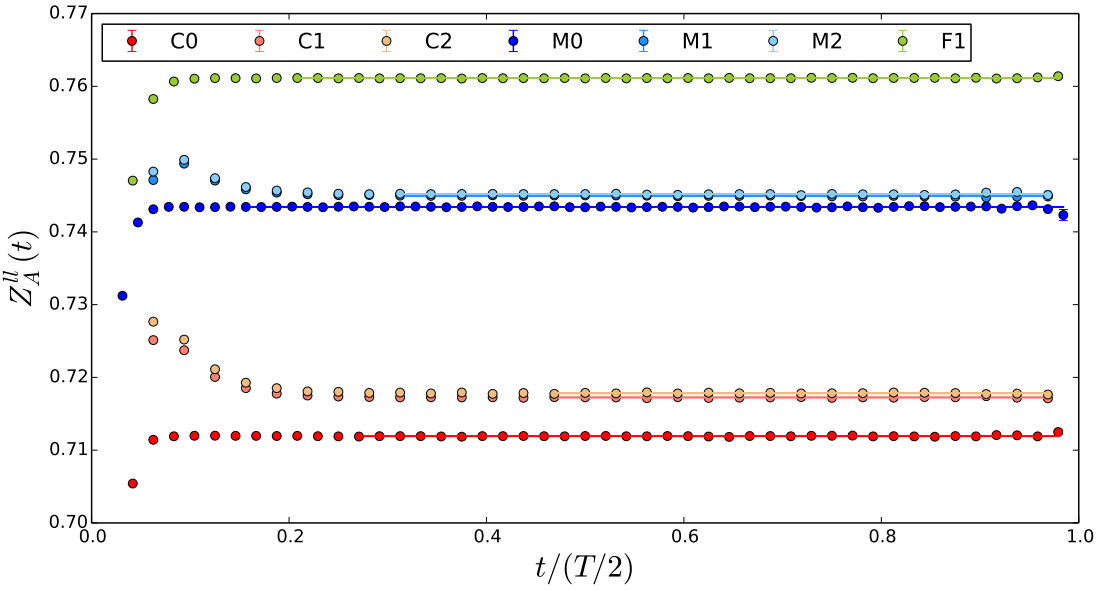


Figure 6.9: The time behaviour of $Z_A^{\text{eff}}(t)$ scaled to the interval $[0, 1]$ for all ensembles. The solid lines correspond to the fit results obtained by fitting a constant to the plateau region of the data. The fit results are summarised in table 6.7.

| ens | $Z_A^{ll}$ |
|---|---|
| C0 | 0.711920(24) |
| C1 | 0.717247(67) |
| C2 | 0.717831(53) |
| M0 | 0.743436(16) |
| M1 | 0.744949(39) |
| M1 | 0.745190(40) |
| F1 | 0.761125(19) |

Table 6.7: The values for $Z_A$ for the various ensembles found from fitting a constant to the time dependence shown in figure 6.9.

observe little heavy quark mass dependence but a significant light quark dependence. Moreover, we observe that as the pion mass increases the value of the ratio of decay constants approaches unity. This is in agreement with intuitive understanding since in the limit of $m_l = m_s$ we reach the $SU(3)$ symmetric point and $D_s$ and $D$ become indistinguishable.

Figure 6.11 shows the renormalised values of $\Phi_P$ in physical units for $P = D$ (left) and $P = D_s$ (right). We can observe a number of features of the data shown here. Both, the $D$ and the $D_s$ meson decay constants show a strong dependence on the heavy quark mass and - at the level of our statistical resolution - a linear behaviour as a function of the inverse $\eta_c$ mass. In the case of the $D$-meson a strong light quark mass dependence is visible, which is expected due to the valence light quark present in the $D$ meson. From comparing the data for C0 and M0, we find that the lattice spacing behaviour appears

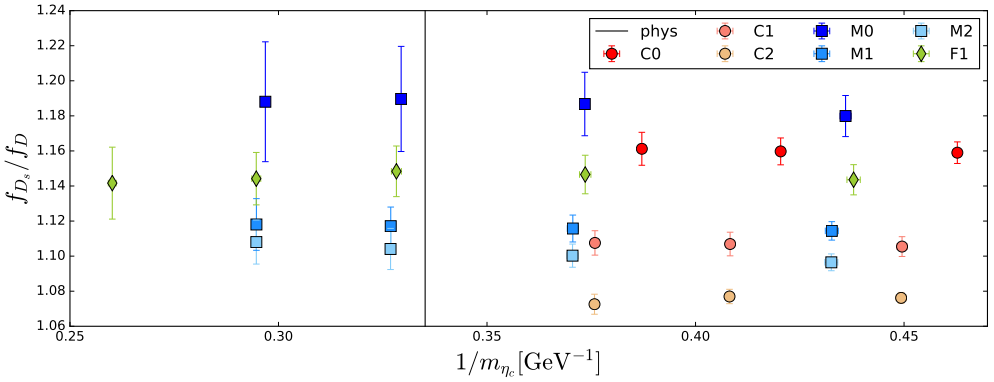


Figure 6.10: The ratio of the decay constants as a function of the inverse $\eta_c$ mass. The black vertical solid line (labelled 'phys') corresponds to the physical value of $m_{\eta_c}$ as stated by the Particle Data Group [1]. The red circles, blue squares and green diamonds show data from the coarse, medium and fine ensembles, respectively.

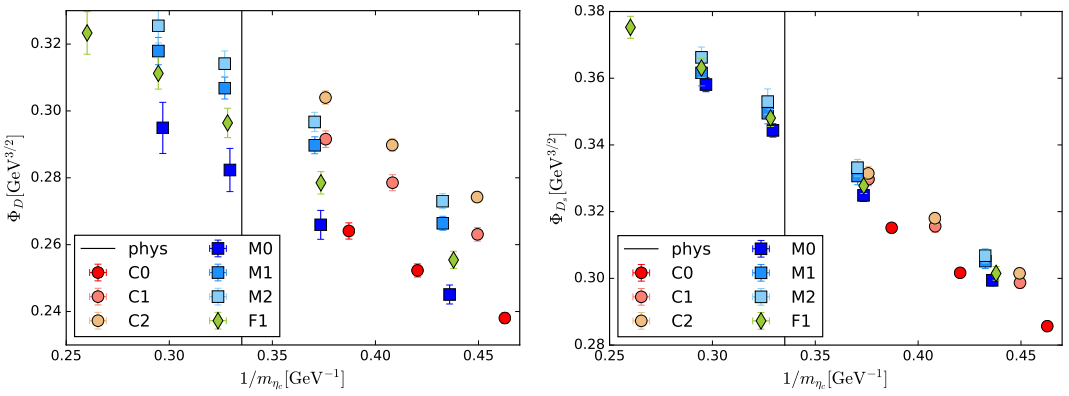


Figure 6.11: The quantity $\Phi_P$ as a function of the inverse $\eta_c$ mass for $P = D$ (left) and $P = D_s$ (right). Again, the black vertical solid lines (labelled 'phys') correspond to the physical value of $m_{\eta_c}$ as stated by the Particle Data Group [1]. The red circles, blue squares and green diamonds show data from the coarse, medium and fine ensembles, respectively.

to be rather mild. Contrary to this, the $D_s$ meson displays a smaller light quark mass dependence (again to be expected, since the light quark only enters as a sea quark).

### 6.5.4 Fit Strategies

As discussed above, we need to obtain the value of each observable at physical quark masses and vanishing lattice spacing, i.e. at $(a = 0, m_l^{\mathrm{phys}}, m_s^{\mathrm{phys}}, m_c^{\mathrm{phys}})$. We have already fixed $m_s$ to its physical value, so it remains to fix the light and the heavy quark and to take the continuum limit.

We will fix the quark masses by considering appropriate meson masses, e.g. we fix the light quark mass by reproducing the physical neutral pion mass $m_{\pi^0} = 134.9766(6)\,\text{MeV}$ [1] as was done in ref [144]. We have a number of choices for the meson $H$ that fixes the charm quark mass. The ones we will consider are $H = D, D_s$ and $\eta_c$. Each of these has slightly different advantages and disadvantages attached. The $D$ meson is comparably noisy and has a strong light quark dependence, making it difficult to disentangle the extrapolation to physical light quark masses from the the interpolation to the physical charm quark mass. The $D_s$ is statistically cleaner and is less affected by the light quark mass than the $D$, but due to the mistuning of the strange quark mass, we had to correct for the value of the $D_s$ mass. Finally the $\eta_c$ is statistically the cleanest, but we do not have the disconnected contributions. However, these are assumed to be small [162] and other collaborations also find good agreement between the two ways to set the charm scale neglecting these contributions [18]. Reference [162] estimates an effect of less than 0.2% for the contributions due to electromagnetic and quark-disconnected distributions to the mass of $\eta_c$.

We will investigate all three choices and use the spread as an indication of potential systematic errors. The masses of these mesons, stated by the Particle Data Group [1] are

$$\begin{aligned} m_{D^\pm} &= 1.8695(4)\,\text{GeV} \\ m_{D_s^\pm} &= 1.9690(14)\,\text{GeV} \\ m_{\eta_c} &= 2.9836(6)\,\text{GeV}. \end{aligned} \tag{6.6}$$

We will now proceed in two steps. First we will carry out a *local* analysis of the data and consider the parameters that need to be fixed, one-by-one. For this study we will first fix the heavy quark mass by introducing a set of reference masses $m_H^{\text{ref}}$. We will interpolate the data on all ensembles to these values to obtain $\mathcal{O}(a, m_l, m_s^{\text{phys}}, m_h^{\text{ref}})$. We then carry out a combined chiral-continuum limit to obtain $\mathcal{O}(a = 0, m_l^{\text{phys}}, m_s^{\text{phys}}, m_h^{\text{ref}})$. In a final step we then interpolate the results obtained to the physical value of $m_H$ to fix the charm quark mass to its physical value. In the second analysis we fix all parameters in one *global* fit. In the case of a correlated fit, this allows for a meaningful $\chi^2$-value and a probabilistic interpretation of the quality of the fit via the $p$-value.

### 6.5.5 *Local Fit* to Extrapolate to the Physical Point

To minimise light quark effects and avoid effects from the strange quark mass correction we choose $H = \eta_c$ to fix the heavy quark mass. We introduce reference masses linearly in $1/m_{\eta_c}$ such that one of the reference masses corresponds to the physical $\eta_c$ mass and such that the range where we have data is fully covered. The data is linearly interpolated to these reference masses. This is shown for the observables $\Phi_D$ and $\Phi_{D_s}$ in figure 6.12. Note that for the lowest three reference masses we have 3 distinct lattice spacings, whilst at other two reference masses we only have two lattice spacings.

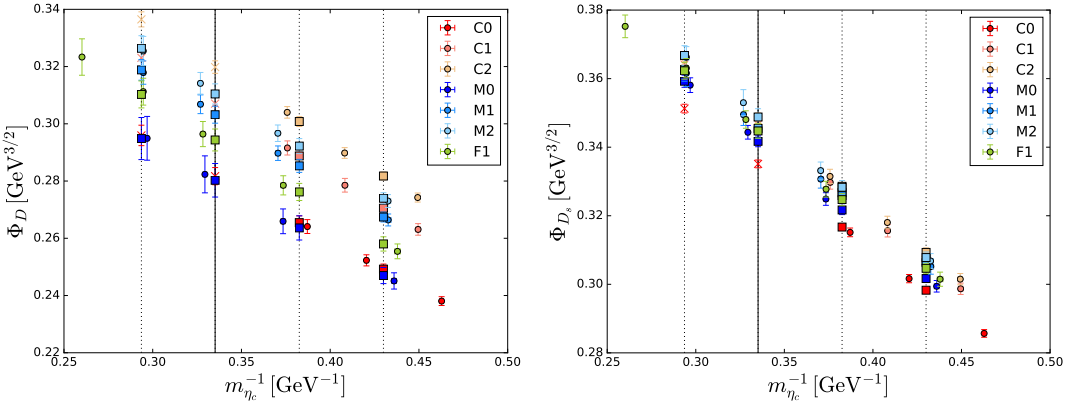


Figure 6.12: $\Phi_P$ as a function of the inverse $\eta_c$ mass for $P = D$ (left) and $P = D_s$ (right). The simulated data is shown by the circles. The dotted lines correspond to the reference masses, the solid line to the physical charm mass. At these reference masses, the interpolated data on all ensembles is shown (squares). The crosses are the extrapolated data points for the coarse ensembles.

In the second step we do a combined chiral-continuum limit fit to this data at each reference mass using the ansatz

$$\mathcal{O}(a, m_l, m_h^{\text{ref}}) = \mathcal{O}(0, m_l^{\text{phys}}, m_h^{\text{ref}}) + C_{CL}(m_h^{\text{ref}})\, a^2 + C_\chi(m_h^{\text{ref}}) \left( m_\pi^2 - \left( m_\pi^{\text{phys}} \right)^2 \right). \quad (6.7)$$

This assumes the same slope with the pion mass for all ensembles. The results of all chiral and continuum limit fits are listed in table 6.8. Examples of this interpolation for two reference masses in the case of the $D_s$ meson are shown in figure 6.13. In the left plot of this figure, all lattice spacings are present, whilst the coarse ensembles can not reach the heavy quark mass of the right plot. In each plot the left-hand panel shows the extrapolation to the physical pion mass whilst the right-hand side shows the extrapolation to vanishing lattice spacing. The dotted coloured lines correspond to the fit result for the given lattice spacing (left-hand panels) and pion masses (right-hand panels). We can see that the result is far better constrained in the region with 3 distinct lattice spacings.

Finally the data needs to be interpolated to the physical charm quark mass. This is done by fitting the values obtained at the reference masses $m_h^{\text{ref}}$ to the functional form

$$\mathcal{O}(0, m_l^{\text{phys}}, m_s^{\text{phys}}, m_c^{\text{phys}}) = \mathcal{O}(0, m_l^{\text{phys}}, m_s^{\text{phys}}, m_h) + C_h \left( \frac{1}{m_{\eta_c}} - \frac{1}{m_{\eta_c}^{\text{phys}}} \right). \quad (6.8)$$

Figure 6.14 shows this interpolation in the heavy quark mass. In each case the magenta star shows the result obtained at the physical value. The results of the heavy quark interpolation in table 6.9.

| observable | $m_{\eta_c}^{\text{ref}}$ [GeV] | $\mathcal{O}(a = 0, m_l^{\text{phys}})$ | $C_\chi$ | $C_{CL}$ | $\chi^2$/d.o.f |
|---|---|---|---|---|---|
| $\Phi_D$ [GeV$^{3/2}$] | 2.3256 | 0.2531(25) | 0.202(12) | -0.0129(95) | 1.172 |
| | 2.6138 | 0.2707(33) | 0.216(16) | -0.016(12) | 0.688 |
| | 2.9836 | 0.292(16) | 0.264(58) | -0.06(11) | 0.543 |
| | 3.4057 | 0.310(20) | 0.276(72) | -0.07(13) | 0.394 |
| $\Phi_{D_s}$ [GeV$^{3/2}$] | 2.3256 | 0.3045(17) | 0.0652(85) | -0.0179(61) | 0.517 |
| | 2.6138 | 0.3256(20) | 0.071(10) | -0.0253(73) | 0.715 |
| | 2.9836 | 0.3449(86) | 0.061(26) | -0.019(51) | 0.075 |
| | 3.4057 | 0.3623(100) | 0.063(30) | -0.018(59) | 0.157 |
| $f_{D_s}/f_D$ | 2.3256 | 1.1531(81) | -0.529(42) | 0.028(33) | 1.598 |
| | 2.6138 | 1.159(11) | -0.538(55) | 0.009(42) | 0.693 |
| | 2.9836 | 1.158(57) | -0.65(21) | 0.09(39) | 1.153 |
| | 3.4057 | 1.154(70) | -0.63(26) | 0.11(49) | 0.932 |

Table 6.8: Fit results of the extrapolation to physical pion masses and the continuum for $\Phi_D$, $\Phi_{D_s}$ and $f_{D_s}/f_D$.

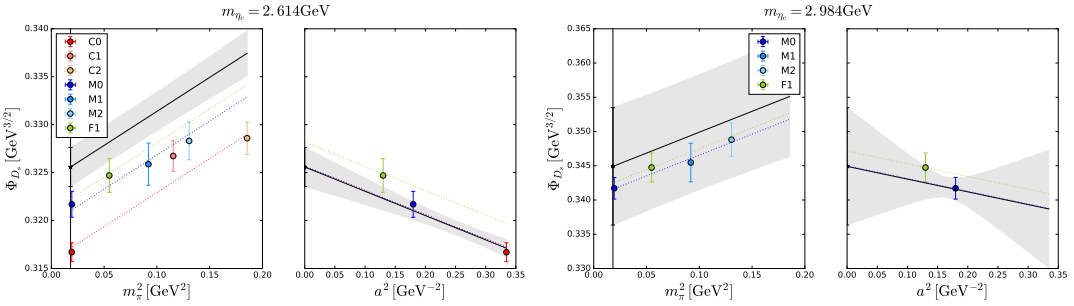


Figure 6.13: Extrapolation to vanishing lattice spacing and physical pion masses for $\Phi_{D_s}$ at two reference masses $m_{\eta_c}^{\text{ref}}$. The solid black lines and shaded regions show the fit results at vanishing lattice spacing (left panels) and at physical pion masses (right panels). The coloured lines show the fit results for the given parameters of that ensemble. For clarity only the lightest pion mass ensemble for each lattice spacing is shown on the right-hand panels and for the lines with the fit results.

| observable | $\mathcal{O}$ | $C_h$ | $\chi^2$/d.o.f |
|---|---|---|---|
| $\Phi_D$ [GeV$^{3/2}$] | 0.2895(61) | -0.385(63) | 0.049 |
| $\Phi_{D_s}$ [GeV$^{3/2}$] | 0.3459(37) | -0.435(38) | 0.035 |
| $f_{D_s}/f_D$ | 1.163(19) | -0.10(20) | 0.031 |

Table 6.9: Fit results of the interpolation in the reference masses to the physical value of $m_{\eta_c}$.

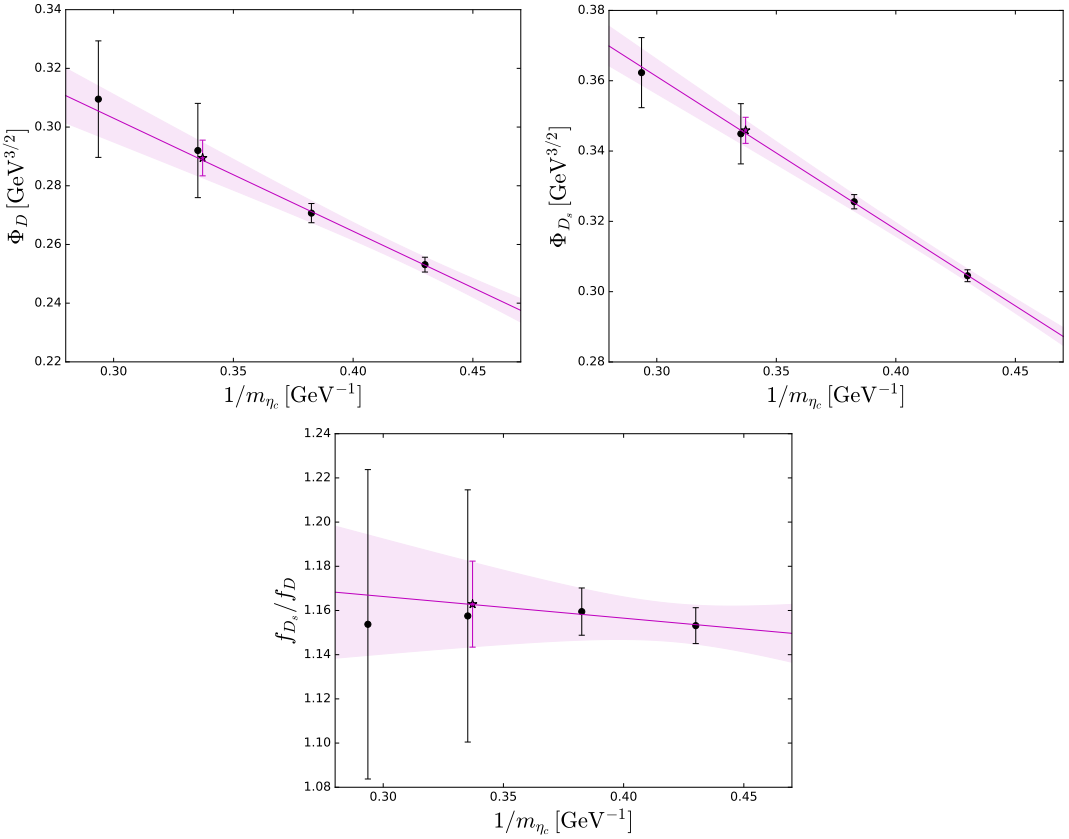


Figure 6.14: Extrapolation in the heavy quark mass to reach the physical heavy quark mass for the case of $\Phi_D$ (top left), $\Phi_{D_s}$ (top right) and the ratio for decay constants (bottom). The black points show the results of the chiral and continuum limit extrapolation at a given reference mass. The larger error bars on the two left-most black points arise due to the continuum limit extrapolation with only two lattice spacings. The magenta band shows the result of the fit. The magenta stars show the result at the physical charm mass. They are horizontally shifted by a small amount for visual convenience.

We also have a consistency check by comparing two different ways of obtaining the ratio $f_{D_s}/f_D$ at physical values. We can either build the ratio *first* on each ensemble and then carry out the analysis (compare the bottom plot in figure 6.14). Alternatively we can build the ratio *after* having obtained the results for $\Phi_D$ and $\Phi_{D_s}$. The values we obtain are

$$\begin{aligned} \left(\frac{f_{D_s}}{f_D}\right)^{\text{extrap}} &= 1.163(19) \\ \frac{f_{D_s}^{\text{extrap}}}{f_D^{\text{extrap}}} &= 1.163(24), \end{aligned} \tag{6.9}$$

which are in good agreement. The slightly larger error when building the ratio of the extrapolated values arises from fewer cancellations between the numerator and the denominator.

Whilst we can assess the goodness-of-fit for each individual step, it is impossible to make a statement about the overall quality of the fit. In particular since the steps we have undertaken are not entirely orthogonal. For example, we expect a small pion mass and lattice spacing dependence in the mass of the $\eta_c$ meson. To asses the overall quality of the fit we will now devise a global fit, guided by our experience from the local fit.

### 6.5.6 Global Fit Ansatz to Extrapolate to the Physical Point

Our fit ansatz is motivated by a Taylor expansion around the physical value of the relevant meson masses and the experience from the previous subsection. It is given by

$$\begin{aligned}\mathcal{O}(a, m_\pi, m_h) = \mathcal{O}(0, m_\pi^{\text{phys}}, m_h^{\text{phys}}) \\ + \left[C^0_{CL} + C^1_{CL}\,\Delta m_H^{-1}\right] a^2 \\ + \left[C^0_{\chi} + C^1_{\chi}\,\Delta m_H^{-1}\right] \left(m_\pi^2 - m_\pi^{2\,\text{phys}}\right) \\ + \left[C^0_h\right] \Delta m_H^{-1},\end{aligned} \tag{6.10}$$

where $\Delta m_H^{-1} = 1/m_H - 1/m_H^{\text{phys}}$ and $H = D, D_s$ or $\eta_c$. This means we simultaneously fit the continuum limit dependence (coefficients $C_{CL}$), the pion mass dependence (coefficients $C_\chi$) and heavy quark dependence (coefficients $C_h$) as well as cross terms (coefficients linear in $\Delta 1/m_h$, i.e. $C^1_\chi$ and $C^1_{CL}$) in one global fit. The coefficients $C^1_{CL}$ and $C^1_\chi$ capture mass dependent continuum limit and pion mass extrapolation terms. This arises by expanding $C_{CL}(m_h)$ and $C_\chi(m_h)$ in powers of $\Delta m_H^{-1}$. Following the ansatz from the local study we assume a linear behaviour in $m_\pi^2$ and ignore any chiral logarithms. This is motivated by our observations that the behaviour with the pion mass is linear (compare table 6.8 and figure 6.13).

We will monitor the behaviour when employing different cuts in the data that enters the fit. For example, we have data for pion masses in the range $139\,\text{MeV} \leq m_\pi \leq 430\,\text{MeV}$ but will consider the cuts

$$m_\pi^{\text{max}} = 450\,\text{MeV},\ 400\,\text{MeV},\ 350\,\text{MeV}. \tag{6.11}$$

Another variation we have already mentioned is the choice of the meson that fixed the charm quark mass. Finally we can modify the fit form (6.10) by setting some of the parameters to zero by hand, which we will do when the data is not sufficiently accurate to resolve them clearly.

### 6.5.7 Global Fit Results for the Ratio of Decay Constants $f_{D_s}/f_D$

Figure 6.15 gives one example of a fully correlated fit for the ratio of decay constants. The fit shown here has a pion mass cut of $m_\pi < 400\,\text{MeV}$ and uses the $\eta_c$ mass to fix the

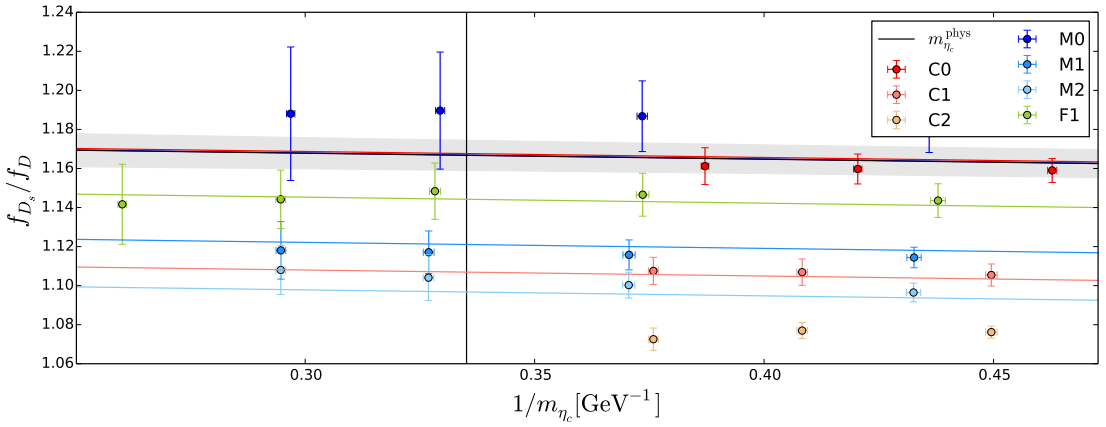


Figure 6.15: One example for the global fit according to (6.10) for the case of the observable $f_{D_s}/f_D$. In the case presented here the charm quark mass is fixed by the $\eta_c$ meson and a pion mass cut of $m_\pi < 400\,\text{MeV}$ is employed. The grey band shows the fit result at physical pion masses and vanishing lattice spacing. The coloured bands correspond to the fit projected to the given pion mass and lattice spacing for the corresponding ensembles. In this fit we ignore heavy mass dependent continuum and pion mass terms.

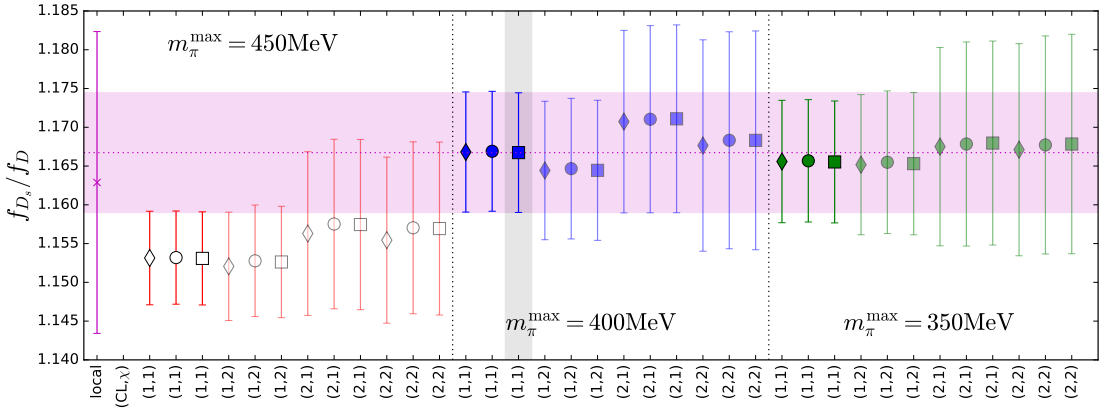


Figure 6.16: Comparison of the results of the different choices in the global fit. The grey and magenta bands highlight the fit shown in figure 6.15. The different symbols indicate different ways of fixing the heavy quark mass, i.e. $H = D(\diamond)$, $D_s(\bigcirc)$, and $\eta_c^{\text{connected}}(\square)$. Fainter data points indicate that at least one of the heavy mass dependent coefficients is compatible with zero at the one sigma level. More detail about the data shown here is given in the text.

charm quark mass. Furthermore, heavy mass dependent coefficients of the continuum limit and the extrapolation to physical pion masses are ignored (i.e. $C_{CL}^1 = 0$ and $C_\chi^1 = 0$). This choice was made since neither of them could be resolved within our statistics. This fit gives $\chi^2/\text{dof} = 0.319$ and a $p$-value of 0.002. The pion mass cut was chosen due to variations of the pion mass cut as described below.

Table D.1 summarises the results of all fit variations for $f_{D_s}/f_D$. The results of these are

also shown in figure 6.16. The magenta data point to the very left is the fit result obtained from the local fit in the previous section. The red (blue, green) data points correspond to pion mass cuts of $m_\pi^{\max} = 450\,\text{MeV}$ (400 MeV, 350 MeV). The different symbols indicate different ways of fixing the heavy quark mass, i.e. $H = D(\diamond)$, $D_s(\bigcirc)$, and $\eta_c^{\text{connected}}(\square)$. Finally the label on the x-axis describes which fit was used by stating the number of coefficients for the continuum limit $(CL)$and pion mass limit $(\chi)$ respectively. E.g. fits results labelled $(2, 2)$ correspond to the fit form (6.10) whilst $(2, 1)$ corresponds to keeping two coefficients for the continuum limit extrapolation, but only one coefficient for the pion mass extrapolation by setting $C_\chi^1$ to zero. Cases where one of the coefficients $C_{CL}^1$ and $C_\chi^1$ is compatible with zero at the one sigma level are indicated by the corresponding data point being partially transparent.

From the results shown in figure 6.16 we can make a few observations. We find that the global fit allows for a more precise determination of the ratio of decay constants. We also find that the ratio of decay constants is insensitive to the way we fix the charm quark mass. This is not surprising as the ratio of decay constants does not strongly depend on the heavy quark mass (compare figure 6.15). We find that a dependence is observed when including pions with $m_\pi > 400\,\text{MeV}$, for this reason we restrict ourselves to $m_\pi \leq 400\,\text{MeV}$. We can also see that when allowing for heavy mass dependent pion mass and continuum extrapolation terms, these can not be resolved with the present data. They also do not significantly change the central value of the fit result but increases the statistical error. This is again not surprising, given the mild behaviour with heavy quark mass displayed by the data.

From this discussion we choose the highlighted fit (i.e. the one presented in figure 6.15) as our final fit result and as statistical error. We then assign a systematic error associated with the fit from the spread in the fit results as we vary the parameters of the fit, maintaining $m_\pi \leq 400\,\text{MeV}$. From this we quote

$$\frac{f_{D_s}}{f_D} = 1.1667(77)\left(^{+44}_{-23}\right)_{\text{fit}}\,, \tag{6.12}$$

where the first error is statistic and the second error captures the systematic error associated with the chiral-continuum limit as well as the way the charm quark mass is fixed. This error budget is not yet complete. The full systematic error budget will be devised in section 6.6.

### 6.5.8 Global Fit Results for $\Phi_D$ and $\Phi_{D_s}$

Figure 6.17 shows the chosen fit results for $\Phi_D$ (top) and $\Phi_{D_s}$ (bottom) respectively. In both cases the heavy quark mass is fixed by the $\eta_c$ mass and a pion mass cut of $m_\pi^{\max} \leq 400\,\text{MeV}$ is used. Contrary to the fit of the ratio of decay constants, correlated fit of $\Phi_D$ and $\Phi_{D_s}$ proved to be unstable. Therefore, the fits presented here are uncorrelated,

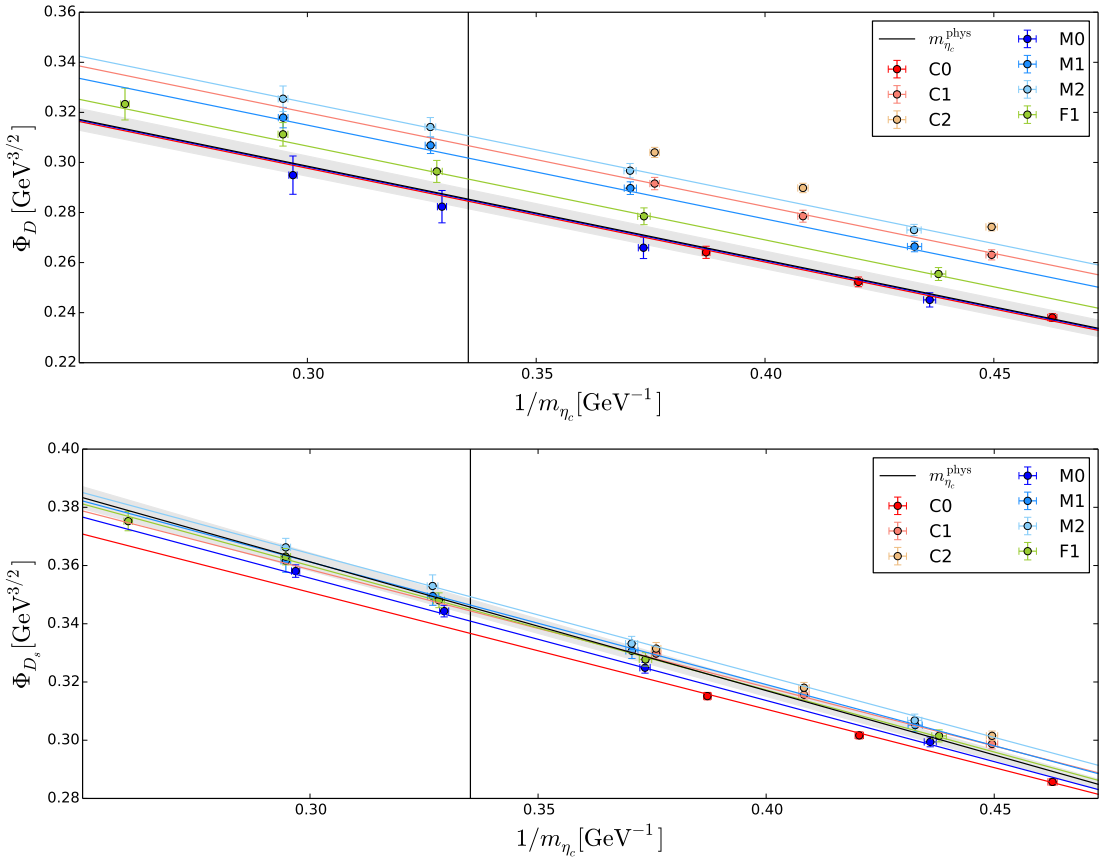


Figure 6.17: Examples for the global fit according to (6.10) for the case of the observables $\Phi_D$ (top) and $\Phi_{D_s}$ (bottom). In both cases the charm quark mass is fixed by the $\eta_c$ meson and a pion mass cut of $m_\pi < 400\,\text{MeV}$ is employed. Again, the grey band shows the fit result at physical pion masses and vanishing lattice spacing. The coloured bands correspond to the fit projected to the given pion mass and lattice spacing for the corresponding ensembles. More details about these fits can be found in the text.

which leads to slightly larger errors. In the case of $\Phi_D$ we restrict ourselves to $C^1_{CL} = 0$ and $C^1_\chi = 0$ whilst in the case of $\Phi_{D_s}$ we resolve the coefficient $C^1_{CL}$. This choice is made since we can consistently resolve $C^1_{CL}$ for the case of $\Phi_{D_s}$ as can be seen in figure 6.18.

Tables D.2 and D.2 summarise the results of all fit variations for $\Phi_D$ and $\Phi_{D_s}$ respectively. Similar to the previous section we can vary the fit parameters to see how stable the fit is under these variations. We find that we can consistently resolve the $C^1_{CL}$ coefficient in the case of $\Phi_{D_s}$, whilst this is less clear in the case of $\Phi_D$. For this reason we choose $(CL, \chi) = (1, 1)$ for the case of $\Phi_D$ and $(CL, \chi) = (2, 1)$ for the case of $\Phi_{D_s}$. Again, little dependence is observed in the case of $m_\pi^{\text{max}} \leq 400\,\text{MeV}$ so this pion mass cut is used. The dependence is larger in the case of $\Phi_D$ than for $\Phi_{D_s}$ in agreement with intuition. Again, we see little dependence in the way the heavy quark mass is fixed, even though (contrary to the ratio of decay constants) the heavy mass dependence is now significant. Overall we see more variation in the results of the fit than we have for the ratio of decay

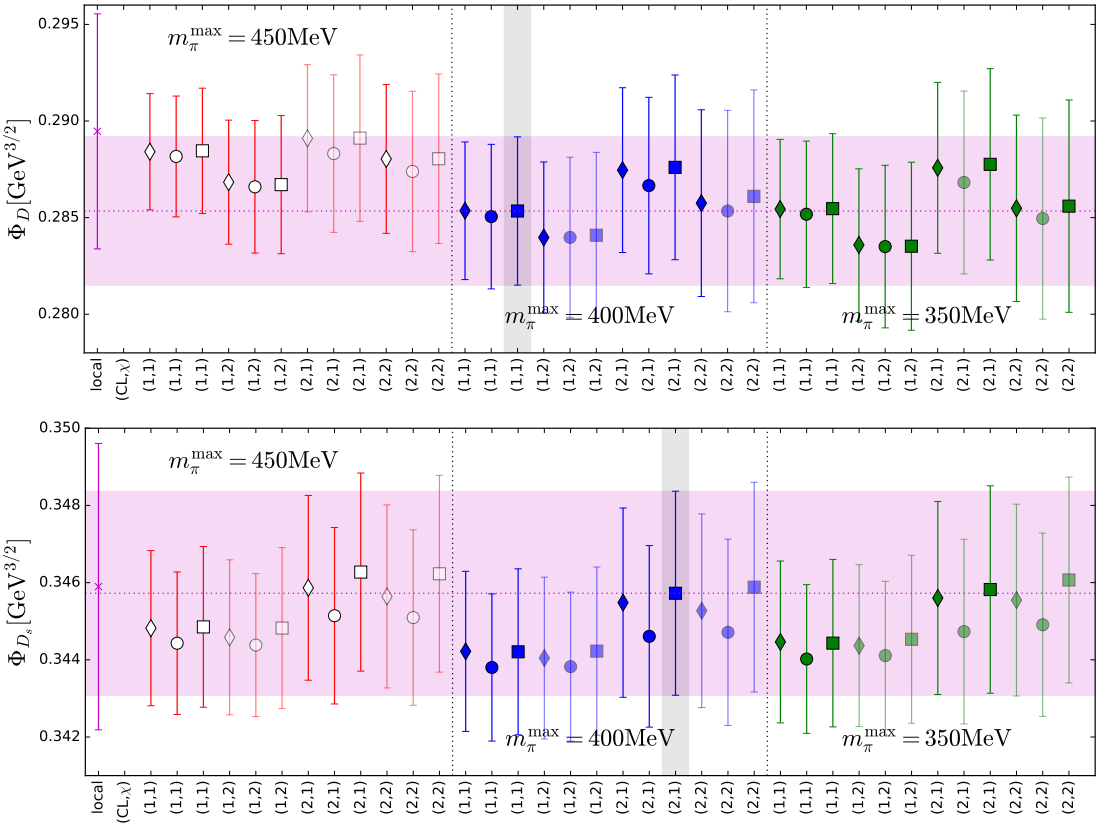


Figure 6.18: Comparison of the results of the different choices in the global fit for $\Phi_D$ (top) and $\Phi_{D_s}$ (bottom). The grey and magenta bands highlight the fit shown in figure 6.17. The different symbols indicate different ways of fixing the heavy quark mass, i.e. $H = D(\diamond)$, $D_s(\bigcirc)$, and $\eta_c^{\text{connected}}(\square)$. Fainter data points indicate that at least one of the heavy mass dependent coefficients is compatible with zero at the one sigma level. More detail about the data shown here is given in the text.

constants. Following the same procedure to determine the systematic error associated with the fit as above we find

$$\begin{aligned} \Phi_D &= 0.2853(38)(^{+24}_{-18})_{\text{fit}}\,\text{GeV}^{3/2}, \\ \Phi_{D_s} &= 0.3457(26)(^{+\ 3}_{-19})_{\text{fit}}\,\text{GeV}^{3/2}. \end{aligned} \tag{6.13}$$

## 6.6 Systematic Error Estimation

We have found central values, statistical errors and the systematic errors due to the fit for the value of $\Phi_D$, $\Phi_{D_s}$ and $f_{D_s}/f_D$. Now we need to address the systematic error budget. There are a number of sources of systematic error that could potentially contribute. Firstly we have to address any systematic errors arising from fits such as the correlation function fit and the global fit ansatz leading to the continuum limit results at physical quark masses. Secondly we need to address the systematic errors from the scale setting

and the setting of the quark masses. Thirdly we need to address the effects of the assumptions we make in the lattice formulation, namely the finite volume, the fact that we neglect sea charm quark loops, the assumption of mass degenerate up and down quarks and neglecting electromagnetic effects. Finally, we have renormalised the data using the renormalisation constant from the flavour diagonal light-light conserved current, instead of the mixed action current that we use in the calculation of the correlation functions.

Recall that we have chosen conservative fit ranges in section 6.4, so that any variation of $t_{\text{min}}$ and $t_{\text{max}}$ leads to results that are well within the statistical error from the correlation function fits. We also fitted the first excited state in addition to the ground state, so any excited state contamination to the results presented here would have to arise from higher excited states. We claim that this systematic error is already included in the statistic error due to our conservative choice.

Similarly the systematic error attached to the global fit result already accounts for the way the charm quark mass (variation between $D$, $D_s$ and $\eta_c$) and the light quark mass (pion mass) are fixed. Stability of the fit ansatz is also tested.

The uncertainty in determining the lattice spacing is propagated by creating a bootstrap distribution with the correct width which has been used throughout the analysis. The uncertainty in the physical strange quark masses arising from ref [144] has been treated in the same way and is therefore already included in the statistical error.

We have already discussed the systematic error arising from the correction of the mistuning of the strange quark in section 6.5.1 and came to the conclusion that this yields an uncertainty of $0.000009\,\text{GeV}^{3/2}$ for $\Phi_{D_s}$ and 0.0003 for $f_{D_s}/f_D$.

In the data presented so far we have used the renormalisation constant obtained from the light-light conserved current (compare section 6.5.2). However, the current that needs to be renormalised is a mixed action current due to the change in $M_5$ between the light and the heavy sector for which we do not have a conserved current. This does not affect the ratio of decay constants since the renormalisation constants cancel. To assess the systematic error arising from this choice, a study leading to the ratio of amputated vertex functions $\Lambda(M_5^1, M_5^2)$ between the different combinations of actions $((M_5^1, M_5^2) = (1.8, 1.8), (1.6, 1.8), (1.6, 1.6)$, where $i = 1, 2$ refers to the action of the first and second quark field entering the current operator) was carried out[3]. This has been done on the ensembles C1, M1 and F1 and the ratio of $\Lambda(1.6, 1.6)/\Lambda(1.8, 1.8)$ lies consistently between 0.996 and 0.997, indicating at most a 0.4% effect. We will assign this as a systematic error.

We have already discussed that finite size effects are exponentially suppressed by $m_\pi L$ (compare section 3.8) and are therefore expected to be small for the study presented here. We can, however, give a more concise estimate by noticing that finite volume effects arise

[3]Done by A. Khamseh under the supervision of P. Boyle and L. Del Debbio

from the IR regulator and are therefore insensitive to the choice of discretisation. We will estimate the finite size effects by comparing our values of $m_\pi L$ to a study the MILC collaboration has undertaken [18]. In their work, they have done a simulation of three different volumes whilst keeping the lattice spacings and quark masses constant. This was done for a lattice spacing of 0.12 fm (roughly corresponding to our coarse ensembles) and pion masses of just above 200 MeV. The considered volumes are 2.88 fm, 3.84 fm and 5.76 fm corresponding to values of $m_\pi L$ of 3.2, 4.3 and 5.4 respectively. For the masses of the $D$ and $D_s$ meson they see variations of $\lesssim 1\,\text{MeV}$ and $\lesssim 0.5\,\text{MeV}$ respectively. For the decay constants the variations they find are $< 0.3\%$ and $< 0.15\%$ which we will use to as a symmetric systematic error. From this we find $\delta\Phi_D \approx 0.001\,\text{GeV}^{3/2}$ and $\delta\Phi_{D_s} \approx 0.0006\,\text{GeV}^{3/2}$ which we will assign as our systematic error. Propagating $\delta f_D$ and $\delta f_{D_s}$ as

$$\pm\,\delta\frac{f_{D_s}}{f_D} = \pm\frac{f_{D_s}}{f_D}\frac{\delta f_{D_s}}{f_{D_s}} \pm \frac{f_{D_s}}{f_D}\frac{\delta f_D}{f_D} \tag{6.14}$$

and treating variations in $f_{D_s}$ and $f_D$ as independent and therefore adding the two terms above in quadrature, we find $\delta\frac{f_{D_s}}{f_D} \sim 0.0039$. Given that the minimum value of $m_\pi L$ for our ensembles is 3.8, results derived from these numbers are a good conservative estimate.

In our simulations we treat the up and down quark masses as degenerate, which is not the case in nature and neglect electromagnetic effect. This affects in particular the masses of the mesons we consider. In principle these effects cannot be disentangled. We neglect electromagnetic effects in the determination of the decay constants since they are defined as pure QCD quantities. However, for the determination of the CKM matrix elements these effects will need to be taken into account [1, 18].

We devise a systematic error associated to the way we fix the heavy quark mass by considering how much the fit result for $\Phi_D$ changes when we replace the input mass $m_{D^\pm} = 1.86961(09)\,\text{GeV}$ by $m_{D^0} = 1.86484(05)\,\text{GeV}$ [1]. We estimate the effect of this shift using the fit result of the coefficient $C_h^0$ for the case of $h = D$ and multiplying these by $\left|m_{D^0}^{-1} - m_{D^\pm}^{-1}\right| \sim 0.0014\,\text{GeV}^{-1}$. From this we find $\delta\Phi_D \sim 0.00037\,\text{GeV}^{3/2}$, $\delta\Phi_{D_s} \sim 0.00044\,\text{GeV}^{3/2}$ and $\delta\frac{f_{D_s}}{f_D} \sim 0.00003$. For the quantity $f_{D_s}/f_D$ this is negligible. As a probe for the same effect in the light quark mass fixing, we consider the effect of choosing $m_{\pi^\pm}$ instead of $m_{\pi^0}$ as input mass, i.e. calculating $C_\chi^0\left(m_{\pi^\pm}^2 - m_{\pi^0}^2\right)$. From this we find $\delta\Phi_D \sim 0.00029\,\text{GeV}^{3/2}$, $\delta\Phi_{D_s} \sim 0.00001\,\text{GeV}^{3/2}$ and $\delta\frac{f_{D_s}}{f_D} \sim -0.00080$. Adding these two effects in quadrature we obtain the values listed in the column $m_u \neq m_d$ in table 6.10.

Given that the continuum limit coefficient $C_{CL}^0$ is compatible with zero for the fits chosen for $\Phi_D$ ($C_{CL}^0 = -0.003(11)\,\text{GeV}^{7/2}$) and $f_{D_s}/f_D = 0.005(25)\,\text{GeV}^2$, we neglect higher order $O(a^4)$ effects. For $\Phi_{D_s}$ we find $C_0^{CL} = -0.027(10)\,\text{GeV}^{7/2}$ (the heavy mass dependent continuum limit term vanishes at the physical charm quark mass). Assume

| observable | central | stat | total systematic | fit sys | finite volume | h.o. CL | $m_u \neq m_d$ | renormalisation | strange quark |
|---|---|---|---|---|---|---|---|---|---|
| | | $\times 10^4$ | | $\times 10^4$ | | | | | |
| $\Phi_D$ [GeV$^{3/2}$] | 0.2853 | 38 | $^{+29}_{-24}$ | $^{+24}_{-18}$ | 10 | - | 4.7 | 11 | - |
| $\Phi_{D_s}$ [GeV$^{3/2}$] | 0.3457 | 26 | $^{+18}_{-26}$ | $^{+\ 3}_{-19}$ | 6 | 7 | 4.4 | 14 | 0.9 |
| $f_{D_s}/f_D$ | 1.1667 | 77 | $^{+60}_{-46}$ | $^{+44}_{-23}$ | 39 | - | 8 | - | 3 |

Table 6.10: Summary of the systematic error budget for the quantities $\Phi_D$, $\Phi_{D_s}$ and the ratio of decay constants. Details of the discussion leading to these results can be found in the text.

fourth order discretisation effects and rewrite

$$\frac{\delta\Phi_{D_s}}{\Phi_{D_s}} = \frac{1}{\Phi_{D_s}}\left[C^0_{CL}a^2 + D^0_{CL}a^4\right] = \frac{C^0_{CL}a^2}{\Phi_{D_s}}\left[1 + \frac{D^0_{CL}}{C^0_{CL}}a^2\right]. \tag{6.15}$$

Substituting the numbers for $C^0_{CL}$ and the coarsest and finest lattice spacings we find $C^0_{CL}a^2/\Phi_{D_s} \sim 0.026$ and 0.010 respectively. Assuming $D^0_{CL}/C^0_{CL} = (0.5\,\text{GeV})^2$ (i.e. setting the scale such that discretisation effects grow as $a/\Lambda$ with $\Lambda = 500\,\text{MeV}$) we find $D^0_{CL}/C^0_{CL}a^2 \sim 0.008$ and $\sim 0.003$. So the residual discretisation effects are 8% (3%) of the leading discretisation effects, yielding at most 0.2% of the absolute value.

Combining these errors in quadrature and using the masses of $D^\pm$ and $D_s^\pm$ (compare (6.6) [1]), we arrive at our final value

$$\begin{aligned} \Phi_D &= 0.2853(38)_{\text{stat}}(^{+29}_{-24})_{\text{sys}}\,\text{GeV}^{3/2} \quad \Rightarrow \quad f_D = 208.7(2.8)_{\text{stat}}(^{+2.1}_{-1.8})_{\text{sys}}\,\text{MeV} \\ \Phi_{D_s} &= 0.3457(26)_{\text{stat}}(^{+18}_{-26})_{\text{sys}}\,\text{GeV}^{3/2} \quad \Rightarrow \quad f_{D_s} = 246.4(1.9)_{\text{stat}}(^{+1.3}_{-1.9})\,\text{MeV}\ . \end{aligned} \tag{6.16}$$

We are now in a position to compare our results to the results of the literature presented in section 6.1. Adding our results to those presented in the most recent FLAG report [8] we obtain the plots in figure 6.19. The smaller error bar presents the statistic error only, whilst the larger error bar shows the full error (statistic and systematic). In all cases the error budget is dominated by the statistical error. We find good agreement with the literature and have errors competitive with the other results displayed in figure 6.19 [18, 158, 162, 181–194].

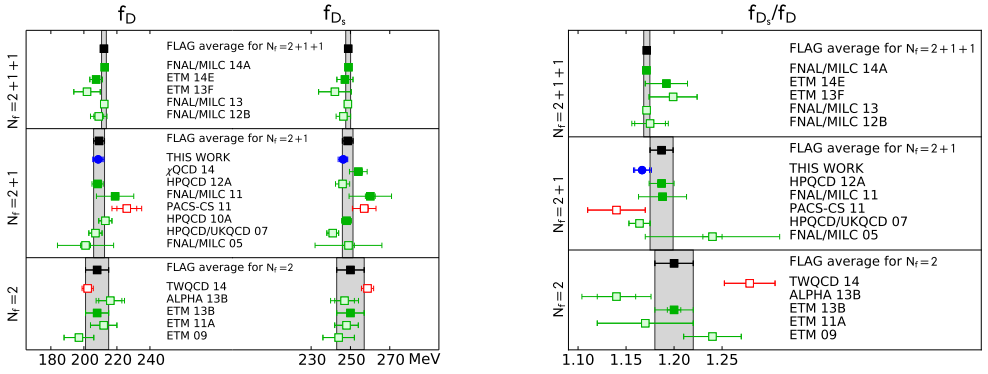


Figure 6.19: Superposition of our results (blue circles) to the data presented in the most recent FLAG report [8]. The small error bar shows the statistic error only, whilst the large error band includes both, the statistic and the systematic error.

## 6.7 CKM Matrix Elements

Having obtained the decay constants, we can make a prediction of the CKM matrix elements $|V_{cd}|$ and $|V_{cs}|$. However, the values shown in (6.1) [168] are obtained in nature and therefore we need to adjust these values to those of an isospin symmetric theory. In other words, the measured decay rate $|V_{cq}|\, f_{D_q}$ does include electroweak and isospin breaking effects, so before extracting $|V_{cq}|$ we need to correct the decay rate for these effects. Ref. [18] distinguishes between universal long-distance electromagnetic (EM) effects, universal short distance electroweak (EW) effects and structure dependent EM effects. All of these modify the decay rate to match the experimental value to the theory in which we simulate. The combined effect of the universal long-distance EM and short-distance EW effects is to lower the decay rate by 0.7% [18, 202, 203]. We adjust the decay rates from (6.1) and then calculate the CKM matrix elements from this. We find

$$\begin{aligned} |V_{cd}| &= 0.2185(50)_{\text{exp}}(^{+35}_{-37})_{\text{lat}} \\ |V_{cs}| &= 1.011(16)_{\text{exp}}(^{+11}_{-\ 9})_{\text{lat}}. \end{aligned} \tag{6.17}$$

Again, we can superimpose our results to those obtained in the most recent FLAG report [8], shown in figure 6.20. This combines the results of refs [18, 158, 162, 181, 185–187, 204, 205]. Again we find good agreement between previous works and obtain a competitive error.

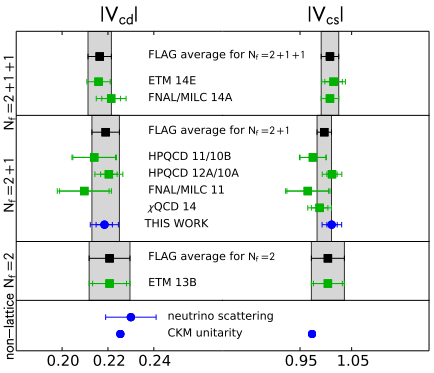


Figure 6.20: Superposition of our results (blue circles) to the data presented in the most recent FLAG report [8]. The smaller error bars of our results shows the lattice error only, whilst the large error band includes both, the theoretical and the experimental error, added in quadrature.

# Chapter 7

# Conclusions and Outlook

Whilst the SM has made many precision predictions which are in agreement with experiments, we know that there are experimental observations that it cannot reproduce. One way to test the SM is to over-constrain its parameters, e.g. the elements of the CKM matrix. Whilst perturbative methods are able to make ab initio high precision predictions for processes governed by the weak and the electromagnetic interactions, these methods fail for hadronic quantities. LQFT provides a tool for making such ab initio predictions even for strongly coupled system in general, and QCD in particular. This allows for the calculation of non-perturbative quantities such as masses and decay constants of hadrons which combined with experimental input allow to compute CKM matrix elements.

Whilst simulations of up, down and strange valence quarks have been done with a large variety of fermion discretisations, the larger mass of the charm quark poses additional difficulties. In this work we investigated the suitability of simulating heavy valence quarks with domain wall fermions, in the hope to be able to simulate charm quarks directly at their physical mass whilst keeping lattice artifacts under control. First, to assess this, we undertook a quenched pilot study, investigating the parameter space of domain wall fermions. Secondly, based on the results of this pilot study, we determined $D$ and $D_s$ decay constants from three lattice spacings and including pion masses as small as $m_\pi = 139\,\mathrm{MeV}$. Finally, we deduce the corresponding CKM matrix elements and compare our results to the literature.

For the pilot study we created four quenched ensembles in a small spatial volume ($L \sim 1.6\,\mathrm{fm}$) at inverse lattice spacings varying from $2.0\,\mathrm{GeV}$ to $5.7\,\mathrm{GeV}$. On these ensembles we explored the domain wall fermion parameter space to investigate a region where we can safely simulate charm quarks with mild discretisation errors. We found this region to be defined by

$$\begin{aligned} M_5 &= 1.6 \\ am_h &\leq 0.4. \end{aligned} \tag{7.1}$$

We then undertook scaling studies of heavy-strange and heavy-heavy mesons on these ensembles. In particular we found that the discretisation effects present in the heavy-strange dispersion relation and the decay constants of heavy-strange pseudoscalar mesons are mild and can be well described by an ansatz linear in $a^2$. We find that it is possible to closely approach the physical value of the charm quark mass even on the coarsest quenched ensemble ($a^{-1} \sim 2.0\,\mathrm{GeV}$) whilst maintaining the condition $am_h \leq 0.4$.

The continuum limit of the dispersion relation of heavy-heavy mesons is well described by $O(a^2)$ effects provided that either the momenta remain small ($p^2 \lesssim 0.6\,\mathrm{GeV}$). We further found that the dispersion relation of heavy-heavy mesons is stronger affected by discretisation effects, but we can recover the correct continuum limit by taking $O(a^4)$ effects into account for large undemocratic momenta.

Having established a frame work for the simulation of charm quarks with domain wall fermions, we measured heavy-light and heavy-strange correlation functions on RBC/UKQCD's dynamical $2+1f$ ensembles with inverse lattice spacings ranging from 1.73 GeV to 2.77 GeV and pion masses as low as 139 MeV. We deduced the values of the $D$ and $D_s$ meson decay constants on each ensemble and interpolated them to physical quark masses and vanishing lattice spacing. We assessed all systematic errors present in our simulations and, using experimental input, deduced values for the CKM matrix elements $|V_{cd}|$ and $|V_{cs}|$. We then compared these results to those of the literature. We find good agreement between our work and published results and obtain competitive errors. The main results of this thesis are summarised below:

$$\begin{aligned} f_D &= 208.7(2.8)_{\mathrm{stat}} \left(^{+2.1}_{-1.8}\right)_{\mathrm{sys}} \text{ MeV} \\ f_{D_s} &= 246.4(1.9)_{\mathrm{stat}} \left(^{+1.3}_{-1.9}\right)_{\mathrm{sys}} \text{ MeV} \\ \frac{f_{D_s}}{f_D} &= 1.1667(77)_{\mathrm{stat}} \left(^{+60}_{-46}\right)_{\mathrm{sys}} \\ &\text{and} \\ |V_{cd}| &= 0.2185(50)_{\mathrm{exp}}(^{+35}_{-37})_{\mathrm{lat}} \\ |V_{cs}| &= 1.011(16)_{\mathrm{exp}}(^{+11}_{-\ 9})_{\mathrm{lat}}. \end{aligned} \tag{7.2}$$

Having laid the groundwork for charm physics with domain wall fermions, our current work focusses on extending the charm physics program to semi-leptonic decays of $D$ and $D_s$ mesons as well as applying the ratio method to our data to deduce the values of $f_B$ and $f_{B_s}$.

# Appendix A

# Algebraic Properties

## A.1 Generators of $SU(2)$ and $SU(3)$

### A.1.1 $SU(2)$

The generators $\tau_i$ of $SU(2)$ can be expressed in terms of the Pauli matrices $\sigma_i$

$$\tau_i = \frac{1}{2}\sigma_i. \tag{A.1}$$

$\sigma_i$ are given by

$$\sigma_1 = \begin{pmatrix} 0 & 1 \\ 1 & 0 \end{pmatrix} \qquad \sigma_2 = \begin{pmatrix} 0 & -i \\ i & 0 \end{pmatrix} \qquad \sigma_3 = \begin{pmatrix} 1 & 0 \\ 0 & -1 \end{pmatrix} \tag{A.2}$$

### A.1.2 $SU(3)$

The generators of $SU(3)$ can be found from a generalisation of the Pauli matrices. The eight Gell-Mann matrices are defined as

$$\begin{aligned}
\lambda_1 &= \begin{pmatrix} 0 & 1 & 0 \\ 1 & 0 & 0 \\ 0 & 0 & 0 \end{pmatrix}, \quad \lambda_2 = \begin{pmatrix} 0 & -i & 0 \\ i & 0 & 0 \\ 0 & 0 & 0 \end{pmatrix}, \quad \lambda_3 = \begin{pmatrix} 1 & 0 & 0 \\ 0 & -1 & 0 \\ 0 & 0 & 0 \end{pmatrix}, \\
\lambda_4 &= \begin{pmatrix} 0 & 0 & 1 \\ 0 & 0 & 0 \\ 1 & 0 & 0 \end{pmatrix}, \quad \lambda_5 = \begin{pmatrix} 0 & 0 & -i \\ 0 & 0 & 0 \\ i & 0 & 0 \end{pmatrix}, \\
\lambda_6 &= \begin{pmatrix} 0 & 0 & 0 \\ 0 & 0 & 1 \\ 0 & 1 & 0 \end{pmatrix}, \quad \lambda_7 = \begin{pmatrix} 0 & 0 & 0 \\ 0 & 0 & -i \\ 0 & i & 0 \end{pmatrix}, \quad \lambda_8 = \frac{1}{\sqrt{3}} \begin{pmatrix} 1 & 0 & 0 \\ 0 & 1 & 0 \\ 0 & 0 & -2 \end{pmatrix}.
\end{aligned} \tag{A.3}$$

## A.2 Dirac Matrices

### A.2.1 Minkowski Space

The Dirac matrices $\gamma_\mu$ in Minkowski space are defined by obeying the Clifford algebra

$$\{\gamma_\mu, \gamma_\nu\} = 2g_{\mu\nu}\mathbb{1}, \tag{A.4}$$

where $g_{\mu\nu}$ is the metric tensor defined by

$$g_{\mu\nu} = \mathrm{diag}(+1, -1, -1, -1) \tag{A.5}$$

and $\mu, \nu$ runs over the indices $0, \cdots 3$. A convenient fifth $\gamma$ matrix is defined by

$$\gamma_5 = i\gamma_0\gamma_1\gamma_2\gamma_3. \tag{A.6}$$

Note the useful relations

$$\begin{aligned} \gamma_0^\dagger &= \gamma_0 \\ \gamma_i^\dagger &= -\gamma_i \\ \gamma_0\gamma_\mu^\dagger\gamma_0 &= \gamma_\mu \\ \left(\gamma_5^2\right) &= \mathbb{1} \\ \gamma_5\gamma_\mu &= -\gamma_\mu\gamma_5 \\ \gamma_5^\dagger &= \gamma_5 \end{aligned} \tag{A.7}$$

### A.2.2 Euclidean Space

Upon Wick rotation, we make the replacements

$$\begin{aligned} \gamma_i^E &= -i\gamma_1^M \\ \gamma_4^E &= \gamma_0^M, \end{aligned} \tag{A.8}$$

so that the Euclidean Gamma matrices now obey the Euclidean Clifford algebra

$$\left\{\gamma_\mu^E, \gamma_\nu^E\right\} = 2\delta_{\mu\nu}\mathbb{1}, \tag{A.9}$$

where $\delta_{\mu\nu}$ is the Kronecker delta. We can also define the fifth gamma matrix by

$$\gamma_5^E = \gamma_1\gamma_2\gamma_3\gamma_4. \tag{A.10}$$

In the following we will drop the superscript 'E'. Some of the properties (A.7) become

$$\begin{aligned} \gamma_\mu^\dagger &= \gamma_\mu = \gamma_\mu^{-1} \\ \gamma_5^\dagger &= \gamma_5 = \gamma_5^{-1} \\ \gamma_5\gamma_\mu &= -\gamma_\mu\gamma_5, \end{aligned} \tag{A.11}$$

where $\mu = 1, \cdots, 4$.

In a particular basis called the *chiral basis*, the we can find a specific form for the gamma matrices

# Appendix B

# Correlator Fit Results from the Quenched Pilot Study

| tag | $am$ | $af$ | $\chi^2$/d.o.f. | $am$ | $af$ | $\chi^2$/d.o.f. |
|---|---|---|---|---|---|---|
| | $am_s = 0.036$ | | | $am_s = 0.037$ | | |
| ss | 0.3433(16) | 0.11309(57) | 0.6033 | 0.3479(16) | 0.11360(57) | 0.5384 |
| sh0 | 0.4738(15) | 0.12710(81) | 0.3443 | 0.4764(12) | 0.12775(73) | 0.4052 |
| sh1 | 0.5628(14) | 0.13452(83) | 0.3609 | 0.5654(12) | 0.13519(80) | 0.4885 |
| sh2 | 0.6448(14) | 0.13960(85) | 0.3471 | 0.6463(13) | 0.13991(85) | 0.3455 |
| sh3 | 0.7215(13) | 0.14292(88) | 0.3456 | 0.7227(14) | 0.14314(90) | 0.3522 |
| sh4 | 0.7938(14) | 0.14480(92) | 0.3825 | 0.7953(13) | 0.14501(91) | 0.2996 |
| sh5 | 0.8614(15) | 0.1447(10) | 0.2965 | 0.8628(15) | 0.1451(10) | 0.2925 |
| sh6 | 0.9254(16) | 0.1439(11) | 0.3610 | 0.9266(15) | 0.1443(10) | 0.3577 |

Table B.1: Fit results for strange-strange and strange-heavy pseudoscalar masses and decay constants in lattice units for the ensembles $\beta = 4.41$.

| tag | $am$ | $af$ | $\chi^2$/d.o.f. | $am$ | $af$ | $\chi^2$/d.o.f. |
|---|---|---|---|---|---|---|
| | $am_s = 0.024$ | | | $am_s = 0.026$ | | |
| ss | 0.23894(93) | 0.07812(48) | 0.7714 | 0.24883(90) | 0.07926(47) | 0.8466 |
| sh0 | 0.3294(11) | 0.08816(86) | 0.8914 | 0.3333(11) | 0.08871(85) | 0.9314 |
| sh1 | 0.3919(11) | 0.09311(83) | 0.9179 | 0.3955(11) | 0.09381(84) | 0.9530 |
| sh2 | 0.4494(10) | 0.09678(84) | 0.9083 | 0.4528(11) | 0.09766(90) | 0.9559 |
| sh3 | 0.5033(10) | 0.09930(84) | 0.9123 | 0.5063(11) | 0.09997(86) | 0.9319 |
| sh4 | 0.5545(10) | 0.10099(84) | 0.8906 | 0.5573(10) | 0.10167(82) | 0.8719 |
| sh5 | 0.6033(10) | 0.10200(84) | 0.8382 | 0.6059(10) | 0.10269(82) | 0.8245 |
| sh6 | 0.6491(13) | 0.1019(10) | 0.8190 | 0.6518(12) | 0.10272(97) | 0.8216 |
| sh7 | 0.6931(13) | 0.10114(92) | 0.8668 | 0.6962(13) | 0.10248(98) | 0.7454 |
| sh8 | 0.7357(13) | 0.10037(93) | 0.7866 | 0.7387(13) | 0.1016(10) | 0.6989 |
| sh9 | 0.7768(15) | 0.0996(11) | 0.6151 | 0.7793(14) | 0.1004(10) | 0.6358 |
| sh10 | 0.8151(15) | 0.0973(10) | 0.6496 | 0.8181(15) | 0.0984(11) | 0.5990 |

Table B.2: Fit results for strange-strange and strange-heavy pseudoscalar masses and decay constants in lattice units for the ensembles $\beta = 4.66$.

| tag | $am$ | $af$ | $\chi^2$/d.o.f. | $am$ | $af$ | $\chi^2$/d.o.f. |
|---|---|---|---|---|---|---|
| | $am_s = 0.018$ | | | $am_s = 0.020$ | | |
| ss | 0.1773(10) | 0.05630(37) | 0.9652 | 0.1872(10) | 0.05739(36) | 0.8819 |
| sh0 | 0.28568(95) | 0.06578(66) | 0.7877 | 0.28925(85) | 0.06647(60) | 0.6169 |
| sh1 | 0.35566(88) | 0.06991(68) | 0.5133 | 0.35889(79) | 0.07058(60) | 0.4933 |
| sh2 | 0.41960(90) | 0.07189(70) | 0.4931 | 0.42283(84) | 0.07277(66) | 0.4966 |
| sh3 | 0.47922(98) | 0.07256(76) | 0.4981 | 0.48239(90) | 0.07352(70) | 0.5273 |
| sh4 | 0.53492(93) | 0.07213(78) | 0.7555 | 0.53775(89) | 0.07311(74) | 0.7476 |
| sh5 | 0.58831(97) | 0.07138(80) | 0.7290 | 0.59103(92) | 0.07241(76) | 0.7275 |
| sh6 | 0.6391(10) | 0.07023(81) | 0.7054 | 0.6419(10) | 0.07130(80) | 0.7394 |
| sh7 | 0.6872(10) | 0.06876(83) | 0.6944 | 0.6899(10) | 0.06962(82) | 0.7975 |
| sh8 | 0.73280(96) | 0.06700(65) | 0.7404 | 0.7352(10) | 0.06809(85) | 0.6866 |

Table B.3: Fit results for strange-strange and strange-heavy pseudoscalar masses and decay constants in lattice units for the ensembles $\beta = 4.89$.

| tag | $am$ | $af$ | $\chi^2$/d.o.f. | $am$ | $af$ | $\chi^2$/d.o.f. |
|---|---|---|---|---|---|---|
| | $am_s = 0.0118$ | | | $am_s = 0.0133$ | | |
| ss | 0.1214(10) | 0.03785(60) | 0.0600 | 0.12879(99) | 0.03869(60) | 0.0562 |
| sh0 | 0.18333(99) | 0.04361(82) | 0.0018 | 0.18474(97) | 0.04382(81) | 0.0016 |
| sh1 | 0.2549(10) | 0.04765(80) | 0.0039 | 0.2562(10) | 0.04790(79) | 0.0046 |
| sh2 | 0.3190(10) | 0.04947(75) | 0.0049 | 0.3201(10) | 0.04974(75) | 0.0056 |
| sh3 | 0.3782(11) | 0.04994(82) | 0.0027 | 0.3792(11) | 0.05020(82) | 0.0032 |
| sh4 | 0.4340(12) | 0.04985(82) | 0.0036 | 0.4351(12) | 0.05011(82) | 0.0045 |
| sh5 | 0.4869(13) | 0.04930(84) | 0.0052 | 0.4879(13) | 0.04956(83) | 0.0067 |
| sh6 | 0.5371(14) | 0.04845(86) | 0.0079 | 0.5381(14) | 0.04871(86) | 0.0101 |

Table B.4: Fit results for strange-strange and strange-heavy pseudoscalar masses and decay constants in lattice units for the ensembles $\beta = 5.20$.

| **n** | $(0,0,0)$ | $(1,0,0)$ | $(1,1,0)$ | $(1,1,1)$ | $(0,0,0)$ | $(1,0,0)$ | $(1,1,0)$ | $(1,1,1)$ |
|---|---|---|---|---|---|---|---|---|
| | $am_s = 0.034$ | | | | $am_s = 0.036$ | | | |
| ss | 0.3321(19) | - | - | - | 0.3415(18) | - | - | - |
| sh0 | 0.4699(15) | 0.619(12) | 0.755(16) | 0.725(68) | 0.4735(14) | 0.621(12) | 0.757(15) | 0.729(65) |
| sh1 | 0.5591(14) | 0.686(10) | 0.800(14) | 0.793(39) | 0.5624(14) | 0.689(10) | 0.801(13) | 0.796(38) |
| sh2 | 0.6410(14) | 0.750(10) | 0.852(12) | 0.853(32) | 0.6440(14) | 0.7528(98) | 0.854(11) | 0.856(31) |
| sh3 | 0.7174(14) | 0.8143(89) | 0.904(10) | 0.917(25) | 0.7203(14) | 0.8166(87) | 0.906(10) | 0.920(24) |
| sh4 | 0.7894(14) | 0.8763(82) | 0.9566(94) | 0.977(21) | 0.7922(13) | 0.8787(80) | 0.9588(92) | 0.980(20) |
| sh5 | 0.8572(14) | 0.9367(78) | 1.0049(90) | 1.033(18) | 0.8599(14) | 0.9389(77) | 1.0072(87) | 1.035(18) |
| sh6 | 0.9209(14) | 0.9935(76) | 1.0561(84) | 1.086(17) | 0.9235(14) | 0.9957(75) | 1.0584(81) | 1.088(16) |

Table B.5: Fit results for the energy of strange-strange and strange-heavy pseudoscalar mesons in lattice units as a function of the momentum for the ensemble $\beta = 4.41$.

| **n** | $(0,0,0)$ | $(1,0,0)$ | $(1,1,0)$ | $(1,1,1)$ | $(0,0,0)$ | $(1,0,0)$ | $(1,1,0)$ | $(1,1,1)$ |
|---|---|---|---|---|---|---|---|---|
| | $am_s = 0.024$ | | | | $am_s = 0.026$ | | | |
| ss | 0.23749(89) | - | - | - | 0.24723(86) | - | - | - |
| sh0 | 0.32942(73) | 0.419(16) | 0.477(19) | 0.583(26) | 0.33328(71) | 0.422(15) | 0.480(19) | 0.585(25) |
| sh1 | 0.39143(72) | 0.473(12) | 0.529(14) | 0.615(32) | 0.39492(71) | 0.476(12) | 0.532(13) | 0.617(31) |
| sh2 | 0.44837(73) | 0.524(11) | 0.577(13) | 0.650(42) | 0.45163(72) | 0.527(10) | 0.579(12) | 0.652(40) |
| sh3 | 0.50185(74) | 0.572(10) | 0.620(10) | 0.668(48) | 0.50496(72) | 0.5744(98) | 0.621(10) | 0.672(46) |
| sh4 | 0.55252(76) | 0.6178(96) | 0.6603(94) | 0.699(40) | 0.55552(74) | 0.6206(93) | 0.6629(89) | 0.702(38) |
| sh5 | 0.60091(78) | 0.6623(91) | 0.7010(85) | 0.724(39) | 0.60382(76) | 0.6651(88) | 0.7036(81) | 0.727(37) |
| sh6 | 0.64723(81) | 0.7054(87) | 0.7407(78) | 0.757(33) | 0.65007(78) | 0.7081(84) | 0.7433(74) | 0.761(32) |
| sh7 | 0.69161(83) | 0.7468(84) | 0.7792(73) | 0.790(29) | 0.69440(80) | 0.7495(82) | 0.7819(69) | 0.794(28) |
| sh8 | 0.73410(87) | 0.7868(82) | 0.8166(69) | 0.823(26) | 0.73685(84) | 0.7895(80) | 0.8192(65) | 0.827(25) |
| sh9 | 0.77473(90) | 0.8264(84) | 0.8526(66) | 0.856(24) | 0.77744(86) | 0.8291(81) | 0.8553(62) | 0.859(23) |
| sh10 | 0.81346(93) | 0.8632(83) | 0.8873(63) | 0.881(24) | 0.81614(89) | 0.8659(80) | 0.8899(60) | 0.885(23) |

Table B.6: Fit results for the energy of strange-strange and strange-heavy pseudoscalar mesons in lattice units as a function of the momentum for the ensemble $\beta = 4.66$.

| **n** | $(0,0,0)$ | $(1,0,0)$ | $(1,1,0)$ | $(1,1,1)$ | $(0,0,0)$ | $(1,0,0)$ | $(1,1,0)$ | $(1,1,1)$ |
|---|---|---|---|---|---|---|---|---|
| | $am_s = 0.018$ | | | | $am_s = 0.020$ | | | |
| ss | 0.17758(75) | - | - | - | 0.18735(73) | - | - | - |
| sh0 | 0.28700(56) | 0.350(10) | 0.4032(50) | 0.430(23) | 0.29061(54) | 0.3529(97) | 0.4058(48) | 0.432(22) |
| sh1 | 0.35690(58) | 0.4085(78) | 0.4562(36) | 0.480(16) | 0.36016(56) | 0.4110(74) | 0.4588(34) | 0.483(15) |
| sh2 | 0.42074(60) | 0.4653(66) | 0.5063(35) | 0.530(13) | 0.42380(58) | 0.4678(63) | 0.5089(33) | 0.533(12) |
| sh3 | 0.48047(61) | 0.5186(63) | 0.5542(36) | 0.579(11) | 0.48339(58) | 0.5211(60) | 0.5567(34) | 0.582(11) |
| sh4 | 0.53680(65) | 0.5717(59) | 0.6029(32) | 0.6257(90) | 0.53964(62) | 0.5742(56) | 0.6054(31) | 0.6285(87) |
| sh5 | 0.59020(67) | 0.6222(57) | 0.6502(30) | 0.6727(84) | 0.59298(64) | 0.6247(54) | 0.6527(28) | 0.6755(81) |
| sh6 | 0.64086(69) | 0.6697(58) | 0.6958(28) | 0.7180(80) | 0.64359(66) | 0.6722(55) | 0.6983(26) | 0.7208(77) |
| sh7 | 0.68882(72) | 0.7161(55) | 0.7398(26) | 0.7620(84) | 0.69150(68) | 0.7186(53) | 0.7423(24) | 0.7648(80) |
| sh8 | 0.73401(74) | 0.7598(56) | 0.7814(25) | 0.8031(83) | 0.73667(70) | 0.7623(53) | 0.7840(23) | 0.8059(79) |

Table B.7: Fit results for the energy of strange-strange and strange-heavy pseudoscalar mesons in lattice units as a function of the momentum for the ensemble $\beta = 4.89$.

| **n** | $(0,0,0)$ | $(1,0,0)$ | $(1,1,0)$ | $(1,1,1)$ | $(0,0,0)$ | $(1,0,0)$ | $(1,1,0)$ | $(1,1,1)$ |
|---|---|---|---|---|---|---|---|---|
| | $am_s = 0.011$ | | | | $am_s = 0.013$ | | | |
| ss | 0.1143(13) | - | - | - | 0.1246(11) | - | - | - |
| sh0 | 0.17940(63) | 0.246(13) | 0.2454(78) | 0.269(16) | 0.18322(60) | 0.248(12) | 0.2495(74) | 0.272(15) |
| sh1 | 0.25110(52) | 0.302(12) | 0.3035(51) | 0.327(14) | 0.25441(49) | 0.304(11) | 0.3074(47) | 0.330(13) |
| sh2 | 0.31470(52) | 0.358(11) | 0.3590(43) | 0.374(13) | 0.31778(49) | 0.360(10) | 0.3625(40) | 0.377(12) |
| sh3 | 0.37356(56) | 0.412(11) | 0.4116(38) | 0.430(13) | 0.37651(52) | 0.414(10) | 0.4148(34) | 0.433(12) |
| sh4 | 0.42894(61) | 0.465(11) | 0.4625(36) | 0.477(11) | 0.43180(58) | 0.466(10) | 0.4656(32) | 0.481(11) |
| sh5 | 0.48138(67) | 0.516(10) | 0.5114(35) | 0.524(10) | 0.48419(62) | 0.517(10) | 0.5143(31) | 0.527(10) |
| sh6 | 0.53114(72) | 0.564(11) | 0.5582(34) | 0.5689(99) | 0.53390(67) | 0.566(10) | 0.5611(30) | 0.5723(95) |

Table B.8: Fit results for the energy of strange-strange and strange-heavy pseudoscalar mesons in lattice units as a function of the momentum for the ensemble $\beta = 5.20$.

# Appendix C

# Correlator Fit Results from the $D$ and $D_s$ Decay Constant Study

| ens | $am_\pi$ | $m_\pi$ [MeV] |
|---|---|---|
| C0 | 0.08046(11) | 139.15(36) |
| C1 | 0.19038(42) | 339.789(12) |
| C2 | 0.24129(41) | 430.648(14) |
| M0 | 0.059080(78) | 139.35(46) |
| M1 | 0.12724(36) | 303.248(14) |
| M2 | 0.15159(41) | 361.281(16) |
| F1 | 0.08446(18) | 234.297(10) |

Table C.1: Fit results for the mass of the pions on all ensembles used.

| ens | $am_D$ | $af_D^{\text{bare}}$ | $m_D$ [GeV] | $f_D^{\text{ren}}$ [GeV] |
|---|---|---|---|---|
| C0 | 0.82242(82) | 0.16211(85) | 1.4224(33) | 0.1996(11) |
| | 0.8995(10) | 0.1643(11) | 1.5558(37) | 0.2023(14) |
| | 0.9727(12) | 0.1654(13) | 1.6823(41) | 0.2036(17) |
| C1 | 0.83111(95) | 0.1687(10) | 1.4834(44) | 0.2114(14) |
| | 0.9075(11) | 0.1710(12) | 1.6198(49) | 0.2142(16) |
| | 0.9802(11) | 0.1722(12) | 1.7495(52) | 0.2157(16) |
| C2 | 0.84129(65) | 0.17468(62) | 1.5015(43) | 0.21883(99) |
| | 0.91722(77) | 0.17679(80) | 1.6370(47) | 0.2215(12) |
| | 0.98995(85) | 0.17851(86) | 1.7669(51) | 0.2236(12) |
| M0 | 0.63066(95) | 0.1146(11) | 1.4875(51) | 0.2010(21) |
| | 0.7259(13) | 0.1159(17) | 1.7122(61) | 0.2032(31) |
| | 0.8146(18) | 0.1162(25) | 1.9214(72) | 0.2037(44) |
| | 0.8975(22) | 0.1156(28) | 2.1168(81) | 0.2027(50) |
| M1 | 0.63804(77) | 0.12168(65) | 1.5206(57) | 0.2145(14) |
| | 0.73315(92) | 0.12345(80) | 1.7473(66) | 0.2176(16) |
| | 0.8211(12) | 0.1235(11) | 1.9570(75) | 0.2178(20) |
| | 0.9027(14) | 0.1221(14) | 2.1513(83) | 0.2152(25) |
| M2 | 0.64237(80) | 0.12424(73) | 1.5310(57) | 0.2190(15) |
| | 0.73731(98) | 0.12603(97) | 1.7572(66) | 0.2221(19) |
| | 0.8252(12) | 0.1261(13) | 1.9668(76) | 0.2223(24) |
| | 0.9068(16) | 0.1247(17) | 2.1611(85) | 0.2197(32) |
| F1 | 0.53696(70) | 0.09913(79) | 1.4895(57) | 0.2093(18) |
| | 0.61936(88) | 0.1006(10) | 1.7181(67) | 0.2125(23) |
| | 0.6960(11) | 0.1010(13) | 1.9307(77) | 0.2133(29) |
| | 0.7682(12) | 0.1010(13) | 2.1309(85) | 0.2132(29) |
| | 0.8612(16) | 0.0991(18) | 2.3889(98) | 0.2092(38) |

Table C.2: Fit results for the masses and decay constants of the $D$ meson on all ensembles. The second set of columns is renormalised where the renormalisation constants are obtained from the light-light conserved current as described in the text.

| ens | $am_{D_s}$ | $af_{D_s}^{\text{bare}}$ | $m_{D_s}$ [GeV] | $f_{D_s}^{\text{ren}}$ [GeV] |
|---|---|---|---|---|
| C0 | 0.88227(13) | 0.18809(17) | 1.5249(37) | 0.23134(64) |
| | 0.95671(16) | 0.19073(22) | 1.6536(40) | 0.23458(67) |
| | 1.02773(18) | 0.19225(25) | 1.7765(42) | 0.23644(69) |
| C1 | 0.87662(43) | 0.18654(45) | 1.5646(49) | 0.23369(96) |
| | 0.95114(46) | 0.18923(53) | 1.6976(53) | 0.2371(10) |
| | 1.02215(51) | 0.19071(62) | 1.8243(56) | 0.2389(11) |
| C2 | 0.87804(42) | 0.18799(43) | 1.5671(49) | 0.23551(94) |
| | 0.95235(48) | 0.19040(56) | 1.6998(52) | 0.2385(11) |
| | 1.02309(56) | 0.19146(74) | 1.8260(56) | 0.2399(12) |
| M0 | 0.678132(88) | 0.135920(96) | 1.5946(56) | 0.23710(92) |
| | 0.77124(10) | 0.13829(13) | 1.8144(62) | 0.24118(96) |
| | 0.85813(13) | 0.13897(19) | 2.0195(68) | 0.2423(10) |
| | 0.93926(16) | 0.13817(24) | 2.2109(74) | 0.2408(11) |
| M1 | 0.67420(41) | 0.13560(46) | 1.6068(66) | 0.2390(13) |
| | 0.76723(47) | 0.13774(64) | 1.8285(73) | 0.2428(15) |
| | 0.85376(57) | 0.13800(86) | 2.0348(81) | 0.2433(18) |
| | 0.93420(71) | 0.1365(12) | 2.2265(88) | 0.2406(23) |
| M2 | 0.67472(41) | 0.13623(41) | 1.6081(66) | 0.2401(12) |
| | 0.76794(50) | 0.13866(56) | 1.8302(73) | 0.2444(14) |
| | 0.85470(84) | 0.1393(11) | 2.0370(83) | 0.2455(23) |
| | 0.93539(64) | 0.13812(74) | 2.2293(88) | 0.2435(17) |
| F1 | 0.57222(21) | 0.11343(20) | 1.5867(67) | 0.2394(12) |
| | 0.65271(24) | 0.11546(26) | 1.8100(75) | 0.2436(12) |
| | 0.72795(28) | 0.11611(34) | 2.0188(82) | 0.2450(13) |
| | 0.79862(33) | 0.11562(43) | 2.2148(89) | 0.2440(15) |
| | 0.89021(44) | 0.11320(61) | 2.4689(99) | 0.2388(17) |

Table C.3: Fit results for the masses and decay constants of the $D_s$ meson on all ensembles. The second set of columns is renormalised where the renormalisation constants are obtained from the light-light conserved current as described in the text. The results stated here are those for the strange quark mass closest to the physical one.

| ens | $am_{\eta_c}$ | $m_{\eta_c}$ [GeV] |
|---|---|---|
| C0 | 1.249409(56) | 2.1609(47) |
| | 1.375320(51) | 2.3786(51) |
| | 1.493579(48) | 2.5831(56) |
| C1 | 1.24641(20) | 2.2246(62) |
| | 1.37227(19) | 2.4492(68) |
| | 1.49059(17) | 2.6604(74) |
| C2 | 1.24701(20) | 2.2257(62) |
| | 1.37276(18) | 2.4501(68) |
| | 1.49102(16) | 2.6612(74) |
| M0 | 0.972488(49) | 2.2937(70) |
| | 1.135329(46) | 2.6778(81) |
| | 1.287084(43) | 3.0357(92) |
| | 1.428269(40) | 3.369(10) |
| M1 | 0.96975(18) | 2.3112(83) |
| | 1.13226(15) | 2.6985(97) |
| | 1.28347(13) | 3.059(11) |
| | 1.42374(12) | 3.393(12) |
| M2 | 0.97000(19) | 2.3118(83) |
| | 1.13246(18) | 2.6990(97) |
| | 1.28365(16) | 3.059(11) |
| | 1.42384(15) | 3.393(12) |
| F1 | 0.82322(10) | 2.2836(83) |
| | 0.965045(93) | 2.6770(98) |
| | 1.098129(86) | 3.046(11) |
| | 1.223360(80) | 3.394(12) |
| | 1.385711(74) | 3.844(14) |

Table C.4: Fit results for the masses of the connected part of the $\eta_c$ meson on all ensembles.

# Appendix D

# Global Fit Results for $f_{D_s}/f_D$, $\Phi_D$ and $\Phi_{D_s}$

| $H$ | $m_\pi^{\text{cut}}$ | $f_{D_s}/f_D$ | $C^0_{\text{CL}}$ | $C^1_{\text{CL}}$ | $C^0_\chi$ | $C^1_\chi$ | $C^0_h$ | $\chi^2$/dof | $p$ |
|---|---|---|---|---|---|---|---|---|---|
| $\eta_c$ | 450 | 1.1531(60) | 0.037(22) | - | -0.529(24) | - | -0.022(16) | 0.739 | 0.803 |
| $\eta_c$ | 450 | 1.1526(72) | 0.036(23) | - | -0.523(59) | -0.03(26) | -0.020(28) | 0.773 | 0.756 |
| $\eta_c$ | 450 | 1.157(11) | 0.019(44) | 0.10(21) | -0.527(25) | - | -0.048(56) | 0.762 | 0.769 |
| $\eta_c$ | 450 | 1.157(11) | 0.016(46) | 0.11(21) | -0.515(61) | -0.06(26) | -0.045(57) | 0.798 | 0.719 |
| $D_s$ | 450 | 1.1532(60) | 0.036(22) | - | -0.529(24) | - | -0.019(14) | 0.737 | 0.806 |
| $D_s$ | 450 | 1.1528(72) | 0.036(23) | - | -0.523(58) | -0.02(22) | -0.017(24) | 0.771 | 0.759 |
| $D_s$ | 450 | 1.158(11) | 0.018(44) | 0.08(17) | -0.527(25) | - | -0.041(47) | 0.760 | 0.772 |
| $D_s$ | 450 | 1.157(11) | 0.016(46) | 0.09(18) | -0.516(61) | -0.05(22) | -0.038(48) | 0.796 | 0.722 |
| $D$ | 450 | 1.1531(60) | 0.036(22) | - | -0.531(25) | - | -0.016(12) | 0.740 | 0.801 |
| $D$ | 450 | 1.1521(70) | 0.035(23) | - | -0.516(56) | -0.06(19) | -0.011(20) | 0.772 | 0.758 |
| $D$ | 450 | 1.156(11) | 0.023(43) | 0.06(15) | -0.530(25) | - | -0.031(40) | 0.769 | 0.762 |
| $D$ | 450 | 1.155(11) | 0.019(44) | 0.06(15) | -0.510(58) | -0.07(19) | -0.027(41) | 0.801 | 0.716 |
| $\eta_c$ | 400 | 1.1667(77) | 0.005(25) | - | -0.631(44) | - | -0.031(19) | 0.319 | 0.998 |
| $\eta_c$ | 400 | 1.1644(90) | 0.003(25) | - | -0.591(94) | -0.21(43) | -0.019(31) | 0.324 | 0.997 |
| $\eta_c$ | 400 | 1.171(12) | -0.015(51) | 0.11(23) | -0.628(45) | - | -0.056(57) | 0.324 | 0.997 |
| $\eta_c$ | 400 | 1.168(14) | -0.012(51) | 0.08(24) | -0.597(95) | -0.16(44) | -0.041(69) | 0.335 | 0.995 |
| $D_s$ | 400 | 1.1669(77) | 0.004(25) | - | -0.631(44) | - | -0.026(16) | 0.314 | 0.998 |
| $D_s$ | 400 | 1.1647(91) | 0.003(25) | - | -0.592(94) | -0.17(36) | -0.016(27) | 0.319 | 0.997 |
| $D_s$ | 400 | 1.171(12) | -0.015(50) | 0.09(19) | -0.628(45) | - | -0.047(48) | 0.320 | 0.997 |
| $D_s$ | 400 | 1.168(14) | -0.012(51) | 0.07(20) | -0.598(94) | -0.13(37) | -0.034(58) | 0.332 | 0.995 |
| $D$ | 400 | 1.1668(78) | 0.004(25) | - | -0.634(45) | - | -0.022(14) | 0.319 | 0.998 |
| $D$ | 400 | 1.1644(89) | 0.002(25) | - | -0.592(91) | -0.16(31) | -0.013(22) | 0.321 | 0.997 |
| $D$ | 400 | 1.171(12) | -0.014(48) | 0.07(16) | -0.631(46) | - | -0.040(42) | 0.325 | 0.997 |
| $D$ | 400 | 1.168(14) | -0.010(49) | 0.05(17) | -0.598(92) | -0.13(32) | -0.027(50) | 0.335 | 0.995 |
| $\eta_c$ | 350 | 1.1655(79) | 0.006(26) | - | -0.636(55) | - | -0.025(22) | 0.352 | 0.989 |
| $\eta_c$ | 350 | 1.1653(92) | 0.006(26) | - | -0.63(12) | -0.03(54) | -0.024(32) | 0.377 | 0.982 |
| $\eta_c$ | 350 | 1.168(13) | -0.005(53) | 0.06(25) | -0.635(55) | - | -0.039(65) | 0.373 | 0.982 |
| $\eta_c$ | 350 | 1.168(14) | -0.005(53) | 0.06(25) | -0.63(12) | -0.01(54) | -0.039(70) | 0.402 | 0.970 |
| $D_s$ | 350 | 1.1657(79) | 0.005(26) | - | -0.637(55) | - | -0.022(18) | 0.349 | 0.990 |
| $D_s$ | 350 | 1.1655(92) | 0.005(26) | - | -0.63(12) | -0.02(45) | -0.021(28) | 0.374 | 0.982 |
| $D_s$ | 350 | 1.168(13) | -0.004(53) | 0.04(21) | -0.635(55) | - | -0.032(55) | 0.371 | 0.983 |
| $D_s$ | 350 | 1.168(14) | -0.004(53) | 0.04(21) | -0.63(12) | -0.01(45) | -0.032(59) | 0.400 | 0.971 |
| $D$ | 350 | 1.1656(79) | 0.005(26) | - | -0.639(56) | - | -0.018(16) | 0.352 | 0.989 |
| $D$ | 350 | 1.1652(90) | 0.005(26) | - | -0.63(12) | -0.04(39) | -0.017(23) | 0.377 | 0.982 |
| $D$ | 350 | 1.168(13) | -0.003(52) | 0.03(18) | -0.638(56) | - | -0.027(47) | 0.375 | 0.982 |
| $D$ | 350 | 1.167(14) | -0.003(52) | 0.03(18) | -0.63(12) | -0.03(39) | -0.025(50) | 0.403 | 0.970 |

Table D.1: Fit results of the different versions of the global fit ansatz (6.10) for the observable $f_{D_s}/f_D$

| $H$ | $m_\pi^{\text{cut}}$ | $\Phi_D[\text{GeV}^{3/2}]$ | $C^0_{\text{CL}}$ | $C^1_{\text{CL}}$ | $C^0_\chi$ | $C^1_\chi$ | $C^0_h$ | $\chi^2$/dof |
|---|---|---|---|---|---|---|---|---|
| $\eta_c$ | 450 | 0.2885(32) | -0.010(10) | - | 0.203(13) | - | -0.3797(86) | 0.555 |
| $\eta_c$ | 450 | 0.2867(36) | -0.012(10) | - | 0.234(26) | -0.36(21) | -0.354(18) | 0.459 |
| $\eta_c$ | 450 | 0.2891(43) | -0.014(17) | 0.05(11) | 0.204(13) | - | -0.390(30) | 0.577 |
| $\eta_c$ | 450 | 0.2880(44) | -0.021(17) | 0.11(12) | 0.237(26) | -0.39(21) | -0.374(31) | 0.460 |
| $D_s$ | 450 | 0.2882(31) | -0.018(10) | - | 0.200(12) | - | -0.3061(70) | 0.540 |
| $D_s$ | 450 | 0.2866(34) | -0.020(10) | - | 0.228(23) | -0.29(16) | -0.285(15) | 0.447 |
| $D_s$ | 450 | 0.2883(41) | -0.019(16) | 0.009(91) | 0.201(12) | - | -0.308(24) | 0.565 |
| $D_s$ | 450 | 0.2874(42) | -0.025(16) | 0.056(94) | 0.230(24) | -0.31(17) | -0.296(25) | 0.460 |
| $D$ | 450 | 0.2884(30) | -0.0202(95) | - | 0.176(11) | - | -0.2717(59) | 0.578 |
| $D$ | 450 | 0.2868(32) | -0.0228(96) | - | 0.205(21) | -0.30(13) | -0.251(12) | 0.446 |
| $D$ | 450 | 0.2891(38) | -0.024(14) | 0.043(77) | 0.177(12) | - | -0.281(20) | 0.598 |
| $D$ | 450 | 0.2880(39) | -0.030(15) | 0.081(80) | 0.209(22) | -0.32(14) | -0.267(21) | 0.443 |
| $\eta_c$ | 400 | 0.2853(38) | -0.003(11) | - | 0.230(22) | - | -0.3747(97) | 0.300 |
| $\eta_c$ | 400 | 0.2841(43) | -0.005(11) | - | 0.255(40) | -0.32(33) | -0.356(22) | 0.255 |
| $\eta_c$ | 400 | 0.2876(48) | -0.017(18) | 0.17(13) | 0.233(23) | - | -0.409(32) | 0.269 |
| $\eta_c$ | 400 | 0.2861(55) | -0.015(19) | 0.14(14) | 0.254(40) | -0.28(34) | -0.386(44) | 0.237 |
| $D_s$ | 400 | 0.2851(37) | -0.011(11) | - | 0.227(22) | - | -0.3016(79) | 0.279 |
| $D_s$ | 400 | 0.2840(42) | -0.012(11) | - | 0.248(37) | -0.25(26) | -0.288(17) | 0.241 |
| $D_s$ | 400 | 0.2867(46) | -0.021(17) | 0.11(10) | 0.230(22) | - | -0.323(25) | 0.265 |
| $D_s$ | 400 | 0.2853(52) | -0.020(18) | 0.08(11) | 0.248(37) | -0.22(27) | -0.306(35) | 0.237 |
| $D$ | 400 | 0.2854(36) | -0.014(11) | - | 0.203(20) | - | -0.2670(66) | 0.316 |
| $D$ | 400 | 0.2840(39) | -0.015(11) | - | 0.230(34) | -0.30(22) | -0.250(14) | 0.232 |
| $D$ | 400 | 0.2875(43) | -0.026(16) | 0.135(87) | 0.207(21) | - | -0.294(22) | 0.271 |
| $D$ | 400 | 0.2857(48) | -0.025(16) | 0.103(92) | 0.229(34) | -0.26(22) | -0.273(29) | 0.209 |
| $\eta_c$ | 350 | 0.2855(39) | -0.005(12) | - | 0.235(25) | - | -0.372(11) | 0.348 |
| $\eta_c$ | 350 | 0.2835(43) | -0.006(12) | - | 0.281(48) | -0.56(40) | -0.346(22) | 0.238 |
| $\eta_c$ | 350 | 0.2878(50) | -0.018(19) | 0.17(14) | 0.239(25) | - | -0.407(35) | 0.312 |
| $\eta_c$ | 350 | 0.2856(55) | -0.017(19) | 0.14(14) | 0.281(48) | -0.53(40) | -0.378(43) | 0.209 |
| $D_s$ | 350 | 0.2852(38) | -0.013(11) | - | 0.232(24) | - | -0.2996(87) | 0.319 |
| $D_s$ | 350 | 0.2835(42) | -0.014(11) | - | 0.272(45) | -0.43(31) | -0.280(17) | 0.225 |
| $D_s$ | 350 | 0.2868(47) | -0.022(18) | 0.11(11) | 0.235(25) | - | -0.322(28) | 0.304 |
| $D_s$ | 350 | 0.2850(52) | -0.022(18) | 0.09(11) | 0.272(45) | -0.41(32) | -0.299(34) | 0.214 |
| $D$ | 350 | 0.2854(36) | -0.015(11) | - | 0.208(23) | - | -0.2639(73) | 0.352 |
| $D$ | 350 | 0.2836(39) | -0.017(11) | - | 0.252(40) | -0.45(25) | -0.244(14) | 0.209 |
| $D$ | 350 | 0.2876(44) | -0.028(17) | 0.134(93) | 0.213(23) | - | -0.292(24) | 0.300 |
| $D$ | 350 | 0.2855(48) | -0.028(17) | 0.111(93) | 0.253(40) | -0.42(26) | -0.268(28) | 0.169 |

Table D.2: Fit results of the different versions of the global fit ansatz (6.10) for the observable $\Phi_D$

| $H$ | $m_\pi^{\text{cut}}$ | $\Phi_{D_s}[\text{GeV}^{3/2}]$ | $C^0_{\text{CL}}$ | $C^1_{\text{CL}}$ | $C^0_\chi$ | $C^1_\chi$ | $C^0_h$ | $\chi^2$/dof |
|---|---|---|---|---|---|---|---|---|
| $\eta_c$ | 450 | 0.3449(21) | -0.0206(68) | - | 0.0655(92) | - | -0.4167(38) | 0.297 |
| $\eta_c$ | 450 | 0.3448(21) | -0.0206(69) | - | 0.066(16) | -0.01(14) | -0.4162(76) | 0.311 |
| $\eta_c$ | 450 | 0.3463(26) | -0.0286(98) | 0.114(65) | 0.0665(92) | - | -0.440(15) | 0.262 |
| $\eta_c$ | 450 | 0.3462(25) | -0.0287(100) | 0.115(66) | 0.068(16) | -0.02(14) | -0.440(16) | 0.274 |
| $D_s$ | 450 | 0.3444(18) | -0.0294(59) | - | 0.0622(80) | - | -0.3345(30) | 0.261 |
| $D_s$ | 450 | 0.3444(19) | -0.0294(60) | - | 0.064(14) | -0.02(10) | -0.3337(56) | 0.273 |
| $D_s$ | 450 | 0.3451(23) | -0.0334(87) | 0.051(50) | 0.0628(80) | - | -0.345(12) | 0.258 |
| $D_s$ | 450 | 0.3451(23) | -0.0336(88) | 0.052(50) | 0.065(14) | -0.02(10) | -0.344(12) | 0.270 |
| $D$ | 450 | 0.3448(20) | -0.0327(66) | - | 0.0364(88) | - | -0.2952(27) | 0.359 |
| $D$ | 450 | 0.3446(20) | -0.0331(67) | - | 0.044(13) | -0.086(91) | -0.2914(50) | 0.349 |
| $D$ | 450 | 0.3459(24) | -0.0388(91) | 0.073(45) | 0.0378(88) | - | -0.311(11) | 0.336 |
| $D$ | 450 | 0.3456(24) | -0.0394(92) | 0.074(45) | 0.045(13) | -0.089(91) | -0.307(10) | 0.323 |
| $\eta_c$ | 400 | 0.3442(22) | -0.0185(68) | - | 0.073(14) | - | -0.4175(40) | 0.278 |
| $\eta_c$ | 400 | 0.3442(22) | -0.0185(69) | - | 0.073(21) | 0.01(18) | -0.4179(77) | 0.293 |
| $\eta_c$ | 400 | 0.3457(26) | -0.027(10) | 0.122(70) | 0.075(14) | - | -0.442(16) | 0.235 |
| $\eta_c$ | 400 | 0.3459(27) | -0.028(10) | 0.127(71) | 0.072(21) | 0.05(18) | -0.445(18) | 0.246 |
| $D_s$ | 400 | 0.3438(19) | -0.0275(59) | - | 0.070(12) | - | -0.3348(32) | 0.243 |
| $D_s$ | 400 | 0.3438(19) | -0.0274(60) | - | 0.069(19) | 0.01(13) | -0.3353(57) | 0.256 |
| $D_s$ | 400 | 0.3446(24) | -0.0322(90) | 0.058(53) | 0.071(12) | - | -0.347(12) | 0.236 |
| $D_s$ | 400 | 0.3447(24) | -0.0324(90) | 0.062(54) | 0.069(19) | 0.03(13) | -0.348(14) | 0.248 |
| $D$ | 400 | 0.3442(21) | -0.0310(66) | - | 0.044(13) | - | -0.2951(28) | 0.358 |
| $D$ | 400 | 0.3440(21) | -0.0314(66) | - | 0.050(19) | -0.08(12) | -0.2920(51) | 0.359 |
| $D$ | 400 | 0.3455(25) | -0.0386(93) | 0.087(48) | 0.046(13) | - | -0.313(11) | 0.318 |
| $D$ | 400 | 0.3453(25) | -0.0382(92) | 0.080(47) | 0.049(19) | -0.05(12) | -0.309(12) | 0.328 |
| $\eta_c$ | 350 | 0.3444(22) | -0.0202(69) | - | 0.079(15) | - | -0.4152(42) | 0.268 |
| $\eta_c$ | 350 | 0.3445(22) | -0.0201(69) | - | 0.075(26) | 0.06(23) | -0.4167(72) | 0.284 |
| $\eta_c$ | 350 | 0.3458(27) | -0.028(10) | 0.113(72) | 0.080(15) | - | -0.438(17) | 0.224 |
| $\eta_c$ | 350 | 0.3461(27) | -0.029(10) | 0.119(68) | 0.073(26) | 0.09(22) | -0.442(16) | 0.232 |
| $D_s$ | 350 | 0.3440(19) | -0.0290(60) | - | 0.075(13) | - | -0.3331(34) | 0.227 |
| $D_s$ | 350 | 0.3441(19) | -0.0290(60) | - | 0.072(22) | 0.04(17) | -0.3344(54) | 0.240 |
| $D_s$ | 350 | 0.3447(24) | -0.0332(91) | 0.052(54) | 0.076(13) | - | -0.344(13) | 0.223 |
| $D_s$ | 350 | 0.3449(24) | -0.0334(90) | 0.056(52) | 0.071(22) | 0.06(16) | -0.346(12) | 0.234 |
| $D$ | 350 | 0.3445(21) | -0.0330(67) | - | 0.049(14) | - | -0.2924(30) | 0.326 |
| $D$ | 350 | 0.3444(21) | -0.0331(67) | - | 0.053(22) | -0.05(15) | -0.2911(48) | 0.346 |
| $D$ | 350 | 0.3456(25) | -0.0398(94) | 0.079(49) | 0.051(14) | - | -0.309(12) | 0.288 |
| $D$ | 350 | 0.3455(25) | -0.0397(93) | 0.077(46) | 0.052(22) | -0.02(15) | -0.308(11) | 0.309 |

Table D.3: Fit results of the different versions of the global fit ansatz (6.10) for the observable $\Phi_{D_s}$

# References


[1] Particle Data Group collaboration, K. A. Olive et al., *Review of Particle Physics*, *Chin. Phys.* **C38** (2014) 090001.

[2] CKMfitter Group collaboration, J. Charles, A. Hocker, H. Lacker, S. Laplace, F. R. Le Diberder, J. Malcles et al., *CP violation and the CKM matrix: Assessing the impact of the asymmetric B factories*, *Eur. Phys. J.* **C41** (2005) 1–131, [hep-ph/0406184].

[3] Particle Data Group collaboration, J. Beringer et al., *Review of Particle Physics (RPP)*, *Phys. Rev.* **D86** (2012) 010001.

[4] Particle Data Group collaboration, K. Nakamura et al., *Review of particle physics*, *J. Phys.* **G37** (2010) 075021.

[5] Particle Data Group collaboration, C. Amsler et al., *Review of Particle Physics*, *Phys. Lett.* **B667** (2008) 1–1340.

[6] Particle Data Group collaboration, W. M. Yao et al., *Review of Particle Physics*, *J. Phys.* **G33** (2006) 1–1232.

[7] Particle Data Group collaboration, S. Eidelman et al., *Review of particle physics. Particle Data Group*, *Phys. Lett.* **B592** (2004) 1–1109.

[8] S. Aoki et al., *Review of lattice results concerning low-energy particle physics*, 1607.00299.

[9] M. E. Peskin and D. V. Schroeder, *An Introduction to quantum field theory*. 1995.

[10] Y.-G. Cho, S. Hashimoto, A. Jüttner, T. Kaneko, M. Marinkovic, J.-I. Noaki et al., *Improved lattice fermion action for heavy quarks*, *JHEP* **05** (2015) 072, [1504.01630].

[11] RBC, UKQCD collaboration, P. Boyle, A. Jüttner, M. K. Marinkovic, F. Sanfilippo, M. Spraggs and J. T. Tsang, *An exploratory study of heavy domain wall fermions on the lattice*, *JHEP* **04** (2016) 037, [1602.04118].

[12] P. A. Boyle, L. Del Debbio, A. Jüttner, A. Khamseh, F. Sanfilippo and J. T. Tsang, *The decay constants* $\mathbf{f_D}$ *and* $\mathbf{f_{D_s}}$ *in the continuum limit of* $\mathbf{N_f = 2 + 1}$ *domain wall lattice QCD*, 1701.02644.

[13] J. T. Tsang, A. Jüttner, F. Sanfilippo, P. Boyle, M. Marinkovic, S. Hashimoto et al., *Charm physics with Moebius Domain Wall Fermions*, *PoS* **LATTICE2014** (2014) 379, [1501.00660].

[14] Y.-G. Cho, S. Hashimoto, J.-I. Noaki, T. Kaneko, A. Jüttner, J. Tsang et al., *Scaling study of an improved fermion action on quenched lattices*, *PoS* **LATTICE2014** (2014) 381, [1412.6206].

[15] A. Jüttner, L. Del Debbio, N. Garron, A. Khamseh, M. Marinkovic, F. Sanfilippo et al., *Charm physics with physical light and strange quarks using domain wall fermions*, *PoS* **LATTICE2014** (2015) 380, [1502.00845].

[16] P. Boyle, L. Del Debbio, A. Khamseh, A. Jüttner, F. Sanfilippo and J. T. Tsang, *Domain Wall Charm Physics with Physical Pion Masses: Decay Constants, Bag and* $\xi$ *Parameters*, *PoS* **LATTICE2015** (2015) 336, [1511.09328].

[17] P. Boyle, L. Del Debbio, A. Jttner, A. Khamseh, F. Sanfilippo, J. T. Tsang et al., *Charm Physics with Domain Wall Fermions and Physical Pion Masses*, 1611.06804.

[18] Fermilab Lattice, MILC collaboration, A. Bazavov et al., *Charmed and light pseudoscalar meson decay constants from four-flavor lattice QCD with physical light quarks*, *Phys. Rev.* **D90** (2014) 074509, [1407.3772].

[19] S. Weinberg, *The Quantum theory of fields. Vol. 1: Foundations*. Cambridge University Press, 2005.

[20] S. Weinberg, *The quantum theory of fields. Vol. 2: Modern applications*. Cambridge University Press, 2013.

[21] C. Gattringer and C. B. Lang, *Quantum chromodynamics on the lattice*, vol. 788. 2010. 10.1007/978-3-642-01850-3.

[22] L. Lellouch, R. Sommer, B. Svetitsky, A. Vladikas and L. F. Cugliandolo, eds., *Modern perspectives in lattice QCD: Quantum field theory and high performance computing. Proceedings, International School, 93rd Session, Les Houches, France, August 3-28, 2009*, 2011.

[23] T. DeGrand and C. E. Detar, *Lattice methods for quantum chromodynamics*. 2006.

[24] M. Creutz, *Quarks, gluons and lattices*. Cambridge Monographs on Mathematical Physics. Cambridge Univ. Press, Cambridge, UK, 1985.

[25] T. D. Lee and C.-N. Yang, *Question of Parity Conservation in Weak Interactions*, *Phys. Rev.* **104** (1956) 254–258.

[26] C. S. Wu, E. Ambler, R. W. Hayward, D. D. Hoppes and R. P. Hudson, *Experimental Test of Parity Conservation in Beta Decay*, *Phys. Rev.* **105** (1957) 1413–1414.

[27] J. H. Christenson, J. W. Cronin, V. L. Fitch and R. Turlay, *Evidence for the* $2\pi$ *Decay of the* $K_2^0$ *Meson*, *Phys. Rev. Lett.* **13** (1964) 138–140.

[28] J. Goldstone, A. Salam and S. Weinberg, *Broken Symmetries*, *Phys. Rev.* **127** (1962) 965–970.

[29] S. Weinberg, *A Model of Leptons*, *Phys. Rev. Lett.* **19** (1967) 1264–1266.

[30] S. L. Glashow, *Partial Symmetries of Weak Interactions*, *Nucl. Phys.* **22** (1961) 579–588.

[31] P. W. Higgs, *Broken symmetries, massless particles and gauge fields*, *Phys. Lett.* **12** (1964) 132–133.

[32] P. W. Higgs, *Broken Symmetries and the Masses of Gauge Bosons*, *Phys. Rev. Lett.* **13** (1964) 508–509.

[33] F. Englert and R. Brout, *Broken Symmetry and the Mass of Gauge Vector Mesons*, *Phys. Rev. Lett.* **13** (1964) 321–323.

[34] G. S. Guralnik, C. R. Hagen and T. W. B. Kibble, *Global Conservation Laws and Massless Particles*, *Phys. Rev. Lett.* **13** (1964) 585–587.

[35] N. Cabibbo, *Unitary Symmetry and Leptonic Decays*, *Phys. Rev. Lett.* **10** (1963) 531–533.

[36] M. Kobayashi and T. Maskawa, *CP Violation in the Renormalizable Theory of Weak Interaction*, *Prog. Theor. Phys.* **49** (1973) 652–657.

[37] H. Fritzsch, M. Gell-Mann and H. Leutwyler, *Advantages of the Color Octet Gluon Picture*, *Phys. Lett.* **B47** (1973) 365–368.

[38] ATLAS collaboration, G. Aad et al., *Observation of a new particle in the search for the Standard Model Higgs boson with the ATLAS detector at the LHC*, *Phys. Lett.* **B716** (2012) 1–29, [1207.7214].

[39] CMS collaboration, S. Chatrchyan et al., *Observation of a new boson at a mass of* 125 GeV *with the CMS experiment at the LHC*, *Phys. Lett.* **B716** (2012) 30–61, [1207.7235].

[40] Super-Kamiokande collaboration, Y. Fukuda et al., *Evidence for oscillation of atmospheric neutrinos*, *Phys. Rev. Lett.* **81** (1998) 1562–1567, [hep-ex/9807003].

[41] SNO collaboration, Q. R. Ahmad et al., *Direct evidence for neutrino flavor transformation from neutral current interactions in the Sudbury Neutrino Observatory*, *Phys. Rev. Lett.* **89** (2002) 011301, [nucl-ex/0204008].

[42] C.-N. Yang and R. L. Mills, *Conservation of Isotopic Spin and Isotopic Gauge Invariance*, *Phys. Rev.* **96** (1954) 191–195.

[43] C. A. Baker et al., *An Improved experimental limit on the electric dipole moment of the neutron*, *Phys. Rev. Lett.* **97** (2006) 131801, [hep-ex/0602020].

[44] H. D. Politzer, *Reliable Perturbative Results for Strong Interactions?*, *Phys. Rev. Lett.* **30** (1973) 1346–1349.

[45] D. J. Gross and F. Wilczek, *Ultraviolet Behavior of Nonabelian Gauge Theories*, *Phys. Rev. Lett.* **30** (1973) 1343–1346.

[46] K. G. Wilson, *Confinement of Quarks*, *Phys. Rev.* **D10** (1974) 2445–2459.

[47] M. Gell-Mann, *The Symmetry group of vector and axial vector currents*, *Physics* **1** (1964) 63–75.

[48] M. Gell-Mann, R. J. Oakes and B. Renner, *Behavior of current divergences under $SU(3) \times SU(3)$*, *Phys. Rev.* **175** (1968) 2195–2199.

[49] J. S. Bell and R. Jackiw, *A PCAC puzzle: $\pi^0 \to \gamma\gamma$ in the $\sigma$-model*, *Nuovo Cim.* **A60** (1969) 47–61.

[50] S. L. Adler, *Axial vector vertex in spinor electrodynamics*, *Phys. Rev.* **177** (1969) 2426–2438.

[51] M. Gell-Mann, "The Eightfold Way: A Theory of strong interaction symmetry." 1961.

[52] M. Gell-Mann, *Symmetries of baryons and mesons*, *Phys. Rev.* **125** (1962) 1067–1084.

[53] L.-L. Chau and W.-Y. Keung, *Comments on the Parametrization of the Kobayashi-Maskawa Matrix*, *Phys. Rev. Lett.* **53** (1984) 1802.

[54] L. Wolfenstein, *Parametrization of the Kobayashi-Maskawa Matrix*, *Phys. Rev. Lett.* **51** (1983) 1945.

[55] A. J. Buras, M. E. Lautenbacher and G. Ostermaier, *Waiting for the top quark mass, $K^+ \to \pi^+ \nu\overline{\nu}$, $B^0_{(s)} - \overline{B}^0_{(s)}$ mixing and CP asymmetries in B decays*, *Phys. Rev.* **D50** (1994) 3433–3446, [hep-ph/9403384].

[56] A. Hocker, H. Lacker, S. Laplace and F. Le Diberder, *A New approach to a global fit of the CKM matrix*, *Eur. Phys. J.* **C21** (2001) 225–259, [hep-ph/0104062].

[57] S. Aoki et al., *Review of lattice results concerning low-energy particle physics*, *Eur. Phys. J.* **C74** (2014) 2890, [1310.8555].

[58] I. I. Y. Bigi, Y. L. Dokshitzer, V. A. Khoze, J. H. Kuhn and P. M. Zerwas, *Production and Decay Properties of Ultraheavy Quarks*, *Phys. Lett.* **B181** (1986) 157–163.

[59] A. S. Kronfeld, *Heavy quarks and lattice QCD*, *Nucl. Phys. Proc. Suppl.* **129** (2004) 46–59, [hep-lat/0310063].

[60] N. Isgur and M. B. Wise, *Weak Decays of Heavy Mesons in the Static Quark Approximation*, *Phys. Lett.* **B232** (1989) 113–117.

[61] N. Isgur and M. B. Wise, *Weak transition form factors between heavy mesons*, *Phys. Lett.* **B237** (1990) 527–530.

[62] H. Georgi, *An Effective Field Theory for Heavy Quarks at Low-energies*, *Phys. Lett.* **B240** (1990) 447–450.

[63] E. Eichten, *Heavy Quarks on the Lattice*, *Nucl. Phys. Proc. Suppl.* **4** (1988) 170.

[64] E. Eichten and B. R. Hill, *An Effective Field Theory for the Calculation of Matrix Elements Involving Heavy Quarks*, *Phys. Lett.* **B234** (1990) 511–516.

[65] E. Eichten and B. R. Hill, *Renormalization of Heavy - Light Bilinears and F(B) for Wilson Fermions*, *Phys. Lett.* **B240** (1990) 193–199.

[66] E. Eichten and B. R. Hill, *Static effective field theory: $1/m$ corrections*, *Phys. Lett.* **B243** (1990) 427–431.

[67] ALPHA collaboration, J. Heitger, A. Jüttner, R. Sommer and J. Wennekers, *Non-perturbative tests of heavy quark effective theory*, *JHEP* **11** (2004) 048, [hep-ph/0407227].

[68] R. Sommer, *Introduction to Non-perturbative Heavy Quark Effective Theory*, in *Modern perspectives in lattice QCD: Quantum field theory and high performance computing. Proceedings, International School, 93rd Session, Les Houches, France, August 3-28, 2009*, pp. 517–590, 2010. 1008.0710.

[69] W. E. Caswell and G. P. Lepage, *Effective Lagrangians for Bound State Problems in QED, QCD, and Other Field Theories*, *Phys. Lett.* **B167** (1986) 437–442.

[70] S. L. Glashow, J. Iliopoulos and L. Maiani, *Weak Interactions with Lepton-Hadron Symmetry*, *Phys. Rev.* **D2** (1970) 1285–1292.

[71] M. A. Shifman, A. I. Vainshtein and V. I. Zakharov, *QCD and Resonance Physics: Applications*, *Nucl. Phys.* **B147** (1979) 448–518.

[72] V. A. Novikov, L. B. Okun, M. A. Shifman, A. I. Vainshtein, M. B. Voloshin and V. I. Zakharov, *Charmonium and Gluons: Basic Experimental Facts and Theoretical Introduction*, *Phys. Rept.* **41** (1978) 1–133.

[73] J. Gasser and H. Leutwyler, *Quark Masses*, *Phys. Rept.* **87** (1982) 77–169.

[74] L. J. Reinders, H. Rubinstein and S. Yazaki, *Hadron Properties from QCD Sum Rules*, *Phys. Rept.* **127** (1985) 1.

[75] J. M. Maldacena, *The Large N limit of superconformal field theories and supergravity*, *Int. J. Theor. Phys.* **38** (1999) 1113–1133, [hep-th/9711200].

[76] G. C. Wick, *Properties of Bethe-Salpeter Wave Functions*, *Phys. Rev.* **96** (1954) 1124–1134.

[77] K. G. Wilson and J. B. Kogut, *The Renormalization group and the epsilon expansion*, *Phys. Rept.* **12** (1974) 75–200.

[78] N. Metropolis, A. W. Rosenbluth, M. N. Rosenbluth, A. H. Teller and E. Teller, *Equation of state calculations by fast computing machines*, *J. Chem. Phys.* **21** (1953) 1087–1092.

[79] P. F. Bedaque, *Aharonov-Bohm effect and nucleon nucleon phase shifts on the lattice*, *Phys. Lett.* **B593** (2004) 82–88, [nucl-th/0402051].

[80] UKQCD collaboration, J. M. Flynn, A. Jüttner and C. T. Sachrajda, *A Numerical study of partially twisted boundary conditions*, *Phys. Lett.* **B632** (2006) 313–318, [hep-lat/0506016].

[81] G. Curci, P. Menotti and G. Paffuti, *Symanzik's Improved Lagrangian for Lattice Gauge Theory*, *Phys. Lett.* **B130** (1983) 205.

[82] M. Lüscher and P. Weisz, *On-Shell Improved Lattice Gauge Theories*, *Commun. Math. Phys.* **97** (1985) 59.

[83] Y. Iwasaki, "Renormalization group analysis of lattice theoreies and improved lattice action. 1. Two-dimensional nonlinear $O(N)$ sigma model." 1983.

[84] Y. Iwasaki, "Renormalization Group Analysis of Lattice Theories and Improved Lattice Action. II. Four-dimensional non-Abelian $SU(N)$ gauge model." 1983.

[85] Y. Iwasaki, *Renormalization Group Analysis of Lattice Theories and Improved Lattice Action: Two-Dimensional Nonlinear $O(N)$ Sigma Model*, *Nucl. Phys.* **B258** (1985) 141–156.

[86] H. B. Nielsen and M. Ninomiya, *No Go Theorem for Regularizing Chiral Fermions*, *Phys. Lett.* **B105** (1981) 219–223.

[87] D. B. Kaplan, *Chiral Symmetry and Lattice Fermions*, in *Modern perspectives in lattice QCD: Quantum field theory and high performance computing. Proceedings, International School, 93rd Session, Les Houches, France, August 3-28, 2009*, pp. 223–272, 2009. 0912.2560.

[88] J. B. Kogut and L. Susskind, *Hamiltonian Formulation of Wilson's Lattice Gauge Theories*, *Phys. Rev.* **D11** (1975) 395–408.

[89] M. Creutz, *Four-dimensional graphene and chiral fermions*, *JHEP* **04** (2008) 017, [0712.1201].

[90] P. T. Matthews and A. Salam, *The Green's functions of quantized fields*, *Nuovo Cim.* **12** (1954) 563–565.

[91] P. T. Matthews and A. Salam, *Propagators of quantized field*, *Nuovo Cim.* **2** (1955) 120–134.

[92] N. Cabibbo and E. Marinari, *A New Method for Updating $SU(N)$ Matrices in Computer Simulations of Gauge Theories*, *Phys. Lett.* **B119** (1982) 387–390.

[93] S. L. Adler, *An Overrelaxation Method for the Monte Carlo Evaluation of the Partition Function for Multiquadratic Actions*, *Phys. Rev.* **D23** (1981) 2901.

[94] M. Creutz, *Overrelaxation and Monte Carlo Simulation*, *Phys. Rev.* **D36** (1987) 515.

[95] A. D. Kennedy and B. J. Pendleton, *Improved Heat Bath Method for Monte Carlo Calculations in Lattice Gauge Theories*, *Phys. Lett.* **B156** (1985) 393–399.

[96] S. Duane, A. D. Kennedy, B. J. Pendleton and D. Roweth, *Hybrid Monte Carlo*, *Phys. Lett.* **B195** (1987) 216–222.

[97] F. Fucito, E. Marinari, G. Parisi and C. Rebbi, *A Proposal for Monte Carlo Simulations of Fermionic Systems*, *Nucl. Phys.* **B180** (1981) 369.

[98] ALPHA collaboration, S. Schaefer, R. Sommer and F. Virotta, *Critical slowing down and error analysis in lattice QCD simulations*, *Nucl. Phys.* **B845** (2011) 93–119, [1009.5228].

[99] R. Sommer, *A New way to set the energy scale in lattice gauge theories and its applications to the static force and alpha-s in $SU(2)$ Yang-Mills theory*, *Nucl. Phys.* **B411** (1994) 839–854, [hep-lat/9310022].

[100] M. Lüscher, *Properties and uses of the Wilson flow in lattice QCD*, *JHEP* **08** (2010) 071, [1006.4518].

[101] S. Borsanyi et al., *High-precision scale setting in lattice QCD*, *JHEP* **09** (2012) 010, [1203.4469].

[102] G. C. Wick, *The Evaluation of the Collision Matrix*, *Phys. Rev.* **80** (1950) 268–272.

[103] M. R. Hestenes and E. Stiefel, *Methods of Conjugate Gradients for Solving Linear Systems*, *Natl. Stand.* **49** (1952) 409–436.

[104] W. H. Press, S. A. Teukolsky, W. T. Vetterling and B. P. Flannery, *Numerical Recipes in C: The Art of Scientific Computing*. 1999.

[105] P. A. Boyle, *Hierarchically deflated conjugate gradient*, 1402.2585.

[106] A. Jüttner and M. Della Morte, *Heavy quark propagators with improved precision using domain decomposition*, *PoS* **LAT2005** (2006) 204, [hep-lat/0508023].

[107] G. Parisi and Y.-s. Wu, *Perturbation Theory Without Gauge Fixing*, *Sci. Sin.* **24** (1981) 483.

[108] G. P. Lepage, *The Analysis of Algorithms for Lattice Field Theory*, in *Boulder ASI 1989:97-120*, pp. 97–120, 1989.

[109] S. Gusken, U. Low, K. H. Mutter, R. Sommer, A. Patel and K. Schilling, *Nonsinglet Axial Vector Couplings of the Baryon Octet in Lattice QCD*, *Phys. Lett.* **B227** (1989) 266–269.

[110] P. A. Boyle, A. Jüttner, C. Kelly and R. D. Kenway, *Use of stochastic sources for the lattice determination of light quark physics*, *JHEP* **08** (2008) 086, [0804.1501].

[111] S.-J. Dong and K.-F. Liu, *Stochastic estimation with $Z_2$ noise*, *Phys. Lett.* **B328** (1994) 130–136, [hep-lat/9308015].

[112] UKQCD collaboration, M. Foster and C. Michael, *Quark mass dependence of hadron masses from lattice QCD*, *Phys. Rev.* **D59** (1999) 074503, [hep-lat/9810021].

[113] UKQCD collaboration, C. McNeile and C. Michael, *Decay width of light quark hybrid meson from the lattice*, *Phys. Rev.* **D73** (2006) 074506, [hep-lat/0603007].

[114] L. Giusti, P. Hernandez, M. Laine, P. Weisz and H. Wittig, *Low-energy couplings of QCD from current correlators near the chiral limit*, *JHEP* **04** (2004) 013, [hep-lat/0402002].

[115] T. A. DeGrand and S. Schaefer, *Improving meson two point functions in lattice QCD*, *Comput. Phys. Commun.* **159** (2004) 185–191, [hep-lat/0401011].

[116] T. Blum, T. Izubuchi and E. Shintani, *New class of variance-reduction techniques using lattice symmetries*, *Phys. Rev.* **D88** (2013) 094503, [1208.4349].

[117] T. Blum, T. Izubuchi and E. Shintani, *Error reduction technique using covariant approximation and application to nucleon form factor*, *PoS* **LATTICE2012** (2012) 262, [1212.5542].

[118] E. Shintani, R. Arthur, T. Blum, T. Izubuchi, C. Jung and C. Lehner, *Covariant approximation averaging*, *Phys. Rev.* **D91** (2015) 114511, [1402.0244].

[119] A. S. Gambhir, A. Stathopoulos and K. Orginos, *Deflation as a Method of Variance Reduction for Estimating the Trace of a Matrix Inverse*, 1603.05988.

[120] Hadron Spectrum collaboration, M. Peardon, J. Bulava, J. Foley, C. Morningstar, J. Dudek, R. G. Edwards et al., *A Novel quark-field creation operator construction for hadronic physics in lattice QCD*, *Phys. Rev.* **D80** (2009) 054506, [0905.2160].

[121] B. Efron, *Bootstrap methods: Another look at the jackknife*, *The Annals of Statistics* **7** (1979) 1–26.

[122] B. Efron, *Computers and the theory of statistics: thinking the unthinkable*, *SIAM Rev.* **21** (1979) 460–480.

[123] ALPHA collaboration, U. Wolff, *Monte Carlo errors with less errors*, *Comput. Phys. Commun.* **156** (2004) 143–153, [hep-lat/0306017].

[124] M. Lüscher, *Volume Dependence of the Energy Spectrum in Massive Quantum Field Theories. 1. Stable Particle States*, *Commun. Math. Phys.* **104** (1986) 177.

[125] G. Colangelo, S. Dürr and C. Haefeli, *Finite volume effects for meson masses and decay constants*, *Nucl. Phys.* **B721** (2005) 136–174, [hep-lat/0503014].

[126] K. Symanzik, *Continuum Limit and Improved Action in Lattice Theories. 1. Principles and $\phi^4$ Theory*, *Nucl. Phys.* **B226** (1983) 187–204.

[127] K. Symanzik, *Continuum Limit and Improved Action in Lattice Theories. 2. $O(N)$ Nonlinear Sigma Model in Perturbation Theory*, *Nucl. Phys.* **B226** (1983) 205–227.

[128] D. B. Kaplan, *A Method for simulating chiral fermions on the lattice*, *Phys. Lett.* **B288** (1992) 342–347, [hep-lat/9206013].

[129] Y. Shamir, *Chiral fermions from lattice boundaries*, *Nucl. Phys.* **B406** (1993) 90–106, [hep-lat/9303005].

[130] Y. Shamir, *Constraints on the existence of chiral fermions in interacting lattice theories*, *Phys. Rev. Lett.* **71** (1993) 2691–2694, [hep-lat/9306023].

[131] V. Furman and Y. Shamir, *Axial symmetries in lattice QCD with Kaplan fermions*, *Nucl. Phys.* **B439** (1995) 54–78, [hep-lat/9405004].

[132] Y. Shamir, *Anomalies and chiral defects fermions*, *Nucl. Phys.* **B417** (1994) 167–180, [hep-lat/9310006].

[133] P. M. Vranas, *Chiral symmetry restoration in the Schwinger model with domain wall fermions*, *Phys. Rev.* **D57** (1998) 1415–1432, [hep-lat/9705023].

[134] S. R. Sharpe, *Future of Chiral Extrapolations with Domain Wall Fermions*, in *Workshop on Domain Wall Fermions at Ten Years Upton, New York, March 15-17, 2007*, 2007. 0706.0218.

[135] UKQCD collaboration, P. A. Boyle, *Conserved currents for Mobius Domain Wall Fermions*, *PoS* **LATTICE2014** (2015) 087, [1411.5728].

[136] P. H. Ginsparg and K. G. Wilson, *A Remnant of Chiral Symmetry on the Lattice*, *Phys. Rev.* **D25** (1982) 2649.

[137] H. Neuberger, *Exactly massless quarks on the lattice*, *Phys. Lett.* **B417** (1998) 141–144, [hep-lat/9707022].

[138] H. Neuberger, *More about exactly massless quarks on the lattice*, *Phys. Lett.* **B427** (1998) 353–355, [hep-lat/9801031].

[139] A. Borici, *Truncated overlap fermions: The Link between overlap and domain wall fermions*, in *Lattice fermions and structure of the vacuum. Proceedings, NATO Advanced Research Workshop, Dubna, Russia, October 5-9, 1999*, pp. 41–52, 1999. hep-lat/9912040.

[140] A. D. Kennedy, *Algorithms for dynamical fermions*, hep-lat/0607038.

[141] R. C. Brower, H. Neff and K. Orginos, *Möbius fermions: Improved domain wall chiral fermions*, *Nucl. Phys. Proc. Suppl.* **140** (2005) 686–688, [hep-lat/0409118].

[142] R. C. Brower, H. Neff and K. Orginos, *Möbius fermions*, *Nucl. Phys. Proc. Suppl.* **153** (2006) 191–198, [hep-lat/0511031].

[143] R. C. Brower, H. Neff and K. Orginos, *The Möbius Domain Wall Fermion Algorithm*, 1206.5214.

[144] RBC, UKQCD collaboration, T. Blum et al., *Domain wall QCD with physical quark masses*, *Phys. Rev.* **D93** (2016) 074505, [1411.7017].

[145] A. X. El-Khadra, A. S. Kronfeld and P. B. Mackenzie, *Massive fermions in lattice gauge theory*, *Phys. Rev.* **D55** (1997) 3933–3957, [hep-lat/9604004].

[146] S. Aoki, Y. Kuramashi and S.-i. Tominaga, *Relativistic heavy quarks on the lattice*, *Prog. Theor. Phys.* **109** (2003) 383–413, [hep-lat/0107009].

[147] N. H. Christ, M. Li and H.-W. Lin, *Relativistic Heavy Quark Effective Action*, *Phys. Rev.* **D76** (2007) 074505, [hep-lat/0608006].

[148] L. Del Debbio, G. M. Manca and E. Vicari, *Critical slowing down of topological modes*, *Phys. Lett.* **B594** (2004) 315–323, [hep-lat/0403001].

[149] J. Flynn, A. Jüttner, A. Lawson and F. Sanfilippo, *Precision study of critical slowing down in lattice simulations of the $CP^{N-1}$ model*, 1504.06292.

[150] CLEO collaboration, M. Artuso et al., *Improved measurement of $B(D^+ \to \mu^+\nu)$ and the pseudoscalar decay constant $f_{D^+}$*, *Phys. Rev. Lett.* **95** (2005) 251801, [hep-ex/0508057].

[151] CLEO collaboration, M. Artuso et al., *Measurement of the decay constant $f(D_s^+)$ using $D_s^+ \to \ell^+\nu$*, *Phys. Rev. Lett.* **99** (2007) 071802, [0704.0629].

[152] CLEO collaboration, P. Naik et al., *Measurement of the Pseudoscalar Decay Constant $f_{D_s}$ Using $D_s^+ \to \tau^+\nu$, $\tau^+ \to \rho^+\overline{\nu}$ Decays*, *Phys. Rev.* **D80** (2009) 112004, [0910.3602].

[153] CLEO collaboration, K. M. Ecklund et al., *Measurement of the absolute branching fraction of $D_s^+ \to \tau^+\nu_\tau$ decay*, *Phys. Rev. Lett.* **100** (2008) 161801, [0712.1175].

[154] BESIII collaboration, G. Huang, *Recent Results from BESIII*, in *Proceedings, 10th Conference on Flavor Physics and CP Violation (FPCP 2012)*, 2012. 1209.4813.

[155] Belle collaboration, A. Zupanc et al., *Measurements of branching fractions of leptonic and hadronic $D_s^+$ meson decays and extraction of the $D_s^+$ meson decay constant*, *JHEP* **09** (2013) 139, [1307.6240].

[156] BaBar collaboration, J. P. Lees et al., *Measurement of the Branching Fraction for $D_s^+ \to \tau^+\nu_\tau$ and Extraction of the Decay Constant $f_{D_s}$*, 1003.3063.

[157] ETM collaboration, B. Blossier et al., *A Proposal for B-physics on current lattices*, *JHEP* **04** (2010) 049, [0909.3187].

[158] ETM collaboration, N. Carrasco et al., *B-physics from $N_f = 2$ tmQCD: the Standard Model and beyond*, *JHEP* **03** (2014) 016, [1308.1851].

[159] SciDAC, LHPC, UKQCD collaboration, R. G. Edwards and B. Joo, *The Chroma software system for lattice QCD*, *Nucl. Phys. Proc. Suppl.* **140** (2005) 832, [hep-lat/0409003].

[160] F. Sanfilippo. https://github.com/sunpho84/nissa.

[161] R. Hudspith. https://github.com/RJhudspith/GLU.

[162] C. T. H. Davies, C. McNeile, E. Follana, G. P. Lepage, H. Na and J. Shigemitsu, *Update: Precision $D_s$ decay constant from full lattice QCD using very fine lattices*, *Phys. Rev.* **D82** (2010) 114504, [1008.4018].

[163] G. Liu, *Quark Eigenmodes and Lattice QCD*. PhD thesis, Columbia University, NYC, 2003.

[164] K. Jansen and M. Schmaltz, *Critical momenta of lattice chiral fermions*, *Phys. Lett.* **B296** (1992) 374–378, [hep-lat/9209002].

[165] C. Best, M. Gockeler, R. Horsley, E.-M. Ilgenfritz, H. Perlt, P. E. L. Rakow et al., *$\pi$ and $\rho$ structure functions from lattice QCD*, *Phys. Rev.* **D56** (1997) 2743–2754, [hep-lat/9703014].

[166] HPQCD collaboration, C. T. H. Davies, E. Follana, I. D. Kendall, G. P. Lepage and C. McNeile, *Precise determination of the lattice spacing in full lattice QCD*, *Phys. Rev.* **D81** (2010) 034506, [0910.1229].

[167] N. H. Christ, X. Feng, A. Jüttner, A. Lawson, A. Portelli and C. T. Sachrajda, *First exploratory calculation of the long-distance contributions to the rare kaon decays $K \to \pi\ell^+\ell^-$*, 1608.07585.

[168] J. L. Rosner, S. Stone and R. S. Van de Water, *Leptonic Decays of Charged Pseudoscalar Mesons - 2015*, *Submitted to: Particle Data Book* (2015) , [1509.02220].

[169] CLEO collaboration, M. Artuso et al., *Improved measurement of $B(D^+ \to \mu^+\nu)$ and the pseudoscalar decay constant $f_{D^+}$*, *Phys. Rev. Lett.* **95** (2005) 251801, [hep-ex/0508057].

[170] CLEO collaboration, M. Artuso et al., *Measurement of the decay constant $f(D_S^+)$ using $D_S^+ \to \ell^+\nu$*, *Phys. Rev. Lett.* **99** (2007) 071802, [0704.0629].

[171] CLEO collaboration, B. I. Eisenstein et al., *Precision Measurement of $B(D^+ \to \mu^+\nu)$ and the Pseudoscalar Decay Constant $f_{D^+}$*, *Phys. Rev.* **D78** (2008) 052003, [0806.2112].

[172] CLEO collaboration, J. P. Alexander et al., *Measurement of $B(D_s^+ \to \ell^+\nu)$ and the Decay Constant $f_{D_s^+}$ from 600 $pb^{-1}$ of $e^+e^-$ annihilation data near 4170 MeV*, *Phys. Rev.* **D79** (2009) 052001, [0901.1216].

[173] CLEO collaboration, K. M. Ecklund et al., *Measurement of the absolute branching fraction of $D_s^+ \to \tau^+\nu_\tau$ decay*, *Phys. Rev. Lett.* **100** (2008) 161801, [0712.1175].

[174] CLEO collaboration, P. U. E. Onyisi et al., *Improved Measurement of Absolute Branching Fraction of $D_s^+ \to \tau^+\nu_\tau$*, *Phys. Rev.* **D79** (2009) 052002, [0901.1147].

[175] BESIII collaboration, M. Ablikim et al., *Precision measurements of $B(D^+ \to \mu^+\nu_\mu)$, the pseudoscalar decay constant $f_{D^+}$, and the quark mixing matrix element $|V_{cd}|$*, *Phys. Rev.* **D89** (2014) 051104, [1312.0374].

[176] Belle collaboration, A. Zupanc et al., *Measurements of branching fractions of leptonic and hadronic $D_s^+$ meson decays and extraction of the $D_s^+$ meson decay constant*, *JHEP* **09** (2013) 139, [1307.6240].

[177] BaBar collaboration, P. del Amo Sanchez et al., *Measurement of the Absolute Branching Fractions for $D_s^- \to \ell^- \bar{\nu}_\ell$ and Extraction of the Decay Constant $f_{D_s}$*, *Phys. Rev.* **D82** (2010) 091103, [1008.4080].

[178] HPQCD, UKQCD collaboration, E. Follana, Q. Mason, C. Davies, K. Hornbostel, G. P. Lepage, J. Shigemitsu et al., *Highly improved staggered quarks on the lattice, with applications to charm physics*, *Phys. Rev.* **D75** (2007) 054502, [hep-lat/0610092].

[179] K. Osterwalder and E. Seiler, *Gauge Field Theories on the Lattice*, *Annals Phys.* **110** (1978) 440.

[180] G. Colangelo et al., *Review of lattice results concerning low energy particle physics*, *Eur. Phys. J.* **C71** (2011) 1695, [1011.4408].

[181] N. Carrasco et al., *Leptonic decay constants $f_K, f_D$, and $f_{D_s}$ with $N_f = 2+1+1$ twisted-mass lattice QCD*, *Phys. Rev.* **D91** (2015) 054507, [1411.7908].

[182] P. Dimopoulos, R. Frezzotti, P. Lami, V. Lubicz, E. Picca, L. Riggio et al., *Pseudoscalar decay constants $f_K/f_\pi$, $f_D$ and $f_{D_s}$ with $N_f = 2+1+1$ ETMC configurations*, *PoS* **LATTICE2013** (2014) 314, [1311.3080].

[183] Fermilab Lattice, MILC collaboration, A. Bazavov et al., *Charmed and strange pseudoscalar meson decay constants from HISQ simulations*, *PoS* **LATTICE2013** (2014) 405, [1312.0149].

[184] Fermilab Lattice, MILC collaboration, A. Bazavov et al., *Pseudoscalar meson physics with four dynamical quarks*, *PoS* **LATTICE2012** (2012) 159, [1210.8431].

[185] Y.-B. Yang et al., *Charm and strange quark masses and $f_{D_s}$ from overlap fermions*, *Phys. Rev.* **D92** (2015) 034517, [1410.3343].

[186] H. Na, C. T. H. Davies, E. Follana, G. P. Lepage and J. Shigemitsu, *$|V_{cd}|$ from D Meson Leptonic Decays*, *Phys. Rev.* **D86** (2012) 054510, [1206.4936].

[187] Fermilab Lattice, MILC collaboration, A. Bazavov et al., *$B$- and $D$-meson decay constants from three-flavor lattice QCD*, *Phys. Rev.* **D85** (2012) 114506, [1112.3051].

[188] PACS-CS collaboration, Y. Namekawa et al., *Charm quark system at the physical point of* $2+1$ *flavor lattice QCD*, *Phys. Rev.* **D84** (2011) 074505, [1104.4600].

[189] HPQCD, UKQCD collaboration, E. Follana, C. T. H. Davies, G. P. Lepage and J. Shigemitsu, *High Precision determination of the* $\pi$*,* $K$*,* $D$ *and* $D_s$ *decay constants from lattice QCD*, *Phys. Rev. Lett.* **100** (2008) 062002, [0706.1726].

[190] C. Aubin et al., *Charmed meson decay constants in three-flavor lattice QCD*, *Phys. Rev. Lett.* **95** (2005) 122002, [hep-lat/0506030].

[191] TWQCD collaboration, W.-P. Chen, Y.-C. Chen, T.-W. Chiu, H.-Y. Chou, T.-S. Guu and T.-H. Hsieh, *Decay Constants of Pseudoscalar D-mesons in Lattice QCD with Domain-Wall Fermion*, *Phys. Lett.* **B736** (2014) 231–236, [1404.3648].

[192] J. Heitger, G. M. von Hippel, S. Schaefer and F. Virotta, *Charm quark mass and D-meson decay constants from two-flavour lattice QCD*, *PoS* **LATTICE2013** (2014) 475, [1312.7693].

[193] ETM collaboration, P. Dimopoulos et al., *Lattice QCD determination of* $m_b$*,* $f_B$ *and* $f_{B_s}$ *with twisted mass Wilson fermions*, *JHEP* **01** (2012) 046, [1107.1441].

[194] ETM collaboration, B. Blossier et al., *Pseudoscalar decay constants of kaon and D-mesons from* $N_f = 2$ *twisted mass Lattice QCD*, *JHEP* **07** (2009) 043, [0904.0954].

[195] RBC, UKQCD collaboration, C. Allton et al., $2+1$ *flavor domain wall QCD on a* $(2\,\mathrm{fm})^3$ *lattice: Light meson spectroscopy with* $L_s = 16$, *Phys. Rev.* **D76** (2007) 014504, [hep-lat/0701013].

[196] RBC-UKQCD collaboration, C. Allton et al., *Physical Results from* $2+1$ *Flavor Domain Wall QCD and* $SU(2)$ *Chiral Perturbation Theory*, *Phys. Rev.* **D78** (2008) 114509, [0804.0473].

[197] RBC, UKQCD collaboration, Y. Aoki et al., *Continuum Limit Physics from* $2+1$ *Flavor Domain Wall QCD*, *Phys. Rev.* **D83** (2011) 074508, [1011.0892].

[198] RBC/UKQCD collaboration, T. Blum et al., *Lattice calculation of the leading strange quark-connected contribution to the muon* $g-2$, *JHEP* **04** (2016) 063, [1602.01767].

[199] T. Janowski, P. A. Boyle, A. Jüttner and C. Sachrajda, $K-\pi$ *scattering lengths at physical kinematics*, *PoS* **LATTICE2014** (2014) 080.

[200] T. Blum et al., $K \to \pi\pi$ $\Delta I = 3/2$ *decay amplitude in the continuum limit*, *Phys. Rev.* **D91** (2015) 074502, [1502.00263].

[201] G. Martinelli, C. Pittori, C. T. Sachrajda, M. Testa and A. Vladikas, *A General method for nonperturbative renormalization of lattice operators*, *Nucl. Phys.* **B445** (1995) 81–108, [hep-lat/9411010].

[202] T. Kinoshita, *Radiative corrections to $\pi - e$ decay*, *Phys. Rev. Lett.* **2** (1959) 477.

[203] A. Sirlin, *Large $m(W)$, $m(Z)$ Behavior of the $O(\alpha)$ Corrections to Semileptonic Processes Mediated by $W$*, *Nucl. Phys.* **B196** (1982) 83–92.

[204] H. Na, C. T. H. Davies, E. Follana, G. P. Lepage and J. Shigemitsu, *The $D \to K, l\nu$ Semileptonic Decay Scalar Form Factor and $|V_{cs}|$ from Lattice QCD*, *Phys. Rev.* **D82** (2010) 114506, [1008.4562].

[205] H. Na, C. T. H. Davies, E. Follana, J. Koponen, G. P. Lepage and J. Shigemitsu, *$D \to \pi, l\nu$ Semileptonic Decays, $|V_{cd}|$ and $2^{nd}$ Row Unitarity from Lattice QCD*, *Phys. Rev.* **D84** (2011) 114505, [1109.1501].